MONASH University

Cyclic Peptides Targeting SPSB Proteins as Potential Anti-Infective Agents

Maiada Mohsen Mohamed Sadek Hassan

B.Pharm.Sci (Hons), M.Pharm.Chem

A thesis submitted for the degree of Doctor of Philosophy at Monash University in 2018

Medicinal Chemistry

Faculty of Pharmacy and Pharmaceutical Sciences

Copyright notice

This thesis is dedicated to my beloved daughter,

Farida

Table of Contents

Thesis Abstract

SPRY domain-containing SOCS box proteins (SPSB1, SPSB2 and SPSB4) are involved in the proteasomal degradation of inducible nitric oxide synthase (iNOS). Inhibition of this SPSB-iNOS interaction prolongs the lifespan of iNOS, thus increasing cellular nitric oxide (NO) production, and has been proposed as a potential strategy for killing intracellular pathogens. The cyclic heptapeptides, **CP1** and **CP2**, have been reported as potent inhibitors of the SPSB-iNOS interaction. However, poor membrane permeability limits the potential development of these inhibitors into therapeutic leads.

In this study, I attempted to develop potent cell-permeable SPSB-iNOS inhibitors using a structure-based design approach. Initially, the crystal structures of human SPSB4 bound to **CP1** and **CP2** and human SPSB2 bound to **CP2** were determined using X-ray crystallography. A potent low molecular weight pentapeptide (**CP3**) was designed based on the bound structure of **CP2** in the **CP2**-hSPSB2 complex by replacing a main chain intramolecular hydrogen bond by a C-C linker. Binding studies revealed an approximately 8-fold improvement in binding affinity of **CP3** (K_D =7 nM) to the iNOS binding site of hSPSB2 compared to **CP2** (K_D =32 nM) using surface plasmon resonance (SPR) and ^{19}F NMR. **CP3** also displaced full-length iNOS in macrophage lysates. The crystal structure of the **CP3**-hSPSB2 complex was solved, validating my design methodology. **CP3**, however, was passively impermeable as shown by the parallel membrane artificial permeability assay (PAMPA).

To improve permeability of **CP3**, 29 analogues were designed and synthesised based on the crystal structure analysis of **CP3**-hSPSB2 complex. The impact of three different approaches (decreasing hydrogen bond donors, increasing lipophilicity, and reducing the size) on the affinity and permeability of **CP3** was assessed using SPR and PAMPA. Fourteen analogues were able to bind to hSPSB2 with K_D between 10-700 nM. None of them showed measurable permeability through the artificial membrane, shifting the focus of the study towards conjugating **CP3** to cell-penetrating peptides (CPP).

Two **CP3**-CPP conjugates were designed and synthesised in which **CP3** was fused with a cyclic CPP, (FΦRRRR, Φ=L-naphthylAla), producing a bicyclic peptide or directly conjugated to a linear TAT (RRRQRRKKR) motif. Both conjugates retained binding to hSPSB2 with K_D of 65 and 10 nM, as determined by SPR. Preliminary Griess assay results suggest that these conjugates can deliver the **CP3** cargo into the cytoplasm and increase the NO level, although

extensive additional work needs to be done to confirm the permeability properties of the conjugates. In order to highlight other methods to detect NO, a novel fluorescent blue 'turn-on' coumarin-based probe (**CB**) was investigated in RAW264.7 macrophages. **CB** was able to detect the change in NO levels specifically in real time using confocal microscopy and therefore can be used in future assessment of NO following the internalisation of **CP3**-CPP conjugates.

This research has identified several cyclic and bicyclic peptides as inhibitors of SPSB-iNOS interaction. The structural requirements for this interaction were revealed by crystal structures and SAR of the generated peptide. Hence, this study will be the basis for future engineering of potent and permeable SPSB-iNOS inhibitors as potential anti-infective agents.

Declaration

This thesis contains no material, which has been accepted for the award of any other degree or diploma at any university or equivalent institution and that, to the best of my knowledge and belief, this thesis contains no material previously published or written by another person, except where due reference is made in the text of the thesis.

Signature:

Print Name: Maiada Hassan

Date: 31/12/2018

Publications during enrolment

Sadek, M. M.; Barlow, N.; Leung, E. W. W.; Williams-Noonan, B. J.; Yap, B. K.; Shariff, F. M.; Caradoc-Davies, T. T.; Nicholson, S. E.; Chalmers, D. K.; Thompson, P. E.; Law, R. H. P.; Norton, R. S., A cyclic peptide Inhibitor of the iNOS-SPSB protein-protein Interaction as a potential anti-infective agent. *ACS Chem Biol*. **2018,** *13*, 2930-2938.

Sadek, M. M.; Barzegar Amiri Olia, M.; Nowell, C. J.; Barlow, N.; Schiesser, C. H.; Nicholson, S. E.; Norton, R. S., Characterisation of a novel coumarin-based fluorescent probe for monitoring nitric oxide production in macrophages. *Bioorg Med Chem.* **2017,** *25*, 5743-5748.

Sadek, M. M.; Barlow, N.; Thompson, P. E. ;Chalmers, D. K.; and Norton, R. S. (2018) Cyclic Peptide as a Potential Anti-infective Agent, Aus Patent (Provisional).

Chittoor, B.; Krishnarjuna, B.; Morales, R. A. V.; MacRaild, C. A.; **Sadek, M. M**; Leung, E. W. W.; Robinson, S. D.; Pennington, M. W.; Norton, R. S., The Single Disulfide-Directed β-Hairpin Fold. Dynamics, Stability, and Engineering. *Biochemistry*. **2017,** *56*, 2455-2466.

Thesis including published works declaration

I hereby declare that this thesis contains no material which has been accepted for the award of any other degree or diploma at any university or equivalent institution and that, to the best of my knowledge and belief, this thesis contains no material previously published or written by another person, except where due reference is made in the text of the thesis.

This thesis includes two original papers published in peer reviewed journals. The core theme of the thesis is Medicinal Chemistry. The ideas, development and writing up of all the papers in the thesis were the principal responsibility of myself, the student, working within the Medicinal chemistry under the supervision of Professor Raymond Norton and associate supervision of Dr. David Chalmers and Dr. Nicholas Barlow.

(The inclusion of co-authors reflects the fact that the work came from active collaboration between researchers and acknowledges input into team-based research.)

In the case of Chapters 2 and 5 my contribution to the work involved the following:

Thesis Chapter	**Publication Title**	**Status** *(published, in press, accepted or returned for revision, submitted)*	**Nature and % of student contribution**	**Co-author name(s) Nature and % of Co-author's contribution***	**Co-author(s), Monash student Y/N***
2	A cyclic peptide inhibitor of the iNOS-SPSB protein-protein interaction as a potential anti-infective agent	Published	*65%. Concept, experiment design, collecting data and writing first draft.*	1) Barlow, N. 6% Experiment design 2) Leung, E. W. W. 2% Data collection 3) Williams-Noonan, B J. 1% Data collection 4) Yap, B. K 1% Manuscript preparation 5) Shariff, F. M.; 1% Manuscript preparation 6) Caradoc-Davies, T. T.;1% Data collection 7) Nicholson, S. E. 1% Manuscript preparation	*yes*

				8) Chalmers, D. K. 1% Manuscript preparation 9) Thompson, P. E.1% Manuscript preparation 10) Law, R. H. P.10% Data collection and Manuscript preparation 11) Norton, R. S 10% Manuscript preparation	
5	Characterisation of a novel coumarin-based fluorescent probe for monitoring nitric oxide production in macrophages	Published	*55%. Concept, experiment design , collecting data and writing first draft.*	1) Barzegar Amiri Olia, M. 30% Experiment design, data collection and Manuscript preparation 2) Nowell, C. J. 7 %; Data collection 3) Barlow, N 1%. Manuscript preparation 4) Schiesser, C. H. 1%; Manuscript preparation 5) Nicholson, S. E. 1%; Manuscript preparation 6) Norton, R. S 5%. Manuscript preparation	

I have not renumbered sections of submitted or published papers in order to generate a consistent presentation within the thesis.

Student signature: Date: 31/12/2018

The undersigned hereby certify that the above declaration correctly reflects the nature and extent of the student's and co-authors' contributions to this work. In instances where I am not the responsible author I have consulted with the responsible author to agree on the respective contributions of the authors.

Main Supervisor signature: Date: 31/12/2018

Acknowledgements

Firstly, I would like to express my sincere gratitude to my supervisor Professor Ray Norton for the continuous support of my PhD study and related research, for his patience, motivation, and immense knowledge. His guidance helped me in all the time of research and writing of this thesis. I could not have imagined having a better advisor and mentor for my PhD study.

I would also like to thank my co-supervisors Dr David Chalmers and Dr Nick Barlow for their constant support, availability and constructive suggestions, which were determinant for the accomplishment of the work presented in this thesis.

Thanks to the members of my PhD committee (current and past): Professor Michelle Mclntosh and Associate Professor Bim Graham for generously offering their time. I am also very grateful to Associate Professor Sandra Nicholson who gave me access to her laboratory. This opportunity has allowed me to pick up some useful skills and techniques.

My sincere thanks also go to SPSB team members: Professor Phil Thompson, I have often looked towards him for valuable suggestion, and he always helped me whenever I needed support in my research. The same applies to Dr Eleanor Leung, Dr Steven Yap, and Cameron Nowell for their insightful comments and encouragement.

I thank my fellow labmates and officemates (current and past) for the stimulating discussions, help and support, and for all the fun, we have had in the last three and a half years. Dr Rodrigo Morales, Dr. Krishnarjuna Bankala, Dr Indu Chandrasekaran, Dr Christopher MacRaild, Dr Jeff Seow, Oscar, Khaled, Sreedam, Arfatur, Manusra, Balu, Estelle, Billy, Amanda and Amali. A special note of thanks also to Michela Mitchell, Sanjeevini Babu Reddiar and Noha Badawy for being there to share the ups and downs, and for their love and support throughout this journey.

Many thanks go to my friends from Egypt (Heba, Inas, Gina, Souha, Aliya, Raniya, Walaa and Noha Helmy), who have always encouraged and supported me.

I gratefully acknowledge financial support by Monash University, Monash Graduate Scholarship (MGS) program.

Last but not least, words cannot express how grateful I am to my mother, father, sister, brother and husband for all of the sacrifices that they have made on my behalf. Thank you all

again for your support, understanding and patience. I also would like to thank my beloved daughter, Farida, for being such a good kid and an inspiration to me.

Abbreviations

2D	two-dimensional
Abu	4-aminobutyric acid
Alloc	allyloxycarbonyl
AU	arbitrary units
BMDM	murine bone marrow-derived macrophages
CHIP	Hsp70-interacting protein
clogP	calculated logP
CPP	cell-penetrating peptides
CSA	Cyclosporine A
CTC	cholorotrityl chloride resin
Dab	2,4 diaminobutyric acid
DAF-FM	4-amino-5-methylamino-2 ,7 -difluorofluorescein
DBU	1, 8-diazabicyclo[5.4.0]undec-7-ene
DCM	dichloromethane
DCM	dichloromethane
DIPEA	*N*, *N*-diisopropylethylamine
Dmab	4-{N-[1-(4,4-dimethyl-2,6-dioxocyclohexylidene)-3-methylbutyl] amino}-benzyl
DMEM	Dulbecco's modified Eagle's medium
DMF	dimethylformamide
DMSO	dimethyl sulphoxide
DPBS	Dulbecco's phosphate-buffered saline
DQF-COSY	double-quantum filtered correlation spectroscopy
DTT	dithioerithritol
EDT	1,2-ethanedithiol
EDTA	ethylenediaminetetraacetic acid
eNOS	endothelial nitric oxide synthase
FBDD	fragment-based drug discovery
FBS	fetal bovine serum
Fmoc	fluorenylmethyloxycarbonyl

GalNAc	*N*-acetylgalactosamine
GST	glutathione-*S*-transferase
HBA	hydrogen bond acceptors
HBD	hydrogen bond donors
HCTU	O-(1H-6-chlorobenzotriazole-1-yl)-1,1,3,3 tetramethyluronium hexafluorophosphate
HFIP	hexafluoro-2-propanol
hSPSB	human SPRY domain- and SOCS box-containing protein
HSQC	heteronuclear single quantum coherence
IFN- ɣ	Interferon-ɣ
iNOS	inducible nitric oxide synthase
IPTG	isopropyl β-*D*-1-thio-galactopyranoside
K_D	binding affinity
k_{off}	dissociation rate
k_{on}	association rate
LB	Luria broth
LC-MS	liquid chromatography-mass spectroscopy
L-NMMA	N^G-monomethyl arginine
LPS	lipolysachharide
MD	molecular dynamics
MRSA	Methicillin-resistant *Staphylococcus aureus*
mSPSB	murine SPRY domain- and SOCS box-containing protein
MTT	3-(4,5-dimethylthiazol-2-yl)-2,5-diphenyltetrazolium bromide
MW	Molecular weight
NEMO	NF-κB essential modulator
NMR	nuclear magnetic resonance
nNOS	neuronal nitric oxide synthase
NO	nitric oxide
O-NBS-Cl	O-nitrobenzenylsulfonyl chloride
PAMPA	parallel membrane artificial permeability assay
PDB	protein data bank
PI	propidium iodide
Pin1	prolyl cis-trans isomerase

PPI	protein-protein interaction
PSA	polar surface area
PyClock	6-chloro-benzotriazol- 1-yloxy-tris-pyrrolidinophosphonium hexafluorophosphate
RMSD	root mean square deviation
RMSE	root mean square error
ROESY	rotating frame Overhauser effect spectroscopy
RP-HPLC	reversed-phase high performance liquid chromatography
RU	response units
SAR	structure-activity relationship
SDS	sodium dodecyl sulphate
SDS-PAGE	sodium dodecyl sulphate polyacrylamide gel electrophoresis
SEM	standard error of the mean
SOFAST-HMQC	so fast heteronuclear multiple-quantum coherence
SPPS	solid-phase peptide synthesis
SPR	surface plasmon resonance
SPSB	SPRY domain- and SOCS box-containing protein
TAT	transactivator of transcription
TB	tuberculosis
TCEP.HCl	tris-(2-carboxyethyl)phosphine hydrochloride
TFA	trifluoroacetic acid
TIPS	triisopropylsilane
TOCSY	total correlation spectroscopy
WHO	world Health Organisation
XDR-TB	extensively drug resistant TB

Chapter 1

Introduction

1.1 Antibiotic resistance

Anti-microbial resistance has been a major global health issue for decades.[1] The intensive misuse of antibiotics in human and veterinary medicine has caused the spread of highly resistant pathogenic bacteria worldwide, especially in developing countries (**Figure 1.1a)**.[2] Over the past decade, bacterial resistance has been reported to almost all clinically used antibiotics. Recently, the multidrug resistant pathogens, ESKAPE, an acronym referring to *Enterococcus faecium, Staphylococcus aureus, Klebsiella pneumoniae, Acinetobacter baumannii, Pseudomonas aeruginosa, and Enterobacter species*, were reported as being resistant to cephalosporins, quinolones and carbapenems.[3] One of the most dangerous resistant bacteria identified to date is the Methicillin-resistant *Staphylococcus aureus* (MRSA).[4] This bacterial strain was shown to be resistant to beta-lactam antibiotics (penicillins, cephalosporins, carbapenems) and macrolides**.**[4] MRSA is also associated with several difficult-to-treat infections and high levels of morbidity.[5]

Another example of life-threatening pathogens is MDR-TB (multidrug resistant *Mycobacterium tuberculosis).* MDR-TB is caused by strains of *M. tuberculosis* that are resistant to at least rifampicin and isoniazid, two key drugs in the treatment of the disease. Extensively drug resistant TB (XDR-TB) is also resistant to any fluoroquinolone and to at least one of the injectable drugs, kanamycin, capreomycin or amikacin.[6] More recently, a new TB strain has developed resistance to all antibiotics tested.[4, 7] In 2016, 600,000 new cases of MDR-TB were recorded, resulting in 240,000 deaths.[8] Generally, antimicrobial resistance is expected to threaten the lives of over 10 million people worldwide by the year 2050 according to WHO **(Figure 1.1b).**

a)

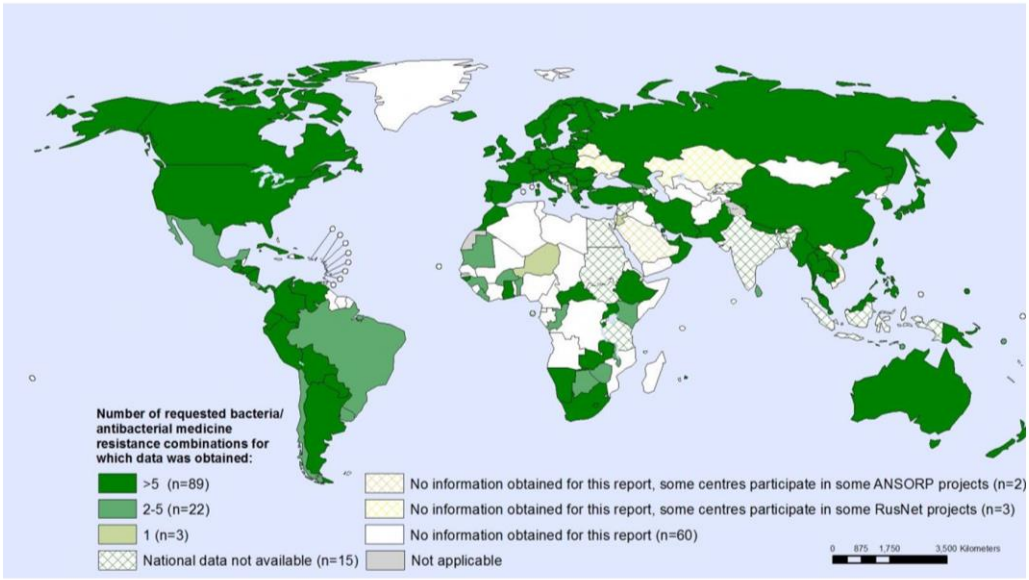

b)

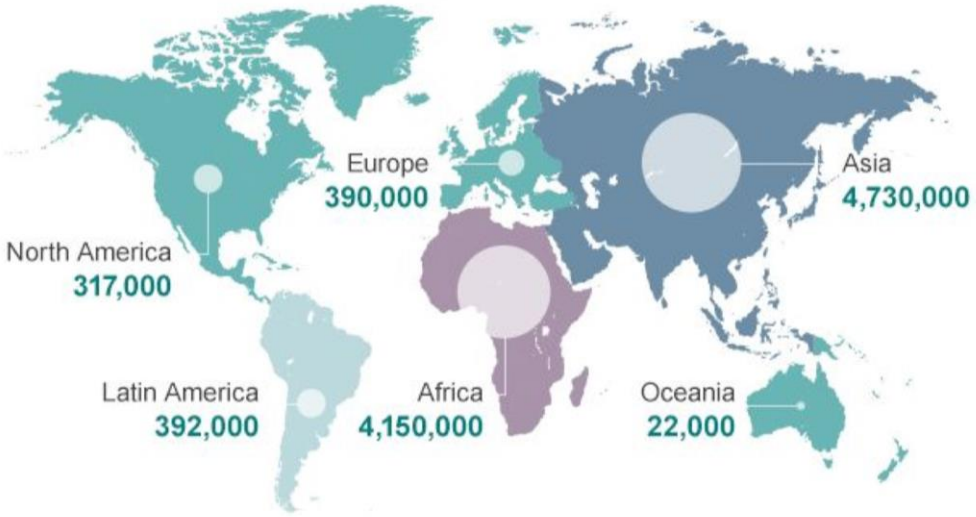

Figure 1.1. a) Global drug resistance overview for selected bacterial-antibacterial drug combinations in 2014. b) Estimated number of deaths caused by resistant bacterial worldwide every year by 2050. Images reproduced from the WHO antimicrobial resistance global report on surveillance 2014.[2]

1.2 Antimicrobial alternative strategies

In the past, discovery of new antibiotics was the main approach for combating resistant bacteria, but since bacterial evolution is uncertain and the timeline for the development of resistance is unpredictable, this strategy may not be effective in the future.[9] Additionally, most pharmaceutical companies have abandoned antimicrobial research owing to the lack of financial rewards.

In order to address these shortcomings, the WHO has implemented a number of strategies to contain this issue in which one of them is to encourage investment in the research and development of new antibiotics, vaccines, diagnostics and other tools.[2, 10] This strategy indeed has renewed interest in finding novel non-conventional anti-infective agents. Czaplewski *et al.* in 2016, summarised the top ten substitutes for antibiotics[11] including phage lysins and antibodies. Lysins kill bacteria directly through destroying the cell wall, or indirectly through weakening of the bacterial biofilms. Antibodies bind to pathogens and inactivate their virulence factors and toxins. Another promising approach is the strategic targeting of host immunity, for example through enhancing the expression of innate antimicrobial peptides using vitamin D and phenyl butyrate.[11]

1.3 Role of inducible nitric oxide synthase in innate immunity

Innate immunity plays a vital role in combating bacterial infections. One of the key components of the innate immune system are macrophages which are responsible for detecting, engulfing and destroying pathogens using bactericidal peptides, enzymes, toxic reactive oxygen species and reactive nitrogen species.[12-13]

Nitric oxide (NO) is a source of reactive nitrogen species produced by the macrophage in response to infection, and exerts its antimicrobial effect in a concentration-dependent manner.[14] Invading pathogens are engulfed by the macrophage where they are exposed to a high concentration of NO that covalently binds to DNA, lipids and proteins of pathogens and kills them.[15] The production of NO is catalysed by an enzyme known as inducible nitric oxide synthase (iNOS/NOS2) through oxidative conversion of L-arginine, oxygen and NADPH to NO and L-citrulline.[16]

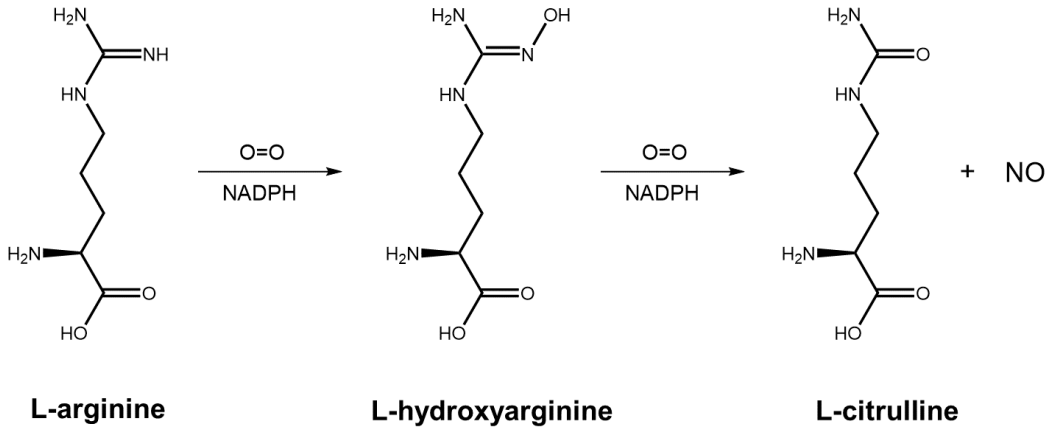

Figure 1.2. Biosynthesis of nitric oxide by iNOS. The enzyme catalyses the oxidation of L-arginine to form nitric oxide and L-citrulline.

The role of iNOS in innate immunity was first identified when it was found that iNOS-deficient mice failed to survive infections including *Listeria* m*onocytogenes*[17], *Leishmania major*[18] or *Mycobacterium tuberculosis* infection.[19] In addition, Nicholson and co-workers reported the loss of antimicrobial activity of alveolar macrophages of *M. tuberculosis* infected patients when treated with iNOS inhibitors.[20] Excessive NO production *via* iNOS is involved in the pathophysiology of multiple human diseases such as asthma, arthritis, multiple sclerosis, colitis, psoriasis, neurodegenerative diseases, tumour development, transplant rejection and septic shock.[21] While iNOS-derived NO is thought to be contained within the activated macrophage, high levels of NO may be deleterious to the macrophage. Consequently, the expression of iNOS is tightly regulated at both transcriptional and post-translational levels (role of gene expression by controlling at DNA and RNA levels, respectively).[22]

At the transcriptional level, iNOS expression is controlled through the binding of transcription factors (e.g. NFκB, STAT1) to the DNA which in return controls the iNOS promotor and subsequently regulation of iNOS expression. At the post-translational level, iNOS is regulated through a number of mechanisms including 1) degradation of the mRNA *via* interaction with RNA-binding proteins (AUF1, HuR, KSRP, PTB and TTP)[23], 2) autoregulation of iNOS expression by NO itself *via* aggresome production,[24] 3) modulation of iNOS protein through protein partners such as Cav-1, Src, ubiquitin ligases[25]. iNOS interacts with either the *C*-terminus of Hsp70-interacting protein (CHIP)[26] or SPRY domain- and SOCS box-containing proteins, which are ubiquitin E3 ligases that target iNOS for proteasomal degradation (**Figure 1.3)**. [25, 27]

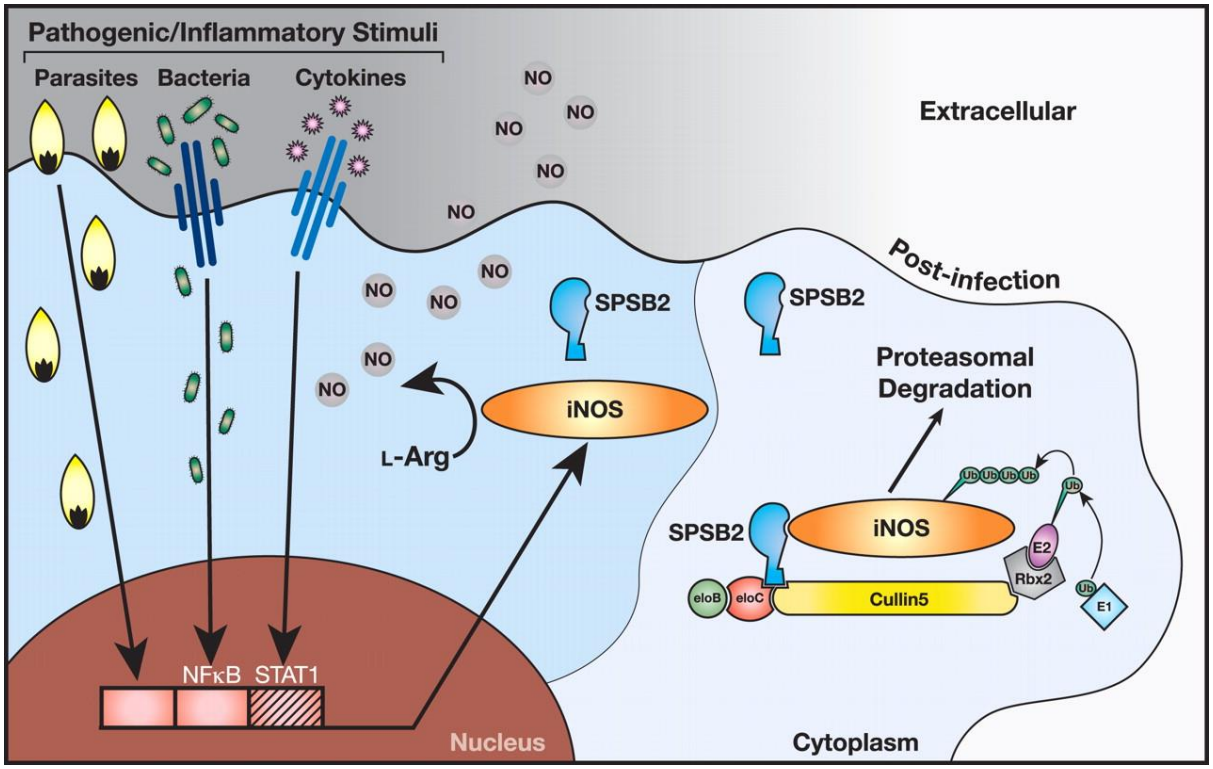

Figure 1.3. Role of SPSB in regulation of iNOS expression in macrophages in response to microbial pathogens and cytokines. *(Figure from Kuang et al. 2010)*[25].

1.4. SPRY domain-containing SOCS box proteins

SPRY domain-containing SOCS box (SPSB) proteins are a family of four members (SPSB 1, 2, 3 and 4) characterised by a central SPRY protein interaction domain that determines the substrate for ubiquitination and a C-terminal SOCS box that recruits an E3 ubiquitin ligase complex.[28] One of the first binding partners discovered for the SPSB protein family was the hepatocyte growth factor receptor, c-Met.[29-30] A subsequent study by Masters *et al.* in 2006 showed that SPSB1, 2 and 4 interact with the human prostate apoptosis response protein-4 (hPar-4).[29] Additionally, the DEAD-box RNA helicase VASA was also found to interact with the *Drosophila* SPSB homologue GUSTAVUS.[31]

The SPRY domain of SPSB proteins can recognise the common motif NNN which is present in both the VASA (DINNNN) and hPar-4 (ELNNNL) sequences, whereas c-Met has a different recognition motif suggesting that c-Met interacts with an alternate binding site on the SPRY domain of the SPSB family.[30] Owing to the absence of the NNN sequence in mouse and human VASA and mouse h-Par4, they are not considered as the physiological target for mammalian SPSB proteins. Using sequence analysis, Kuang *et al.* identified the DINNN motif as conserved in the N-terminus of iNOS (but not e-NOS or n-NOS) among different species, suggesting that

iNOS is biologically relevant to mammalian SPSB (**Figure 1.4**).[25] In the same study, SPSB2 knock-out macrophages showed enhanced nitric oxide production upon lipolysachharide (LPS) stimulation, prolonging iNOS expression and enhancing the killing of pathogens such as *M. tuberculosis* and *Leishmania major* (**Figure 1.5**). Similarly, SPSB1 and SPSB4 were found to be important in the negative regulation of iNOS expression in macrophages.[32]

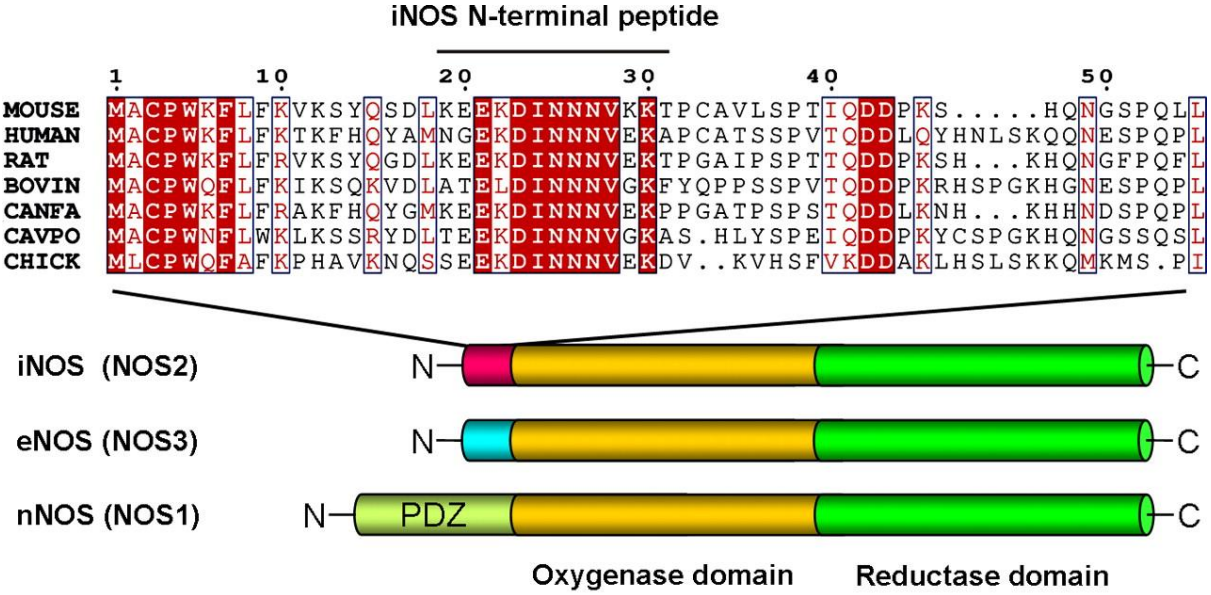

Figure 1.4. DINNN is the motif mediating the SPSB-iNOS interaction. DINNN is conserved among different species in iNOS and not e-NOS or n-NOS *(Figure from Kuang et al. 2010).*[25]

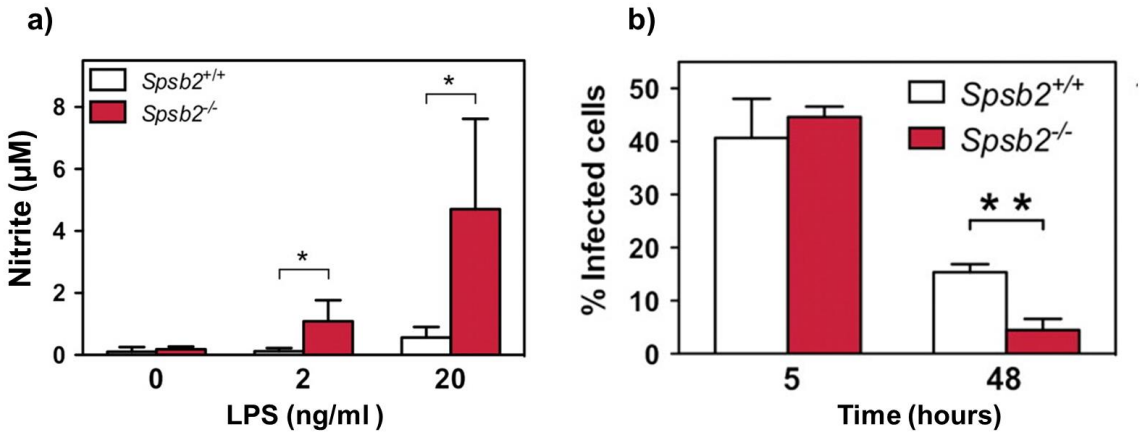

Figure 1.5. Role of SPSB proteins in combating infections. SPSB2-deficient macrophages show a) an increase in nitric oxide production in response to LPS stimulation and b) a decrease in the pathogen load in response to infection with *Leishmania major* parasite. Data are shown as mean ± SD (n = 3, where each replicate represents cells derived from individual mice). *, $P < 0.05$; **, $P < 0.005$. (*Figure reproduced from Kuang et al. 2010).*[25]

1.5 Molecular interactions between SPSB and DINNN containing peptides

Several crystal structures of the free and bound forms of the SPSB proteins have been solved, including apo murine SPSB2 (mSPSB2) (PDB ID: 3EK9)[33], apo human SPSB4 (hSPSB4) (PDB ID: 2V24)[34], the hPar-4/hSPSB1 (PDB ID: 2JK9)[34] VASA/hSPSB1 (PDB ID: 3F2O)[34] and VASA/the hSPSB2 (PDB ID: 3EMW)[34]. Recently, You *et al.* reported the first experimentally determined structure of SPSB2 in complex with an RGD-containing peptide derived from iNOS (PDB ID: 5XN3)[35] and targeting $\alpha_3\beta_3$ integrins.[35]

All SPSB proteins share the same conserved SPRY domain fold, with two short N-terminal helices packed against a bent β-sandwich, comprising two 7-stranded β-sheets (**Figure 1.6a**).[29, 33, 36] The shallow binding pocket is formed by the sidechains of Arg68, Pro70, Thr102, Tyr120, Val206, Trp207 and Gly208 in hSPSB2.[34] Site-directed mutagenesis and two-dimensional (2D) heteronuclear single quantum coherence ([^{1}H,^{15}N]-HSQC) chemical shift perturbation studies using the linear peptide Ac-KEEKDINNNVKKT-NH_2 (K_D 13 nM) further suggested that Arg100, Gly101, Thr102, His103, Leu123, Leu124, Leu125, Ser126, Asn127, Ser128, Val206, and Trp207 in mSPSB2 also contribute to binding.[33]

Comparison of the binding modes of peptides VASA, hPar-4 and RGD-containing peptides shows that the three peptides form extensive hydrogen bonding networks with SPSB residues.[34-35] The conserved NNN residues contribute to seven intermolecular hydrogen bonds between the peptides and SPSB proteins including three between the first Asn and hSPSB2 Thr102 (Thr111 in hSPSB1) and Gly208 in hSPSB2 (Gly218 in hSPSB1) whereas the second Asn forms a hydrogen bond with Gly208, and the third Asn forms three hydrogen bonds with hSPSB2 Arg68 (Arg77 in hSPB1), Tyr120 (Tyr129 in hSPSB1) and Val206 (Val 216 in hSPSB1).[34-35] An additional hydrogen bond was observed between the carboxylic acid side chain of Asp in VASA and the RGD-containing peptide (Glu in h-Par4) (**Figure 1.6a**).[34-35] Further surface plasmon resonance (SPR) and nuclear magnetic resonance (NMR) studies reported the additional conserved flanking residues (Lys22, Val28 and Lys30) of the DINNN sequence in iNOS linear peptides as important in enhancing iNOS-SPSB2 binding, although they have no direct contact with SPSB2 in the crystal structure.[25, 37]

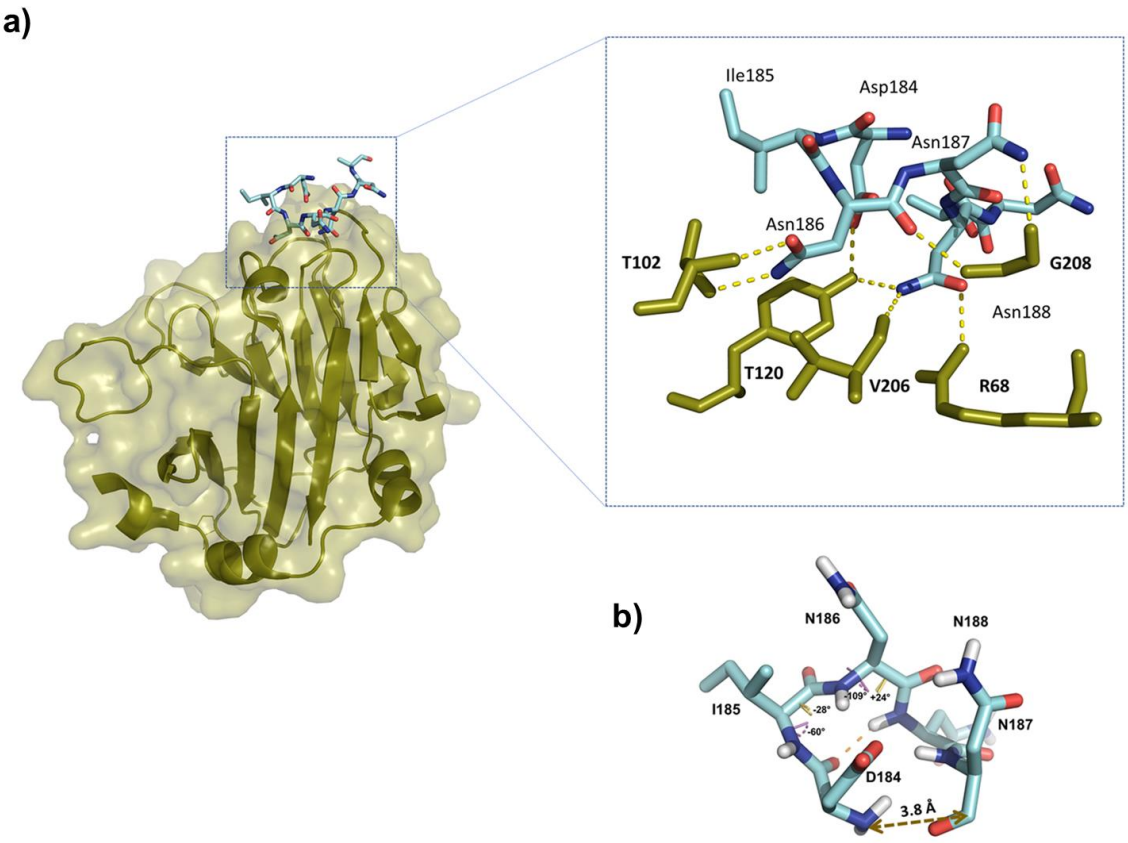

Figure 1.6. Crystal structures of the hSPSB2 (green) complex bound to VASA (blue sticks) (PDB ID: 3EMW).[34] a) Eight conserved intermolecular hydrogen bonds (yellow dashes) are observed between the DINNN of VASA and the SPSB2 proteins. b) DINNN adopts a Type-I β-turn conformation upon binding to SPSB2 with a 3.8 Å distance between the N- and C-terminus of the peptide *(Figure reproduced from Yap et al. 2014).*[38]

1.6. SPSB-iNOS inhibitors

Various approaches have been explored to target the SPSB-iNOS protein-protein interaction (PPI) including a fragment-based design approach (FBDD) and designing cyclic peptides and peptidomimetics. [38-40] *In silico* and NMR-guided FBDD adapted by Yap *et al.* have had limited success in discovering small molecule inhibitors targeting the iNOS binding site of SPSB. The best fragment hit STK441224, was found to bind SPSB2 with a K_D of 1.8 mM by SPR.[41] Further druggability mapping analysis of the binding site showed that the SPSB-iNOS interface is wide, shallow and appears to be less suitable for small molecule binding. Alternatively, the same group designed and synthesised macrocyclic peptide inhibitors based on the SPSB-iNOS binding motif DINNN utilising an i*n silico* structure-based drug design approach.[38,42]

The linear peptide DINNN (K_D= 318 nM) adopts a type I β-turn conformation in the crystal structure of VASA/hSPSB2 (PDB ID: 3EMW),[34, 38] where a key hydrogen bond is formed

between the backbone carbonyl group of Asp184 and the backbone amino group of Asn187 with a distance <7 Å between Cα(i) and Cα(i + 3).[34, 38] It was also observed that the distance between the *N*- and *C*-terminus of the DINNN peptide was <4 Å. Based on these observations, Yap *et al.* designed and synthesised the first cyclic peptide SPSB2-iNOS inhibitor by joining the end of the DINNN linear peptide with a disulfide bridge to increase the biological stability and activity (**Figure 1.6b**).[38]

Among the cyclic peptide models generated, the disulfide-bridged cyclic peptide Ac-c[CVDINNNC]-NH_2 (**CP0**) had the lowest backbone RMSD between the model peptide and the crystal structure of linear DINNN bound to SPSB2 (0.1−0.15 Å). The linear peptide was synthesised using standard solid-phase peptide synthesis (SPPS) procedures followed by cyclisation in solution with 0.1 M ammonium bicarbonate. The binding properties of **CP0** were characterised using SPR and NMR. It was found that the disulfide peptide binds to SPSB2 with K_D = 4 nM, 73-fold better than the linear peptide DINNN (K_D = 318 nM), suggesting that cyclisation has played a role in enhancing the binding affinity presumable due to the increase in conformational rigidity.[38]

Leung *et al.* described a ^{19}F NMR method that provides a simple and reliable assay of peptide interactions with the iNOS binding site on SPSB2.[43] In these experiments an analogue of SPSB2 was prepared in which all six Trp residues of SPSB2 were replaced with 5-F-Trp.[37, 43] Trp207, which is located in the target binding site, proved to be particularly valuable for probing these interactions.[37, 43] The ^{19}F NMR signal of Trp207 shifted downfield upon binding to the cyclic peptide **CP0** to the 5-F-Trp SPSB2, confirming that the cyclic peptide bound to the iNOS binding site on mSPSB2 (**Figure 1.7a**).[38, 43]

CP0 was able to compete with full-length iNOS for binding to SPSB2 in cell lysates using a GST pull-down assay. A GST-SPSB2-SPRY construct, with and without the cyclic peptide analogue, was added to the cell lysates of murine bone marrow-derived macrophages (BMDM) containing endogenous iNOS (induced in response to LPS and IFN-γ) and recovered using glutathione-Sepharose beads. Western blotting with anti-iNOS antibodies indicated that the **CP0** can compete with the endogenous iNOS on the iNOS binding site of SPSB2 (**Figure 1.7b**). The cyclic peptide (**CP0**) was also found to be stable in the presence of digestive enzymes (trypsin, α-chymotrypsin and pepsin) and human plasma.[38] However, **CP0** is unstable in reducing environments owing to the presence of the disulfide linker.[38]

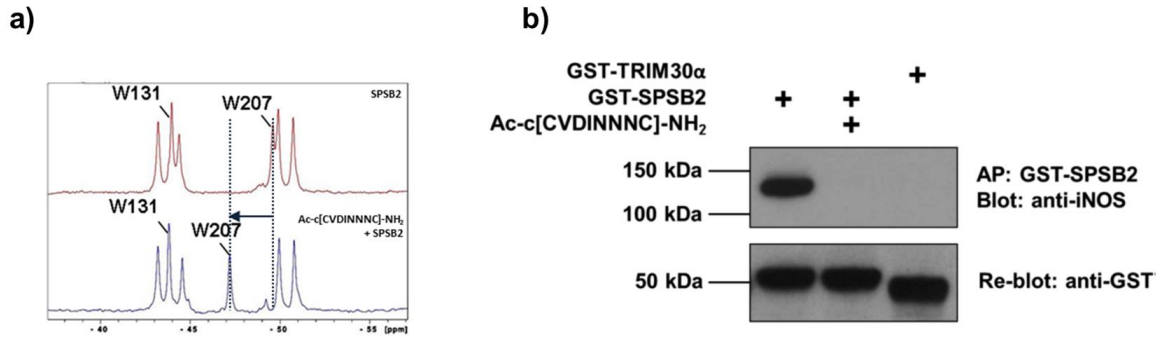

Figure 1.7. Characteristics of **CP0** peptide**.** a) ^{19}F NMR spectrum shows a significant shift in the tryptophan 207 in hSPSB2 after addition of **CP0** (lower panel) which confirms that **CP0** bind to the iNOS binding site of SPSB2. b) **CP0** is able to compete with the iNOS endogenous peptide in BMDM cell lysates. A GST pull down of the recombinant SPSB2v was used in the the presence (+) and absence of **CP0**. The complex was analysed using western blotting with either anti-iNOS antibody (upper panel) or anti-GST antibody (lower panel) (F*igure from Yap et al. 2016)*.[38]

Norton and co-workers designed a number of redox stable analogues to overcome the redox liability issues of **CP0** where the *N*- and *C*-terminus of the DINNN linear motif were cyclised by a redox stable amino acid linker or organic linkers. A cystathionine analogue of Ac-c[CVDINNNC]-NH_2 (**CP1**) and the backbone-cyclised [WDINNNβA] (**CP2**) peptides were designed and synthesised in which the S-S disulfide bond in **CP0** was replaced by a thioether or lactam bridges, respectively (**Figure 1.8).** [40]Both **CP1** and **CP2** were resistant to reduction by dithioerithritol (DTT).[40]

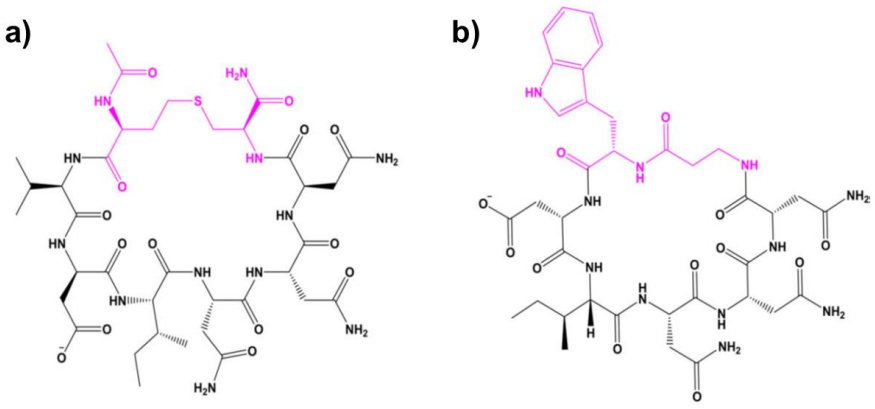

Figure 1.8 Chemical structures of a) **CP1** and b) **CP2** with the redox stable linkers in purple *(Figure is taken from Yap et al. 2016)*. [40]

The other approach to generate redox-stable peptide was to employ an interactive *de novo* design of peptidomimetics (**M1-M4**) in which the backbone of the DINNN peptide was replaced by suitable organic scaffolds (**Figure 1.9**).[39] **M1-M4** mimetics building blocks were retrosynthetically designed and synthesised then incorporated in the peptide sequence using standard solid-phase peptide synthesis (SPPS).

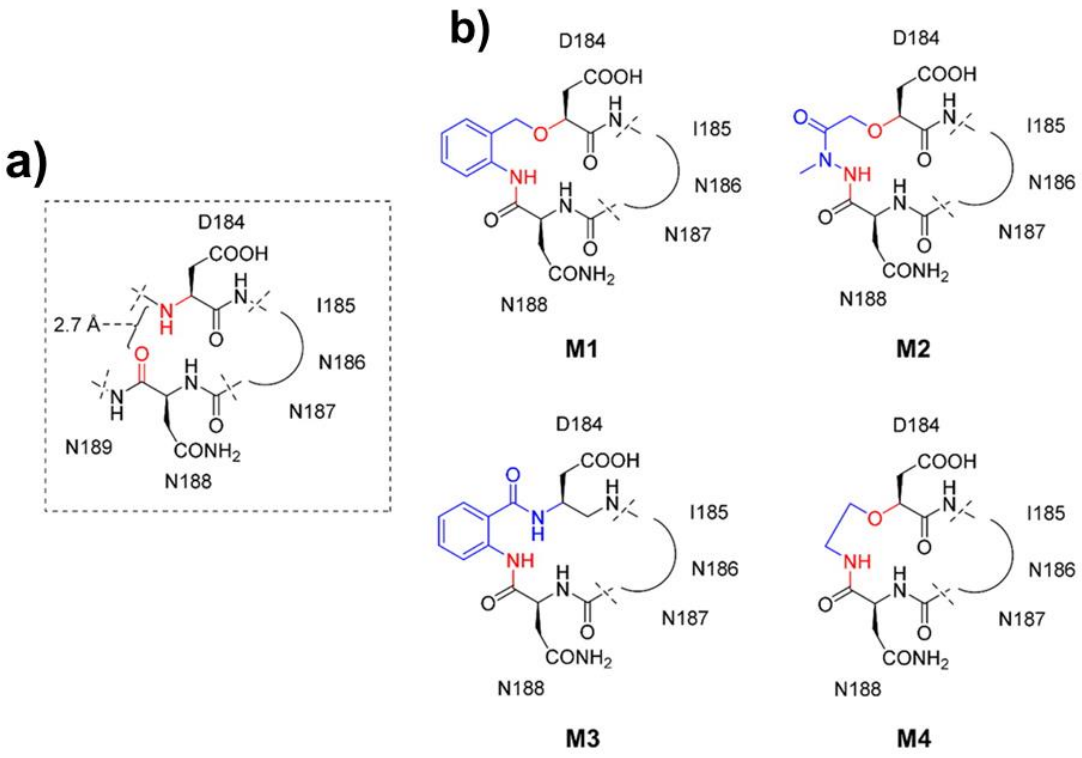

Figure 1.9. Peptidomimetic structures**.** a) SPSB2-DINNN structure showing the N−O distance of 2.7 Å. b) the structure of the peptidomimetics **M1-M4** showing the organic linkers used in each (blue) benzyl, hydrazide, anthranilamide, or ethyl functional group, respectively (*Figure from Harjani et al. 2016).* [39]

Table 1.1. Binding affinities of **CP0** analogues (*Data adapted from Ref. 38, 39 and 40*)

Peptides/mimetic	**CP0**	**CP1**	**CP2**	**M1**	**M2**	**M3**	**M4**
K_D (nM)	4	31	21	29	99	54	465

The cyclic peptides, **CP1** and **CP2**, and the peptide mimetics, **M1-M4**, were found to bind the mSPSB2 with nanomolar binding affinities as measured by SPR (**Table 1.1**).[39-40] ^{19}F NMR experiments further showed that the analogues can perturb or sharpen the W207 signal of

SPSB2, suggesting that they all bind to iNOS binding site of SPSB2.[39-40] All analogues were able to compete with full-length endogenous iNOS for binding to SPSB2 in cell lysates.[39-40 40, 44] As **CP2** is the most active inhibitor of all the redox-stable analogues and can be easily synthesised and derivatised, the Norton group attempted to target the delivery of **CP2** analogues into the cytoplasm of macrophages to ensure that these inhibitors can exert the desired pharmacological responses at the target site.

1.7 Macrophage-targeted delivery

Macrophages express carbohydrate receptors such as the macrophage mannose receptor (CD206), which can recognise mannose and N-acetylglucosamine containing carriers, thereby providing a potential delivery system via receptor-mediated endocytosis.[45] Song *et al.* showed that the fluorescently-labelled mannose- and N-acetylglucosamine (GalNAC)-containing glycopolymers can be used to determine macrophage-specific targeting both *in vitro* and *in vivo* in a dose-dependent manner.[42]

Similarly, Yap *et al.* synthesised GalNAc and mannose polymers bearing a diphenol maleimide moiety to anchor the SPSB-iNOS inhibitors. The thiol side chain of a Cys-containing **CP2** analogue was conjugated to the glycopolymers through a redox-labile disulfide bond. The peptide-glycoploymer conjugates were designed to enter the cells through selective receptor-mediated endocytosis where they would subsequently release the cargo peptide in the reducing environment of the cytoplasm (**Figure 1.10**). Both mannose- and GalNAc-glycopolymers conjugates were further labelled with a rhodamine dye to visualise the peptides in live cells.[46] The rhodamine-labelled conjugates were observed using confocal microscopy and organelle-specific dyes such as LysoGreen as an indicator for late endosomes and lysosomes. Preliminary results showed that the conjugates were successful in targeting the macrophage carbohydrate receptors, but they remain trapped inside the endosomes and were not able to reach the cytoplasmic SPSB (**Figure 1.11)**.

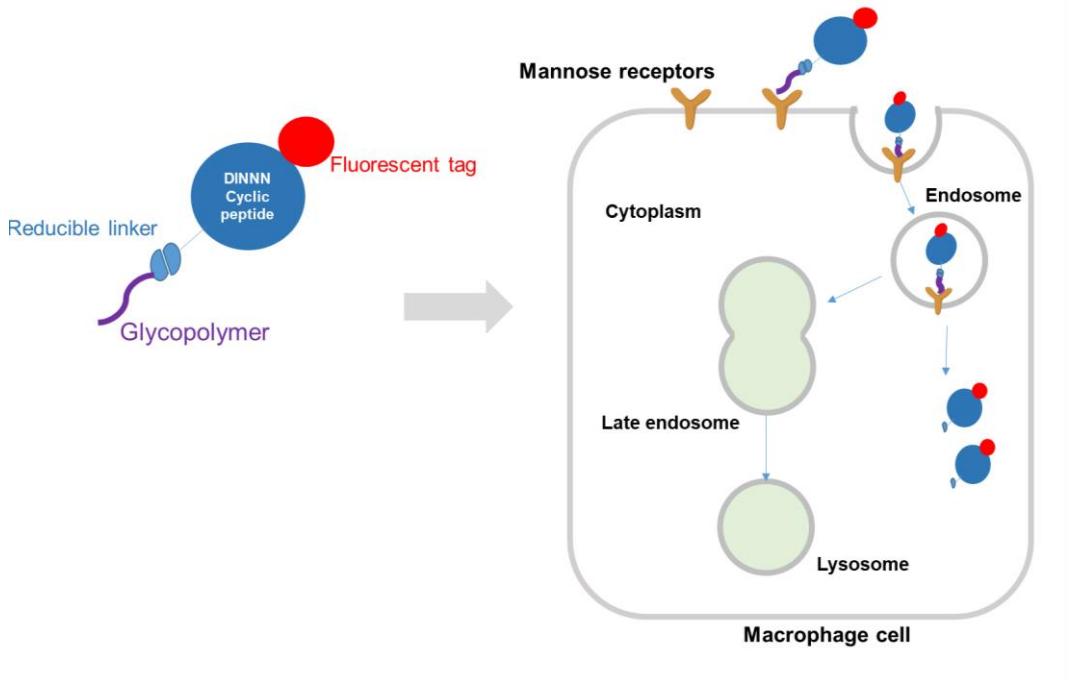

Figure 1.10 Schematic diagram of the expected mechanism of internalisation of **CP2** analogues in macrophages.

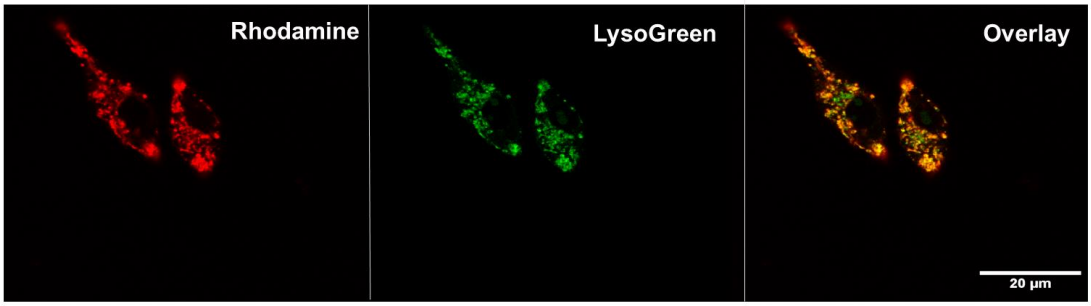

Figure 1.11 Localisation of cyclic peptide-glycoploymer conjugate in late endosomes of RAW 264.7 cells. The images show the rhodamine labelled peptide (red), lysoGreen (green) and overlay image (orange). Scale bar represents 20 µm.

1.8 Scope of the thesis

The increase in antimicrobial resistance and the slow development of new antibiotics suggest the need to explore alternative approaches to treat antibiotic-resistant infections. One attractive approach is to harness the host immune system and the SPSB-iNOS pathway possibly can meet this need. The inhibition of SPSB-iNOS interaction can promote the iNOS levels and enhance the killing of pathogens (*M. tuberculosis* and *L. major* parasites) in macrophages from SPSB2 knock-out mice. Several cyclic peptides have been reported to inhibit the interaction between

SPSB2 and iNOS in macrophage cell lysates. Nevertheless, attempts to target the delivery of these inhibitors to macrophages, in order to inhibit the cytosolic SPSB2-iNOS interaction, had very limited success due to poor membrane permeability and lack of endosomal escape. Therefore, the main aim of this study is to design SPSB-iNOS inhibitors that could penetrate the cell membrane either by direct translocation (passive permeability) or endocytosis (active transport) followed by endosomal escape. These cell-permeable inhibitors would demonstrate the effect of disrupting SPSB-iNOS pathway on enhancing the killing of intracellular pathogens in macrophages cells and support the progress of this class as novel anti-infective agents.

Chapter 2 describes the design and synthesis of a cyclic pentapeptide inhibitor as an attempt to enhance the passive permeability of the previously reported heptapeptide inhibitors. Briefly, investigation into the mode of binding of the heptapeptides was performed through determination of their bound crystal structure complexes with hSPSB proteins. The structural analysis of the peptide-protein complexes facilitated the engineering of low molecular weight pentapeptide using hydrogen bond surrogates. The ability of this peptide to bind to the iNOS binding site of the hSPSB2 was determined by SPR and ^{19}F NMR. An *in vitro* affinity enrichment and immunoblotting assay was employed to investigate the ability of the peptide to displace the endogenous iNOS in macrophages lysates. Furthermore, the crystal structure of the pentapeptide in complex with the hSPSB2 was determined in order to explore the key structural requirements for this interaction.

In Chapter 3, the *in vitro* passive permeability of the cyclic pentapeptide was described using PAMPA assay. Based on this result, several analogues of the cyclic peptide were designed by single residue modifications using natural and unnatural amino acids. The effect of these structural modifications on the overall binding of these analogues to hSPSB2 and cell membrane permeability was investigated by SPR and PAMPA assay respectively.

Chapter 4 reveals an alternative approach to generate cell membrane inhibitors through conjugation to cell-penetrating motifs (CPPs). Two conjugates were designed and synthesised. The effect of incorporation the CPPs moieties on binding to SPSB2 was investigated by SPR. Furthermore, the change in nitric oxide levels was assessed using Griess assay as an indication of permeability.

In Chapter 5, a reported blue turn on nitric oxide probe was investigated in order to further explore different techniques to detect NO in live cells. The ability of the probe to monitor the

NO levels in macrophage cell line in response to bacterial infections and LPS stimulation was studied using confocal microscope. The ability of this probe to track the dynamics of NO production was also evaluated. Furthermore, the cellular toxicity and the biorthogonal compatibility of this probe in a multi-dye system was also explored.

Finally, the major findings from this study are summarised in Chapter 6. The potential future directions of this project are also discussed in the same chapter.

1.9 References

(1) Llor, C.; Bjerrum, L., Antimicrobial resistance: risk associated with antibiotic overuse and initiatives to reduce the problem. *Ther Adv Drug Saf.* **2014,** *5*, 229-241.

(2) WHO, Antimicrobial resistance: global report on surveillance. **2014**.

(3) Richardson, L. A., Understanding and overcoming antibiotic resistance. *PLOS Biol.* **2017,** *15*, e2003775.

(4) Tong, S. Y.; Davis, J. S.; Eichenberger, E.; Holland, T. L.; Fowler, V. G., Staphylococcus aureus infections: epidemiology, pathophysiology, clinical manifestations, and management. *Clin Microbiol Rev.* **2015,** *28*, 603-661.

(5) Boswihi, S. S.; Udo, E. E., Methicillin-resistant Staphylococcus aureus: An update on the epidemiology, treatment options and infection control. *J Curr Med Res Pract.* **2018,** *8*, 18-24.

(6) Gandhi, N. R.; Nunn, P.; Dheda, K.; Schaaf, H. S.; Zignol, M.; van Soolingen, D.; Jensen, P.; Bayona, J., Multidrug-resistant and extensively drug-resistant tuberculosis: a threat to global control of tuberculosis. *The Lancet.* **2010,** *375*, 1830-1843.

(7) Parida, S. K.; Axelsson-Robertson, R.; Rao, M. V.; Singh, N.; Master, I.; Lutckii, A.; Keshavjee, S.; Andersson, J.; Zumla, A.; Maeurer, M., Totally drug-resistant tuberculosis and adjunct therapies. *J Intern Med.* **2015,** *277*, 388-405.

(8) WHO, Multidrug-ResistantTuberclosis (MDR-TB). **2017**.

(9) Ventola, C. L., The antibiotic resistance crisis: part 1: causes and threats. *P T.* **2015,** *40*, 277-283.

(10) Tacconelli, E.; Carrara, E.; Savoldi, A.; Harbarth, S.; Mendelson, M.; Monnet, D. L.; Pulcini, C.; Kahlmeter, G.; Kluytmans, J.; Carmeli, Y.; Ouellette, M.; Outterson, K.; Patel, J.; Cavaleri, M.; Cox, E. M.; Houchens, C. R.; Grayson, M. L.; Hansen, P.; Singh, N.; Theuretzbacher, U.; Magrini, N.; Aboderin, A. O.; Al-Abri, S. S.; Awang Jalil, N.; Benzonana, N.; Bhattacharya, S.; Brink, A. J.; Burkert, F. R.; Cars, O.; Cornaglia, G.; Dyar, O. J.; Friedrich,

A. W.; Gales, A. C.; Gandra, S.; Giske, C. G.; Goff, D. A.; Goossens, H.; Gottlieb, T.; Guzman Blanco, M.; Hryniewicz, W.; Kattula, D.; Jinks, T.; Kanj, S. S.; Kerr, L.; Kieny, M.-P.; Kim, Y. S.; Kozlov, R. S.; Labarca, J.; Laxminarayan, R.; Leder, K.; Leibovici, L.; Levy-Hara, G.; Littman, J.; Malhotra-Kumar, S.; Manchanda, V.; Moja, L.; Ndoye, B.; Pan, A.; Paterson, D. L.; Paul, M.; Qiu, H.; Ramon-Pardo, P.; Rodríguez-Baño, J.; Sanguinetti, M.; Sengupta, S.; Sharland, M.; Si-Mehand, M.; Silver, L. L.; Song, W.; Steinbakk, M.; Thomsen, J.; Thwaites, G. E.; van der Meer, J. W. M.; Van Kinh, N.; Vega, S.; Villegas, M. V.; Wechsler-Fördös, A.; Wertheim, H. F. L.; Wesangula, E.; Woodford, N.; Yilmaz, F. O.; Zorzet, A., Discovery, research, and development of new antibiotics: the WHO priority list of antibiotic-resistant bacteria and tuberculosis. *Lancet Infect Dis.* **2018,** *18*, 318-327.

(11) Czaplewski, L.; Bax, R.; Clokie, M.; Dawson, M.; Fairhead, H.; Fischetti, V. A.; Foster, S.; Gilmore, B. F.; Hancock, R. E.; Harper, D.; Henderson, I. R.; Hilpert, K.; Jones, B. V.; Kadioglu, A.; Knowles, D.; Olafsdottir, S.; Payne, D.; Projan, S.; Shaunak, S.; Silverman, J.; Thomas, C. M.; Trust, T. J.; Warn, P.; Rex, J. H., Alternatives to antibiotics-a pipeline portfolio review. *Lancet Infect Dis.* **2016,** *16*, 239-51.

(12) Hirayama, D.; Iida, T.; Nakase, H., The phagocytic function of macrophage-enforcing innate immunity and tissue homeostasis. *Int J Mol Sci.* **2017,** *19*, 92.

(13) Gasteiger, G.; D'Osualdo, A.; Schubert, D. A.; Weber, A.; Bruscia, E. M.; Hartl, D., Cellular innate immunity: An old game with new players. *J Innate Immun.* **2017,** *9*, 111-125.

(14) Coleman, J. W., Nitric oxide in immunity and inflammation. *Int Immunopharmacol.* **2001,** *1*, 1397-406.

(15) Bogdan, C.; Rollinghoff, M.; Diefenbach, A., The role of nitric oxide in innate immunity. *Immunol Rev.* **2000,** *173*, 17-26.

(16) Bogdan, C., Nitric oxide synthase in innate and adaptive immunity: an update. *Trends Immunol.* **2015,** *36*, 161-78.

(17) MacMicking, J. D.; Nathan, C.; Hom, G.; Chartrain, N.; Fletcher, D. S.; Trumbauer, M.; Stevens, K.; Xie, Q. W.; Sokol, K.; Hutchinson, N.; et al., Altered responses to bacterial infection and endotoxic shock in mice lacking inducible nitric oxide synthase. *Cell.* **1995,** *81*, 641-50.

(18) Diefenbach, A.; Schindler, H.; Donhauser, N.; Lorenz, E.; Laskay, T.; MacMicking, J.; Rollinghoff, M.; Gresser, I.; Bogdan, C., Type 1 interferon (IFNalpha/beta) and type 2 nitric oxide synthase regulate the innate immune response to a protozoan parasite. *Immunity.* **1998,** *8*, 77-87.

(19) Chakravortty, D.; Hensel, M., Inducible nitric oxide synthase and control of intracellular bacterial pathogens. *Microbes Infect.* **2003,** *5*, 621-7.

(20) Nicholson, S.; Bonecini-Almeida Mda, G.; Lapa e Silva, J. R.; Nathan, C.; Xie, Q. W.; Mumford, R.; Weidner, J. R.; Calaycay, J.; Geng, J.; Boechat, N.; Linhares, C.; Rom, W.; Ho, J. L., Inducible nitric oxide synthase in pulmonary alveolar macrophages from patients with tuberculosis. *J Exp Med.* **1996,** *183*, 2293-302.

(21) Zamora, R.; Vodovotz, Y.; Billiar, T. R., Inducible nitric oxide synthase and inflammatory diseases. *Mol Med.* **2000,** *6*, 347-73.

(22) Aktan, F., iNOS-mediated nitric oxide production and its regulation. *Life Sci.* **2004,** *75*, 639-53.

(23) Pautz, A.; Art, J.; Hahn, S.; Nowag, S.; Voss, C.; Kleinert, H., Regulation of the expression of inducible nitric oxide synthase. *Nitric Oxide.* **2010,** *23*, 75-93.

(24) Kolodziejska, K. E.; Burns, A. R.; Moore, R. H.; Stenoien, D. L.; Eissa, N. T., Regulation of inducible nitric oxide synthase by aggresome formation. *Proc Natl Acad Sci USA.* **2005,** *102*, 4854-4859.

(25) Kuang, Z.; Lewis, R. S.; Curtis, J. M.; Zhan, Y.; Saunders, B. M.; Babon, J. J.; Kolesnik, T. B.; Low, A.; Masters, S. L.; Willson, T. A.; Kedzierski, L.; Yao, S.; Handman, E.; Norton, R. S.; Nicholson, S. E., The SPRY domain-containing SOCS box protein SPSB2 targets iNOS for proteasomal degradation. *J Cell Biol.* **2010,** *190*, 129-41.

(26) Chen, L.; Kong, X.; Fu, J.; Xu, Y.; Fang, S.; Hua, P.; Luo, L.; Yin, Z., CHIP facilitates ubiquitination of inducible nitric oxide synthase and promotes its proteasomal degradation. *Cell Immunol.* **2009,** *258*, 38-43.

(27) Matsumoto, K.; Nishiya, T.; Maekawa, S.; Horinouchi, T.; Ogasawara, K.; Uehara, T.; Miwa, S., The ECS(SPSB) E3 ubiquitin ligase is the master regulator of the lifetime of inducible nitric-oxide synthase. *Biochem Biophys Res Commun.* **2011,** *409*, 46-51.

(28) Hilton, D. J.; Richardson, R. T.; Alexander, W. S.; Viney, E. M.; Willson, T. A.; Sprigg, N. S.; Starr, R.; Nicholson, S. E.; Metcalf, D.; Nicola, N. A., Twenty proteins containing a C-terminal SOCS box form five structural classes. *Proc Natl Acad Sci U S A.* **1998,** *95*, 114-9.

(29) Masters, S. L.; Yao, S.; Willson, T. A.; Zhang, J. G.; Palmer, K. R.; Smith, B. J.; Babon, J. J.; Nicola, N. A.; Norton, R. S.; Nicholson, S. E., The SPRY domain of SSB-2 adopts a novel fold that presents conserved Par-4-binding residues. *Nat Struct Mol Biol.* **2006,** *13*, 77-84.

(30) Wang, D.; Li, Z.; Messing, E. M.; Wu, G., The SPRY domain-containing SOCS box protein 1 (SSB-1) interacts with MET and enhances the hepatocyte growth factor-induced Erk-Elk-1-serum response element pathway. *J Biol Chem.* **2005,** *280*, 16393-401.

(31) Styhler, S.; Nakamura, A.; Lasko, P., VASA localization requires the SPRY-domain and SOCS-box containing protein, GUSTAVUS. *Dev Cell.* **2002,** *3*, 865-76.

(32) Nishiya, T.; Matsumoto, K.; Maekawa, S.; Kajita, E.; Horinouchi, T.; Fujimuro, M.; Ogasawara, K.; Uehara, T.; Miwa, S., Regulation of inducible nitric-oxide synthase by the SPRY domain- and SOCS box-containing proteins. *J Biol Chem.* **2011,** *286*, 9009-19.

(33) Kuang, Z.; Yao, S.; Xu, Y.; Lewis, R. S.; Low, A.; Masters, S. L.; Willson, T. A.; Kolesnik, T. B.; Nicholson, S. E.; Garrett, T. J.; Norton, R. S., SPRY domain-containing SOCS box protein 2: crystal structure and residues critical for protein binding. *J Mol Biol.* **2009,** *386*, 662-74.

(34) Filippakopoulos, P.; Low, A.; Sharpe, T. D.; Uppenberg, J.; Yao, S.; Kuang, Z.; Savitsky, P.; Lewis, R. S.; Nicholson, S. E.; Norton, R. S.; Bullock, A. N., Structural basis for Par-4 recognition by the SPRY domain- and SOCS box-containing proteins SPSB1, SPSB2, and SPSB4. *J Mol Biol.* **2010,** *401*, 389-402.

(35) You, T.; Wang, Y.; Li, K.; Zhang, D.; Wei, H.; Luo, Y.; Li, H.; Lu, Y.; Su, X.; Kuang, Z., Crystal structure of SPSB2 in complex with a rational designed RGD-containing cyclic peptide inhibitor of SPSB2-iNOS interaction. *Biochem Biophys Res Commun.* **2017,** *489*, 346-352.

(36) Yao, S.; Liu, M. S.; Masters, S. L.; Zhang, J. G.; Babon, J. J.; Nicola, N. A.; Nicholson, S. E.; Norton, R. S., Dynamics of the SPRY domain-containing SOCS box protein 2: flexibility of key functional loops. *Protein Sci.* **2006,** *15*, 2761-72.

(37) Leung, E. W.; Yagi, H.; Harjani, J. R.; Mulcair, M. D.; Scanlon, M. J.; Baell, J. B.; Norton, R. S., 19F NMR as a probe of ligand interactions with the iNOS binding site of SPRY domain-containing SOCS box protein 2. *Chem Biol Drug Des.* **2014,** *84*, 616-25.

(38) Yap, B. K.; Leung, E. W.; Yagi, H.; Galea, C. A.; Chhabra, S.; Chalmers, D. K.; Nicholson, S. E.; Thompson, P. E.; Norton, R. S., A potent cyclic peptide targeting SPSB2 protein as a potential anti-infective agent. *J Med Chem.* **2014,** *57*, 7006-15.

(39) Harjani, J. R.; Yap, B. K.; Leung, E. W.; Lucke, A.; Nicholson, S. E.; Scanlon, M. J.; Chalmers, D. K.; Thompson, P. E.; Norton, R. S.; Baell, J. B., Design, synthesis, and characterization of cyclic peptidomimetics of the inducible nitric oxide synthase binding epitope that disrupt the protein-protein interaction involving SPRY domain-containing suppressor of cytokine signaling box protein (SPSB) 2 and Inducible nitric oxide synthase. *J Med Chem.* **2016,** *59*, 5799-809.

(40) Yap, B. K.; Harjani, J. R.; Leung, E. W.; Nicholson, S. E.; Scanlon, M. J.; Chalmers, D. K.; Thompson, P. E.; Baell, J. B.; Norton, R. S., Redox-stable cyclic peptide inhibitors of the SPSB2-iNOS interaction. *FEBS Lett.* **2016,** *590*, 696-704.

(41) Devine, S. M.; Mulcair, M. D.; Debono, C. O.; Leung, E. W. W.; Nissink, J. W. M.; Lim, S. S.; Chandrashekaran, I. R.; Vazirani, M.; Mohanty, B.; Simpson, J. S.; Baell, J. B.; Scammells, P. J.; Norton, R. S.; Scanlon, M. J., Promiscuous 2-Aminothiazoles (PrATs): A frequent hitting scaffold. *J Med Chem.* **2015,** *58*, 1205-1214.

(42) Joo, S. H., Cyclic peptides as therapeutic agents and biochemical tools. *Biomol Ther.* **2012,** *20*, 19-26.

(43) Norton, R.; Leung, E.; Chandrashekaran, I.; MacRaild, C., Applications of 19F-NMR in fragment-based drug discovery. *Molecules.* **2016,** *21*, 860.

(44) Jain, N. K.; Mishra, V.; Mehra, N. K., Targeted drug delivery to macrophages. *Expert Opin Drug Deliv.* **2013,** *10*, 353-67.

(45) Lyubov Yu, F.; Natalia, L. K.; Elena, V. K., Targeted delivery of anti-tuberculosis drugs to macrophages: targeting mannose receptors. *Russ Chem Rev.* **2018,** *87*, 374.

(46) Yap, B. K. Inhibitors of SPSB-iNOS interactions as a potential novel class of anti-infectives (unpublished doctoral dissertation). Monash University, Australia, 2016.

Cyclic Peptide Inhibitor of the SPSB-iNOS Protein-Protein Interaction as a Potential Anti-Infective Agent

Chapter 2

2.2 Introduction

In attempt to design inhibitors of SPSB2-iNOS interaction with enhanced passive permeability, a structural based design approach was employed in this Chapter. The mode of binding of the previously reported cyclic heptapeptides, **CP1** and **CP2**, was first identified through the determination of the crystal structure of **CP1**-hSPSB4 and **CP2**-hSPSB2 and **CP2**-hSPSB4 complexes. The **CP2**-hSPSB2 crystal structure was then used to design a cyclic pentapeptide, **CP3**, with low molecular weight, enhanced hydrophobicity and overall drug likeness. The pentapeptide was designed using a hydrogen bond surrogate method in which a main chain intramolecular hydrogen bond in the bound structure of **CP2** was replaced with a covalent linker. The best *in silico* designed and energy minimised model, with lowest backbone RMSD to the crystal structure of **CP2**-hSPSB2, was synthesised and characterised by LC-MS and NMR experiments. The ability of **CP3** to bind to the iNOS binding site of hSPSB2 was examined using ^{19}FNMR and the binding affinity of this interaction was measured by SPR. The ability of the pentapeptide to inhibit SPSB-iNOS interaction in macrophage cell lysates was assessed using affinity enrichment and immunoblotting assay. The crystal structure of **CP3**-hSPSB2 complex was also determined in order to explore the mode of binding of **CP3** to hSPSB2. As the results of this Chapter have been published in *ACS Chemical Biology* journal, they are presented in the format of a published article in the following chapter.

ACS chemical biology

Articles

Cite This: ACS Chem. Biol. 2018, 13, 2930−2938

pubs.acs.org/acschemicalbiology

A Cyclic Peptide Inhibitor of the iNOS−SPSB Protein−Protein Interaction as a Potential Anti-Infective Agent

Maiada M. Sadek,[†] Nicholas Barlow,[†] Eleanor W. W. Leung,[†] Billy J. Williams-Noonan,[†] Beow Keat Yap,[†,@] Fairolniza Mohd Shariff,[∥] Tom T. Caradoc-Davies,[⊥] Sandra E. Nicholson,[‡,§] David K. Chalmers,[†] Philip E. Thompson,[†] Ruby H. P. Law,[*,#] and Raymond S. Norton[*,†]

[†]Medicinal Chemistry, Monash Institute of Pharmaceutical Sciences, Monash University, Parkville Victoria 3052, Australia

[‡]The Walter and Eliza Hall Institute of Medical Research, Parkville Victoria 3052, Australia

[§]The Department of Medical Biology, University of Melbourne, Parkville, Victoria 3052, Australia

[∥]Department of Microbiology, Faculty of Biotechnology and Biomolecular Sciences, Universiti Putra, 43400 Seri Kembangan, Selangor, Malaysia

[⊥]Australian Synchrotron, Victoria 3168, Australia

[#]Department of Biochemistry and Molecular Biology and Australian Research Council Centre of Excellence in Advanced Molecular Imaging, Monash University, Clayton, Victoria 3800, Australia

Supporting Information

ABSTRACT: SPRY domain- and SOCS box-containing proteins SPSB1, SPSB2, and SPSB4 interact with inducible nitric oxide synthase (iNOS), causing the iNOS to be polyubiquitinated and targeted for degradation. Inhibition of this interaction increases iNOS levels, and consequently cellular nitric oxide (NO) concentrations, and has been proposed as a potential strategy for killing intracellular pathogens. We previously described two DINNN-containing cyclic peptides (CP1 and CP2) as potent inhibitors of the murine SPSB−iNOS interaction. In this study, we report the crystal structures of human SPSB4 bound to CP1 and CP2 and human SPSB2 bound to CP2. We then used these structures to design a new inhibitor in which an intramolecular hydrogen bond was replaced with a hydrocarbon linkage to form a smaller macrocycle while maintaining the bound geometry of CP2 observed in the crystal structures. This resulting pentapeptide SPSB−iNOS inhibitor (CP3) has a reduced macrocycle ring size, fewer nonbinding residues, and includes additional conformational constraints. CP3 has a greater affinity for SBSB2 (K_D = 7 nM as determined by surface plasmon resonance) and strongly inhibits the SPSB2−iNOS interaction in macrophage cell lysates. We have also determined the crystal structure of CP3 in complex with human SPSB2, which reveals the structural basis for the increased potency of CP3 and validates the original design.

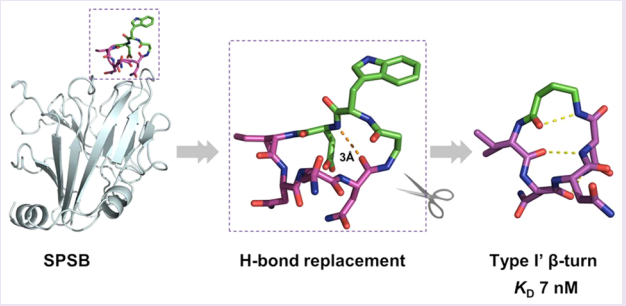

The SPRY domain- and SOCS box-containing protein (SPSB) protein family consists of four members, SPSB1−SPSB4. Each is composed of a central SPRY/B30.2 domain and a C-terminal SOCS box.[1−5] SPSB1, -2, and -4 recruit an E3 ubiquitin ligase complex via the SOCS box to polyubiquitinate iNOS, thereby targeting it for proteasomal degradation.[6−8] Deletion of the SPSB2 gene in mice enhances the killing of intracellular pathogens such as *Mycobacterium tuberculosis* and *Leishmania major* by prolonging the lifetime of iNOS and enhancing nitric oxide (NO) production.[6] This study suggested that inhibitors of the SPSB−iNOS interaction may represent novel anti-infective agents that act by enhancing the host immune response.

The interaction between iNOS and the SPRY domains of SPSB1, -2, and -4 is mediated by the N-terminal region of iNOS, which is disordered and contains a DINNN pentapeptide sequence.[6−9] Isothermal titration calorimetry and surface plasmon resonance (SPR) binding studies on a range of peptides containing the DINNN sequence show that all residues contribute to binding to SPSB proteins, with the Asp and the first and third Asn residues being the most important.[6,10] As the linear DINNN peptide binds to murine SPSB2 (mSPSB2) with only modest affinity (K_D = 318 nM),[10,11] we have developed a number of structurally diverse cyclic peptides and peptidomimetics that inhibit interactions between the SPSB proteins and iNOS with a higher affinity and are more stable than the linear sequence.[11−13] Our designs have been informed by X-ray crystal structures of DINNN-containing linear peptides bound to human SPSB proteins.[9]

Received: June 17, 2018
Accepted: September 5, 2018
Published: September 18, 2018

DOI: 10.1021/acschembio.8b00561
ACS Chem. Biol. 2018, 13, 2930−2938

The disulfide-constrained cyclic peptide Ac-c[CVDINNNC]-NH_2 (designated CP0) binds potently to murine SPSB2 (K_D = 4 nM). Although reduction of the disulfide bond causes a significant loss of activity,[11] we have shown that the disulfide bond in CP0 can be replaced with a reduction-resistant thioether to create the cystathionine analogue of Ac-c[CVDINNNC]-NH_2 (designated CP1) or with an amide linker to create c[WDINNNbA] (designated CP2) while retaining nanomolar affinities.[13] CP1 and CP2 bind to the iNOS binding site of mSPSB2 with affinities of 31 and 21 nM, respectively, and compete with full-length iNOS for binding to mSPSB2 in macrophage cell lysates.[13]

The binding of CP1 and CP2 to SPSB2 has been investigated by ^{19}F nuclear magnetic resonance (NMR).[13,14] These studies confirm that the peptides bind to the iNOS binding site, but they do not define their exact binding pose. In addition, although crystal structures of other SPSB proteins with bound linear peptides have been determined,[9] only one structure of a complex of human SPSB2 (hSPSB2) with a cyclic peptide has been reported.[15]

In this work, we report the crystal structures of the CP1 and CP2 peptides bound to hSPSB4 and of CP2 bound to hSPSB2. Comparison of the bound structures of CP1 and CP2 provided a detailed understanding of the key contacts between these two peptides and human SPSB proteins. On the basis of these structures, we have designed and synthesized a smaller and more potent cyclic pentapeptide (CP3) in which an intramolecular hydrogen bond was replaced with a hydrocarbon linkage to reduce macrocyclic size while maintaining the bound geometry of CP2 observed in the crystal structures. Using ^{19}F NMR experiments, we show that the CP3 peptide binds to the iNOS binding site of hSPSB2. We also show that CP3 can inhibit the interaction of full-length iNOS with hSPSB2 in macrophage lysates. Finally, we have determined the crystal structure of CP3 bound to hSPSB2. This development of CP3, a stable cyclic peptide with a mass of just 540 Da, coupled with the structural information reported here, provides a foundation for the design of new conformationally constrained peptidomimetics or small molecule inhibitors of the SPSP2−iNOS interaction as potential anti-infective agents.

RESULTS AND DISCUSSION

Crystal Structures of CP1 and CP2 Bound to Human SPSB2 and Human SPSB4. To gain further insight into the molecular basis for cyclic peptide−SPSB interactions, we determined the crystal structures of CP1 bound to the SPRY domain of hSPSB4 and CP2 bound to the SPRY domains of hSPSB2 and hSPSB4. Constructs encoding the SPRY domain of human SPSB2 and SPSB4 proteins were expressed in *Escherichia coli* strain BL21 (DE3). After purification via Ni-affinity chromatography, the His-tagged proteins were cleaved with TEV protease and further purified by gel filtration chromatography. The identity and purity of the proteins were assessed using liquid chromatography and mass spectrometry (LC−MS) and ^{1}H NMR (Figure S1). Peptides CP1 and CP2 were synthesized and characterized as reported previously.[13] SPR studies showed K_D values for binding of CP1 and CP2 to hSPSB2 of 20 and 32 nM, respectively (Table 1), in good agreement with the previously reported values for binding of CP1 and CP2 to murine SPSB2 (mSPSB2) of 31 and 21 nM, respectively.[12,13] Comparison of the kinetic profiles of CP1 and CP2 with hSPSB2 (Table 1) also revealed that the peptides bound to hSPSB2 with k_{on} and k_{off} values similar to those reported for mSPSB2.[13] The CP1−hSPSB4 crystal diffracted to 1.75 Å with three copies in the asymmetric unit; the CP2−hSPSB4 crystal diffracted to 1.4 Å with two copies in the asymmetric unit, and the CP2−hSPSB2 diffracted to 2.4 Å with one copy in the asymmetric unit (Table S2 and Figure S2). Both human SPSB2 and SPSB4 retain the conserved SPRY domain fold reported previously (Figure 1a).[9,16]

Table 1. Interaction Kinetics of Binding of CP1−CP3 to hSPSB2

cyclic peptide	K_D (nM)[a]	k_{on} ($\times 10^6$ M^{-1} s^{-1})	k_{off} (s^{-1})
CP1	20 ± 3	1.76 ± 0.3	0.03 ± 0.005
CP2	32 ± 4	0.84 ± 0.3	0.026 ± 0.006
CP3	7 ± 2	0.5 ± 0.1	0.0032 ± 0.0004

[a]All values are means ± the standard error (n = 3).

Superimposition of the three co-crystal structures shows that, in each case, the DINNN motifs of CP1 and CP2 adopt very similar backbone conformations, with mean pairwise Cα root-mean-square deviations (RMSDs) of 0.1−0.2 Å. Both CP1 and CP2 make intramolecular hydrogen bonds that stabilize their bound conformation. The intramolecular hydrogen bonds include four bonds, one between the backbone CO of Asp3 in CP1 (Asp2 in CP2) and the backbone NH of Asn6 in CP1 (Asn5 in CP2), two between the side chain OD1 of Asp3 and backbone NH of Asn7 in CP1 (Asn6 in CP2) and Asn5 in CP1 (Asn4 in CP2), and one between the backbone CO of Asn5 in CP1 (Asn4 in CP2) and the side chain NH of Asn7 (Asn6 in CP2). One additional bond exists in CP2 between the backbone NH of Asp2 and the backbone CO of Asn6 (Figure 1b). Our previously reported *in silico* models of the DINNN sequence of CP1 and CP2 bound to mSPSB2[13] closely match these crystal structures, with Cα RMSDs of 0.8−1.4 Å. The main differences between the experimental structures and the models are around the Trp1 residue in CP2, the cystathionine linker, and the Val2 residue in CP1 (Figure S3). These residues extend outside the binding pocket and thus have little influence on the binding pose of the DINNN motif with respect to the SPSB protein.[11,13]

The hSPSB4−CP1, hSPSB4−CP2, and hSPSB2−CP2 protein−peptide complexes are stabilized by a network of five conserved hydrogen bonds (Figure 2 and Figure S2). One hydrogen bond is found between the carboxyl group of Asp3 in CP1 (Asp2 in CP2) and the phenolic hydroxyl of Tyr129 (hSPSB4) or Tyr120 (hSPSB2); two hydrogen bonds are found between the carboxamide side chain of Asn5 (Asn4 in CP2) and the backbone amide and the hydroxyl side chain of Thr111 (hSPSB4) or Thr102 (hSPSB2), and two hydrogen bonds between the backbone carbonyl group of Asn6 (Asn5 in CP2) and the backbone amide of Gly218 (hSPSB4) or Gly208 (hSPSB2) and the amide side chain of Asn6 (Asn5 in CP2) and the backbone carbonyl group of Gly218 (hSPSB4) or Gly208 (hSPSB2). An additional intermolecular hydrogen bond was also observed between the carboxyl side chain of Asp2 in CP2 and the side chain NH of Gln73 in the CP2−hSPSB2 complex.

The functionally important side chain of Asn7 in CP1 (Asn6 in CP2)[6] contributes four additional interactions with the side chain of Arg68 in hSPSB2 (Arg77 in hSPSB4), the phenolic hydroxyl of Tyr120 in hSPSB2 (Tyr129 in hSPSB4), the backbone carbonyl of Val206 in hSPSB2 (Val216 in hSPSB4), and the backbone amide of Val71 in hSPSB2 (Val80 in hSPSB4) (Figure 2 and Figure S2).

DOI: 10.1021/acschembio.8b00561
ACS Chem. Biol. 2018, 13, 2930−2938

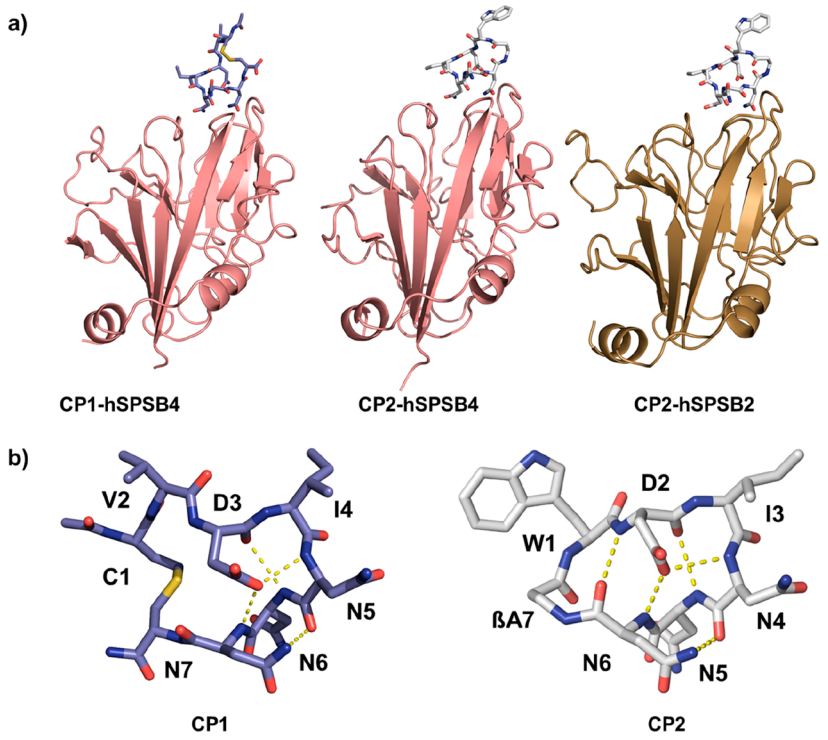

Figure 1. (a) Cartoon representations of the crystal structures of hSPSB4 (pink) bound to CP1 (blue, PDB entry 6DN8) and CP2 (white, PDB entry 6DN7) and hSPSB2 (brown) bound to CP2 (white, PDB entry 6DN5). C1 and C2 are shown as sticks. (b) Stick representation of CP1 (blue) and CP2 (white) showing the intrachain hydrogen bonding. Conserved hydrogen bonds stabilize the bound conformation of the cyclic peptides; hydrogen bonds are indicated by yellow dashed lines.

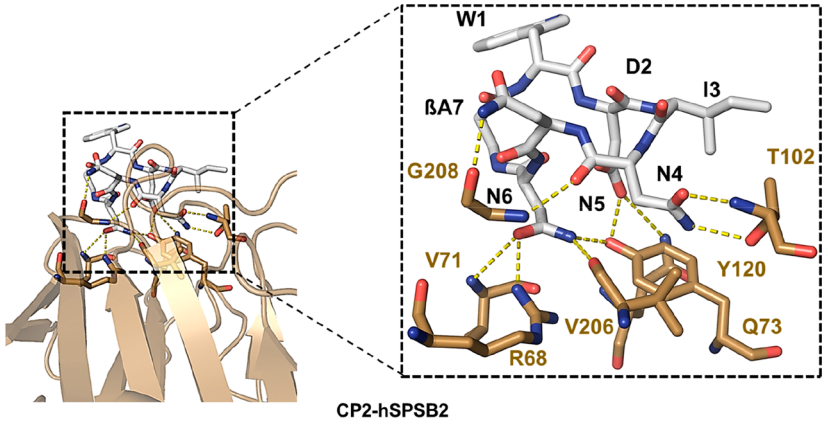

Figure 2. Intermolecular interactions between CP2 and hSPSB2. Dashed lines show the 10 intermolecular hydrogen bonds formed between CP2 (white) and hSPSB2 (brown) (PDB entry 6DN5). Similar bonds are formed in the complexes of CP1 and CP2 with hSPSB4.

Structure-Based Design and Synthesis of a Nanomolar Pentapeptide Inhibitor, CP3. On the basis of the crystal structure of the CP2−hSPSB2 complex, we designed a new inhibitor with improved hydrophobicity and drug-likeness. In designing this inhibitor, we aimed to replace an intramolecular hydrogen bond with a hydrocarbon linkage to maintain the bound geometry of CP2 observed in the crystal structure and reduce the entropic cost of binding. Of the four intramolecular hydrogen bonds found in the bound CP2 structure, the hydrogen bond between the Asn6 backbone carbonyl group and the Asp2 backbone nitrogen (3.1 Å) was identified as a potentially useful position for covalent replacement. This allows the removal of the Trp1 and βA7 residues, which do not interact directly with the protein (Figure 3). Eliminating these two residues and rotating the Asn6 amide to swap the position of the nitrogen and oxygen atoms then allowed replacement of the hydrogen bond and Asp2 residue with a γ-amino acid (Figure 3a). This strategy provided the new cyclic pentapeptide c[INNNAbu] (CP3), which, when minimized in the iNOS binding site, was found to fit with an RMSD of 0.3 Å between the model peptide and the crystal structure of heptapeptide CP2 (Figure 3b). Designs based on the replacement of other hydrogen bonds disrupted the geometry of the binding pose and provided compounds with poor RMSDs.

The synthetic strategy for CP3 involved solid phase peptide synthesis (SPPS), with both linear synthesis and cyclization performed on resin. Synthesis (Scheme 1) was achieved by initially coupling the side chain of Fmoc-Asp-ODmab to Rink amide resin to provide a side chain-linked Asn. The Dmab

DOI: 10.1021/acschembio.8b00561
ACS Chem. Biol. 2018, 13, 2930−2938

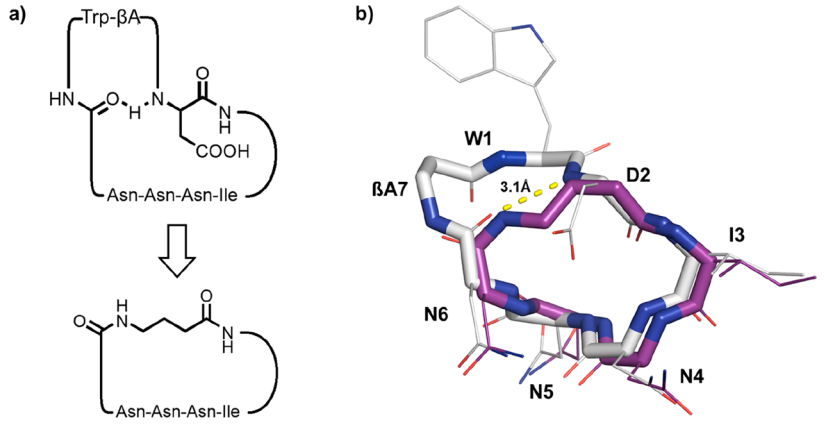

Figure 3. (a) Design of the smaller, less polar peptide, CP3, by replacement of an intramolecular bond with a covalent linkage. (b) Superimposition of the crystal structure of CP2 (white, PDB entry 6DN5) with the *in silico* model of CP3 (purple), showing that the two structures align well over the backbone INNN motif, with a Cα RMSD of 0.3 Å. A hydrogen bond between Asp2 and Asn6 is indicated by a yellow dashed line.

Scheme 1. Synthesis of Cyclic Pentapeptide CP3[a]

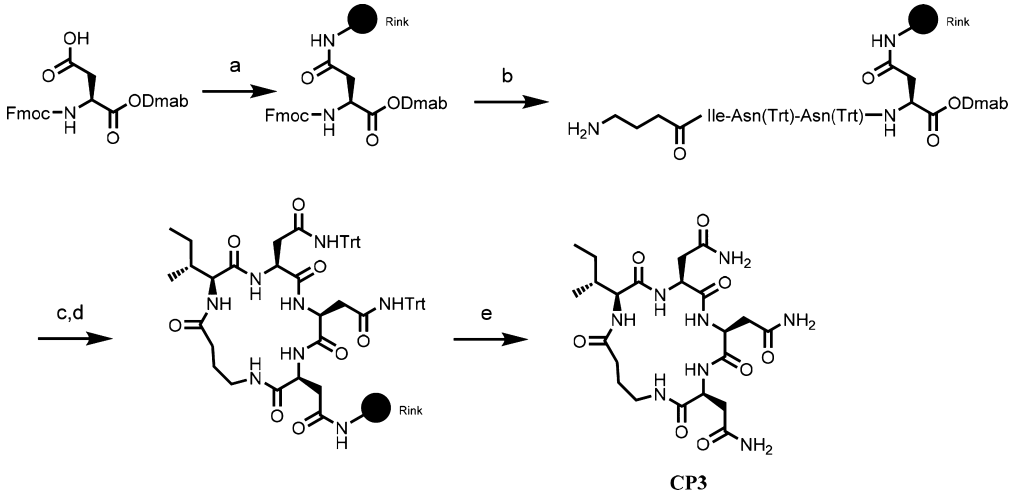

[a]Reagents and conditions: (a) Rink amide resin, HCTU, DIPEA, DMF, 2 h; (b) SPPS, 20% piperidine/DMF, 2 × 5 min followed by an Fmoc-labeled amino acid (3 equiv), HCTU (3 equiv), DIPEA/DMF [7% (v/v)]; (c) 2 equiv of hydrazine hydrate in DMF, 30 min; (d) 3 equiv of PyClock, 10 equiv of DIPEA in DMF, overnight; (e) 92.5% (v/v) TFA, 2.5% (v/v) TIPS, 5% (v/v) DMB, 2 h.

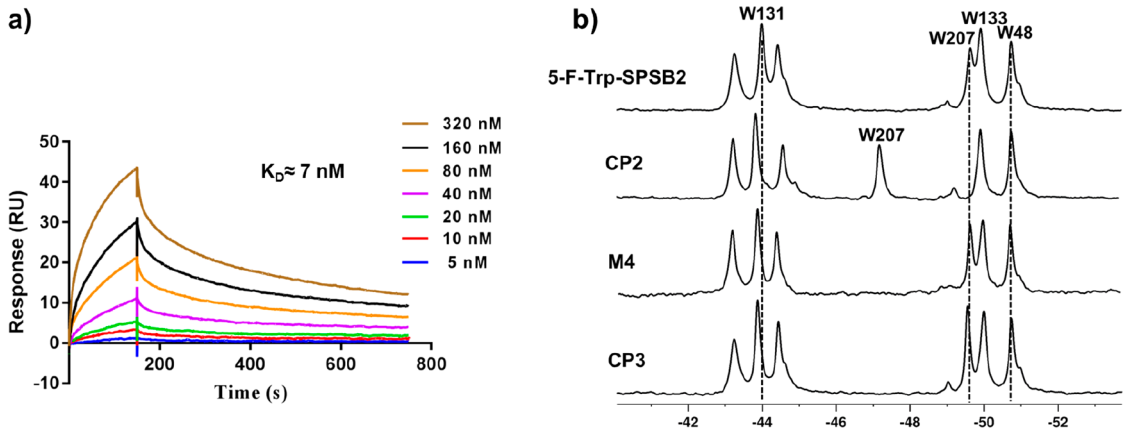

Figure 4. CP3 binds to the iNOS binding site of hSPSB2 with a nanomolar affinity. (a) SPR sensorgrams obtained using seven peptide concentrations ranging from 5 to 320 nM. The *Y* axis shows the response unit (RU) differences after reference subtraction. (b) ^{19}F NMR spectra of 5-F-Trp-labeled mSPSB2 in the absence (top) and presence of cyclic peptides. The intensity of W207 increased in the presence of CP3 and M4, while the peak was significantly shifted downfield by CP2.

group,[17] which is orthogonal to the Fmoc Nα protection, was used to protect the C-terminus, while the N-terminus was elaborated to provide the linear peptide. Upon completion of the linear peptide synthesis, the Dmab group was removed

DOI: 10.1021/acschembio.8b00561
ACS Chem. Biol. 2018, 13, 2930−2938

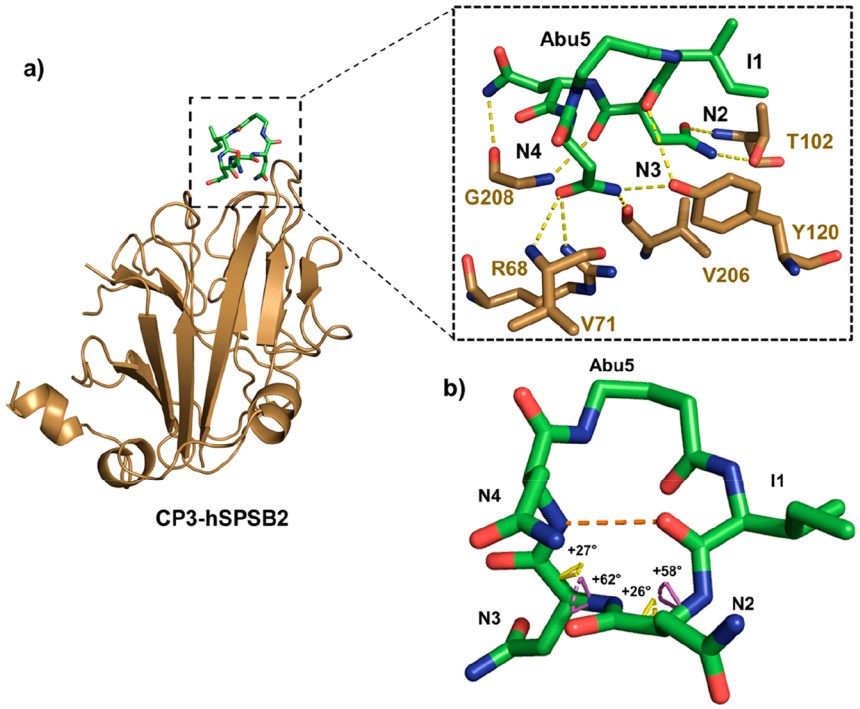

Figure 5. Crystal structure of CP3 bound to human SPSB2 (PDB entry 6DN6). (a) CP3−hSPSB2 intermolecular interactions. Dashed lines show the seven intermolecular hydrogen bonds between CP3 (green) and hSPSB2 (brown). (b) CP3 forms a type I′ β-turn with an intramolecular hydrogen bond between the backbone CO(i) of Ile1 and NH(i + 3) of Asn4 (orange dashed line). Dihedral angles φ and ψ are colored magenta and yellow, respectively.

using 2% hydrazine, and on resin cyclization was performed with 6-chloro-benzotriazol-1-yloxy-tris-pyrrolidinophosphonium hexafluorophosphate (PyClock). Deprotection of the side chain trityl groups and cleavage from the resin were performed using trifluoroacetic acid (TFA) with scavengers. After preparative HPLC, the purity of the peptide was ∼98%, as determined by LC−MS (Figure S4a). One-dimensional ^{1}H NMR of the product showed only a single set of peaks, indicating that it was suitable for structural and binding studies (Figure S4b). NMR resonance assignments were made using the following two-dimensional NMR experiments: ^{1}H−^{1}H ROESY, ^{1}H−^{1}H TOCSY, and ^{1}H−^{15}N SOFAST-HMQC (Table S1 and Figure S5).

CP3 Binds with High Affinity to the iNOS Binding Site of the SPRY Domain of hSPSB2. SPR was performed to measure the affinity and kinetics of binding of CP3 to hSPSB2 (Figure 4a, and Table 1; data for CP1 and CP2 are shown for comparison in Figure S6). hSPSB2 was immobilized on the dextran layer of a CM5 biosensor chip using amine coupling. Using a 1:1 interaction model, the K_D of CP3 was measured to be 7 nM, which corresponds to an approximately 4-fold increase in binding affinity compared to that of CP2 (32 nM). The association rates of CP3 and CP2 are comparable. CP3 has an association rate of 5×10^5 M^{-1} s^{-1}, and CP2 associates with a rate of 8.4×10^5 M^{-1} s^{-1}; CP3 has an approximately 8-fold slower off rate (0.0032 s^{-1} for CP3 compared to 0.026 s^{-1} for CP2).

^{19}F NMR analysis of SPSB2 labeled with 5-F-Trp has proven to be useful in monitoring binding of a ligand to the DINNN binding site.[11,12,18] The ^{19}F resonance corresponding to Trp207, a key residue in the iNOS binding site of SPSB2, is shifted significantly downfield when peptides CP0−CP2 are bound to the iNOS binding site.[11−13] In the case of CP3, an enhancement of the Trp207 resonance intensity was observed rather than a change in chemical shift (Figure 4b). A similar observation was made for peptidomimetic inhibitor M4 of the SPSB−iNOS interaction, which did not perturb the Trp207 resonance in the same way as the other cyclic peptides and mimetics (Figure 4b).[12] However, the increase in the intensity of the Trp207 resonance in the presence of CP3 was greater than that with M4, presumably reflecting the difference in binding affinity between these two analogues (7 nM vs 500 nM).[12] This result indicates that CP3 binds to the iNOS binding site of SPSB2 but has an effect on the local environment of Trp207 different from those of CP0−CP2.[11−13] CP3 also perturbs the resonance of Trp131 to a lesser extent than does CP2 (Figure 4b).

Crystal Structure of CP3 Bound to Human SPSB2. To gain further insight into the binding pose of CP3, we determined the crystal structure of CP3 bound to hSPSB2 at a resolution of 1.6 Å. The asymmetric unit contains one copy of the CP3−hSPSB2 complex, and the overall structure of the SPRY domain in the CP3−hSPB2 complex is largely similar to that in the CP2−hSPSB2 complex, although a few local conformational differences in loop regions occur away from the binding site. The largest deviation between the two structures was the absence of electron density for eight residues in the loop connecting β10 and β11 (Leu153−Glu160) and the presence of electron density for an α-helix (Glu18−Cys25) at the N-terminus of the SPRY domain in the CP3−hSPSB2 complex, which was not resolved in the other hSPSB2 complex structures.

We carefully examined the close crystal packing contacts around the CP3 peptide in the CP3−hSPSB2 complex. A 3 Å contact is present between the backbone amide of Ile1 of CP3 in one complex and the carboxyl side chain of Glu28 of the

DOI: 10.1021/acschembio.8b00561
ACS Chem. Biol. 2018, 13, 2930−2938

symmetry-related hSPSB2 monomer (Figure S7). To assess whether the packing of the crystal lattice may have affected the binding mode of CP3, a 1 μs molecular dynamics (MD) run was performed on an isolated hSPSB2−CP3 complex surrounded only by solvent. This simulation resulted in only a limited change in the ligand position (RMSD ∼ 0.75 Å) across the simulation, indicating that the conformation of CP3 observed in the crystal structure is not significantly influenced by crystal packing (Figure S7).

Examination of the CP3 conformation within the CP3−hSPSB2 complex shows that the NNN motif adopts a conformation similar to that present in the CP2−hSPSB2 complex (Cα RMSD over the NNN sequence of 0.8 Å) and also to the design model of CP3 (Cα RMSD of NNN of 0.3 Å), thus validating our structure-based design process (Figures S2 and S8). However, a few differences were observed between these crystal structures. In particular, the backbone CO groups of the Ile residues (Ile3 in CP2 and Ile1 in CP3) were oriented in opposite directions, with the ψ angle changing from −32° in CP2 to 175° in CP3. As a result, CP3 forms a type I′ β-turn, induced through the formation of an intramolecular main chain hydrogen bond between the carbonyl of Ile1 (i) and the backbone amide of Asn4 (i + 3), with a distance of 5.8 Å between the Cα atoms of residues i and i + 3, and $\phi(i+1)$, $\psi(i+1)$, $\phi(i+2)$, and $\psi(i+2)$ dihedral angles of +58°, +22°, +62°, and +27°, respectively[19] (Figure 5). Two additional intramolecular hydrogen bonds stabilize the bound CP3 conformation: between CO and NH of Abu5 and between the backbone carbonyl of Asn2 and the side chain NH of Asn4. The CP3−hSPSB2 complex retains all of the intermolecular hydrogen bonds observed in the structure of CP2 bound to hSPSB2, except those involving Asp2 in CP2 [the carboxyl side chain of Asp2 with the phenolic hydroxyl of Tyr120 and the amide side chain of Gln73 of human SPSB2 (Figure S2)]. Instead, an additional interaction forms between the backbone carbonyl group of Ile1 and phenolic hydroxyl of Tyr120 (Figure 5 and Figure S2). Comparison of the observed $^3J_{HN-H\alpha}$ coupling constants in our NMR spectra with those predicted from the crystal structure suggests that the solution structure of CP3 may have to undergo a smaller conformational change upon binding than the larger and probably more flexible CP2.

CP3 Inhibits SPSB−iNOS Interactions in Cell Lysates. Having confirmed the binding of CP3 to the iNOS binding site of hSPSB2 *in vitro*, we examined the ability of CP3 to disrupt the interaction of SPSB2 with full-length iNOS in macrophage cell lysates, as a closer mimic of physiological conditions.[11,13] RAW 264.7 macrophages were treated with lipopolysaccharide and interferon-γ (LPS/IFN-γ) to induce iNOS expression. The cells were lysed, and the iNOS−SPSB2 interaction was investigated in the presence of CP3, using CP2 as a positive control. Recombinant His-tagged hSPSB2 and nickel beads were used to enrich iNOS from the macrophage cell lysate in the presence or absence of CP2 or CP3. An immunoblot with anti-iNOS antibodies showed a substantial decrease in the amount of iNOS interacting with SPSB2 in the presence of CP3 and (to a lesser extent) CP2 (Figure 6, top panel). Membranes were reprobed with anti-His antibodies to ensure the recovery of approximately equal amounts of hSPSB2 protein (Figure 6, bottom panel).

On the basis of our crystallographic analyses and the close structural similarity between hSPSB2 and hSPSB4,[9] CP3 would also be expected to disrupt hSPSB4−iNOS interactions. Because SPSB4 induces the ubiquitination of iNOS more

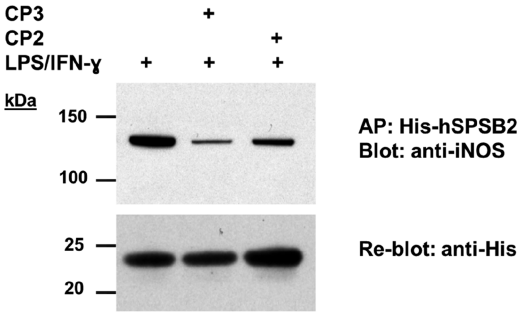

Figure 6. CP3 displaces full-length iNOS from hSPSB2 in RAW 264.7 cell lysates. Macrophages were stimulated with LPS and IFN-γ overnight to induce iNOS expression. Recombinant His-tagged hSPSB2 was added to cell lysates in the absence or presence (+) of 50 μM CP2 or CP3. The SPSB−iNOS complex was captured using Ni-Sepharose beads, separated by SDS−PAGE, and analyzed by immunoblotting with anti-iNOS (top) and anti-His (bottom) antibodies. AP: affinity purification.

potently than does SPSB2,[7] inhibiting the SPSB4−iNOS interaction will presumably increase the levels of NO production even more effectively than for SPSB2. However, estimating the binding affinity of CP3 for hSPSB4 by SPR has proven to be problematic (unpublished data), and we do not yet have a K_D for the binding of CP3 to hSPSB4.

Conclusion. Using a systematic and structure-guided approach, we have developed a potent, low-molecular weight peptide inhibitor of SPSB−iNOS interactions. To achieve this outcome, we have determined the crystal structures of our previously reported cyclic heptapeptides CP1 and CP2 in complex with hSPSB4 and the crystal structure of CP2 in complex with hSPSB2. These crystal structures reveal well-defined intramolecular hydrogen-bonding networks in bound CP1 and CP2 that enhance their binding to hSPSB2 compared to that of the linear DINNN peptides.[10,13] Furthermore, the structures provide direct experimental evidence that validates our original reported designs of CP1 and CP2,[13] which aimed to stabilize the critical binding motif NNN in its bound conformation. These structures were then used to design a smaller, more potent inhibitor, CP3, in which an intramolecular hydrogen bond was replaced with a hydrocarbon linkage to maintain the bound geometry of CP2 and remove non-essential structural features. CP3 has a very high affinity for the iNOS binding site (K_D = 7 nM for hSPSB2) and inhibits the interaction between full-length iNOS and hSPSB2 in cell lysates. With a mass of 540 Da, CP3 is the smallest cyclic peptide inhibitor of the iNOS−SPSB interaction described to date, representing a significant step toward the development of inhibitors of this interaction as anti-infective leads.

METHODS

Solid Phase Peptide Synthesis. CP3 was synthesized on Rink amide resin AM (0.2 mmol/g) via standard Fmoc chemistry using an automated peptide synthesizer (Rainin PS3, Proteins Technologies, Inc.) via Fmoc/tBu chemistry.[20] The typical coupling reaction mixture contained 3 equiv of Fmoc-labeled amino acid, 3 equiv of 2-(6-chloro-1*H*-benzotriazol-1-yl)-1,1,3,3-tetramethylaminium hexafluorophosphate (HCTU), and 10 equiv of diisopropylethylamine (DIPEA), and the reaction was allowed to proceed with mixing for 2 h. The N-terminal Fmoc group was removed by treatment with 20% piperidine in dimethylformamide (DMF). Stepwise deprotection and coupling of amino acids were repeated until the desired linear peptide

DOI: 10.1021/acschembio.8b00561
ACS Chem. Biol. 2018, 13, 2930−2938

was synthesized. After the last Fmoc deprotection, the peptide resin was treated with 2% hydrazine in DMF for the selective removal of Dmab. The peptide was cyclized by treatment with 6-chlorobenzotriazol-1-yloxy-tris-pyrrolidinophosphonium hexafluorophosphate (PyClock) and DIPEA (5 and 10 equiv) in DMF for 12 h. The peptide was deprotected and released from the resin by treatment with a 92.5:5:2.5 (v/v) TFA/dimethoxybenzene (DMB)/TIPS mixture for 3 h and then triturated thrice with cold ethyl ether. The crude peptide was purified by reversed phase HPLC on a Waters Prep LC system incorporating a Waters 486 tunable absorbance detector set at 214 nm and a Phenomenex Luna C8(2) column [250 mm × 21.2 mm (inside diameter), 100 Å, 10 μm] using a gradient from 100% buffer A (0.1% TFA/water) to 60% buffer B (0.1% TFA/acetonitrile) at a flow rate of 7 mL/min over 60 min. LC−MS analysis was performed using a Phenomenex Luna C8(2) column [100 mm × 2.0 mm (inside diameter), 100 Å, 3 μm] at 214 nm, eluting with a gradient from 100% buffer A (0.05% TFA/water) to 60% buffer B (0.05% TFA/acetonitrile) over 10 min at a flow rate of 0.2 mL/min. Mass spectra were acquired in positive ion mode with a scan range of m/z 200−2000.

Protein Expression and Purification. pNIC28-Bsa4 plasmids encoding the SPRY domain of human SPSB2 and human SPSB4 (Addgene, 38983 and 38896, respectively) were cloned with an N-terminal His_6 tag and a TEV cleavage site. *E. coli* strain BL21 (DE3) cells were transformed and grown overnight in 5 mL of LB medium supplemented with 50 μg/mL kanamycin for selection. The overnight culture was then subcultured in fresh LB medium with growth at 37 °C for 5 h until an OD_{600} of 0.5−0.8 was reached. Isopropyl β-D-1-thiogalactopyranoside (IPTG) was added to a final concentration of 0.5 mM, followed by incubation at 18 °C for 18 h. The cultures were centrifuged at 5000 rpm for 10 min, and the cells resuspended in Bug Buster (Millipore). An EDTA-free cOmplete protease inhibitor cocktail tablet (Sigma) was added while the mixture was stirred for 1 h. Cell lysates were cleared by centrifugation at 18000 rpm at 4 °C for 30−45 min. The supernatant was filtered (0.45 μm filter) and loaded onto a Ni-NTA IMAC gravity column. Unbound protein was washed off with 10 mM imidazole in 50 mM 4-(2-hydroxyethyl)-1-piperazineethanesulfonic acid (HEPES) buffer (pH 8.0), 0.15 M NaCl, and 5% glycerol. The protein was eluted from the column with a 250 mM imidazole-containing variant of the buffer described above. To cleave the His tag, 1 mg of in-house TEV protease was added to the sample and left overnight at 4 °C for 16 h. The cleavage reaction mixture was then dialyzed against Ni^{2+} binding buffer for 3 h at 4 °C and reloaded onto a Ni^{2+}-NTA agarose column to separate the cleaved protein; the cleaved protein was recovered from the flow-through, while the uncleaved protein and TEV protease remained bound to the column. Each sample was further purified using a Superdex 75 size exclusion 100/300 column (GE Healthcare) using 20 mM Tris-HCl buffer (pH 8.0), 100 mM NaCl, and 5 mM DTT. Fractions were analyzed using a 15% SDS−PAGE gel with Coomassie staining. His-tagged and cleaved protein samples were concentrated to 20 mg/mL for use in SPR and X-ray crystallographic experiments. 5-F-Trp-labeled mSPSB2 (5-F-Trp mSPSB2) was prepared as described by Leung et al.[18]

Surface Plasmon Resonance. The binding affinities of the peptides were analyzed by SPR, using a Biacore T200 instrument. All experiments were performed in degassed 25 mM HEPES buffer (pH 7.4) containing 150 mM NaCl, 3 mM EDTA,1 mM tris(2-carboxyethyl)phosphine hydrochloride (TCEP), and 0.05% surfactant P-20 at 25 °C. Human SPSB2 was immobilized on a Biacore CM5 biosensor chip by amine coupling as follows. The CM-dextran matrix was activated with 0.2 M 1-ethyl-3-(3-diethylaminopropyl)-carbodiimide hydrochloride (EDC) and 0.05 M *N*-hydroxysuccinimide; 100 μg/mL hSPSB2 in 10 mM sodium acetate (pH 5.5) was then passed over the activated surface at a rate of 10 μL/min for 10 min. Finally, 1 M ethanolamine-HCl (pH 8.5) was injected into both target and reference flow cells to deactivate any remaining activated carboxyl groups on the surface. The peptides were injected onto the surface with a contact time of 200 s, a flow rate of 100 μL/min, and a dissociation time of 600 s. The sensorgram was further corrected for nonspecific binding to the surface by subtracting the signals of the reference surface from those of the target protein surface. The corrected signal was then fitted to a steady state 1:1 interaction model with Biacore T200 Evaluation Software (version 2.0), to estimate the binding affinity (K_D), association rate (k_{on}), and dissociation rate (k_{off}). Sensorgrams were generated using GraphPad Prism (version 6.05).

X-ray Crystallography. Purified SBSP proteins at 20 mg mL^{-1} were incubated with a 10-fold excess of peptides on ice overnight before crystallization trials, with a 1:1 mother liquor:protein suspension drop ratio. Protein−peptide crystals were obtained in the presence of 0.1 M HEPES (pH 7.5), 20% PEG 4000, and 10% isopropanol (CP2−hSBSP2); 0.1 M CHES (pH 9) and 20% PEG 8000 (CP3−hSBSP2); 0.2 M NH_4SO_4, 0.1 M NaAc (pH 4.6), and 25% PEG 4000 (CP1−hSBSP4); and 0.2 M magnesium chloride hexahydrate and 20% (w/v) PEG 3350 (CP2−hSBSP4). Crystals were flash-cooled in liquid nitrogen in the presence of 15% glycerol. Data sets were collected at Australian Synchrotron MX beamlines and processed using XDS.[21,22] The crystal structures of complexes were determined by molecular replacement (using 3EMW as a search model[9]) and the program PHASER from CCP4.[23] Libraries for nonstandard amino acids were generated using the grade Web Server (http://grade.globalphasing.org/cgi-bin/grade/server.cgi). Structural refinement was performed using BUSTER (Bricogne 2017), model building using COOT,[24] and structural analysis using Pymol (Schrödinger, LLC). Structures have been deposited in the Protein Data Bank as entries 6DN8 (CP1−hSBSP4), 6DN7 (CP2−hSBSP4), 6DN5 (CP2−hSBSP2), and 6DN6 (CP3−hSBSP2).

NMR Spectroscopy. CP3 was dissolved in a 90% H_2O/10% ^2H_2O mixture, and spectra were recorded on a Bruker Avance 600 MHz NMR instrument equipped with a 5 mm TCI cryoprobe at 10 °C and pH 5. For resonance assignments, two-dimensional TOCSY[25] and ROESY[26] spectra with mixing times of 70 and 300 ms, respectively, were recorded. For ^{15}N chemical shift assignments, $^1H-^{15}N$ SOFAST HMQC (64 × 2048) spectra[27] were acquired. All NMR spectra were processed using TopSpin (Bruker). ^1H chemical shifts were referenced to 3-(trimethylsilyl)-1-propanesulfonic acid sodium sulfate (DSS), while ^{15}N chemical shifts were referenced indirectly, using their gyromagnetic ratio. Chemical shift assignments are summarized in Figure S5 and Table S1.

^{19}F NMR spectra of 50 μM 5-F-Trp SPSB2 in 50 mM sodium phosphate buffer (pH 7.4), 2 mM EDTA, 10 mM DTT, 0.02% sodium azide, and 50 mM NaCl were recorded at 30 °C in the presence and absence of 100 μM peptide. ^{19}F NMR chemical shifts were referenced against 0.005% trifluoroethanol. All spectra were processed using an exponential window function with a line broadening of 40 Hz.

Affinity Enrichment and Immunoblotting. RAW 264.7 cells were collected 16 h after treatment with 10 ng/mL LPS and 20 ng/mL IFN-γ and lysed in a buffer [50 mmol/L Tris-HC1 (pH 7.5), 150 mmol/L NaCl, and 1% (v/v) Triton X-100] containing Roche's EDTA-free cOmplete mini protease inhibitor cocktail and 1 mM phenylmethanesulfonyl fluoride on ice for 30 min. The cell lysates were incubated with 2 μg/mL recombinant His-tagged hSPSB2-SPRY domain in the absence and presence of 50 μM peptide for 2 h. To recover the SPSB2−iNOS complexes, cell lysates were incubated with precharged Ni-Sepharose beads (GE Healthcare) for 2 h, rotating at 4 °C. Proteins were eluted in SDS sample buffer and boiled for 5 min, prior to separation on 12% SDS−PAGE gels and transfer to nitrocellulose (Millipore) using a semidry blotting apparatus (Bio-Rad). Membranes were blocked with 10% skim milk in PBS containing 0.1% Tween 20 overnight at 4 °C and incubated with the mouse monoclonal anti-iNOS antibody (BD Biosciences, 1:1000 dilution) for 2 h. Membranes were washed and incubated with the anti-mouse immunoglobulin antibody conjugated to horseradish peroxidase (Amersham Biosciences, 1:10000) for 1 h at room temperature in PBS containing 0.1% Tween 20. Immunostained bands were visualized using the chemiluminescence method (ECL system, GE Healthcare).

DOI: 10.1021/acschembio.8b00561
ACS Chem. Biol. 2018, 13, 2930−2938

■ ASSOCIATED CONTENT

Supporting Information

The Supporting Information is available free of charge on the ACS Publications website at DOI: 10.1021/acschembio.8b00561.

Description of molecular dynamics simulations, Figures S1−S8, and Tables S1 and S2 (PDF)

Accession Codes

Structures of peptide−SPSB complexes have been deposited in the Protein Data Bank as entries 6DN8 (hSPSB4−CP1), 6DN7 (hSPSB4−CP2), 6DN5 (hSPSB2−CP2), and 6DN6 (SPSB2−CP3).

■ AUTHOR INFORMATION

Corresponding Authors

*E-mail: ray.norton@monash.edu. Telephone: (+61) 3 9903 9167. Fax: (+61) 3 9903 9582.
*E-mail: ruby.law@monash.edu. Telephone: (+61) 3 9902 9308. Fax: (+61) 3 9902 9500.

ORCID

Maiada M. Sadek: 0000-0003-2808-646X
Nicholas Barlow: 0000-0002-5749-3542
David K. Chalmers: 0000-0003-2366-569X
Raymond S. Norton: 0000-0001-8893-0584

Present Address

@B.K.Y.: School of Pharmaceutical Sciences, Universiti Sains Malaysia, 11800 USM, Penang, Malaysia.

Notes

The authors declare no competing financial interest.

■ ACKNOWLEDGMENTS

This study was supported in part by the Australian National Health and Medical Research Council (NHMRC) (Grant 1099428). R.S.N. acknowledges fellowship support from the Australian National Health and Medical Research Council. M.S. is supported by a Monash Graduate Scholarship. The authors thank Dr. Bankala Krishnarjuna for help with the NMR analyses.

■ ABBREVIATIONS

DIPEA, *N*,*N*-diisopropylethylamine; Dmab, 4-{*N*-[1-(4,4-dimethyl-2,6-dioxocyclohexylidene)-3-methylbutyl]amino}-benzyl; DMF, dimethylformamide; DTT, dithiothreitol; Fmoc, fluorenylmethyloxycarbonyl; HCTU, *O*-(1*H*-6-chlorobenzotriazol-1-yl)-1,1,3,3-tetramethyluronium hexafluorophosphate; HPLC, high-performance liquid chromatography; IFN-γ, interferon-γ; iNOS, inducible nitric oxide synthase; k_{on}, association rate; k_{off}, dissociation rate; K_D, binding constant; LPS, lipopolysaccharide; MD, molecular dynamics; NO, nitric oxide; PDB, Protein Data Bank; PyClock, 6-chloro-benzotriazol-1-yloxy-tris-pyrrolidinophosphonium hexafluorophosphate; ROESY, rotating-frame Overhauser spectroscopy; SDS−PAGE, sodium dodecyl sulfate−polyacrylamide gel electrophoresis; SOFAST-HMQC, so fast heteronuclear multiple-quantum coherence; SPR, surface plasmon resonance; SPSB, SPRY domain- and SOCS box-containing protein; SPPS, solid phase peptide synthesis; TCEP, tris(2-carboxyethyl)phosphine hydrochloride; TFA, trifluoroacetic acid; TIPS, triisopropylsilane; TOCSY, total correlation spectroscopy

■ REFERENCES

(1) Hilton, D. J., Richardson, R. T., Alexander, W. S., Viney, E. M., Willson, T. A., Sprigg, N. S., Starr, R., Nicholson, S. E., Metcalf, D., and Nicola, N. A. (1998) Twenty proteins containing a C-terminal SOCS box form five structural classes. *Proc. Natl. Acad. Sci. U. S. A. 95*, 114−119.

(2) Masters, S. L., Yao, S., Willson, T. A., Zhang, J. G., Palmer, K. R., Smith, B. J., Babon, J. J., Nicola, N. A., Norton, R. S., and Nicholson, S. E. (2006) The SPRY domain of SSB-2 adopts a novel fold that presents conserved Par-4-binding residues. *Nat. Struct. Mol. Biol. 13*, 77−84.

(3) Perfetto, L., Gherardini, P. F., Davey, N. E., Diella, F., Helmer-Citterich, M., and Cesareni, G. (2013) Exploring the diversity of SPRY/B30.2-mediated interactions. *Trends Biochem. Sci. 38*, 38−46.

(4) Wang, D., Li, Z., Messing, E. M., and Wu, G. (2005) The SPRY domain-containing SOCS box protein 1 (SSB-1) interacts with MET and enhances the hepatocyte growth factor-induced Erk-Elk-1-serum response element pathway. *J. Biol. Chem. 280*, 16393−16401.

(5) D'Cruz, A. A., Babon, J. J., Norton, R. S., Nicola, N. A., and Nicholson, S. E. (2013) Structure and function of the SPRY/B30.2 domain proteins involved in innate immunity. *Protein Sci. 22*, 1−10.

(6) Kuang, Z., Lewis, R. S., Curtis, J. M., Zhan, Y., Saunders, B. M., Babon, J. J., Kolesnik, T. B., Low, A., Masters, S. L., Willson, T. A., Kedzierski, L., Yao, S., Handman, E., Norton, R. S., and Nicholson, S. E. (2010) The SPRY domain-containing SOCS box protein SPSB2 targets iNOS for proteasomal degradation. *J. Cell Biol. 190*, 129−141.

(7) Nishiya, T., Matsumoto, K., Maekawa, S., Kajita, E., Horinouchi, T., Fujimuro, M., Ogasawara, K., Uehara, T., and Miwa, S. (2011) Regulation of inducible nitric-oxide synthase by the SPRY domain- and SOCS box-containing proteins. *J. Biol. Chem. 286*, 9009−9019.

(8) Lewis, R. S., Kolesnik, T. B., Kuang, Z., D'Cruz, A. A., Blewitt, M. E., Masters, S. L., Low, A., Willson, T., Norton, R. S., and Nicholson, S. E. (2011) TLR regulation of SPSB1 controls inducible nitric oxide synthase induction. *J. Immunol. 187*, 3798−3805.

(9) Filippakopoulos, P., Low, A., Sharpe, T. D., Uppenberg, J., Yao, S., Kuang, Z., Savitsky, P., Lewis, R. S., Nicholson, S. E., Norton, R. S., and Bullock, A. N. (2010) Structural basis for Par-4 recognition by the SPRY domain- and SOCS box-containing proteins SPSB1, SPSB2, and SPSB4. *J. Mol. Biol. 401*, 389−402.

(10) Leung, E. W. W., Mulcair, M. D., Yap, B. K., Nicholson, S. E., Scanlon, M. J., and Norton, R. S. (2017) Molecular insights into the interaction between the SPRY domain-containing SOCS box protein SPSB2 and peptides based on the binding motif from iNOS. *Aust. J. Chem. 70*, 191−200.

(11) Yap, B. K., Leung, E. W., Yagi, H., Galea, C. A., Chhabra, S., Chalmers, D. K., Nicholson, S. E., Thompson, P. E., and Norton, R. S. (2014) A potent cyclic peptide targeting SPSB2 protein as a potential anti-infective agent. *J. Med. Chem. 57*, 7006−7015.

(12) Harjani, J. R., Yap, B. K., Leung, E. W., Lucke, A., Nicholson, S. E., Scanlon, M. J., Chalmers, D. K., Thompson, P. E., Norton, R. S., and Baell, J. B. (2016) Design, synthesis, and characterization of cyclic peptidomimetics of the inducible nitric oxide synthase binding epitope that disrupt the protein-protein interaction involving SPRY domain-containing suppressor of cytokine signaling box protein (SPSB) 2 and inducible nitric oxide synthase. *J. Med. Chem. 59*, 5799−5809.

(13) Yap, B. K., Harjani, J. R., Leung, E. W., Nicholson, S. E., Scanlon, M. J., Chalmers, D. K., Thompson, P. E., Baell, J. B., and Norton, R. S. (2016) Redox-stable cyclic peptide inhibitors of the SPSB2-iNOS interaction. *FEBS Lett. 590*, 696−704.

(14) Norton, R., Leung, E., Chandrashekaran, I., and MacRaild, C. (2016) Applications of ^{19}F-NMR in fragment-based drug discovery. *Molecules 21*, 860.

(15) You, T., Wang, Y., Li, K., Zhang, D., Wei, H., Luo, Y., Li, H., Lu, Y., Su, X., and Kuang, Z. (2017) Crystal structure of SPSB2 in complex with a rational designed RGD-containing cyclic peptide inhibitor of SPSB2-iNOS interaction. *Biochem. Biophys. Res. Commun. 489*, 346−352.

DOI: 10.1021/acschembio.8b00561
ACS Chem. Biol. 2018, 13, 2930−2938

(16) Kuang, Z., Yao, S., Xu, Y., Lewis, R. S., Low, A., Masters, S. L., Willson, T. A., Kolesnik, T. B., Nicholson, S. E., Garrett, T. J., and Norton, R. S. (2009) SPRY domain-containing SOCS box protein 2: crystal structure and residues critical for protein binding. *J. Mol. Biol. 386*, 662−674.
(17) Chan, W. C., Bycroft, B. W., Evans, D. J., and White, P. D. (1995) A novel 4-aminobenzyl ester-based carboxy-protecting group for synthesis of atypical peptides by Fmoc-But solid-phase chemistry. *J. Chem. Soc., Chem. Commun.*, 2209−2210.
(18) Leung, E. W., Yagi, H., Harjani, J. R., Mulcair, M. D., Scanlon, M. J., Baell, J. B., and Norton, R. S. (2014) ^{19}F NMR as a probe of ligand interactions with the iNOS binding site of SPRY domain-containing SOCS box protein 2. *Chem. Biol. Drug Des. 84*, 616−625.
(19) Venkatachalam, C. M. (1968) Stereochemical criteria for polypeptides and proteins. V. Conformation of a system of three linked peptide units. *Biopolymers 6*, 1425−1436.
(20) Chang, C. D., and Meienhofer, J. (1978) Solid-phase peptide synthesis using mild base cleavage of N α-fluorenylmethyloxycarbonylamino acids, exemplified by a synthesis of dihydrosomatostatin. *Int. J. Pept. Protein Res. 11*, 246−249.
(21) Kabsch, W. (2010) XDS. *Acta Crystallogr., Sect. D: Biol. Crystallogr. 66*, 125−132.
(22) Kabsch, W. (2010) Integration, scaling, space-group assignment and post-refinement. *Acta Crystallogr., Sect. D: Biol. Crystallogr. 66*, 133−144.
(23) McCoy, A. J., Grosse-Kunstleve, R. W., Adams, P. D., Winn, M. D., Storoni, L. C., and Read, R. J. (2007) Phaser crystallographic software. *J. Appl. Crystallogr. 40*, 658−674.
(24) Emsley, P., Lohkamp, B., Scott, W. G., and Cowtan, K. (2010) Features and development of Coot. *Acta Crystallogr., Sect. D: Biol. Crystallogr. 66*, 486−501.
(25) Braunschweiler, L., and Ernst, R. R. (1983) Coherence transfer by isotropic mixing: Application to proton correlation spectroscopy. *J. Magn. Reson. 53*, 521−528.
(26) Jeener, J., Meier, B. H., Bachmann, P., and Ernst, R. R. (1979) Investigation of exchange processes by two-dimensional NMR spectroscopy. *J. Chem. Phys. 71*, 4546−4553.
(27) Schanda, P., and Brutscher, B. (2005) Very fast two-dimensional NMR spectroscopy for real-time investigation of dynamic events in proteins on the time scale of seconds. *J. Am. Chem. Soc. 127*, 8014−8015.

DOI: 10.1021/acschembio.8b00561
ACS Chem. Biol. 2018, 13, 2930−2938

Supporting Information

A Cyclic Peptide Inhibitor of the iNOS-SPSB Protein–Protein Interaction as a Potential Anti-infective Agent

Maiada M. Sadek,[¥] Nicholas Barlow,[¥] Eleanor WW. Leung,[¥] Billy J. Williams-Noonan,[¥] Beow Keat Yap,[¥,₸] Fairolniza Mohd Shariff,[§] Tom T. Caradoc-Davies,[†] Sandra E. Nicholson, [‡,⊥] David K. Chalmers,[¥] Philip E. Thompson, [¥] Ruby H.P. Law[‖,*] and Raymond S. Norton[¥,*]

[¥] Medicinal Chemistry, Monash Institute of Pharmaceutical Sciences, Monash University, Parkville, Victoria 3052, Australia
[‡] The Walter and Eliza Hall Institute of Medical Research, Parkville, Victoria 3052, Australia
[⊥] The Department of Medical Biology, University of Melbourne, Parkville, Victoria 3052, Australia
[§] Department of Microbiology, Faculty of Biotechnology and Biomolecular Sciences, Universiti Putra, Malaysia
[†] Australian Synchrotron, Clayton, Victoria 3168, Australia
[‖] Department of Biochemistry and Molecular Biology, and Australian Research Council Centre of Excellence in Advanced Molecular Imaging, Monash University, Clayton, Victoria 3800, Australia
[₸] Current Address: School of Pharmaceutical Sciences, Universiti Sains Malaysia, 11800 USM, Penang, Malaysia

Experimental: Molecular dynamics simulations

EXPERIMENTAL SECTION

Molecular Dynamics Simulations

Protein model generation. The simulation model for the CP3-hSPSB2 complex was generated by using the Protein Preparation Wizard[1] tool of Maestro[2] to protonate the crystal structure. A heavy atom restrained minimization was then performed to alleviate potential clashes using the Macromodel tool in Maestro, using the GBSA implicit solvent model[3], and harmonic position constraints on all heavy atoms, with a force constant (k) of 0.1 kcal.$Å^{-1}$ mol^{-1}. Subsequently, the protein-ligand complex was centred in an orthorhombic periodic cell[4-5] and fitted with OPLS-2005[6] parameters using Desmond.[7] These periodic boundary conditions were constructed such that the minimum distance of protein-ligand complex from the 'face' of the cell was 10 Å. Further, the system was then solvated with SPC water to a density of 1 $g.mL^{-1}$. Na^+ and Cl^- ions were added to neutralize the system and bring the salt concentration of the system to 150 mM.

Simulation. Using Desmond,[7] an unconstrained, steepest descent energy minimization was performed on the system over a maximum of 2000 steps, using a convergence threshold of 0.1 kcal mol^{-1}. The minimised system was then equilibrated and relaxed using the default Desmond relaxation protocol,[8] which involves a series of minimizations and short MD simulations, to bring the system from its original state, to NVT (constant temperature) conditions and then to NPT (constant pressure) conditions. The final equilibration phase was conducted using the RESPA integrator[9] with a 2 fs time step, the Nose-Hoover thermostat[10] with τ_T = 1 ps to maintain a temperature of 300 K, and the Martyna-Tobias-Klein barostat[11] using τ_P = 2 ps to sustain an average pressure of 1.0 bar. Short-range Coulombic and vdW interactions were calculated with a 9.0 Å cut-off. These short-range electrostatics were evaluated every time step, while long range interactions were determined every three time steps. Finally, the 1.0 μs MD production run was performed using the same NPT conditions as the last equilibration phase described above. Structures were written to the trajectory at a rate of 1 frame per ns. Analysis of the trajectory was performed using VMD.[12]

References to Experimental

1. Schrödinger, L., Protein preparation wizard. *Epik version.* **2011,** *2*.
2. Release, S., 1: MacroModel, version 10.3. *Schrödinger, LLC, New York, NY.* **2014**.
3. Wang, J.; Tan, C.; Tan, Y.-H.; Lu, Q.; Luo, R., Poisson-Boltzmann solvents in molecular dynamics simulations. *Commun Comput Phys.* **2008,** *3*, 1010-1031.
4. Williams-Noonan, B. J.; Yuriev, E.; Chalmers, D. K., Free energy methods in drug design: prospects of "alchemical perturbation" in medicinal chemistry: miniperspective. *J Med Chem.* **2017,** *61*, 638-649.
5. Dubin, D. H., First-order anharmonic correction to the free energy of a coulomb crystal in periodic boundary conditions. *Phys Rev A.* **1990,** *42*, 4972-4982.
6. Ergon, R., PLS post-processing by similarity transformation (PLS+ ST): a simple alternative to OPLS. *J Chemom.* **2005,** *19*, 1-4.
7. Release, S., 1: Desmond Molecular Dynamics System, version 3.7. *DE Shaw Research, New York, NY, Maestro-Desmond Interoperability Tools, version.* **2014,** *3*.
8. Wang, L.; Deng, Y.; Knight, J. L.; Wu, Y.; Kim, B.; Sherman, W.; Shelley, J. C.; Lin, T.; Abel, R., Modeling local structural rearrangements using FEP/REST: application to relative binding affinity predictions of CDK2 inhibitors. *J Chem Theory Comput.* **2013,** *9*, 1282-1293.
9. Leimkuhler, B.; Margul, D. T.; Tuckerman, M. E., Stochastic, resonance-free multiple time-step algorithm for molecular dynamics with very large time steps. *Mol Phys.* **2013,** *111*, 3579-3594.
10. Evans, D. J.; Holian, B. L., The nose–hoover thermostat. *J Chem Phys.* **1985,** *83*, 4069-4074.
11. Martyna, G. J.; Tobias, D. J.; Klein, M. L., Constant pressure molecular dynamics algorithms. *J Chem Phys.* **1994,** *101*, 4177-4189.
12. Humphrey, W.; Dalke, A.; Schulten, K., VMD: visual molecular dynamics. *J Mol Graph.* **1996,** *14*, 33-38.

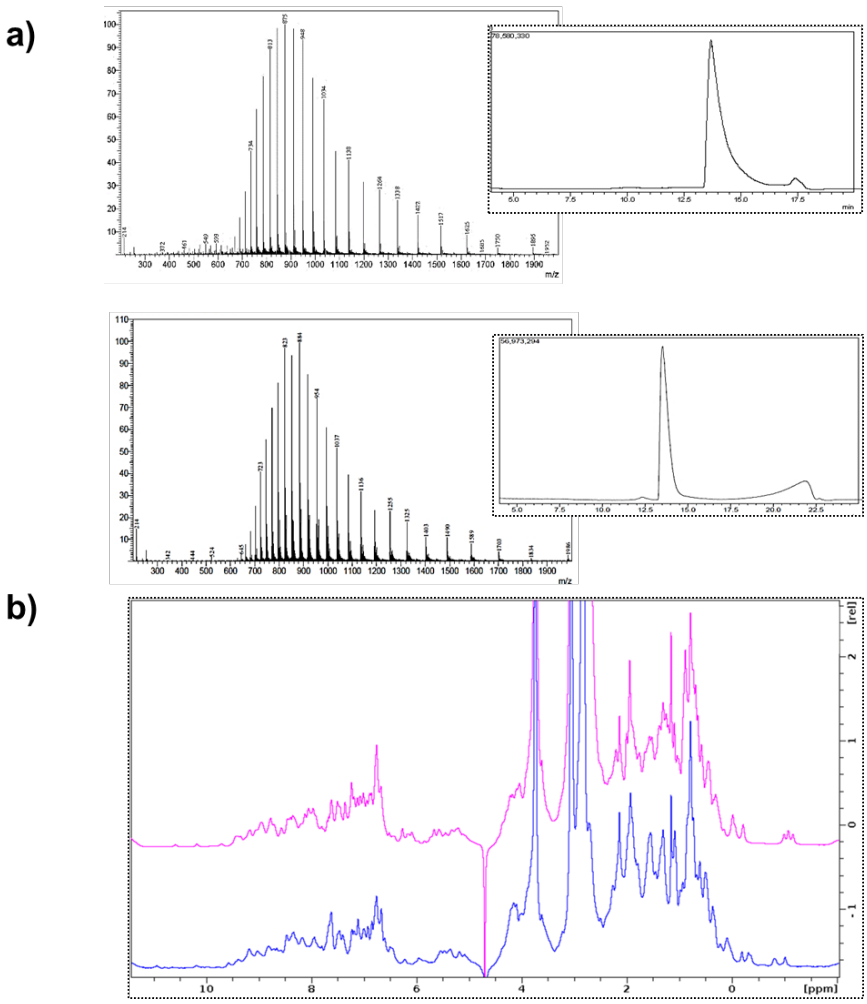

Figure S1. a) LC-MS profile of hSPSB2 (top panel) and hSPSB4 (bottom panel). The theoretical m/z values and corresponding convoluted masses are 23,824 and 23,819 Da for hSPSB2 and 22,734 and 22,726 Da for hSPSB4 respectively, b) 1D ^{1}H NMR spectra of hSPSB2 (blue) and hSPSB4 (pink)

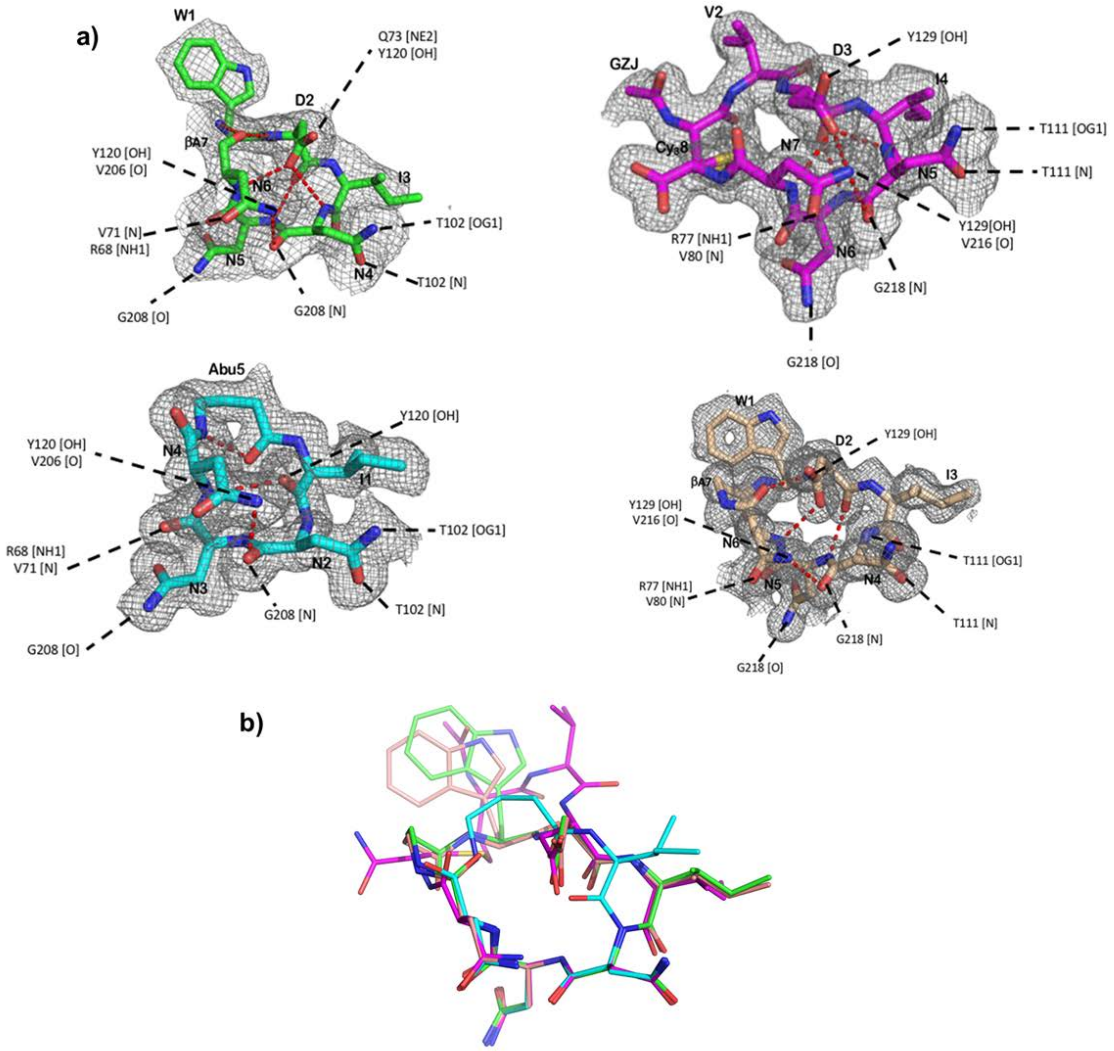

Figure S2. **(a)** Electron density maps for the bound peptides in the peptide-hSPSB complex structures. Structure of cyclic peptide inhibitors are shown in sticks and coloured - CP2 and CP3 bound to hSPSB2 (green and cyan, respectively) and CP1 and CP2 bound to hSPSB4 (magenta and salmon, respectively) - and labelled. The 2Fo-Fc omit maps of the inhibitors (grey) were contoured at 1.0 sigma. The inter-molecular electrostatic interactions between the inhibitors and the hSPSBs are labelled and shown as black dashed lines. Intramolecular H-bonds are shown as red dashed lines. Protein Data Bank id codes: CP1-hSBSP4, 6DN8; CP2-hSBSP4, 6DN7; CP2-hSBSP2, 6DN5; CP3-hSBSP2, 6DN6. **(b)** Superposition of CP1, CP2 and CP3 in the bound conformation in the crystal structures, shown in lines and colored as in (a).

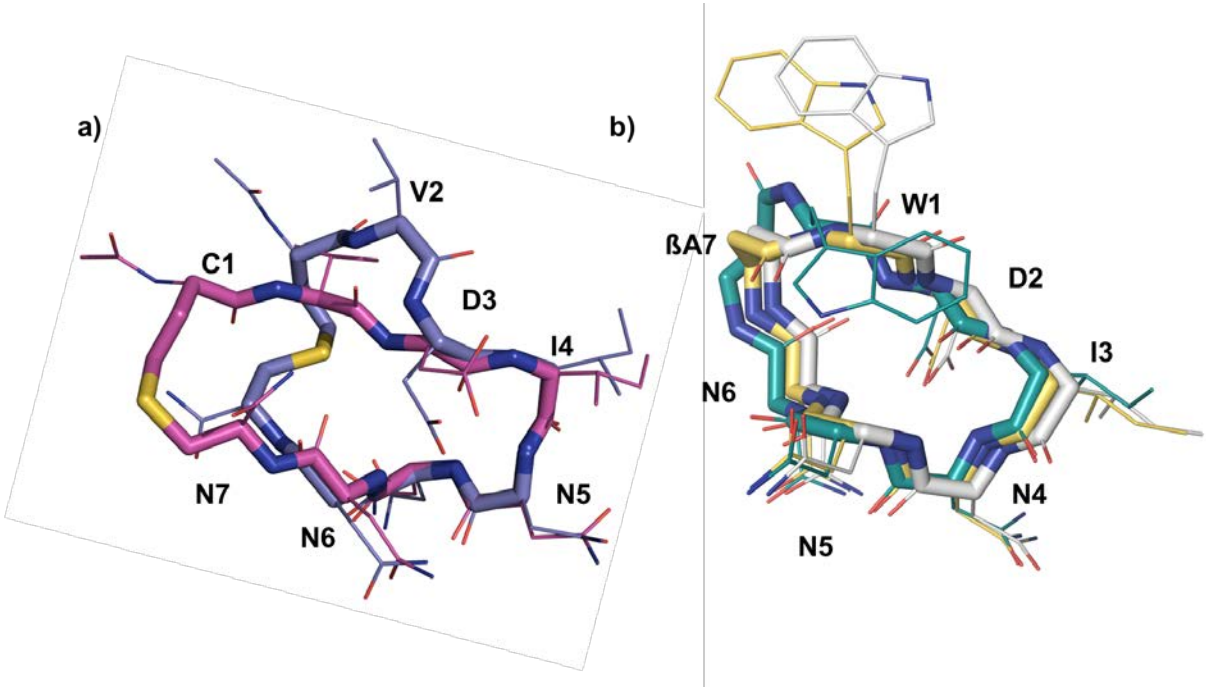

Figure S3. Superimposed structures of *in silico* modelling and the crystal structures of a) CP1 in complex with hSPSB4, and b) CP2 in complex with hSPSB2 and hSPSB4. The Cα-RMSD between the CP1 structure (blue) and its model shown in pink is 1.4 Å, and the Cα-RMSD between the two model structures (CP2 (green) and the complex (white in human SPSB2 and yellow in hSPSB4) are 0.8 and 1 Å, respectively.

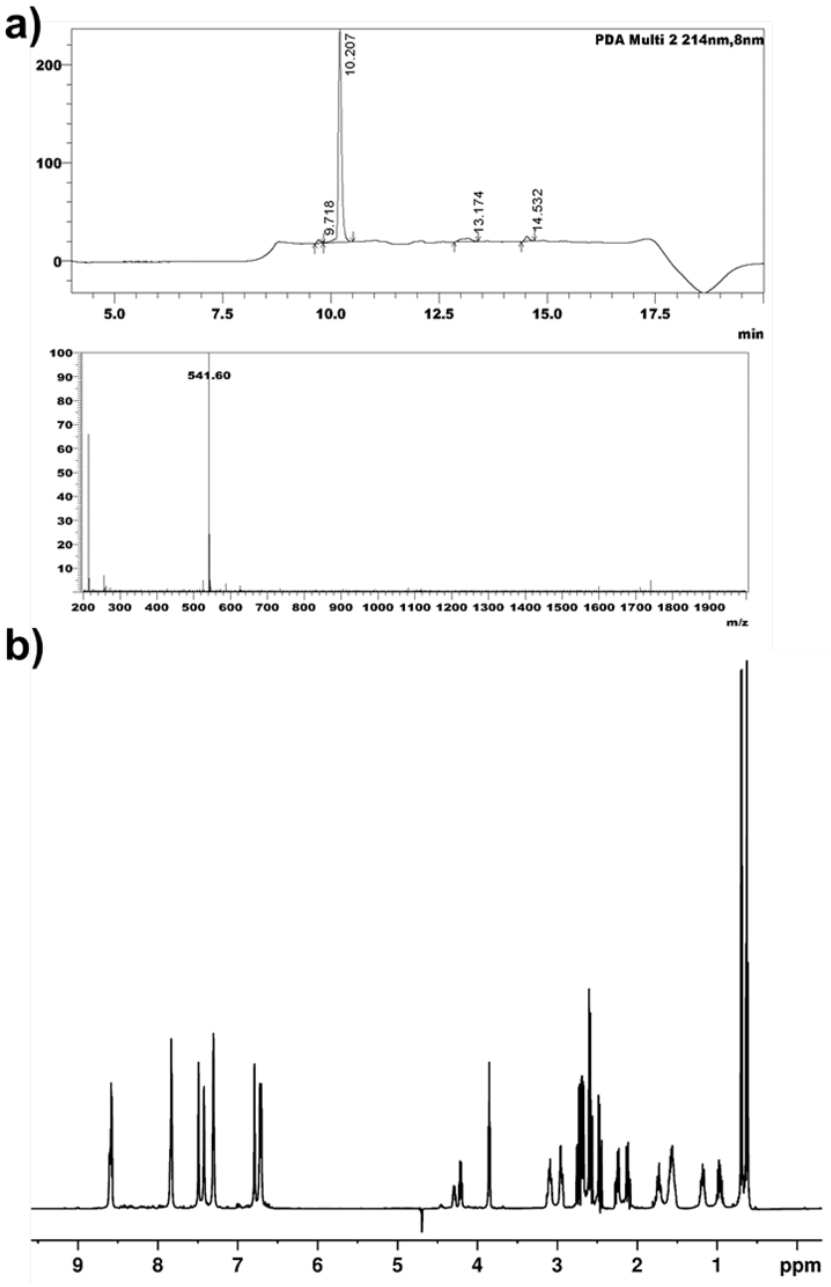

Figure S4. a) LC-MS profile of the purified pentapeptide CP3. Purity is ~98%, based on the peak area in the chromatogram. (b) 1D ^{1}H NMR spectrum of CP3 in water, pH 5, acquired at 10 °C on a 600 MHz spectrometer.

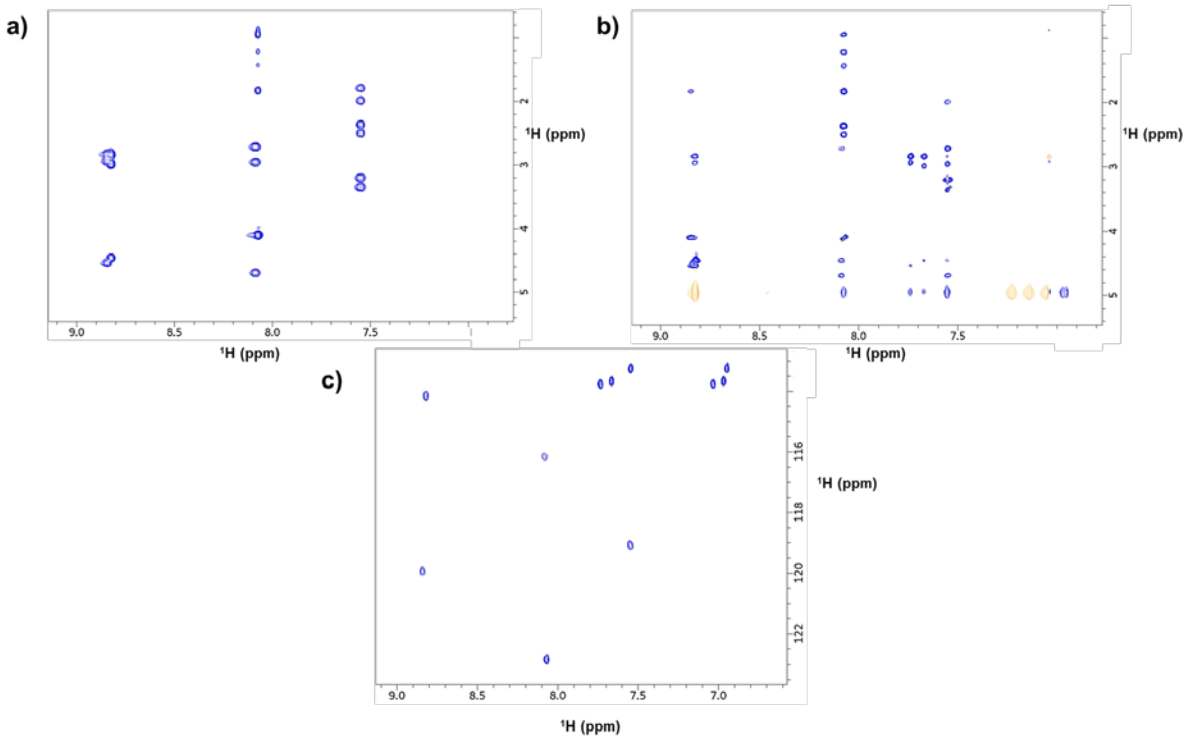

Figure S5. a) 2D [^{1}H,^{1}H]-TOCSY , b) [^{1}H,^{1}H]-ROESY and c) [^{1}H-^{15}N] SOFAST-HMQC spectra of CP3 in water, pH 5, acquired at 10 °C on a 600 MHz spectrometer.

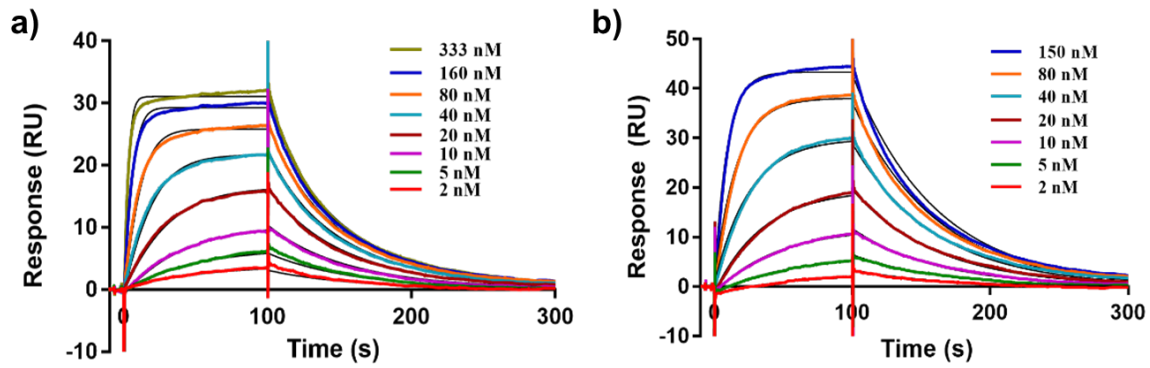

Figure S6. Representative sensorgrams of the cyclic peptides a) CP1 and b) CP2 binding to hSPSB2.

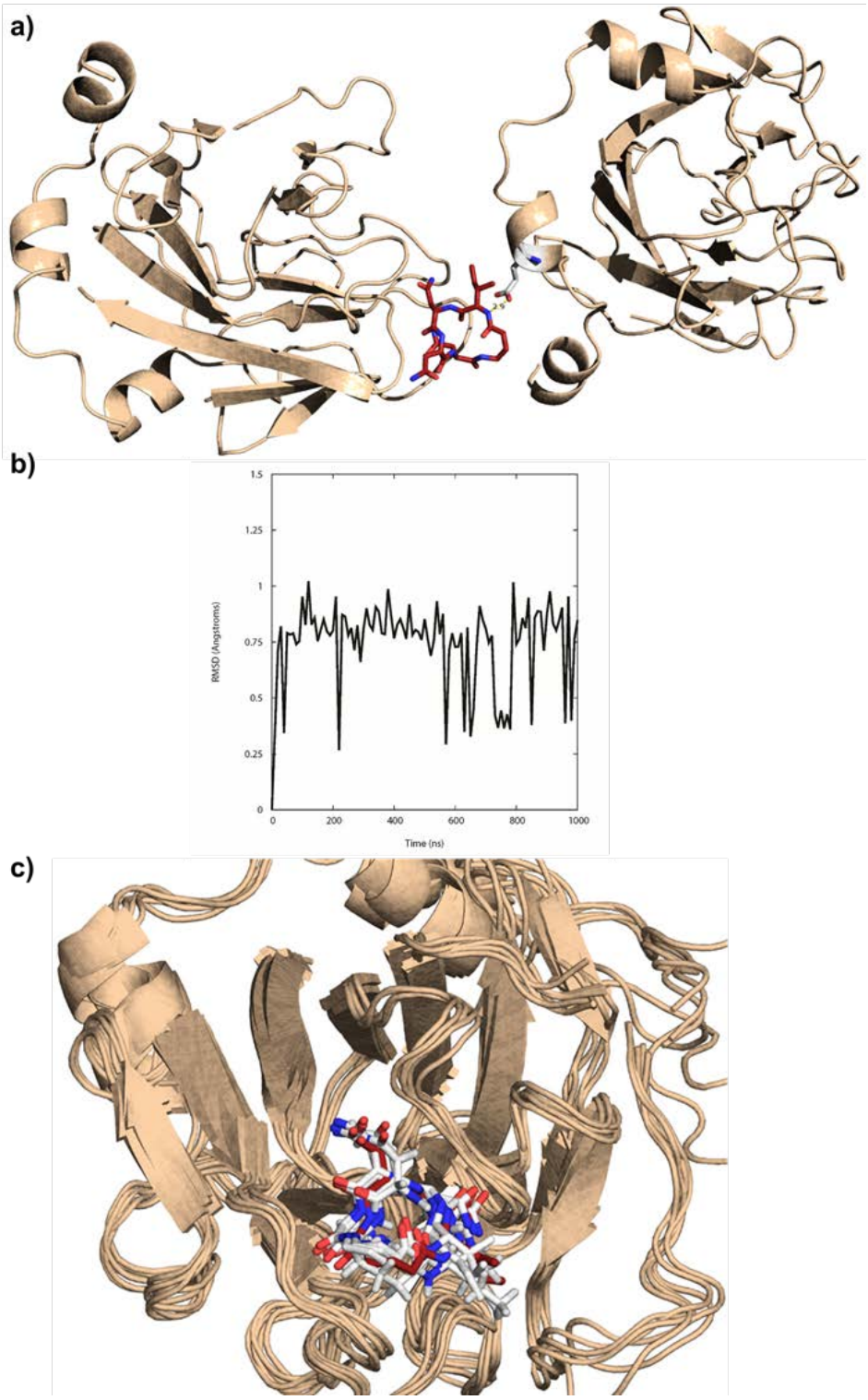

Figure S7. a) Crystal packing of CP3-hSPSB2 complex showing the close contact between Ile1 in CP3 and Glu28 in hSPSB2 of the other protein in the crystal. The protein is displayed as golden ribbons and the ligand in its bound mode is given a stick representation with carbon (brown), oxygen (red), nitrogen (blue), and hydrogen (white). b) A plot of the backbone RMSD of CP3 against simulation time c) An overlay of five structures for the CP3 complex from across the 1 μs MD production run. hSPSB2 is displayed as gold ribbons. The original bound pose from the crystal structure is shown with dark-red carbon, while the structures spanning the MD run are shown with white carbon.

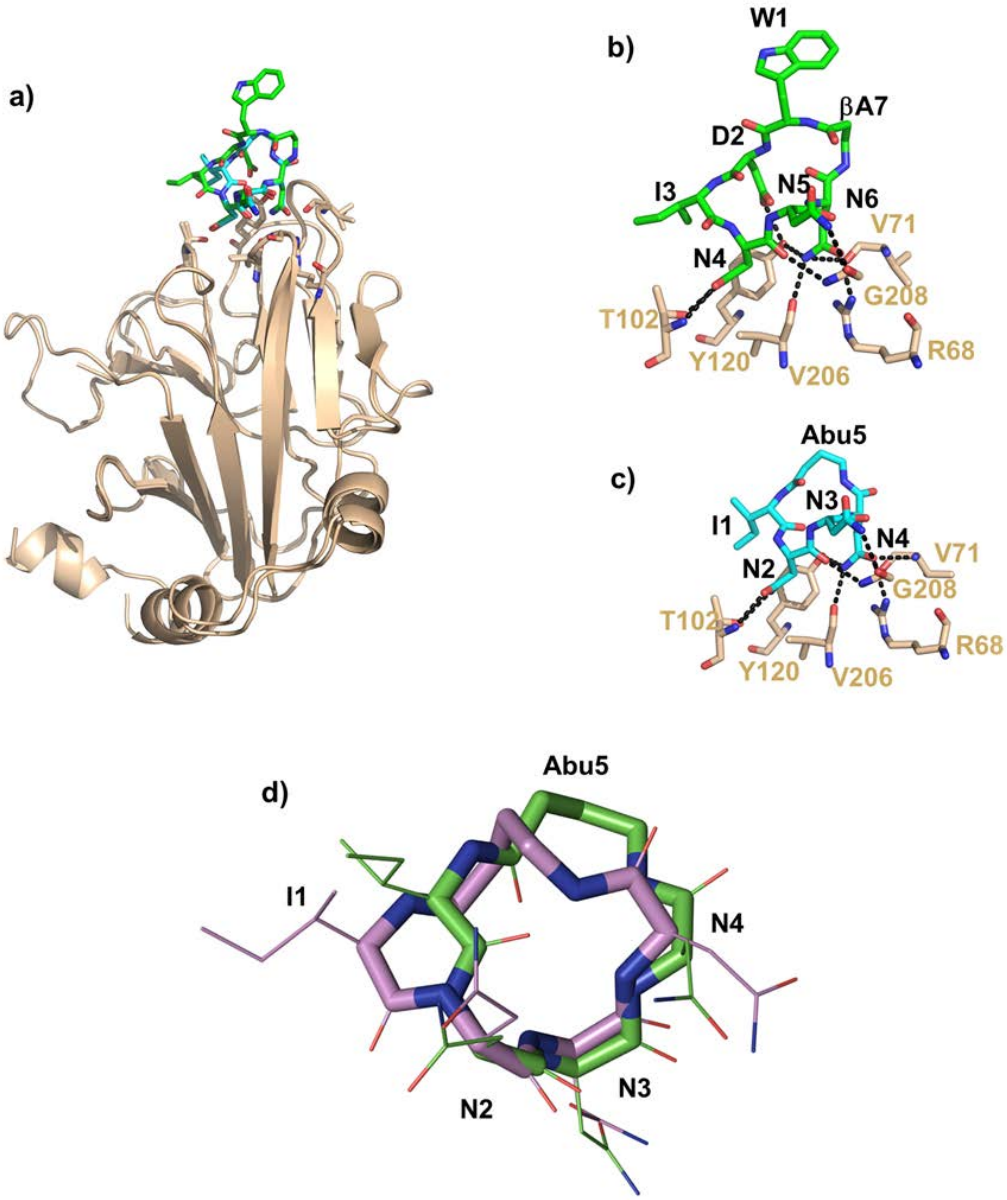

Figure S8. Superposition of the crystal structures of CP2 and CP3 bound to human SPSB2; PDB id 6DN5 and 6DN6, respectively. a) CP2 is shown as green sticks, and CP3 in cyan sticks; hSPSB2 is shown in cartoon (wheat). Intermolecular H-bonds between CP2 (b) and CP3 (c) with and hSPSB2 are shown as black dashed lines. Residues of CP2 and CP3 are labelled in black, and residues in hSPSB2 involved in the intermolecular interactions are shown in sticks and labelled in wheat. d) Overlay of the *in silico* model (purple) and crystal structure of bound CP3 (green) Cα; RMSD of the NNN residues is 0.3 Å.

Table S1. Chemical shifts of CP3 in water at pH 5 and 10 °C, recorded at 600 MHz. Abu = γ-aminobutyric acid.

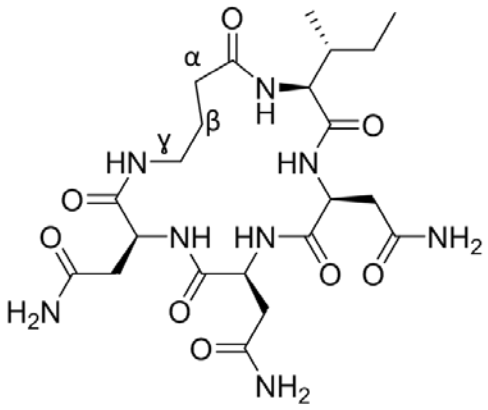

Residues	N	HN	H^{α}	C^{α}	H^{β}	C^{β}	Others
	ppm						
Ile1	8.07	115.9	4.10	62.1	1.83	38.8	$H^{\gamma 1a}$ 1.21 $H^{\gamma 1b}$ 1.42 $H^{\gamma 2}$ 0.94 $H^{\delta 1}$ 0.87 $C^{\gamma 1}$ 27.1 $C^{\gamma 2}$ 17.3 $C^{\delta 2}$ 13.2
Asn2	8.85	119.5	4.54	53.6	2.83 2.93	37.7	$H^{\delta 1}$ 7.74 $H^{\delta 2}$ 7.04 N^{δ} 113.5
Asn3	8.83	113.9	4.46	54.4	2.83 2.98	37.8	$H^{\delta 1}$ 7.67 $H^{\delta 2}$ 6.97 N^{δ} 113.4
Asn4	8.09	122.5	4.70	53.3	2.71 2.95	38.9	$H^{\delta 1}$ 7.55 $H^{\delta 2}$ 6.95 N^{δ} 113.0
Abu5	7.55	118.8	3.20 3.35	42.9	1.79 2.00	24.6	H^{γ} 2.36, 2.49 C^{γ} 35.4

Table S2. Data collection, and refinement statistics. Values in parentheses are for the highest resolution shell.

	CP2-hSPSB2 (PDB id 6DN5)	**CP3-hSPSB2 (PDB id 6DN6)**	**CP1-hSPSB4 (PDB id 6DN8)**	**CP2-hSPSB4 (PDB id 6DN7)**
Data Collection				
Space group	$P2_12_12_1$	$P2_12_12_1$	$P22_12_1$	$P12_11$
Cell dimensions				
a, *b*, *c* (Å)	32.6, 66.0, 110.0	41.0, 62.0, 84.9	49.0, 109.4, 118.1	54.7, 65.4, 69.2
α, β, γ (˚)	90.0, 90.0, 90.0	90.0, 90.0, 90.0	90.0, 90.0, 90.0	90.0, 103.6, 90.0
Resolution range (Å)	42.2 (2.4)	42.5 (1.6)	45.27 (1.75)	32.6 (1.4)
Observed/unique reflections	73281/9853	336506/29881	564844/64838	375252/91682
Mean I/σ(I)	6.6 (2.9)	22.6 (3.2)	16.2 (2.7)	12.7 (2.4)
Completeness (%)	99.4 (96.0)	99.9 (99.6)	99.9 (99.9)	98.3 (98.8)
Redundancy	7.4 (7.2)	11.3 (11.2)	8.7 (8.9)	4.1 (4.1)
R_{merge}	22.5 (68.7)	7.4 (74.3)	8.1 (81.1)	4.8 (47.4)
R_{pim}	9.0 (28.6)	2.4 (24.1)	3 (29.5)	3.1 (32.4)
No. molecules in asymmetric unit	1	1	3	2
Refinement				
Resolution (Å)	2.4	1.6	1.75	1.4
No. reflections (work/free)	2695/2559	2869/2727	4690/4468	6781/6412
R_{work}/R_{free}	17.4/24.6	17.4/20.2	19.4/20.9	19.7/21.3
No Atoms				
Protein	1488	1523	4562	3102
Inhibitor	59	38	189	126
Ion	10	0	22	2
Water	103	254	521	681
B-factors				
Protein	24.1	19	27.5	20.1
Inhibitor	22.2	14.4	32.5	13
Ion	49		46.6	13.5
Water	31.6	32.8	39.3	31
r.m.s deviations				
Bond lengths (Å)	0.01	0.01	0.01	0.01
Bond Angels (°)	1.10	1.01	1.04	1.02
MolProbity analysis				
Ramachandran outlier (%)	0	0	0	0
Ramachandran favoured (%)	98.5	97.9	98.3	99.2
MolProbity score	1.31	1.01	0.97	0.85

Chapter 3

Structure Activity Relationship (SAR) and Permeability of Cyclic Peptide Inhibitors of SPSB-iNOS Interaction

3.1 Introduction

CP3, the c[INNNAbu] pentapeptide, belongs to an emerging class of compounds that inhibits the interaction SPSB and iNOS (Chapter 2).[1] **CP3** was designed and synthesised to decrease the molecular weight, increase the drug likeness and hydrophobicity of previous cyclic heptapeptides inhibitors as an attempt to enhance the passive permeability. The pentapeptide showed an improvement of affinity for hSBSB2 (K_D = 7 nM) compared to its heptapeptide counterpart, **CP2**, c[WDINNNβA] (K_D = 32 nM) (Chapter 2). Furthermore, **CP3** was found to strongly inhibit the SPSB2-iNOS interaction in macrophage cell lysates. The crystal structure of **CP3**-hSPSB2 complex was also determined in order to reveal the molecular interactions of the peptide with the hSPSB2.[1] However, the passive permeability of **CP3** remains yet to be investigated.

In general, poor membrane permeability is considered one of the major hurdles facing the progress of peptides to clinical applications. Most peptides violate the traditional Lipinski's rule of 5 (molecular mass < 500 Da, calculated log P < 5, number of hydrogen bond donors < 5 and number of hydrogen bond acceptors < 10)[2] which predicts the potential of a given molecule for favourable permeability and oral bioavailability.[3] In violation of these rules, the natural product undecacyclic peptide, cyclosporine A (CSA), passively diffuses across the cell membrane with 29% bioavailability, despite high polarity and size (**Figure 3.1**). Recently, alternative metrics for the Lipinski's permeability parameters have been proposed and reviewed extensively in the literature (**Table 3.1**).[4] [5-8] In addition, the polar surface area (PSA), conformational flexibility and number of rotatable bonds were also considered as important determinants for the permeability of macrocyclic compounds.[9-10]

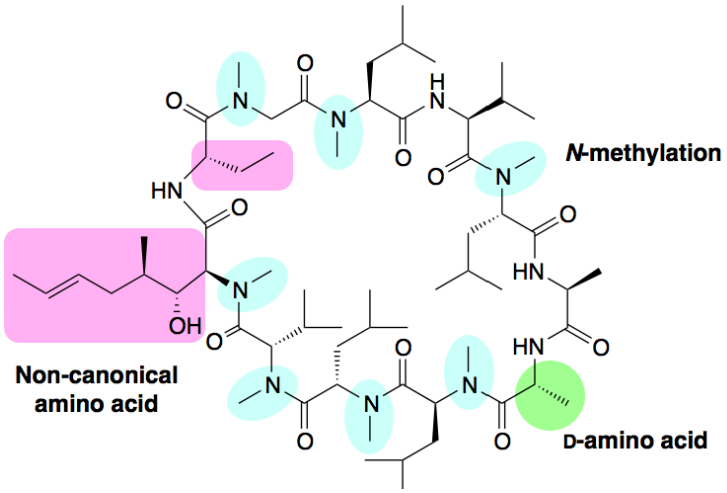

Figure 3.1. Chemical structure of Cyclosporine A showing the essential structural features that accounts for cyclosporine's permeability including N-methylation (highlighted in cyan), non-natural amino acids (highlighted in pink), backbone cyclisation and D-amino acid (highlighted in green) (*Figure taken from Ito et al., 2013)*[11]

Table 3.1. Revised Lipinski's rule for macrocyclic peptides vs small molecules (*Table reproduced from Vorherr et al.*).[5]

Property	Small molecules	Macrocyclic peptides
Molecular weight (MW)	<720	600-1200
Calculated logP	≤ for high MW	-2-6
Polar surface area (PSA)	≤140 Å^2	180-320
H bond acceptors (HBA)	Sum of HBD and HBA ≤12	12-16
H-bond donors (HBD)		≤12

Inspired by CSA (cyclic backbone, seven *N*-methyl groups, and four intramolecular hydrogen bonds), several methods have been reported to improve the passive permeability of peptides. Cyclisation by introducing conformational constraints and linking internal residues of a given peptide using disulfide bridges or hydrocarbon staples may help in stabilising its structure and encourage permeability.[12] Another method of peptide modification is masking of the hydrogen bond donors by N-methylation of the backbone amides, as previously reported in the orally bioavailable somatostatin analogue cyclo(Pro-Phe-$_D$-^{Me}N-Trp-^{Me}N-Lys-Thr-^{Me}N-Phe).[13] Methylation of backbone amides has a significant impact on peptide permeability as it also increases lipophilicity and alters conformational properties.[14] It can also fine-tune the selectivity and therapeutic efficacy of the analogues to a specific receptor.[15] Introduction of hydrophobic amino acids has also proven to be useful in generating cell-permeable cyclic penta- and hexaleucine peptides as demonstrated by Hill *et al.*[16-19] It was also found that the hydrophobic side chains can adopt different conformations which may help in shielding the polar core of the peptide and hence increase permeability.[17, 20]

In this Chapter, the passive permeability of **CP3** using parallel membrane artificial permeability assay (PAMPA) was explored. PAMPA is a high throughput *in vitro* assay that determines permeability using a donor/ acceptor system through an artificial membrane[21-22]. However, **CP3** was expected to be impermeable to the cell membrane due to its hydrophilic nature (three asparagine side chains). Thus, three strategies were attempted to enhance

permeability of **CP3**; 1) reducing hydrogen bond potential using N-methylations and other amino acids replacements, 2) incorporating hydrophobic residues and 3) decreasing the molecular weight of the peptide by designing a shorter tetrapeptide analogue of **CP3**. The cyclic peptide analogues were designed based on the previously reported SPSB2-bound conformation of **CP3** (**Figure 3.2**) (Chapter2).[1] Analogues (**1-29)** were synthesised using solid phase peptide synthesis and their binding affinities to hSPSB2 were evaluated using surface plasmon resonance (SPR). The PAMPA assay was employed to test the passive permeability of the synthesised cyclic peptide analogues.[23]

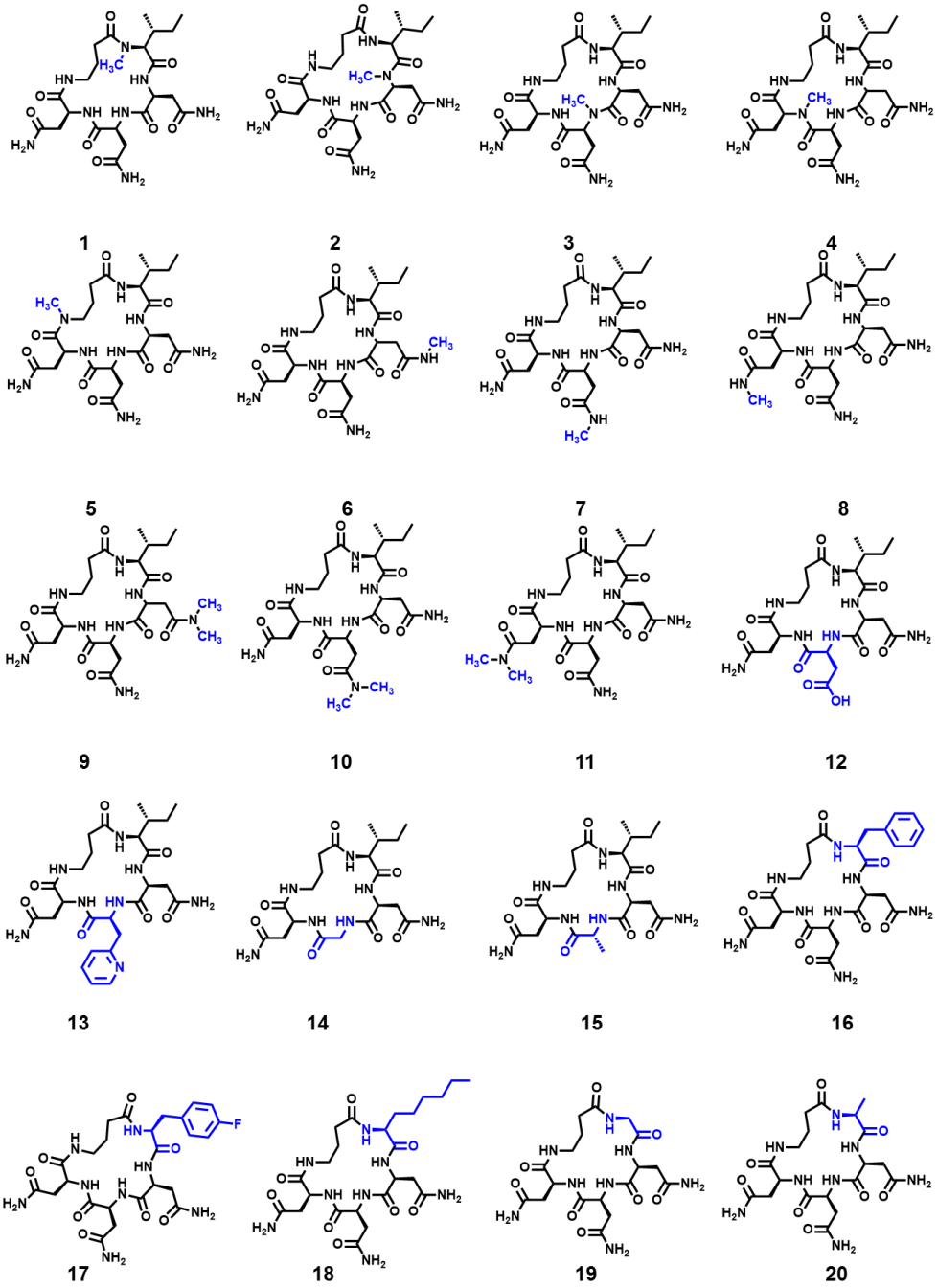

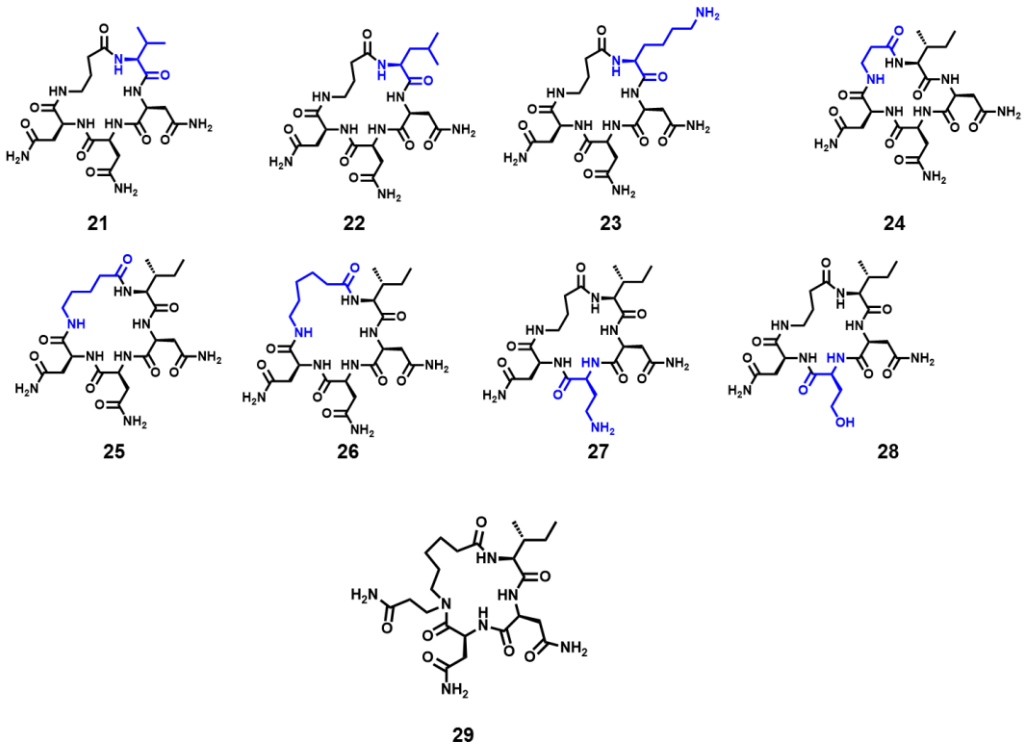

Figure 3.2. Chemical structure of **CP3** analogues generated in this Chapter with backbone N-methylations (**1-5**), side chain single (**6-8**) and double N-methylations (**9-11**) Asp (**12**), 2-pyridyl Ala (**13**), Gly (**14**), D-Ala (**15**). The Ile side chain was modified with Phe **(16)**, 4-F-Phe **(17)**, octyl-Gly **(18)**, Gly **(19)**, Ala **(20)**, Val **(21),** Leu **(22),** Lys **(23)**. β-Ala, 5-valeric acid and 6-amino hexanoic acid replaced γ-Abu in **24, 25** and **26** respectively. Asn3 was substituted by dimainobutyric (Dab) and homoserine in **27** and **28** respectively. Compound **29** is the tetrapeptide analogue of **CP3**. All modifications are highlighted in blue.

3.2 Material and Methods

3.2.1 Synthesis of CP3 analogues

All chemicals used in this study were purchased from Sigma-Aldrich (St Louis, Missouri, USA), Astral Scientific (New South Wales, Australia). Fmoc-protected amino acids and resins were purchased from Chem-Impex International (Wood Dale, Illinois, USA).

3.2.1.1 Pentapeptide analogues

All peptides were synthesised using Rink amide resin and further cyclised on resin as previously described in Chapter 2.

3.2.1.2 N-methylated analogues

The linear peptide was assembled on a chlorotrityl chloride resin using the standard SPPS procedures and Fmoc/t-Bu strategy. The N-terminus Fmoc group was deprotected using 20% piperidine in DMF. The side chain protected peptide was released from the resin using 30% hexafluoro-2-propanol (HFIP) in DCM twice for 30 min followed by evaporating HFIP using N_2 gas. The peptide was dissolved in DMF and cyclised in solution using 6 equivalents of PyClock and 10 equivalents of diisopropylethylamine (DIPEA) for 48 h. After the removal of DMF, the peptide was treated with TFA-containing cleavage cocktail for 3 h to deprotect the side chain and release the cyclic peptide. The TFA scavenger solution was evaporated using N_2 gas to leave a glassy peptide film. The precipitated peptide was washed three times with cold ether, dissolved in water, and lyophilized to yield a white powder.

3.2.1.3 Tetrapeptide

The first amino acid, β-alanine, was conjugated to Rink amide resin using standard SPPS protocols (**Scheme 3.1**). After deprotection of the Fmoc group using 20% piperidine in DMF, the free N-terminus was protected using O-nitrobenzenylsulfonyl (O-NBS)-Cl and DMF. The on-resin alkylation was performed using the allyl protected 6-bromo-hexanoic acid using 1, 8-diazabicyclo[5.4.0]undec-7-ene (DBU) in DMF for 24 h. The peptide was then treated with 2-mercaptoethanol to deprotect the O-NBS-protected peptide, releasing a free N-terminus which was further used for chain elongation. The allyl group was removed using 10 equivalents of phenylsilane and 0.1 equivalent of tetrakistriphenylphosphine palladium zero in DCM (3x15 min) under N_2 gas. The peptide was cyclised on resin using 6 equivalents of PyClock and 10 equivalent DIPEA for 48 h. The peptide was released from the resin as previously described in Chapter 2.

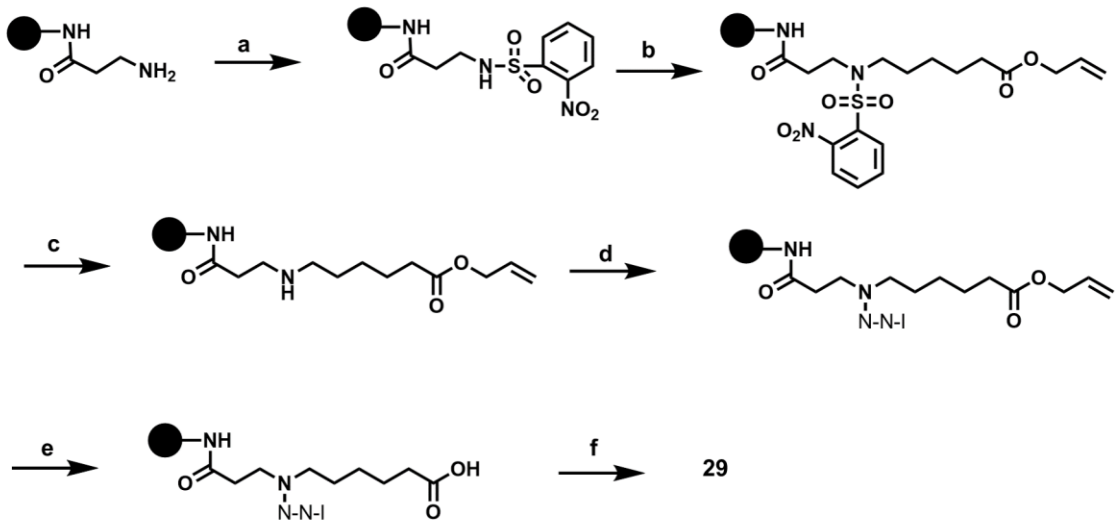

Scheme 3.1: Synthesis of tetrapeptide analogue of **CP3**, **29**. a) O-NBS-Cl, DIPEA, DMF, 30 min b) Allyl-6-bromohexanoate, DBU, DMF (24 h), c) 2-Mercaptoethaonl, DBU, DMF, 1 h (twice), d) SPPS, e) $Pd(Ph_3)_4$, $PhSiH_3$, 2 h (twice), f) PyClock, DIPEA, 12 h.

All peptides were purified using reversed-phase HPLC on a Waters Prep LC system incorporating a Waters 486 tunable absorbance detector set at 214 nm and a Phenomenex Luna C8(2) column [250mm × 21.2 mm (inside diameter), 100 Å, 10 μm] using a gradient from 100% buffer A (0.1% TFA /water) to 60% buffer B (0.1% TFA/acetonitrile) at a flow rate of 7 mL/min over 60 min. LC−MS analysis was performed using a Phenomenex Luna C8(2) column [100 mm ×2.0 mm (inside diameter), 100 Å, 3 μm] at 214 nm, eluting with a gradient from 100% buffer A (0.05% TFA/water) to 60% buffer B (0.05% TFA/acetonitrile) over 10 min at a flow rate of 0.2 mL/min. Mass spectra were acquired in positive ion mode with a scan range of m/z 200−2000. The overall yield of the final purified peptides was approximately 10-20%. Polymerisation was observed among few of these peptides including Gly, Ala and pyridyl Ala containing peptides.

3.2.1 Surface plasmon resonance

hSPSB2 protein expression and purification and the SPR binding experiments were carried out as described in Chapter 2.

3.2.2 Permeability assay

A 96-well microtiter plate (acceptor compartment) and a 96-well filter plate from Millipore (IPVH, 125 μm thick filter, 0.45 μm pore) (donor compartment) known as "sandwich" was purchased from pION Inc. The artificial membrane was prepared as 1% w/v of 1% phosphatidylinositol phosphate in n-dodecane. Stock solutions of water-insoluble peptides were prepared in 1-2% DMSO and further diluted to 200 μM using phosphate buffer, pH= 7.4. 2 μL of the phospholipid membrane solution was added to the filter-containing well and left to air dry before adding the peptide solution. The donor wells were filled with 200 μL of the peptide solution and the acceptor wells with 200 μL of buffer. The sandwich was assembled where the acceptor wells were placed on top of the donor wells. The PAMPA sandwich was incubated at 25ºC in a sealed container for 17 h. The amounts of peptides in the donor and acceptor compartments were measured using LC-MS while using 100 μM propranolol as the control compound. All experiments were done in triplicate.

3.3 Results and Discussion

3.3.1 Evaluation of the passive permeability of CP3

PAMPA was used as the *in vitro* assay for measuring passive permeability of **CP3**. The peptide was incubated in phosphate buffer overnight and its concentration was measured in both the donor and the acceptor compartments using LC-MS. **CP3** traces were not detected in the acceptor compartment suggesting that it may not be able to diffuse across the artificial lipid bilayer presumably due to its relatively high polarity.

3.3.2 Design of CP3 analogues

To improve the passive permeability of **CP3**, the crystal structure of **CP3**-hSPSB2 (Chapter 2) was used as the basis for designing the new analogues. As the side chains of Ile1 and Abu5 extend outside the binding pocket, it was hypothesised that these residues would be amenable to modifications without a loss in affinity (**Figure 3.3**). It was also observed that the side chain amide of Asn3 is only involved in one interaction with hSPSB2.[1] Taken together, these three residues (Ile1, Asn3 and Abu5) were replaced with natural and non-natural amino acids, in order to evaluate the impact of the aforementioned three strategies (decreasing the hydrogen

bonding potential, introducing hydrophobic natural and non-natural amino acids and designing of a shorter peptide) on the binding affinity and permeability of the designed **CP3** analogues.

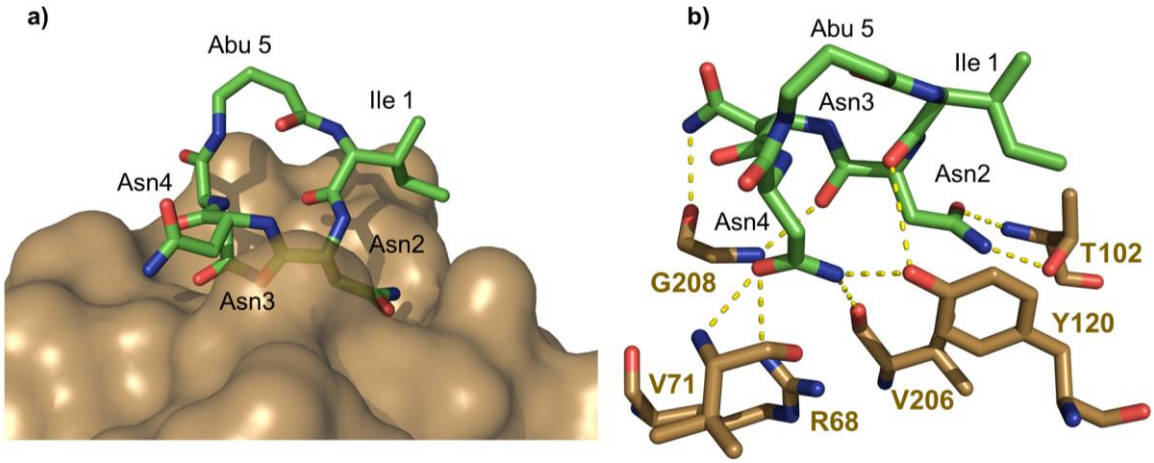

Figure 3.3. Crystal structure of **CP3** bound to hSPSB2 (PDB id 6DN6). a) Both Ile and Abu are pointing out of the binding pocket. b) Molecular interaction between **CP3** (green) and hSPSB2 (brown) showing the eight intermolecular hydrogen bonds involved in the interaction with only one hydrogen bond observed between Asn4 and G208.

Decreasing the hydrogen bonding potential [24]

In order to reduce the hydrogen bonding potential in **CP3**, single backbone Nα-methylations (**1-5**) and single or double Nδ-methylations of the side chains of NNN motif (**6-11**) were introduced (**Figure 3.2**). Another approach was pursued by replacing Asn3 with natural and natural amino acids with low hydrogen bond capabilities such as Asp which can maintain the distance between the side chain NH of Asn3 and the CO of G208 in hSPSB2 (Chapter 2) while replacing the hydrogen bond donors with acceptors (**12**). The non-natural amino acid, 2-pyridyl-alanine was also employed as a bioisostere of Asn (**13**) (**Figure 3.2**)**.** The NH of the pyridyl group can form a hydrogen bond with the backbone NH of the amino acid, thus shielding the backbone amide bonds and potentially enhancing the permeability of the peptide.[25]

Eliminating the hydrophilic side chain and hydrogen bond donors of Asn3 was further employed by replacing Asn3 with Gly (**14**) and D-Ala (**15**). Akshay *et al.* has previously shown that the NNN motif can be substituted by an NGN motif by using phage display with SPSB2-SPRY as bait[26] suggesting that Gly may maintain the binding affinity to hSPSB2. Moreover, reversing the stereochemistry using D-Ala may affect the conformation of the cyclic peptide and impact permeability and stability.

Introducing hydrophobic natural and non-natural amino acids

Another effective approach in tackling permeability is incorporation of hydrophobic amino acids, which increase the overall lipophilicity of the peptides. Phe (**16**), 4-F-Phe (**17**) and octyl-Gly (**18**) were used as hydrophobic substitutes of Ile to explore this hypothesis. To further investigate the importance of the Ile side chain for activity and permeability, it was replaced by amino acids with various side chain length and branching, such as Gly (**19**), Ala (**20**), Val (**21**) and Leu (**22**). The effect of introducing a positive net charge to **CP3** was also investigated by substituting Ile1 with Lys (**23) (Figure 3.2).**

The length of the linear carbon chain of γ- amino butyric acid was also varied between 2-6 carbon spacers (β-alanine, 5-amino valeric acid and 6-amino hexanoic acid) to further understand the effect of the carbon spacer on binding and permeability of the peptides. Asn3 was also replaced by diaminobutyric acid (**27)** and homoserine (**28)**. Both amino acid side chains are more hydrophobic and can approximate the steric properties of Asn through maintaining the relative spacing between the backbone α-carbon and Nδ-position in Asn3.

Designing of a shorter peptide

As the downsizing inhibitor approach proved to be useful in generating low molecular weight peptidic inhibitors of the SPSB-iNOS interaction (Chapter 2),[1] a four-residue peptide was designed in which the backbone carboxamide of Asn4, which is not involved in any interaction with the protein, was replaced with a carbon spacer bearing a pendant amide side chain (**Figure 3.4a**). The tetrapeptide model, when minimised in the iNOS binding site, was found to fit with an RMSD of 0.3 Å between the model peptide and the crystal structure (**Figure 3.4b**). This peptide would be useful in increasing the overall lipophilicity, decreasing the size and reducing the number of hydrogen bond donors in the peptide, which can improve the permeability of the peptide and further clarify the structural requirements for binding. The synthesis of this peptide was based on alkylating the o-NBS protected amine on resin using the in-house synthesised allyl 6-bromohexanoate. After deprotection of O-NBS containing peptide, the chain was further elongated using SPPS. The last Fmoc group was removed followed by the release of free carboxylic group using palladium catalyst. The peptide was cyclised on resin using PyClock in DMF.

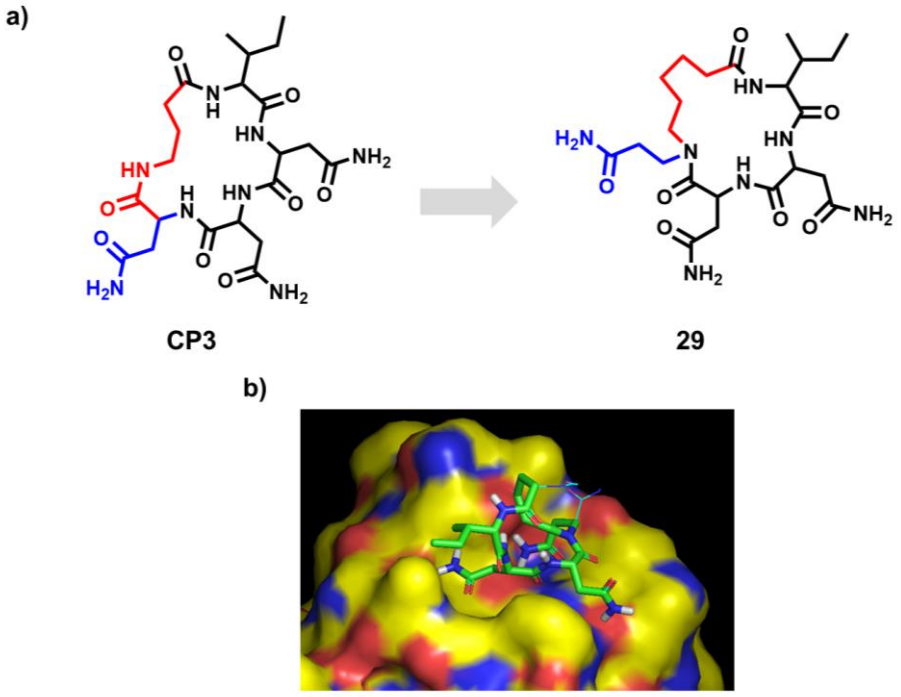

Figure 3.4. a) Design of tetrapeptide analogue of **CP3**, **29**. The highlighted red part shows the C-C spacer with the side chain amine of Asn4 as a pendant to maintain the interactions with the SPSB2 protein. b) Superimposition of the crystal structure of **CP3** (cyan, PDB id 6DN6) with the *in silico* model of the tetrapeptide, **29** (green), showing that the two structures align well over the backbone NNN motif, with Cα RMSD of 0.3 Å.

3.3.3 Evaluation of binding affinity and permeability of CP3 analogues

Binding affinities of the 29 analogues were assessed using SPR. hSPSB2 was immobilised on CM5 chip using the standard amine coupling. The peptides were prepared as 5-7 concentrations ranging from 1 µM-7 nM and run on the immobilised hSPSB2 protein surface. Fourteen analogues were able to bind to hSPSB2 with affinities of 10-700 nM (**Figure 3.5 and Table 3.2**).

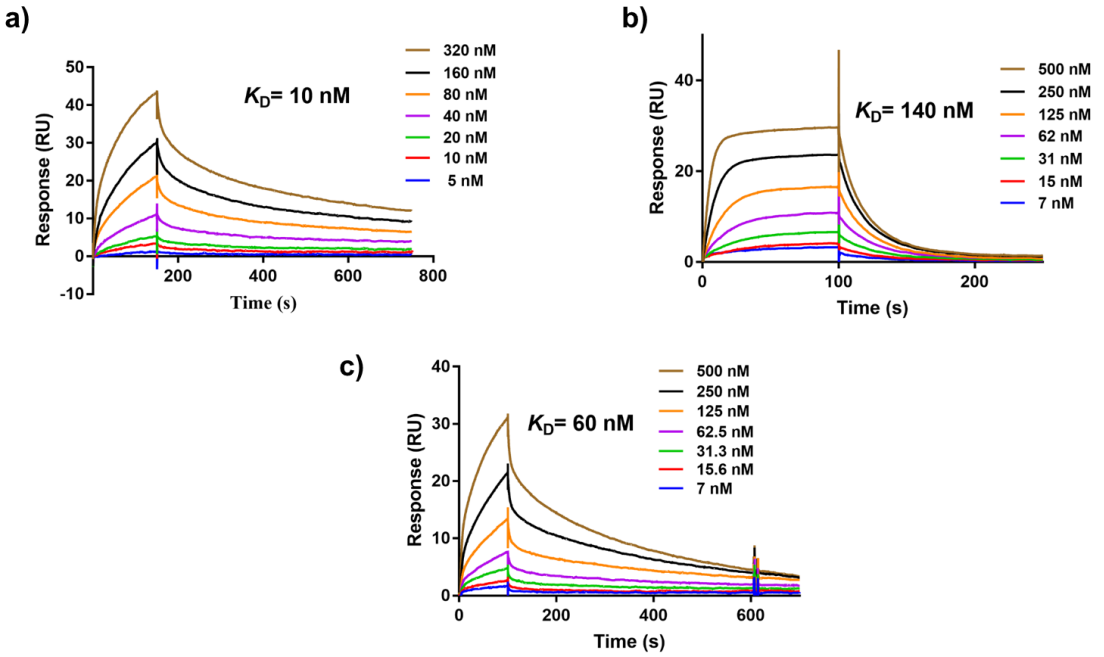

Figure 3.5. Representative sensorgrams of three **CP3** analogues; a) Compound **7**, b) Compound **18** and c) Compound **25** modified at Asn3, Ile1 and Abu5 positions respectively. All peptides were prepared in seven concentrations ranging from 5 nM to 500 µM. The Y axis shows the response unit (RU) differences after reference subtraction.

Table 3.2. Binding affinities of **CP3** analogues as determined by SPR. n.b., no binding to hSPSB2 was observed.

Compound	Modified position	K_D (nM)
1	Ile1	n.b.
2	Asn2	500
3	Asn3	n.b.
4	Asn4	n.b.
5	Abu5	500
6	Asn2	n.b.
7	Asn3	10
8	Asn4	n.b.
9	Asn2	n.b.
10	Asn3	n.b.
11	Asn4	n.b.
12	Asn3	n.b.
13	Asn3	n.b.
14	Asn3	10000
15	Asn3	20000
16	Asn3	300
17	Ile1	380
18	Ile1	140
19	Ile1	700
20	Ile1	500
21	Ile1	310
22	Ile1	250
23	Ile1	380
24	Abu5	n.b.
25	Abu5	60
26	Abu5	66
27	Asn3	500
28	Asn3	n.b.
29	Asn4 and Abu5	n.b.

Compound **7,** with a single N-methylation of the side chain of Asn3, showed the best binding affinity of 10 nM (**Figure 3.5**), whereas compound **10,** with a double methylation on the same Asn side chain, completely lost affinity suggesting the interaction between Asn3 and Gly 208 is crucial for binding. Other side chain N-methylations also (**Figure 3.2**) resulted in a loss of measurable binding affinity by SPR. In the **CP3**-hSPSB2 complex, the side-chains of the Asn2 and Asn4 residues in **CP3** contribute to six hydrogen bonds with hSPSB2 (to Arg68, Val71, Thr102, Tyr120, and Val206) (**Figure 3.3**). These side chains are also involved in additional intramolecular hydrogen bonds (Chapter 2). The loss of these hydrogen bond interactions by Nδ-methylations may be the major cause of the abolished binding.

Among the five main chain N-methylations, only modification of Asn2 (**2**) and Abu5 (**5**) was found out to bind to hSPSB2 (with K_D values of 500 and 700 nM, respectively) representing a 75-fold reduction in binding affinity compared to **CP3** (K_D = 7 nM). This result suggests that the removal of the backbone hydrogen bond potentials and conformational changes by N-methylations may have disrupted the active conformation of the cyclic peptide[14, 27] consistent with a previous finding by Linde and co-workers[28] in which N-methylation was shown to significantly reduce the biological activity of the N-methylated Melanocortin analogues.[28]

Analogues **(12-15 and 28**) failed to retain binding to hSPSB2, although a weak binding (K_D 10 and 20 µM, respectively) was observed for compounds **14** and **15** respectively. Only compound **27** with a Dab amino acid replacing Asn3, maintained a nanomolar affinity of K_D =500 nM. The absence of carbonyl group of the side chain of Asn3 indicate that although the carbonyl group is not involved in any interaction with hSPSB2, it may have some role in binding. All these findings further demonstrate that the interaction between the amine side chain of Asn3 and the G208 of hSPSB2 is critically important for binding.

Modifications of Ile in analogues **16-23** maintained nanomolar affinities of 140-700 nM (**Table 3.2**). The most potent analogue among this series was found to be compound **18** with the octyl-Gly moiety (**Figure 3.5**) while a significant reduction in affinity in analogues **19** and **20** (70- to 100 fold) was observed. Replacement of Ile with aromatic groups containing amino acids (**16** and **17**), branched amino acids, Val and Leu in compounds **21** and **22** respectively, positively charged amino acid (**23**) resulted in approximately 40- fold weaker affinity compared to **CP3.** These findings suggest that Ile position favours bulky and hydrophobic substitutions consistent with the previous observations in the **CP3**-hSPSB2 crystal structure (**Figure 3.3**) (Chapter 2).

The binding affinity of peptides with an extended carbon spacer (analogues **25** and **26**) was found to be 8-fold weaker than **CP3**, with a K_D values of 60 and 66 nM respectively (**Figure 3.5**). This may be due to the high entropic cost associated with introducing more flexibility to the structure. Shortening the spacer by a single carbon atom (**24**) resulted in a complete loss of binding affinity presumably because the peptide could not maintain the interactions of **CP3** observed in the crystal structure (**Figure 3.3**).

Compound **29**, the tetrapeptide analogue of **CP3**, did not bind hSPSB2 sufficiently tightly to be measurable by SPR suggesting that the geometry of the side chain of Asn4 is essential to retain binding. The additional flexibility due to both the six-carbon spacer and the Asn4 side chain pendant may have also contributed in the loss of the constrained conformation and hence affinity.

The PAMPA assay was utilised to evaluate the passive permeability of all peptides. Peptides at concentrations of 100-200 uM were incubated for 17 h in phosphate buffer, then both the donor and acceptor compartments were analysed using LC-MS. Propranolol, well known to permeate through lipid bilayer, was used as a control. None of the analogues were detected in the acceptor compartments. This may be due to the presence of at least two hydrophilic Asn out of five residues which renders the peptides too hydrophilic to readily pass through the lipid bilayer.

The PAMPA data acquired from this study among others were further used by Billy Noonan (Monash Institute of Pharmaceutical Sciences, Australia), in order to generate a permeability model based on a simple linear regression method.[29] The natural log of permeability values (P_e) for all peptides were calculated. These values were found to be correlated (R = 0.71, RMSE = 3.2 fold on a linear scale) with the change in solvation free energy between water and octanol continuum solvents, the Boltzmann weighted polar surface area and the predicted charge states in water.[29] This proposed model may be useful in the future rational design of permeable SPSB-iNOS inhibitors in the future.

3.4 Conclusions

In summary, a series of **CP3** modified peptides that binds to the hSPSB2 protein were designed and synthesised in order to identify features that are important for receptor binding and permeability. These results confirm that the side chains of Ile and Abu in **CP3** are amenable to modification while retaining potency. The present findings also demonstrated that the amide

side chain of Asn3 can be mono-substituted without any significant loss in affinity. None of these analogues showed measurable permeability through the artificial membrane, which suggests the need to find alternative ways to target permeability. The SAR information reported here along with the *in silico* passive permeability predication model generated by Noonan *et al.* will be valuable in the future optimisation of the SPSB-iNOS inhibitors that possess the right balance of potency, metabolic stability and permeability. Apart from passive permeability, the active transport of the peptides could also be explored by other means, such as conjugating the side chain of the Lys-containing analogue to small short peptide motifs known to enhance permeability (cell-penetrating peptides) as described in Chapter 4.

3.5 References

(1) Sadek, M. M.; Barlow, N.; Leung, E. W. W.; Williams-Noonan, B. J.; Yap, B. K.; Shariff, F. M.; Caradoc-Davies, T. T.; Nicholson, S. E.; Chalmers, D. K.; Thompson, P. E.; Law, R. H. P.; Norton, R. S., A cyclic peptide Inhibitor of the iNOS-SPSB protein-protein Interaction as a potential anti-infective agent. *ACS Chem Biol.* **2018,** *13*, 2930-2938.

(2) Lipinski, C. A.; Lombardo, F.; Dominy, B. W.; Feeney, P. J., Experimental and computational approaches to estimate solubility and permeability in drug discovery and development settings. *Adv Drug Deliv Rev.* **2001,** *46*, 3-26.

(3) Matsson, P.; Doak, B. C.; Over, B.; Kihlberg, J., Cell permeability beyond the rule of 5. *Adv Drug Deliv Rev.* **2016,** *101*, 42-61.

(4) Doak, Bradley C.; Over, B.; Giordanetto, F.; Kihlberg, J., Oral druggable space beyond the rule of 5: Insights from drugs and clinical candidates. *Chemistry & Biology.* **2014,** *21*, 1115-1142.

(5) Vorherr, T., Modifying peptides to enhance permeability. *Future Med Chem.* **2015,** *7*, 1009-1021.

(6) Doak, B. C.; Zheng, J.; Dobritzsch, D.; Kihlberg, J., How beyond rule of 5 drugs and clinical candidates bind to their targets. *J Med Chem.* **2016,** *59*, 2312-2327.

(7) Villar, E. A.; Beglov, D.; Chennamadhavuni, S.; Porco Jr, J. A.; Kozakov, D.; Vajda, S.; Whitty, A., How proteins bind macrocycles. *Nat Chem Biol.* **2014,** *10*, 723.

(8) Nielsen, D. S.; Shepherd, N. E.; Xu, W.; Lucke, A. J.; Stoermer, M. J.; Fairlie, D. P., Orally absorbed cyclic peptides. *Chem Rev.* **2017,** *117*, 8094-8128.

(9) Veber, D. F.; Johnson, S. R.; Cheng, H. Y.; Smith, B. R.; Ward, K. W.; Kopple, K. D., Molecular properties that influence the oral bioavailability of drug candidates. *J Med Chem.* **2002,** *45*, 2615-23.

(10) Ertl, P.; Rohde, B.; Selzer, P., Fast calculation of molecular polar surface area as a sum of fragment-based contributions and its application to the prediction of drug transport properties. *J Med Chem.* **2000,** *43*, 3714-7.

(11) Ito, K.; Passioura, T.; Suga, H., *Technologies for the Synthesis of mRNA-Encoding Libraries and Discovery of Bioactive Natural Product-Inspired Non-Traditional Macrocyclic Peptides*. 2013; Vol. 18, p 3502-3528.

(12) Yang, N. J.; Hinner, M. J., Getting across the cell membrane: an overview for small molecules, peptides, and proteins. *Methods Mol Biol.* **2015,** *1266*, 29-53.

(13) Biron, E.; Chatterjee, J.; Ovadia, O.; Langenegger, D.; Brueggen, J.; Hoyer, D.; Schmid, H. A.; Jelinek, R.; Gilon, C.; Hoffman, A.; Kessler, H., Improving oral bioavailability of peptides by multiple N-methylation: Somatostatin analogues. *Angew Chem Int Ed* **2008,** *47*, 2595-2599.

(14) White, T. R.; Renzelman, C. M.; Rand, A. C.; Rezai, T.; McEwen, C. M.; Gelev, V. M.; Turner, R. A.; Linington, R. G.; Leung, S. S. F.; Kalgutkar, A. S.; Bauman, J. N.; Zhang, Y.; Liras, S.; Price, D. A.; Mathiowetz, A. M.; Jacobson, M. P.; Lokey, R. S., On-resin N-methylation of cyclic peptides for discovery of orally bioavailable scaffolds. *Nat Chem Biol.* **2011,** *7*, 810-817.

(15) Mas-Moruno, C.; Beck, J. G.; Doedens, L.; Frank, A. O.; Marinelli, L.; Cosconati, S.; Novellino, E.; Kessler, H., Increasing αvβ3 selectivity of the anti-angiogenic drug cilengitide by N-methylation. *Angew Chem Int Ed* **2011,** *50*, 9496-9500.

(16) Aldrich, J. V., CHAPTER 7 Peptide Lead Optimization—Strategies and Tactics. In *Peptide-based Drug Discovery: Challenges and New Therapeutics*, The Royal Society of Chemistry: 2017; pp 192-222.

(17) Walport, L. J.; Obexer, R.; Suga, H., Strategies for transitioning macrocyclic peptides to cell-permeable drug leads. *Curr Opin Biotechnol.* **2017,** *48*, 242-250.

(18) Wang, C. K.; Craik, D. J., Cyclic peptide oral bioavailability: Lessons from the past. *Biopolymers.* **2016,** *106*, 901-909.

(19) Sawyer, T. K., CHAPTER 1 Renaissance in Peptide Drug Discovery: The Third Wave. In *Peptide-based Drug Discovery: Challenges and New Therapeutics*, The Royal Society of Chemistry: 2017; pp 1-34.

(20) Hill, T. A.; Lohman, R.-J.; Hoang, H. N.; Nielsen, D. S.; Scully, C. C. G.; Kok, W. M.; Liu, L.; Lucke, A. J.; Stoermer, M. J.; Schroeder, C. I.; Chaousis, S.; Colless, B.; Bernhardt, P. V.; Edmonds, D. J.; Griffith, D. A.; Rotter, C. J.; Ruggeri, R. B.; Price, D. A.; Liras, S.; Craik, D. J.; Fairlie, D. P., Cyclic penta- and hexaleucine peptides without N-methylation are orally absorbed. *ACS Med Chem Lett.* **2014,** *5*, 1148-1151.

(21) Yu, H.; Wang, Q.; Sun, Y.; Shen, M.; Li, H.; Duan, Y., A new PAMPA model proposed on the basis of a synthetic phospholipid membrane. *PLoS One.* **2015,** *10*, e0116502.

(22) Kansy, M.; Senner, F.; Gubernator, K., Physicochemical high throughput screening: parallel artificial membrane permeation assay in the description of passive absorption processes. *J Med Chem.* **1998,** *41*, 1007-10.

(23) Rezai, T.; Bock, J. E.; Zhou, M. V.; Kalyanaraman, C.; Lokey, R. S.; Jacobson, M. P., Conformational flexibility, internal hydrogen bonding, and passive membrane permeability: successful in silico prediction of the relative permeabilities of cyclic peptides. *J Am Chem Soc.* **2006,** *128*, 14073-80.

(24) Räder, A. F. B.; Reichart, F.; Weinmüller, M.; Kessler, H., Improving oral bioavailability of cyclic peptides by N-methylation. *Bioorg Med Chem.* **2018,** *26*, 2766-2773.

(25) Thansandote, P.; Harris, R. M.; Dexter, H. L.; Simpson, G. L.; Pal, S.; Upton, R. J.; Valko, K., Improving the passive permeability of macrocyclic peptides: Balancing permeability with other physicochemical properties. *Bioorg Med Chem.* **2015,** *23*, 322-327.

(26) D'Cruz, A. Introducing cell permebale peptides to inhibit the SPRY domain-containing SOCS box protein 2 (SPSB2), the negative regulator of inducible nitric oxide synthase (iNOS) (Unpublished doctoral dissertation). University of Melbourne, Australia, 2014.

(27) Chatterjee, J.; Rechenmacher, F.; Kessler, H., N-Methylation of peptides and proteins: An important element for modulating biological functions. *Angew Chem Int Ed* **2013,** *52*, 254-269.

(28) Linde, Y.; Ovadia, O.; Safrai, E.; Xiang, Z.; Portillo, F. P.; Shalev, D. E.; Haskell-Luevano, C.; Hoffman, A.; Gilon, C., Structure-activity relationship and metabolic stability studies of backbone cyclization and N-methylation of melanocortin peptides. *Biopolymers.* **2008,** *90*, 671-682.

(29) Williams-Noonan, B. J.; Barlow, N.; Sadek, M. M.; Yuriev, E.; Norton, R. S.; Chalmers, D. K., In silico computation of macrocycle permeability by conformational scanning, Maxwell-Boltzmann averaging and QSAR. *manuscript in prepration* **2018**.

Chapter 4

Bicyclic and TAT-Conjugated Inhibitors of the SPSB-iNOS Protein–Protein Interaction

4.1 Introduction

Chapter 3 documented the attempts to enhance the permeability of **CP3** peptide through introducing hydrophobic amino acids, masking hydrogen bonds and decreasing the molecular weight of **CP3**.[1] Based on the crystal structure of the **CP3**-hSPSB2 complex (Chapter 2), **CP3** analogues were designed and synthesised. K_D values of 140-700 nM values for 14 **CP3** analogues were obtained by SPR, while the others failed to bind to hSPSB2. These modifications introduced on **CP3** were not successful in enhancing the passive permeability as determined by the PAMPA assay. In this Chapter, the use of cell-penetrating peptides (CPPs) are described as an alternative approach for enhancing the permeability of **CP3** analogues.

Cell-penetrating peptides are a large class of short amino acid sequences (5–30 residues) that are able to traverse biological membranes.[2] The transactivator of transcription (TAT) of human immunodeficiency virus and penetratin peptides were the first linear CPPs described in the literature.[3-4] Inspired by these natural peptides, various classes of CPPs including positively and negatively charged, amphipathic and non-amphipathic peptides were also reported and utilised in intracellular delivery strategies.[5-6] CPPs can effectively deliver different types of cargos such as small molecules,[7] proteins[8] and nucleic acids[9] to cells. Recently, Ma *et al.* reported a novel synthetic CPP, PepB, that is able to facilitate the delivery of retinoic acid to human neural stem cells and promote neuronal differentiation.[10]

The fundamental basis for cell entry of CPPs remains a subject of controversy in the literature.[11-12] Generally speaking, two mechanisms have been proposed for the internalisation of cationic CPPs containing arginine or lysine residues. The first is the direct membrane translocation, where the positively charged amino acids side chains interact with the negatively charged phospholipids of the plasma membrane to generate neutral ions that diffuse passively across the membranes.[12-13] In the second mechanism, the CPPs internalise into cells through energy-dependent endocytosis.[12] The peptides bind to cell surface receptors such as heparin sulfate and and/or membrane phospholipids and are internalised by clathrin-mediated endocytosis, caveolae/lipid-raft-mediated endocytosis, and/or receptor-independent macropinocytosis.[12, 14] The majority of the CPPs and their cargos, however, may remain confined in the endosomes following endocytosis and are typically degraded without having the possibility to reach their target sites to exert their biological activity.[15]

Several methods have been envisaged to overcome this hurdle, including the use of acid–labile bonds, endosome-disrupting peptides or polymers, rupture of endosomal membranes

with lasers and cyclisation of the linear CPPs.[16-17] Cyclisation offers the opportunity to improve the cyclic CPPs penetration efficiency and/or internalisation kinetics.[18] Cyclic CPPs provide an optimal spatial distribution of the positive charged groups for interaction with the membrane.[19] In 2011, a study showed that the larger arginine side chain separation in cyclic TAT maximises the membrane contacts, leading to a more controlled distribution of the positive charge compared to the less constrained linear TAT and hence increased uptake efficiency.[18]

Recently, Pei *et al.* discovered a family of cyclic amphipathic peptides cFΦR$_4$, (Φ = L-2-naphthylylalanine), which are internalised by endocytosis with enhanced cellular uptake up to 60-fold higher than TAT (**Figure 4.1a**).[20-21] The presence of two aromatic groups with three arginine residues in a cyclic arrangement significantly enhanced the internalisation in HeLa cells.[22] These novel peptides were reported to escape the early endosome by inducing endosomal membrane curvature and budding of small vesicles, which eventually collapse and release the CPPs into the cytoplasm (**Figure 4.1b**).[22] The same group also incorporated these cell-penetrating peptides into bicyclic peptides to target difficult intracellular protein-protein interactions[22] such as a peptidyl-prolyl *cis-trans* isomerase (Pin1) inhibitors[23] and inhibitors of IκB kinase α/β (IKKα/β)-binding domain of NF-κB essential modulator (NEMO)-IκB kinase.[24] These bicyclic peptide inhibitors were able to bind efficiently to their cytoplasmic targets owing to their increased stability and permeability.[22-24]

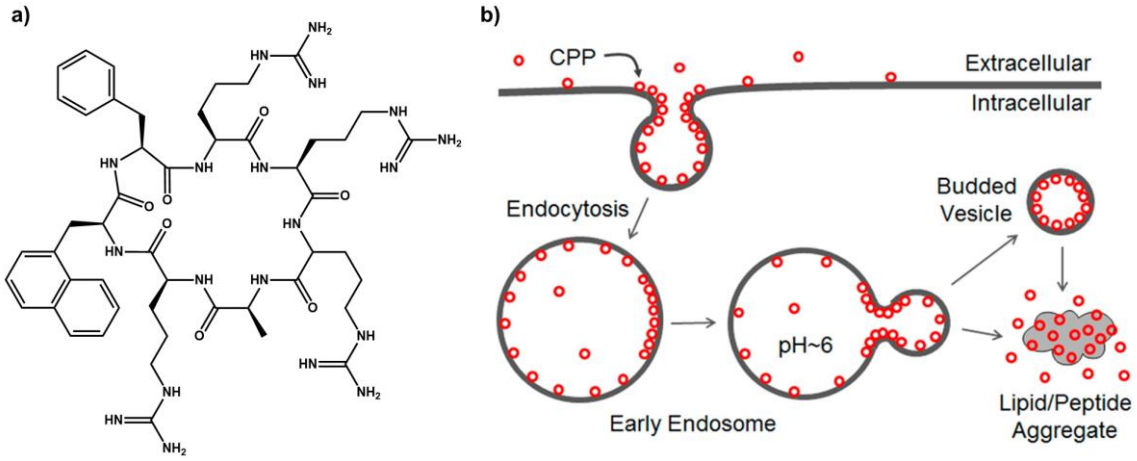

Figure 4.1. a) Chemical structure of amphipathic CPP, cFΦR$_4$. b) Representative diagram of the novel endosomal escape mechanism suggested for cFΦR$_4$. The peptides escape the early endosome through budding of small vesicles followed by collapse in the cytoplasm to release the peptide (*Figure taken from Pei et al.)* [21-22]

Herein, the possibility of developing bifunctional cyclic peptides containing both cell-penetrating (cFΦR$_4$) and SPSB inhibitory (**CP3**) sequences as cell-permeable inhibitors against SPSB proteins was explored (**Figure 4.2a**). It was envisaged that the bicyclic system would enable the two rings to function independently of each other. In addition, the increased conformational rigidity of bicyclic peptides could improve their target-binding affinity and permeability.[25] A novel synthetic strategy was developed to synthesise the bicyclic peptide, where the orthogonal protection was used to provide a second ring-closing step, providing the cyclic peptide inhibitor and the cyclic CPP. A linear version of the TAT peptide was also conjugated to an analogue of **CP3** to assess the effect of bicyclisation on the permeability of the peptides (**Figure 4.2b**). The effect of the CPP motif on binding affinity of the two conjugates for hSPSB2 was determined using surface plasmon resonance (SPR). The Griess assay was used to evaluate the ability of the peptides to block SPSB-iNOS interaction in macrophage cell cultures and enhance nitric oxide production following internalisation.

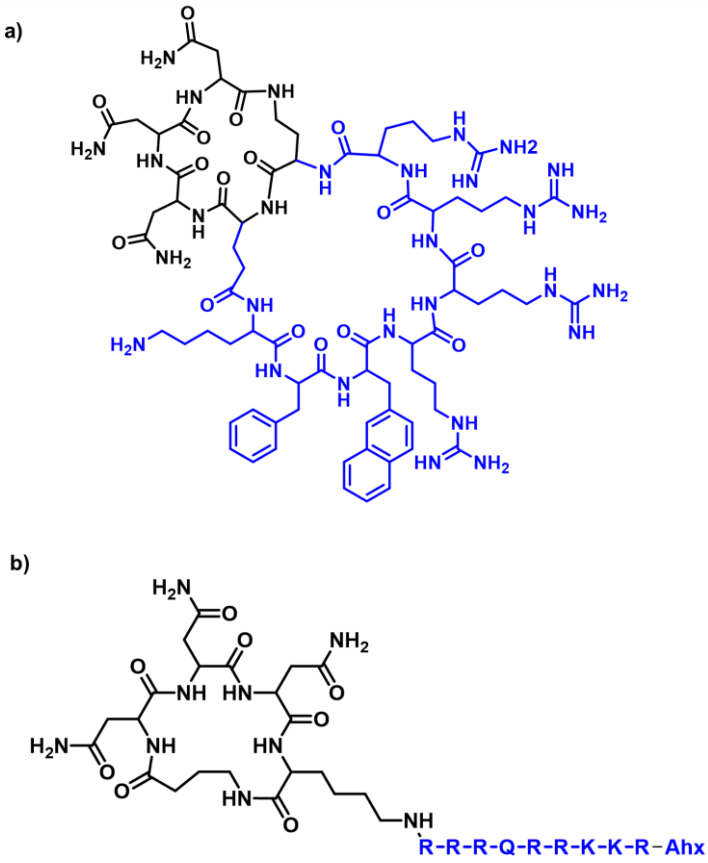

Figure 4.2. Cyclic peptide conjugates of **CP3** generated in this Chapter, a) bicyclic **CP3** peptide and b) TAT-conjugated peptide. SPSB-iNOS inhibitor and CPP motifs are highlighted in black and blue, respectively.

4.2 Materials and Methods

4.2.1 Peptide synthesis

4.2.1.1 Bicyclic peptide

The synthetic strategy for the bicyclic peptide **CP3**-CPP involved SPPS using an orthogonal Dmab/Alloc protecting group strategy (**Scheme 4.1).** The linear peptide sequence was synthesised on cholorotrityl chloride (CTC) (0.2 mmol/g) via standard Fmoc chemistry using an automated peptide synthesiser (Rainin PS3, Protein Technologies, Inc.). Stepwise deprotection and coupling of amino acids was repeated until the desired linear peptide was synthesised. The typical coupling reaction contained 3 equiv of Fmoc-amino acid, 3 equiv of 2-(6-chloro-1-H-benzotriazole-1-yl)-1,1,3,3-tetramethylaminiumhexafluorophosphate (HCTU) and 10 equiv. of diisopropylethylamine (DIPEA) and was allowed to proceed with mixing for 2 h. An additional lysine residue was incorporated in the linear peptide to facilitate the conjugation of a fluorophophore for future permeability studies using confocal microscopy. Followed by the deprotection of the last Fmoc group using 20% piperidine in DMF, the N-terminus was further tritylated overnight (2 equiv of trityl chloride in DMF) to avoid unfavourable cyclisation of the free amine of linear peptide during the deprotection of the Dmab group. The Alloc group was deprotected in a single step by $PhSi_3$/Pd in DCM for 2 h, releasing the side chain amine of Dab for further chain elongation using the standard SPPS protocol.

After Fmoc deprotection of the last amino acid, the Dmab protecting group of glutamic acid was removed using 2 equiv of hydrazine hydrate for 1 h. The **CP3**-containing motif (Ring A) was first cyclised on resin using PyClock (3 equiv.) and DIPEA (10 equiv.) in DMF for 48 h to form an amide bond between the asparagine side chain and Cα of glutamic acid. The side chain protected peptide was then released from the resin by acid hydrolysis using 30% HFIP in DCM, which concomitantly deprotected the acid labile trityl group of the N-terminus of the linear peptide. The second head-to-tail cyclisation (CPP-containing motif, Ring B) between the free carboxylic and amino termini was performed using 5 equiv of PyClock and 10 equiv of DIPEA in dilute DMF for 48 h. The side chain protecting groups were removed using cleavage cocktail K [TFA/thioanisole/water/phenol/1,2-ethanedithiol (EDT) (82.5:5:5:5:2.5 v/v)] for 4 h. The peptides was purified using reversed-phase HPLC on a Waters Prep LC system incorporating a Waters 486 tunable absorbance detector set at 214 nm and a Phenomenex Luna C8(2) column [250 mm × 21.2 mm (inside diameter), 100 Å, 10 μm] using a gradient from

100% buffer A (0.1% TFA /water) to 60% buffer B (0.1% TFA/acetonitrile) at a flow rate of 7 mL/min over 60 min. LC−MS analysis was performed on a Shimadzu LCMS2020 instrument using a Phenomenex Luna C8(2) column [100 mm ×2.0 mm (inside diameter), 100 Å, 3 μm] at 214 nm, eluted with a gradient from 100% buffer A (0.05% TFA/water) to 60% buffer B (0.05% TFA/acetonitrile) over 10 min at a flow rate of 0.2 mL/min. Mass spectra were acquired in positive ion mode with a scan range of m/z 200−2000. The yield of the final purified bicyclic peptide was 1-2 % owing to the multistep synthesis and increased polymerisation (**Figure 4.3**).

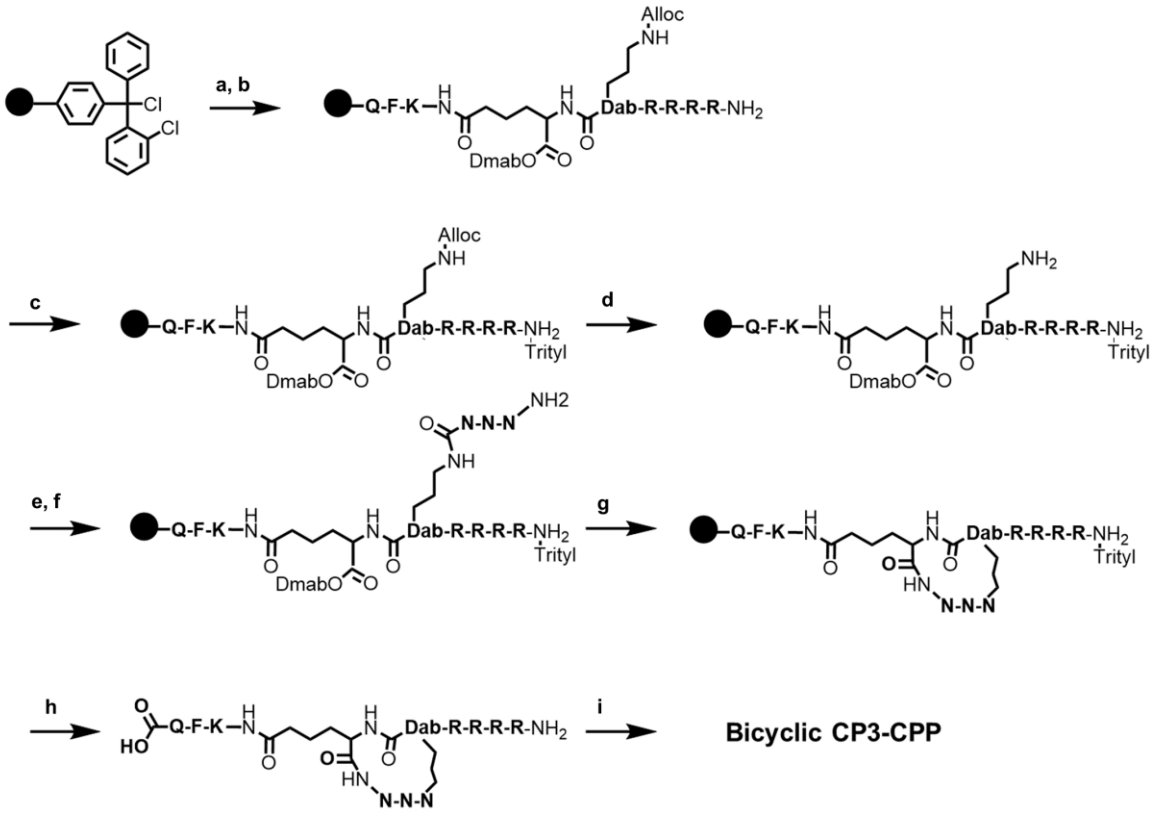

Scheme 4.1. Synthesis of the bicyclic **CP3**-CPP conjugate. Reagents and conditions: (a) Fmoc-a.acid (3 equiv), HCTU (3 equiv) DIPEA/DMF (7% v/v), 2 h (b) SPPS; 20% piperidine/DMF, 2 x 5 min followed by Fmoc-amino acid (3 equiv), HCTU (3 equiv), DIPEA/DMF (7% v/v) (c) 2 equiv Trityl chloride in DMF, overnight (d) 3 equiv. $PhSi_3/Pd(PPh_3)_4$ in DCM/N_2 gas, 2 h (e) SPPS; 20% piperidine/DMF, 2 x 5 min followed by Fmoc-amino acid (3 equiv), HCTU (3 equiv), DIPEA/DMF (7% v/v) (f) 2 equiv. of hydrazine hydrate in DMF, 1 hr (g) 3 equiv. of PyClock, 10 equiv. of DIPEA in DMF, 48 h (h) 30% HFIP in DCM, 30 mins (i) (g) 5 equiv. of PyClock, 10 equiv. of DIPEA in DMF, 48 h (e) 82.5% (v/v)TFA, 5% (v/v) thioanisole, 5% (v/v) water, 5% (v/v) phenol, 2.5% (v/v) EDT, 4 h.

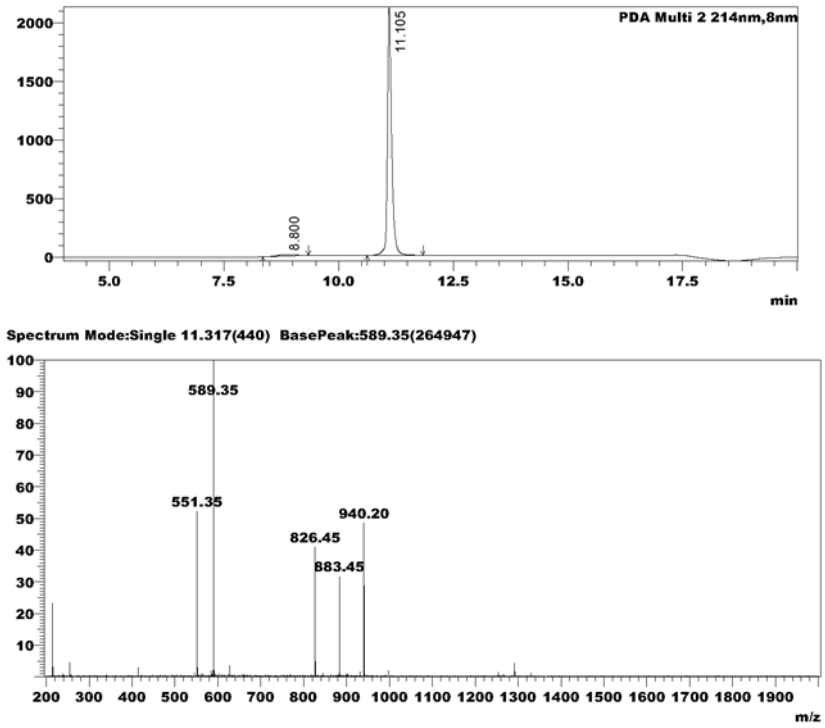

Figure 4.3. LC-MS traces of bicyclic **CP3**-CPP conjugate. Purity is ~98%, based on the peak area in the chromatogram.

4.2.1.2 TAT conjugated peptide.

The linear peptide was assembled on Rink amide AM resin (0.34 mmol/g) using standard Fmoc SPPS procedures (**Scheme 4.2**). The Fmoc protecting group on the resin was first removed by 20% (v/v) piperidine in DMF prior coupling to the amino acid residue for 2 h per coupling cycle using 3 equiv of O-(1H-6-chlorobenzotriazole-1-yl)-1,1,3,3-tetramethyluronium hexafluorophosphate (HCTU) and 7% (v/v) DIPEA in DMF. Following the deprotection of the last Fmoc using 20% piperidine in DMF, the Dmab group was removed using hydrazine hydrate in DMF for 30 min. The peptide was cyclised on-resin using PyClock (3 equiv.) and DIPEA (10 equiv.) in DMF for 48 h as described in Chapter 2. The Alloc group of Lys was then deprotected using $PhSi_3$/Pd in DCM for 2 h and the free amine group was employed for the assembly of linear TAT by standard SPPS protocol. To generate a fluorolabelled peptide, 4-aminohexanoic acid was added to the N-terminus following the last Fmoc-deprotection. Reagent K, TFA/thioanisole/water/phenol/EDT (82.5:5:5:5:2.5 v/v), was used to cleave the peptide from the resin, which also removes the side chain protecting groups. The crude peptide was recovered by precipitation with cold diethyl ether, isolated by centrifugation (2 x 10 min;

3000 rpm). The peptide was purified as previously described for the bicyclic peptide (**Figure 4.4**). The overall yield of final purified CP3-TAT conjugate was approximately 10-20%.

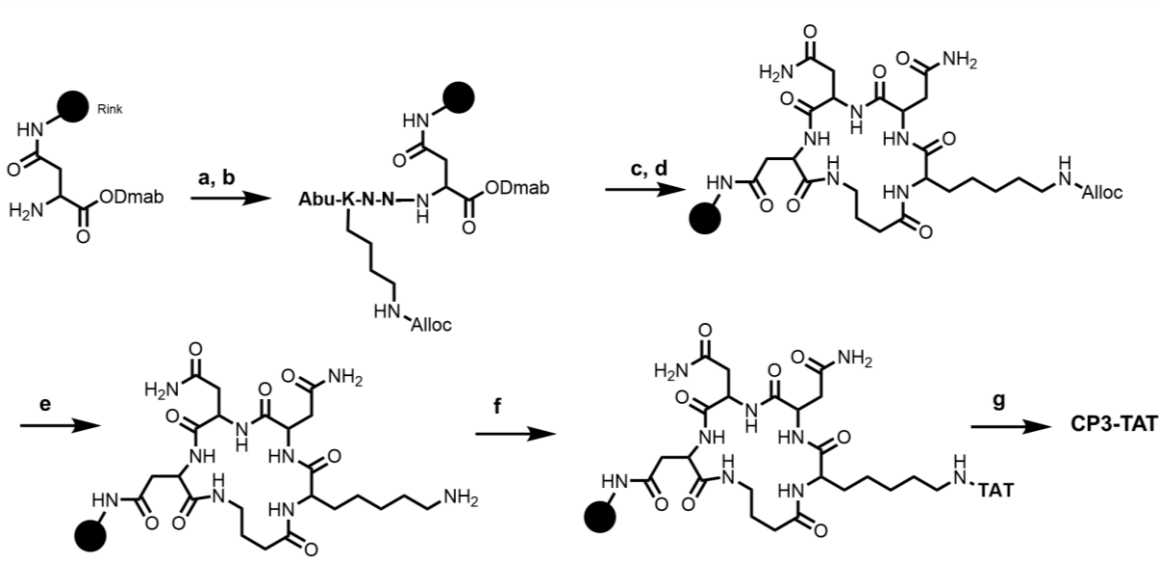

Scheme 4.2. Synthesis of **CP3**-TAT conjugate. Reagents and conditions: (a) Rink amide resin, HCTU, DIPEA, DMF, 2 h (b) SPPS; 20% piperidine/DMF, 2 x 5 min followed by Fmoc-amino acid (3 equiv), HCTU (3 eq), DIPEA/DMF (7% v/v) (c) 2 equiv. of hydrazine hydrate in DMF, 30 min (d) 3 equiv. of PyClock, 10 equiv of DIPEA in DMF, overnight (e) 3 equiv. $PhSi_3/Pd(PPh_3)_4$ in DCM/N_2 gas, 2 h (f) SPPS; 20% piperidine/DMF, 2 x 5 min followed by Fmoc-amino acid (3 equiv), HCTU (3 equiv), DIPEA/DMF (g) (e) 82.5% (v/v)TFA, 5% (v/v) thioanisole, 5% (v/v) water, 5% (v/v) phenol, 2.5% (v/v) EDT, 4 h.

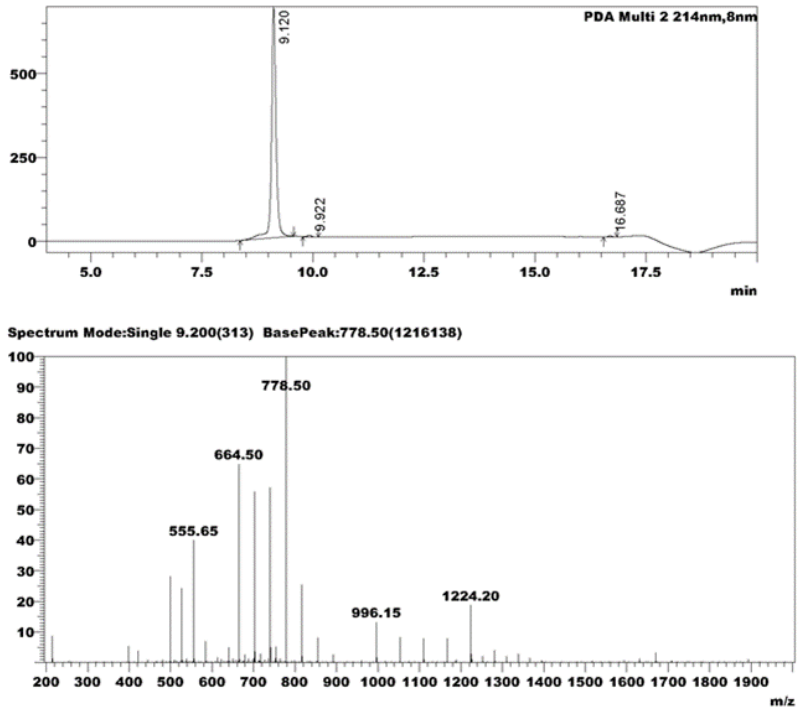

Figure 4.4. LC-MS profiles of the purified of **CP3**-TAT conjugate. Purity is ~95%, based on the peak area in the chromatogram.

4.2.2 Surface plasmon resonance

SPSB2 was expressed, purified and the SPR binding experiments was performed as described in Chapter 2.

4.2.3 Cell culture and Griess assay

A murine leukemic macrophage-like cell line, RAW 264.7 (ATCC, USA), was grown in plastic culture flasks in Dulbecco's Modified Eagle's Medium (DMEM) supplemented with heat-inactivated 10% foetal bovine serum (FBS), in a 5% CO_2 incubator at 37 °C. Cells were seeded at an initial density of 1×10^6 cells/well in triplicates (same batch of cells) in a 24-well tissue culture plates. Cells were then challenged with LPS (10 ng/mL) and IFN-γ (20 ng/mL) and incubated for 48 and 72 h with or without 100 µM peptide. Untreated cells were also used as a control to confirm the production of NO upon LPS/IFN-γ stimulation. Cell supernatants were used for the determination of nitrite concentration.

The nitrite concentration was measured as an indicator of NO production, according to the Griess reaction.[26] The Griess assay is a colourimetric assay that measures the concentration of nitrite as the stable product of nitric oxide in biological samples.[26] 150 µL of mixed 1:1sulfanilamide and *N*-(1-naphtyl)ethylendiamine dihydrochloride dissolved in 2.5% H_3PO_4 as 1% and 0.5% solutions, respectively, was incubated with 150 µL of cell culture supernatant for 15 min at room temperature, in the dark. The optical density was measured at 540 nm. Nitrite concentration was determined using sodium nitrite as standard (10-100 µM). Griess assays were performed by Arfatur Rahman (Monash Institute of Pharmaceutical Sciences, Australia).

4.3 Results and Discussion

4.3.1 Design of CP3-CPP conjugates

Based on the structural information acquired from SAR and the crystal structure of the **CP3**-hSPSB2 complex (Chapters 2 and 3), a bicyclic system in which ring A was designed for SPSB binding and ring B (cFΦR$_4$) for cellular entry was explored (**Figure 4.5**). In designing ring A, Dab was utilised to mimic the four-carbon spacer, Abu5 in **CP3**, previously found to be optimal for retaining nanomolar binding affinity (Chapter 3). A glutamic acid in ring A was also

introduced in which the side chain: 1) closely resembles the side chain of Ile in **CP3** and 2) serves as a handle for the assembly of ring B (**Figure 4.5).**

An on/off resin bicyclisation strategy was adapted to synthesise the bicyclic peptide (**Scheme 4.1**), where the side-chain lactamisation occurs on a solid support, followed by a head-to-tail cyclisation in solution. It was hypothesised that the location of ring A precisely in the middle of the extended linear precursor provides an element of rigidity, bringing the two ends of the cyclic peptide together, hence facilitating the cyclisation of ring B (**Scheme 4.1**).

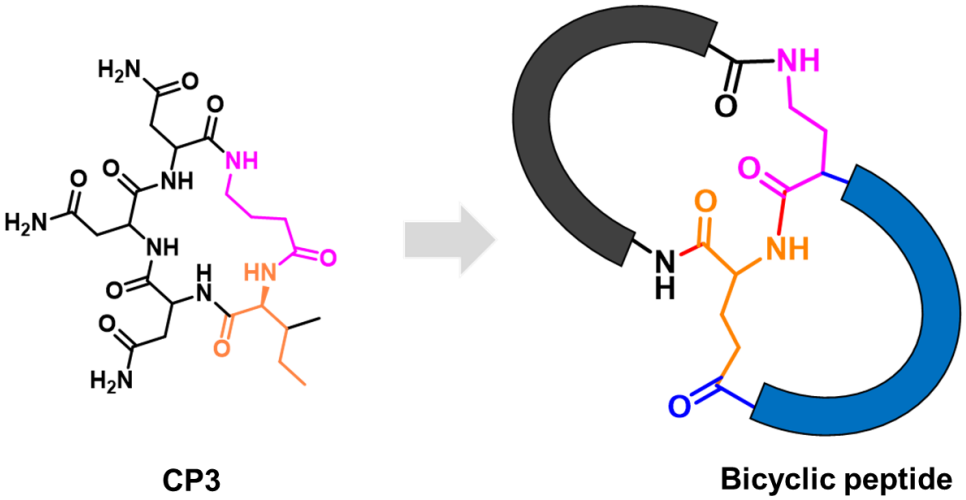

Figure 4.5. Schematic diagram of the design of the bicyclic peptide, by replacement of the Ile side chain in **CP3** with the side chain of Glu (orange) and replacement of γ-Abu with a Dab amino acid (purple).

With the goal of comparing the effect of bicyclisation on the binding affinity and permeability of **CP3**, **CP3**-TAT peptide was designed and synthesised. As the Ile position in **CP3** favours bulky group, as described in Chapter 3, it was replaced with a lysine residue where the free amine side chain of the Lys was used to assemble the linear TAT peptide (RRRQRRKKRR). A modified orthogonal Dmab/Alloc protection strategy was employed to synthesise the cyclic peptide conjugate (**Scheme 2**).

4.3.2 Determination of binding affinity of CP3-CPP conjugates using SPR

The ability of the **CP3**-CPP conjugates to bind to SPSB2 was assessed using SPR. The protein was immobilised on a gold surface of a CM5 chip using the standard amine coupling procedures. The peptides were prepared at 5- 6 concentrations ranging between 7 nM to 250

nM and run on the immobilised SPSB2 protein surface. The bicyclic-**CP3** peptide was found to bind to SPSB with an affinity of 65 nM, approximately 9-fold weaker than that of **CP3** (K_D 7 nM) (**Figure 4.6a**). This result suggests that the additional ring B is well tolerated by the protein and does not significantly affect binding, thus validating my design process. The K_D of **CP3**-TAT was found to be 10 nM, comparable to that of the **CP3** and 35-fold higher than the binding affinity of the lysine analogue of **CP3** (K_D 310 nM) (Chapter 3) (**Figure 4.6b**). This finding is consistent with the previous observation in Chapters 2 and 3 that the Ile side chain can be replaced by bulky moieties without compromising the binding affinity (Chapter 3).

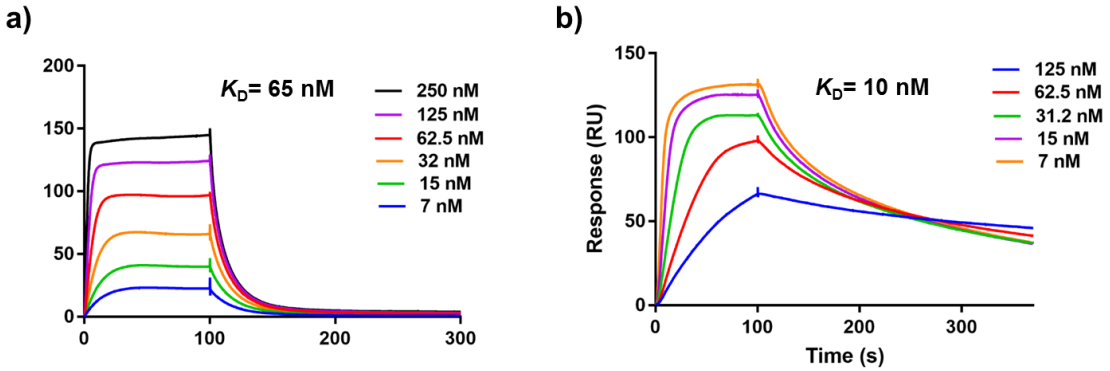

Figure 4.6. **CP3**-CPP conjugates bind to SPSB2 with nM affinity. SPR sensorgrams obtained using five-six concentrations of a) **CP3**-TAT and b) Bicyclic **CP3**-CPP. The *Y* axis shows the response unit (RU) differences after reference subtraction.

4.3.3 Evaluation of the permeability of the CP3-CPP conjugates using RAW 264.7 cells

To assess the ability of **CP3**-TAT and Bicyclic-**CP3** to enter live cells and enhance NO production. LPS/IFN-γ treated RAW264.7 cells were incubated with 100 μM of the peptides for 48 and 72 h. The supernatant was collected and Griess assays were used to compare the levels of NO in the presence and absence of peptides. Both peptides showed a slight increase in the production of nitric oxide after 48 h compared to the control experiment in the absence of the peptide (**Figure 4.7**). After 72 h, **CP3**-TAT showed a 2-fold increase in the level of NO compared to control, while no significant increase was observed for the bicyclic peptide (**Figure 4.7**).

These results are very preliminary and need to be repeated many more times on these and other macrophage cell lines. They suggest that these conjugates can deliver the **CP3** cargo into the cytoplasm and exert the anticipated biological effect, much more extensive experimental evidence will be needed to support these preliminary observations. Optimisation of the Griess assay conditions, including the number of cells, incubation times and concentration of the

peptides, will need to be explored further. Moreover, western blot analysis can be utilised to monitor iNOS protein levels in the cells to confirm the cellular uptake and inhibitory effect of these conjugates on iNOS degradation in RAW 264.7 macrophages.

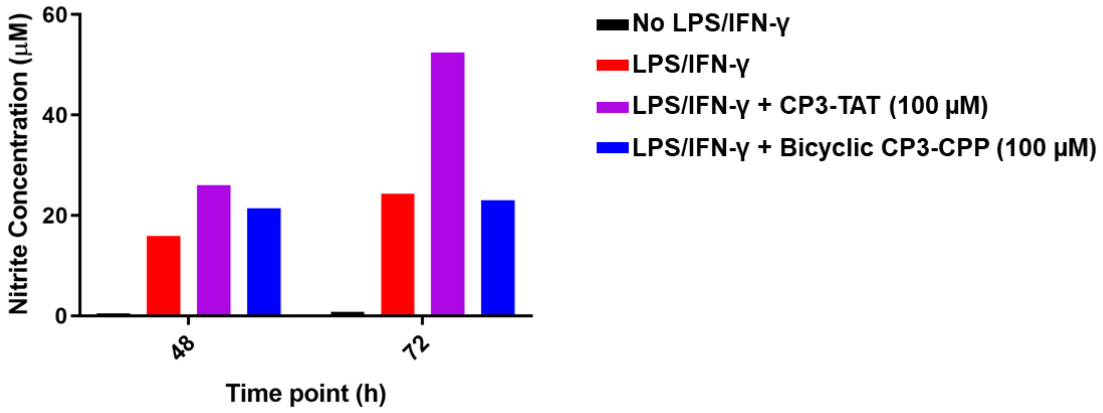

Figure 4.7. Effect of bicyclic **CP3** and **CP3**-TAT on the production of NO. RAW 264.6 cells were treated with LPS (10 ng/mL) and IFN-γ (20 ng/mL) for 48 and 72 h in the presence of **CP3**-CPP conjugates followed by nitrite assay using the Griess assay. Results are the mean of triplicate assays (n=1).

4.4 Conclusions

A bicyclic SPSB-iNOS inhibitor and a TAT-conjugated **CP3** peptide were successfully developed. Based on the previous investigation of the SAR of **CP3** analogues, **CP3**-CPP conjugates that can perform the dual functions of cell penetration and targeting SPSB-iNOS intracellular interactions were designed and synthesised. The **CP3**-CPP peptides bind to SPSB2 with nanomolar affinity. However, the effect of these peptides on NO levels in live cells needs to be further investigated in future, although the preliminary findings were encouraging. These inhibitors will provide useful tools for investigating the functional consequences of inhibiting the SPSB-iNOS interaction and developing SPSB-iNOS inhibitors as anti-infective leads.

4.5 References

(1) Sadek, M. M.; Barlow, N.; Leung, E. W. W.; Williams-Noonan, B. J.; Yap, B. K.; Shariff, F. M.; Caradoc-Davies, T. T.; Nicholson, S. E.; Chalmers, D. K.; Thompson, P. E.; Law, R. H. P.; Norton, R. S., A cyclic peptide Inhibitor of the iNOS-SPSB protein-protein Interaction as a potential anti-infective agent. *ACS Chem Biol.* **2018,** *13*, 2930-2938.

(2) Guidotti, G.; Brambilla, L.; Rossi, D., Cell-penetrating peptides: from basic research to clinics. *Trends Pharmacol Sci.* **2017,** *38*, 406-424.

(3) Frankel, A. D.; Pabo, C. O., Cellular uptake of the tat protein from human immunodeficiency virus. *Cell.* **1988,** *55*, 1189-93.

(4) Dupont, E.; Prochiantz, A.; Joliot, A., Penetratin Story: An Overview. *Methods Mol Biol.* **2015,** *1324*, 29-37.

(5) Ramaker, K.; Henkel, M.; Krause, T.; Rockendorf, N.; Frey, A., Cell penetrating peptides: a comparative transport analysis for 474 sequence motifs. *Drug Deliv.* **2018,** *25*, 928-937.

(6) Borrelli, A.; Tornesello, A. L.; Tornesello, M. L.; Buonaguro, F. M., Cell penetrating peptides as molecular carriers for anti-cancer agents. *Molecules.* **2018,** *23*.

(7) Vale, N.; Ferreira, A.; Fernandes, I.; Alves, C.; Araújo, M. J.; Mateus, N.; Gomes, P., Gemcitabine anti-proliferative activity significantly enhanced upon conjugation with cell-penetrating peptides. *Bioorg Med Chem Lett.* **2017,** *27*, 2898-2901.

(8) Bolhassani, A.; Jafarzade, B. S.; Mardani, G., In vitro and in vivo delivery of therapeutic proteins using cell penetrating peptides. *Peptides.* **2017,** *87*, 50-63.

(9) Bartolami, E.; Bouillon, C.; Dumy, P.; Ulrich, S., Bioactive clusters promoting cell penetration and nucleic acid complexation for drug and gene delivery applications: from designed to self-assembled and responsive systems. *Chem Commun.* **2016,** *52*, 4257-73.

(10) Ma, W.; Jin, G. W.; Gehret, P. M.; Chada, N. C.; Suh, W. H., A novel cell penetrating peptide for the differentiation of human neural stem cells. *Biomolecules.* **2018,** *8*.

(11) Bechara, C.; Sagan, S., Cell-penetrating peptides: 20years later, where do we stand? *FEBS Letters.* **2013,** *587*, 1693-1702.

(12) Madani, F.; Lindberg, S.; Langel, U.; Futaki, S.; Gräslund, A., Mechanisms of cellular uptake of cell-penetrating peptides. *J Biophys.* **2011,** *2011*, 414729-414729.

(13) Perry, S. R.; Hill, T. A.; de Araujo, A. D.; Hoang, H. N.; Fairlie, D. P., Contiguous hydrophobic and charged surface patches in short helix-constrained peptides drive cell permeability. *Org Biomol Chem.* **2018,** *16*, 367-371.

(14) Futaki, S.; Nakase, I.; Tadokoro, A.; Takeuchi, T.; Jones, A. T., Arginine-rich peptides and their internalization mechanisms. *Biochem Soc Trans.* **2007,** *35*, 784-7.

(15) LeCher, J. C.; Nowak, S. J.; McMurry, J. L., Breaking in and busting out: cell-penetrating peptides and the endosomal escape problem. *Biomol Concepts.* **2017,** *8*, 131-141.

(16) Lonn, P.; Kacsinta, A. D.; Cui, X. S.; Hamil, A. S.; Kaulich, M.; Gogoi, K.; Dowdy, S. F., Enhancing endosomal escape for intracellular delivery of macromolecular biologic therapeutics. *Sci Rep.* **2016,** *6*, 32301.

(17) Sánchez-Navarro, M.; Teixidó, M.; Giralt, E., Jumping hurdles: peptides able to overcome biological barriers. *Acc Chem Res.* **2017,** *50*, 1847-1854.

(18) Lättig-Tünnemann, G.; Prinz, M.; Hoffmann, D.; Behlke, J.; Palm-Apergi, C.; Morano, I.; Herce, H. D.; Cardoso, M. C., Backbone rigidity and static presentation of guanidinium groups increases cellular uptake of arginine-rich cell-penetrating peptides. *Nat Commun.* **2011,** *2*, 453.

(19) Peraro, L.; Kritzer, J. A., Emerging methods and design principles for cell-penetrant peptides. *Angew Chem Int Ed Engl.* **2018,** *57*, 11868-11881.

(20) Qian, Z.; Liu, T.; Liu, Y.-Y.; Briesewitz, R.; Barrios, A. M.; Jhiang, S. M.; Pei, D., Efficient delivery of cyclic peptides into mammalian cells with short sequence motifs. *ACS Chem Biol.* **2013,** *8*, 423-431.

(21) Qian, Z.; Martyna, A.; Hard, R. L.; Wang, J.; Appiah-Kubi, G.; Coss, C.; Phelps, M. A.; Rossman, J. S.; Pei, D., Discovery and mechanism of highly efficient cyclic cell-penetrating peptides. *Biochemistry.* **2016,** *55*, 2601-12.

(22) Lian, W.; Jiang, B.; Qian, Z.; Pei, D., Cell-permeable bicyclic peptide inhibitors against intracellular proteins. *J Am Chem Soc.* **2014,** *136*, 9830-9833.

(23) Jiang, B.; Pei, D., A Selective, cell-permeable nonphosphorylated bicyclic peptidyl inhibitor against peptidyl–prolyl isomerase Pin1. *J Med Chem.* **2015,** *58*, 6306-6312.

(24) Rhodes, C. A.; Dougherty, P. G.; Cooper, J. K.; Qian, Z.; Lindert, S.; Wang, Q.-E.; Pei, D., Cell-permeable bicyclic peptidyl inhibitors against NEMO-IκB kinase interaction directly from a combinatorial library. *J Am Chem Soc.* **2018,** *140*, 12102-12110.

(25) Rhodes, C. A.; Pei, D., Bicyclic peptides as next-generation therapeutics. *Chem Eur J.* **2017,** *23*, 12690-12703.

(26) Grisham, M. B.; Johnson, G. G.; Lancaster, J. R., Jr., Quantitation of nitrate and nitrite in extracellular fluids. *Methods Enzymol.* **1996,** *268*, 237-46.

Chapter 5

Characterisation of a Novel Coumarin-Based Fluorescent Probe for Monitoring Nitric Oxide Production in Macrophages

5.1 Introduction

Chapter 4 described the design and the synthesis of two potent CPP-**CP3** conjugates as an attempt to facilitate the active transport of the cargo pentapeptide inhibitor. On the basis of the SAR study conducted in Chapter 3, the cyclic CPP, FΦRRRR, was fused to **CP3** in a bicyclic structure using non-natural amino acids to mimic the Ile and Abu residues in **CP3**. The TAT peptide, however, was conjugated directly to the free amine side chain of the Lys residue in the **CP3** analogue (**23**) (Chapter 3) using the standard SPPS procedures. Both conjugates were able to bind to hSPSB2 with nanomolar affinities (K_D = 65 and 10 nM respectively) as measured by SPR. The Griess assay was used to detect the change in NO production in a macrophage cell line as a downstream effect following the internalisation of the conjugates and subsequent inhibition of the SPSB-iNOS interaction in the cytoplasm. The preliminary results suggested that the CPP conjugates may be able to permeate through the cell membrane however, other techniques need to be explored to further confirm these findings.

Hence, in this Chapter, a novel fluorescent NO probe (**CB**) was investigated as a potential useful tool for future evaluation of the cell-permeable SPSB-iNOS inhibitors. In order to assess its ability to detect endogenously produced NO in stimulated macrophages, confocal microscopy was employed. Furthermore, the increase of NO levels was monitored over a certain period of time, to investigate whether **CB** can detect the dynamics of NO production. Using a cell organelle specific dye, the localisation of the probe inside the cells was also determined. Moreover, the effect of **CB** on the cell viability was evaluated using Operetta® microscopy. These results have been published in the *Bioorganic and Medicinal Chemistry* journal; the formatting of the publication has been retained and is found in the following Chapter.

Bioorganic & Medicinal Chemistry 25 (2017) 5743–5748

Contents lists available at ScienceDirect

Bioorganic & Medicinal Chemistry

journal homepage: www.elsevier.com/locate/bmc

Characterisation of a novel coumarin-based fluorescent probe for monitoring nitric oxide production in macrophages

Maiada M. Sadek [a,g], Mina Barzegar Amiri Olia [b,g], Cameron J. Nowell [c], Nicholas Barlow [a], Carl H. Schiesser [d], Sandra E. Nicholson [e,f], Raymond S. Norton [a,*]

[a] Medicinal Chemistry, Monash Institute of Pharmaceutical Sciences, Monash University, Parkville, Victoria 3052, Australia
[b] School of Chemistry and Bio21 Molecular Science and Biotechnology Institute, University of Melbourne, Victoria 3010, Australia
[c] Drug Discovery Biology, Monash Institute of Pharmaceutical Sciences, Monash University, Parkville, Victoria 3052, Australia
[d] Seleno Therapeutics Pty Ltd, Brighton East, Victoria 3187, Australia
[e] The Walter and Eliza Hall Institute of Medical Research, Parkville, Victoria 3052, Australia
[f] The Department of Medical Biology, University of Melbourne, Parkville, Victoria 3052, Australia

ARTICLE INFO

Article history:
Received 11 July 2017
Revised 24 August 2017
Accepted 30 August 2017
Available online 5 September 2017

Keywords:
Nitric oxide
Fluorescence
Coumarin-based probes
Cell imaging
Macrophages

ABSTRACT

Nitric oxide (NO) is an important effector molecule in host defence against bacterial pathogens. The development of fluorescence imaging to monitor NO production *in vitro* and *in vivo* will increase our understanding of its biological role. Recently, a novel 'trappable' fluorescent blue 'turn-on' Cu(II)-complexed coumarin-based probe (CB) has been developed to detect NO. In this study, CB was investigated to evaluate its ability to detect NO in macrophages. Using confocal microscopy, NO was successfully detected in macrophages in the presence of stimuli that induce nitric oxide synthase (iNOS), the enzyme responsible for production of NO. The time dependence and subcellular compartmentalisation of CB in macrophages were evaluated. The probe can be trapped within cells and reacts directly and specifically with NO, rendering it a promising tool for imaging NO in response to pharmacological agents that modulate its level, for example during bacterial infections.

1. Introduction

Nitric oxide (NO) is a key modulator of numerous biological systems and plays a crucial role in vasodilation, neurotransmission, and the immune response.[1,2] Within the immune system, NO is both a signalling molecule and an antimicrobial agent produced by macrophages and other phagocytes to destroy enveloped pathogens.[3] NO is synthesised during the conversion of L-arginine to L-citrulline by the enzyme inducible nitric oxide synthase (iNOS). Monitoring the production, release and distribution of NO within immune cells is an important aspect of understanding the role of NO in controlling bacterial, viral or protozoan infections.[2,4]

Direct detection of NO in live cells in possible using a number of different bio-imaging techniques such as chemi-luminescence,[5] colorimetry,[6] electron paramagnetic resonance,[7] electrochemistry[8] and fluorometry.[9,10] Of these, fluorescent probes offer distinct advantages, including high sensitivity and selectivity, convenience and high spatio-temporal resolution.[11] Transition metal ligand probes in particular have been investigated as platforms for NO detection, where the fluorophore is part of the ligand.[10,11] Recently, a blue 'turn-on' fluorescent NO probe (CB) based on a Cu(II)-complexed coumarin fluorophore was developed.[12] Scheme 1 shows the mechanism of CB-Cu(II) formation, followed by replacement of the Cu(II) with NO to produce CB-NO. The design of the CB probe was inspired by Apfil et al.,[13] who had employed a benzoresorufin fluorophore rather than a substituted coumarin fluorophore.

In this strategy, 2-methyl-8-aminoquinoline is incorporated into substituted coumarin and acts as a tridentate ligand for Cu (II). Complexation with Cu as a paramagnetic ion results in partial fluorescent quenching of the coumarin. Upon reaction of the CB-Cu (II) with NO, the Cu(II) is displaced by NO, causing restoration of fluorescence. The CB probe fluoresces in the blue spectral region (405 nm) and exhibits excellent selectivity and sensitivity for NO over other reactive nitrogen and oxygen species.[12]

To date, CB has been evaluated only in experiments that monitor and visualise NO production in the biofilm of *Pseudomonas aeruginosa*.[12] However, the blue fluorescent wavelength of this fluorophore suggests its application in multi-wavelength experiments on mammalian cells, where it could be used concurrently

* Corresponding author.
E-mail address: ray.norton@monash.edu (R.S. Norton).
[g] These authors contributed equally to this work.

http://dx.doi.org/10.1016/j.bmc.2017.08.054
0968-0896/

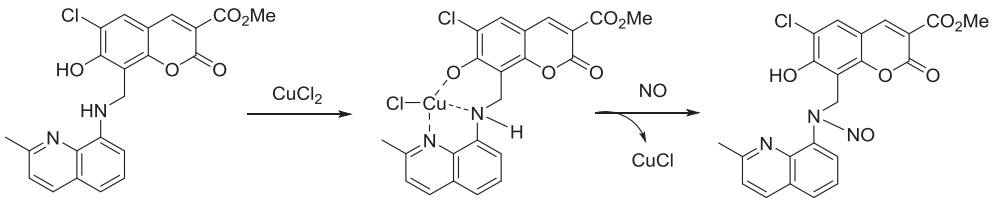

Scheme 1. 'Turn-on' fluorescence mechanism of CB probe.

with other probes that fluoresce at longer wavelengths (green and red).

Whilst NO is protective against bacterial infection, excessive NO can be detrimental to cells. One factor in the fine regulation of NO levels is the lifetime in the cell of the enzyme iNOS. Previously, we showed that the SPSB proteins are key regulators of iNOS lifetime in macrophages as they mediate the interactions that lead to proteolytic degradation of this enzyme.[14,15] Inhibition of SPSB binding to iNOS offers a means of prolonging the lifetime of iNOS, thereby enhancing NO production and pathogen killing.[14,16,17] The ability to measure changes in NO levels in real time will therefore be a useful marker of the inflammatory immune response, particularly in the context of assessing new anti-infectives.

In this study, we have evaluated CB as a tool for the detection of NO in macrophages. We have characterised the concentration range where CB may be used effectively and cell toxicity avoided. We show that modulation of NO levels by stimuli that mimic infection and induce NO expression can be detected and quantified. Moreover, we show that inhibition of NO levels can also be quantified. We further investigate the location and compartmentalisation of CB within macrophages and demonstrate the compatibility of CB with longer-wavelength probes.

2. Material and methods

2.1. Cell culture and live cell imaging

RAW264.7 murine macrophages were cultured in Dulbecco's Modified Eagle Medium (DMEM, Gibco) supplemented with 10% fetal bovine serum (FBS, Gibco), 1% sodium pyruvate, 100 U/ml penicillin, and 100 U/ml streptomycin (Gibco). Cells were passaged and plated into eight-well μ-slides (Ibidi) at a density of 50,000 cells/cm^2 containing 250 μL of complete DMEM, and incubated overnight at 37 °C with 5% CO_2. iNOS was induced in RAW264.7 macrophages with 10 ng/mL lipopolysaccharide (LPS) and 20 ng/mL interferon-γ (IFN-γ) for 16 h. CB was synthesised and characterised as described previously.[12] A 1 mM stock solution of CB was prepared in DMSO. While protected from light, the cells were treated with a freshly prepared solution of CB (1:1 solution of 1 mM $CuCl_2$ and 1 mM CB diluted in phosphate buffered saline (PBS) to give a final concentration of 10 μM CB) and then incubated for 1 h. Cells were washed three times with 250 μL of Dulbecco's PBS (Gibco) prior to imaging using a Leica SP8 confocal microscope with a 63× UPlanApo NA 1.4 objective, fitted with sensitive HyD detectors and 12 kHz resonant scanner at excitation and emission wavelengths of 405 and 445–485 nm, respectively, for the CB probe. All confocal images were processed with ImageJ for intensity level adjustment, quantification and cropping. Control experiments were carried out using the same protocol without adding iNOS inducers (LPS and IFN-γ).

For kinetic studies, cells were incubated with 10 ng/mL LPS, 20 ng/mL IFN-γ and 10 μM CB for 4 h, removed from the incubator and then imaged using the confocal microscope at predetermined time points (6, 8, 10 and 12 h). Cells were imaged using excitation/emission wavelengths as above.

To determine the specificity of NO detected by CB, RAW264.7 were exposed to an iNOS inhibitor, L-N^G-monomethyl arginine (L-NMMA). L-NMMA was diluted from 10 mM to a final concentration of 1 mM in fresh medium and added to cells along with LPS (10 ng/mL) and IFN-γ (20 ng/mL), then incubated for 16 h. The adherent cells were washed with PBS prior to addition of CB (10 μM) to image the change in NO levels in response to L-NMMA. Images were captured at various positions and analysed as described above.

2.2. Cytotoxicity assay

RAW246.7 cells were seeded into 96-well plates in triplicate (100 μL total volume/well, 20,000 cells/well) in complete DMEM and incubated at 37 °C with 5% CO_2 for 12 h. The medium was replaced with phenol-free DMEM (Gibco) and the cells incubated with and without 100 μM–100 nM CB, together with 5 μM of propidium iodide (PI) for another 24 h. Plates were analysed on the PerkinElmer Operetta® High Content Imaging System (PerkinElmer). The maximum intensity projection images were analysed using Harmony® High Content Imaging and Analysis Software and the percent cell survival values are reported relative to those of untreated control cells.

2.3. Fluorescence localisation

In order to assess the intracellular compartmentalisation of CB we used cell-permeable organelle-selective fluorescent probes to label the nuclei and mitochondria. Mitotracker™ Green FM (Invitrogen) was dissolved in DMSO to 1 mM concentration as recommended. RAW246.7 cells were pre-incubated with 10 ng/mL LPS and 20 ng/mL IFN-γ for 12 h, followed by the addition of 10 μM CB, 5 μM DRAQ5™ (Abcam) and 100 nM Mitotracker™ Green FM (Invitrogen) for 30 min. Cells were washed three times with PBS and then bathed in 250 μL of PBS during imaging. Images were acquired by the confocal microscope using excitation/emission wavelengths of 633/616–757 and 490/500–550 nm for DRAQ5™ and Mitotracker™ Green FM, respectively, and were merged for co-localisation studies.

2.4. NO production during bacterial infection

Escherichia coli ATCC 25922 cells were cultured in LB and incubated at 37 °C for 3 h. 1 mL of the resultant mid-log phase culture was washed once with PBS and then resuspended in 1 mL of PBS. 1 μL of this suspended bacteria solution was added to the adherent macrophage cultures. CB (10 μM) was then added to the well, incubated for 1 h at 37 °C, and then washed twice with PBS, prior to analysis using confocal microscopy.

3. Results

3.1. CB detection of endogenously produced NO

Macrophages are an important contributor to host defence, their innate immune sensors detecting bacterial components such as LPS and triggering the production of pro-inflammatory cytokines such as TNF-α and IFN-γ. These signals converge to induce expression of iNOS, which in turn catalyses NO production.[18] RAW264.7 macrophages were used as the model cell line for NO production and confocal microscopy was used to image the CB-loaded cells.

We first evaluated whether the CB probe could permeate through the cell membrane and detect endogenously produced NO in stimulated RAW264.7 cells. Macrophages were incubated with 10 ng/mL LPS and 20 ng/mL IFN-γ for 16 h to induce NO, followed by the addition of 10 μM CB for 1 h. Confocal microscopy showed that the fluorescence signal was retained after washing, confirming that the probe remains trapped inside the cells (Fig. 1A). A predominately cytoplasmic, speckled staining pattern was observed in treated cells (Fig. 1A lower, right panel). Quantification of the fluorescent signal showed a corresponding twofold increase in mean fluorescence intensity with LPS/IFN-γ treatment (Fig. 1B). Only a weak initial fluorescence signal was observed in untreated cells, owing to the fact that CB fluorescence is partially quenched by Cu(II), as reported previously.[12]

This experiment, along with our previous solution studies,[12] strongly supports the hypothesis that CB-Cu(II) is the species responsible for NO detection. The intensity of the observed signal reflects the amount of nitric oxide produced in the activated cells as well as presumably the integrity of the CB-Cu(II) complex intracellularly These findings indicate that the probe is membrane-permeable, trappable and able to detect intracellular NO produced in macrophage cells.

Owing to the dynamic change in the concentration of NO inside live cells, fluorescent probes should be particularly useful for monitoring NO production in a time-dependent manner.[19] Hence, we applied 10 μM of the probe to RAW264.7 macrophages pre-treated with LPS and IFN-γ for 4 h. The fluorescence intensity of the CB probe was monitored by confocal microscope at 2 h intervals over 12 h. The mean fluorescence intensity slowly increased by twofold over time relative to a steady fluorescence signal in the unstimulated cells (Fig. 2 and Fig. S1), confirming that CB can detect changes in NO production inside the cells. This result provides fur-

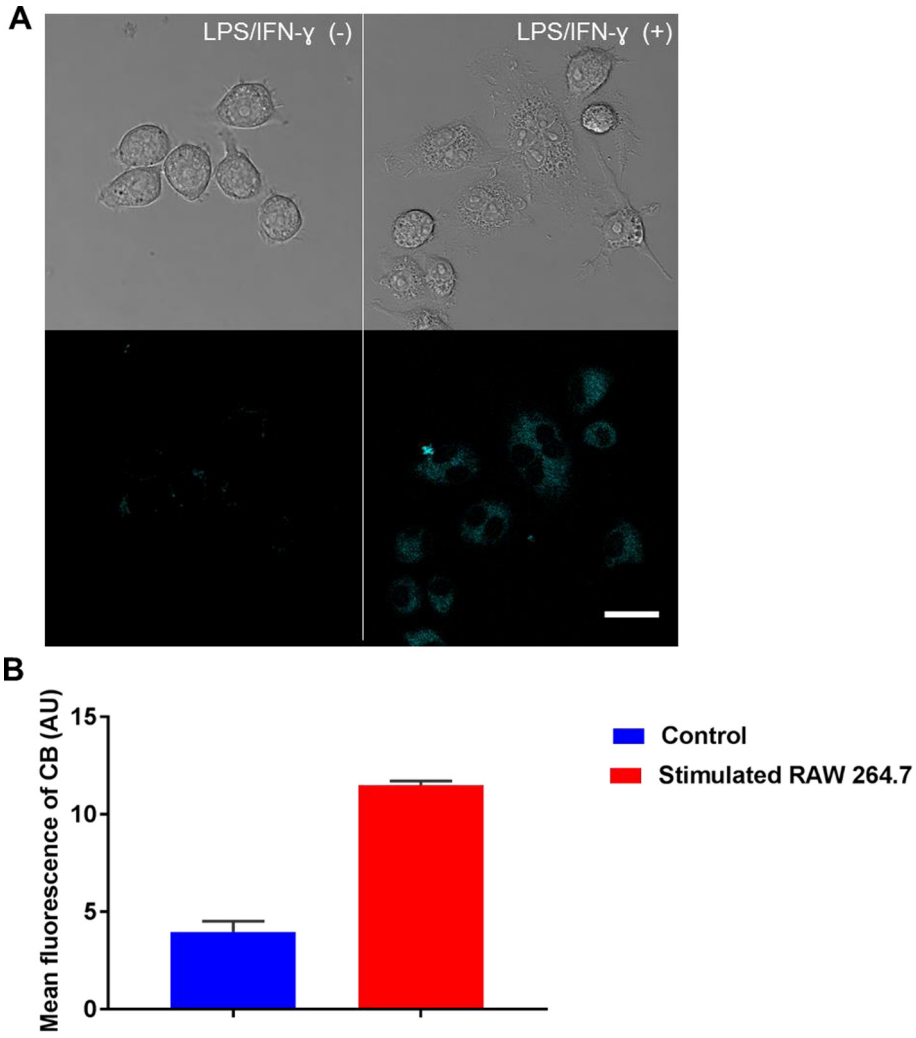

Fig. 1. CB is permeable, trappable, and can detect endogenous NO production in RAW264.7 macrophages. Cells were stimulated with LPS and IFN-γ for 16 h followed by 1 h incubation with CB. A) Bright-field images of cells analysed using differential interference contrast (DIC; top panels) and fluorescent images of cells showing CB detection (emission from blue channel; lower panels). Scale bars, 25 μm. Images were captured on a confocal microscope after washing the cells three times with PBS. Fluorescence intensity was measured and compared to control cells where the LPS/IFN-γ were not added and is expressed as arbitrary units (AU). B) Quantification of fluorescence intensity of CB in RAW264.7 cells with and without LPS/IFN-γ treatment (stimulated). Mean ± standard deviation; n = 3.

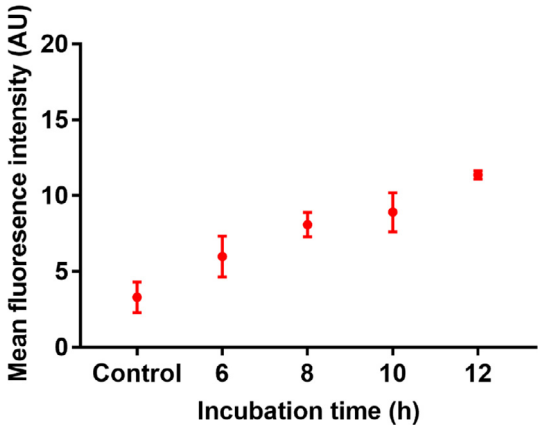

Fig. 2. CB detects NO in a time-dependent manner. CB was added to RAW264.7 cells pre-treated for 4 h with LPS and IFN-γ. Images were taken on Leica SP8 confocal microscope after removing DMEM and washing with PBS at 6, 8, 10 and 12 h and compared to unstimulated control cells. The mean fluorescence intensity of CB was plotted against incubation time. Fluorescence intensity quantification is expressed as arbitrary units (AU). Error bars indicate standard deviation, n = 3.

ther evidence that the turn-on fluorescence signal in the treated cells is due to the direct reaction of CB with NO in the treated cells, and not due to reduction of the Cu(II) ions by intracellular thiols.

We then confirmed that the CB-associated fluorescence specifically detected NO and demonstrated, using L-NMMA (1 mM), a well-characterised and selective NOS inhibitor,[20] that it derived from iNOS activity. Macrophages were treated with L-NMMA in the presence of LPS and IFN-γ for 16 h. The fluorescence intensity

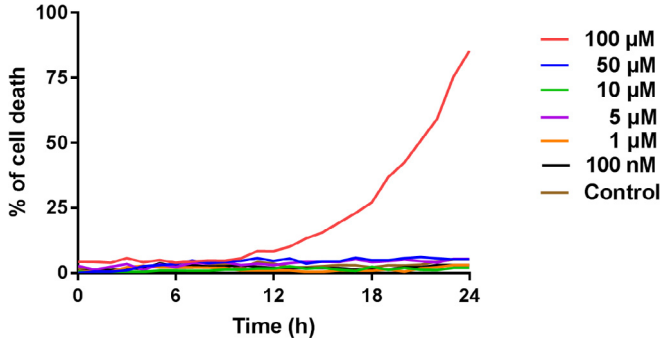

Fig. 4. CB is minimally toxic to RAW264.7 cells. Macrophages were incubated with increasing concentrations of CB (100 nM–100 µM) and PI (5 µM) for 24 h. Images were captured using the Operetta® high-throughput screening microscope. Cell death was determined as the % of PI-positive cells.

observed with CB was significantly attenuated in the presence of L-NMMA (Fig. 3 and Fig. S2). This result is consistent with the hypothesis that CB detects iNOS–dependent production of NO in macrophages.

3.2. Cytotoxicity of CB

An ideal probe should report the accumulation of a target molecule without affecting cell viability.[19] NO insertion in copper-based probes is followed by the release of N-nitrosyl amine and copper ions, which can compromise the viability of the cells.[21] We investigated the potential toxicity of CB towards the RAW264.7 cells

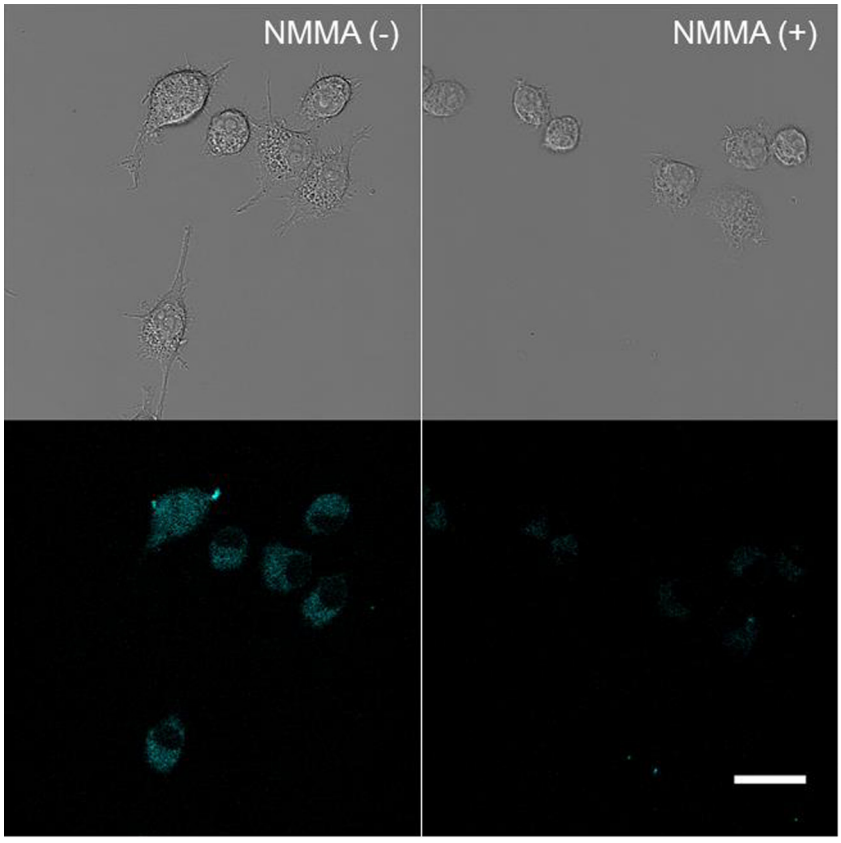

Fig. 3. iNOS production of NO is detected with CB. RAW264.7 macrophages were incubated with LPS/IFN-γ in the presence or absence of the iNOS inhibitor L-NMMA (1 mM; 16 h). Cells were treated with CB for 1 h, washed then imaged using a Leica SP8 confocal microscope. Bright-field images of cells analysed using DIC (top panels) and fluorescent images of cells showing CB detection (emission from blue channel; lower panels). Scale bar 25 µm.

over 24 h. A no-wash image-based assay was performed over a 24 h period to determine the percentage of dead macrophages in the presence of increasing concentrations of the CB probe (100 nM–100 μM) and PI (5 μM). PI is a red fluorescent dye that intercalates with DNA and only permeates through the cell membrane of dead cells.[22] The percentage of dead (PI-positive) cells was calculated. Cell survival was approximately 95% when cells were incubated with 100 nM–100 μM of the fluorescent probe over the first 12 h (Fig. 4). A significant decrease in cell viability, however, was observed in the subsequent 12 h at the highest con-

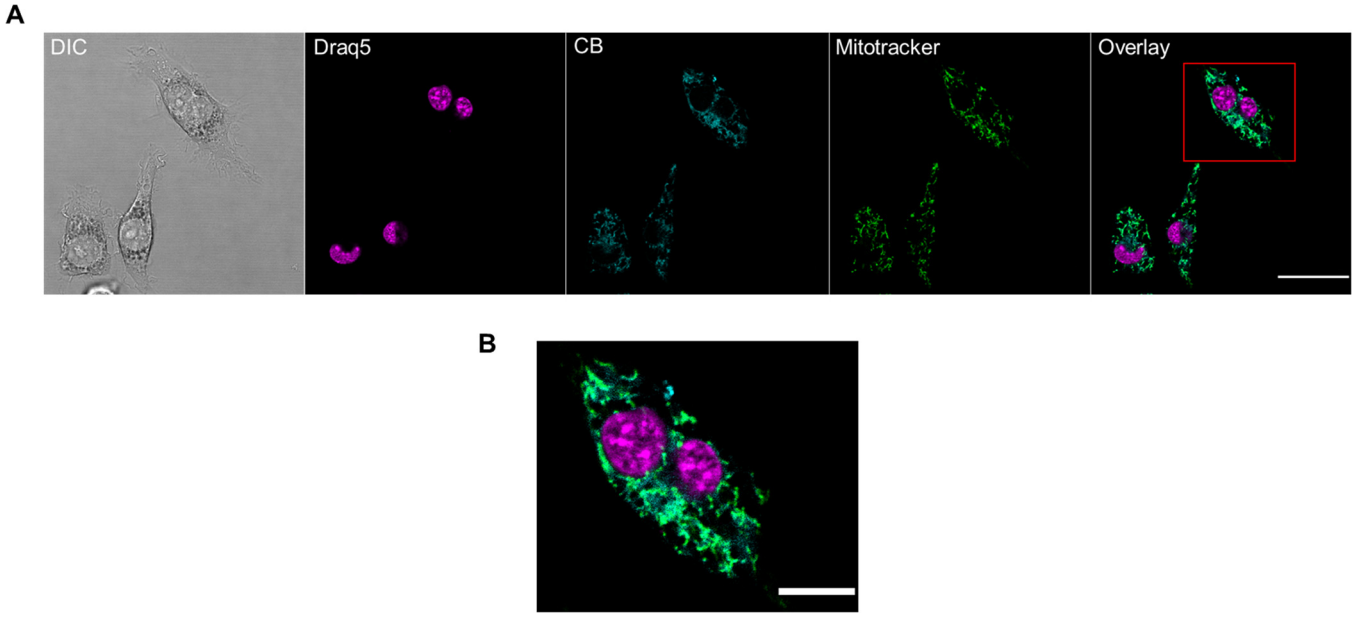

Fig. 5. Localisation of CB in mitochondria. (A) RAW264.7 cells were co-stained with 5 μM of DRAQ5™, 10 μM of CB and 100 nM of Mitotracker™ Green FM for 30 min and examined by confocal microscopy. Scale bar 25 μm. (B) Fluorescence microscopy image of the magnified area marked in the overlay showing Mitotracker and CB coincident distributions. Scale bar 10 μm.

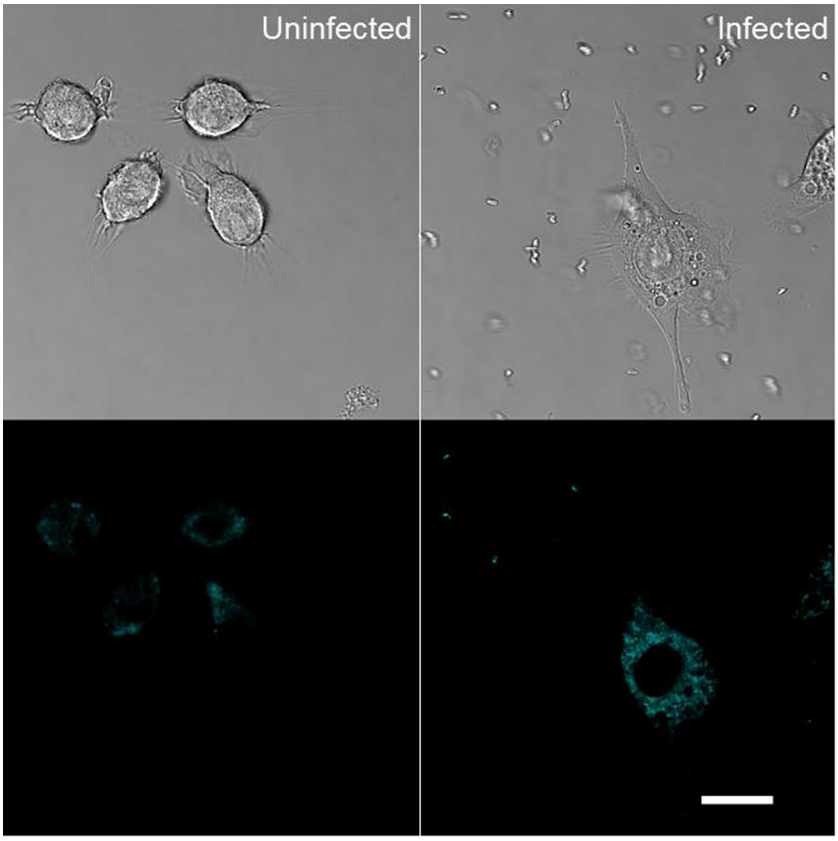

Fig. 6. CB can detect NO production during bacterial infection. Macrophages were incubated with *E. coli* for 3 h prior to the addition of CB (10 μM) for 1 h. The intensity of the probe was monitored using a Leica SP8 confocal microscope. Bright-field images of cells analysed using DIC (top panels) and fluorescent images of cells showing CB detection (emission from blue channel; lower panels). Scale bar 25 μm.

centration of CB tested. These experiments show that CB is minimally cytotoxic to RAW264.7 cells.

3.3. Monitoring NO in subcellular compartments by CB

Localisation studies using cell-organelle specific dyes were performed to determine the sub-cellular localisation of the probe in RAW264.7 macrophages. Cells were incubated with the DNA dye DRAQ5™ and the mitochondrial specific MitoTracker™ Green FM dye, together with CB (10 μM) for 1 h at 37 °C, and images captured using confocal microscopy. Superimposing the fluorescence images showed no overlap in the fluorescence signals of CB and DRAQ5™, indicating that CB probe in not localised in the nucleus (as expected if the ester is converted to the negatively-charged carboxylate in the cells, excluding it from the nucleus through charge repulsion) (Fig. 5).[23,24] Conversely, overlay of the green (MitoTracker™ green FM) and blue (CB) detector channels suggested mitochondrial accumulation of CB (Fig. 5), which allows real-time monitoring of endogenous NO in mitochondria in mammalian cells. Therefore, CB can also be used to provide spatial information about NO production in the cells.

3.4. CB detection of NO during bacterial infection

We next explored the ability of the probe to detect NO produced during bacterial infection. RAW264.7 cells were challenged with *E. coli* for 3 h and then incubated with CB for 1 h and washed prior to imaging. Confocal microscopy indicated that the probe intensity increased moderately compared to background levels observed in control cells without bacteria, indicating that the probe can successfully detect NO produced by macrophages during bacterial encounter (Fig. 6).

4. Discussion

Recently, a novel Cu(II)-complexed coumarin-based imaging probe, CB, was developed for NO detection.[12] The ability of CB to detect NO directly, rapidly and specifically at a physiological pH encouraged us to use it to image live-cell NO production. In the present study, CB was used successfully to image NO in RAW264.7 macrophages. We demonstrated that CB can provide direct dynamic information concerning NO production in live cells, with good photostability, low cellular toxicity and biorthogonal compatibility in a multi-dye system. The observation that the probe remains trapped inside cells implies that the probe could be used in biological experiments where continuous media perfusion is required, such as brain cell imaging.[25] We hope that these properties will make this coumarin-based fluorescent probe useful for future *in vitro* and *in vivo* NO experiments.

Acknowledgements

This study was supported in part by the Australian National Health Medical Research Council (NHMRC) (Grant 1099428) and the Australian Research Council (ARC) (grant DP130100077). R.S. N. acknowledges fellowship support from the Australian National Health and Medical Research Council. M.S. is supported by a Monash Graduate Scholarship. We thank Drs. David Chalmers and Philip Thompson for helpful discussions and Dr. Rodrigo Morales for critical reading of the manuscript.

Notes

The authors declare no competing financial interest.

A. Supplementary data

Supplementary data associated with this article can be found, in the online version, at http://dx.doi.org/10.1016/j.bmc.2017.08.054.

References

1. Moncada S, Palmer RM, Higgs EA. Nitric oxide: physiology, pathophysiology, and pharmacology. *Pharmacol Rev*. 1991;43:109–142.
2. Bogdan C. Nitric oxide and the immune response. *Nat Immunol*. 2001;2:907–916.
3. MacMicking J, Xie QW, Nathan C. Nitric oxide and macrophage function. *Annu Rev Immunol*. 1997;15:323–350.
4. Bogdan C. Nitric oxide synthase in innate and adaptive immunity: an update. *Trends Immunol*. 2015;36:161–178.
5. Brien JF, McLaughlin BE, Nakatsu K, Marks GS. Chemiluminescence headspace-gas analysis for determination of nitric oxide formation in biological systems. *Methods Enzymol*. 1996;268:83–92.
6. Brown F, Finnerty N, Bolger F, Millar J, Lowry J. Calibration of NO sensors for in-vivo voltammetry: laboratory synthesis of NO and the use of UV–visible spectroscopy for determining stock concentrations. *Anal Bioanal Chem*. 2005;381:964–971.
7. Katayama Y, Soh N, Maeda M. A new strategy for the design of molecular probes for investigating endogenous nitric oxide using an EPR or fluorescent technique. *ChemPhysChem*. 2001;2:655–661.
8. Bedioui F, Villeneuve N. Electrochemical nitric oxide sensors for biological samples – principle, selected examples and applications. *Electroanalysis*. 2003;15:5–18.
9. Kojima H, Urano Y, Kikuchi K, et al. Fluorescent indicators for imaging nitric oxide production. *Angew Chem Int Ed*. 1999;38:3209–3212.
10. Franz KJ, Singh N, Lippard SJ. Metal-based NO sensing by selective ligand dissociation. *Angew Chem Int Ed*. 2000;39:2120–2122.
11. Barzegar Amiri Olia M, Schiesser CH, Taylor MK. New reagents for detecting free radicals and oxidative stress. *Org Biomol Chem*. 2014;12:6757–6766.
12. Barzegar Amiri Olia M, Zavras A, Schiesser CH, Alexander S-A. Blue 'turn-on' fluorescent probes for the direct detection of free radicals and nitric oxide in *Pseudomonas aeruginosa* biofilms. *Org Biomol Chem*. 2016;14:2272–2281.
13. Apfel U-P, Buccella D, Wilson JJ, Lippard SJ. Detection of nitric oxide and nitroxyl with benzoresorufin-based fluorescent sensors. *Inorg Chem*. 2013;52:3285–3294.
14. Kuang Z, Lewis RS, Curtis JM, et al. The SPRY domain-containing SOCS box protein SPSB2 targets iNOS for proteasomal degradation. *J Cell Biol*. 2010;190:129–141.
15. Lewis RS, Kolesnik TB, Kuang Z, et al. TLR regulation of SPSB1 controls inducible nitric oxide synthase induction. *J Immunol*. 2011;187:3798–3805.
16. Yap BK, Leung EW, Yagi H, et al. A potent cyclic peptide targeting SPSB2 protein as a potential anti-infective agent. *J Med Chem*. 2014;57:7006–7015.
17. Yap BK, Harjani JR, Leung EW, et al. Redox-stable cyclic peptide inhibitors of the SPSB2-iNOS interaction. *FEBS Lett*. 2016;590:696–704.
18. Hibbs Jr JB, Taintor RR, Vavrin Z, Rachlin EM. Nitric oxide: a cytotoxic activated macrophage effector molecule. *Biochem Biophys Res Commun*. 1988;157:87–94.
19. Li H, Wan A. Fluorescent probes for real-time measurement of nitric oxide in living cells. *Analyst*. 2015;140:7129–7141.
20. Olken NM, Rusche KM, Richards MK, Marletta MA. Inactivation of macrophage nitric oxide synthase activity by NG-methyl-L-arginine. *Biochem Biophys Res Commun*. 1991;177:828–833.
21. Lijinsky W. *Chemistry and Biology of N-Nitroso Compounds*. Cambridge: Cambridge University Press; 1992.
22. Suzuki T, Fujikura K, Higashiyama T, Takata K. DNA staining for fluorescence and laser confocal microscopy. *J Histochem Cytochem*. 1997;45:49–53.
23. Tsien RY. A non-disruptive technique for loading calcium buffers and indicators into cells. *Nature*. 1981;290:527–528.
24. Lansiaux A, Dassonneville L, Facompre M, et al. Distribution of furamidine analogues in tumor cells: influence of the number of positive charges. *J Med Chem*. 2002;45:1994–2002.
25. McQuade LE, Ma J, Lowe G, et al. Visualization of nitric oxide production in the mouse main olfactory bulb by a cell-trappable copper(II) fluorescent probe. *Proc Natl Acad Sci USA*. 2010;107:8525–8530.

Supplementary Material

Characterisation of a novel coumarin-based fluorescent probe for monitoring nitric oxide production in macrophages

Maiada M. Sadek [a,†], Mina Barzegar Amiri Olia, [b,†], Cameron J. Nowell [c], Nicholas Barlow [a], Carl H. Schiesser [d], Sandra. E. Nicholson [e,f], Raymond S. Norton [a,*]

[a] *Medicinal Chemistry, Monash Institute of Pharmaceutical Sciences, Monash University, Parkville, Victoria 3052, Australia*

[b] *School of Chemistry and Bio21 Molecular Science and Biotechnology Institute, University of Melbourne, Victoria, 3010, Australia*

[c] *Drug Discovery Biology, Monash Institute of Pharmaceutical Sciences, Monash University, Parkville, Victoria 3052, Australia*

[d] *Seleno Therapeutics Pty Ltd, Brighton East, Victoria 3187, Australia*

[e] *The Walter and Eliza Hall Institute of Medical Research, Parkville, Victoria 3052, Australia*

[f] *The Department of Medical Biology, University of Melbourne, Parkville, Victoria. 3052, Australia*

* Corresponding author. ray.norton@monash.edu

[†] These authors contributed equally to this work

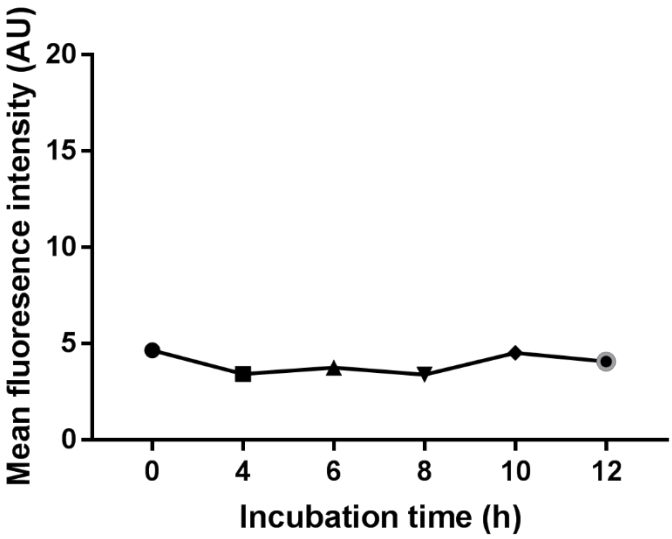

Figure S1. The fluorescence intensity of CB is stable over time in unstimulated cells. Cells were incubated with 10 µM CB, removed from the incubator and then imaged using the confocal microscope at predetermined time points (4, 6, 8, 10 and 12 h) after removing DMEM and washing with PBS. Data are expressed as mean fluorescence intensity (AU) Mean ± standard deviation; n=3.

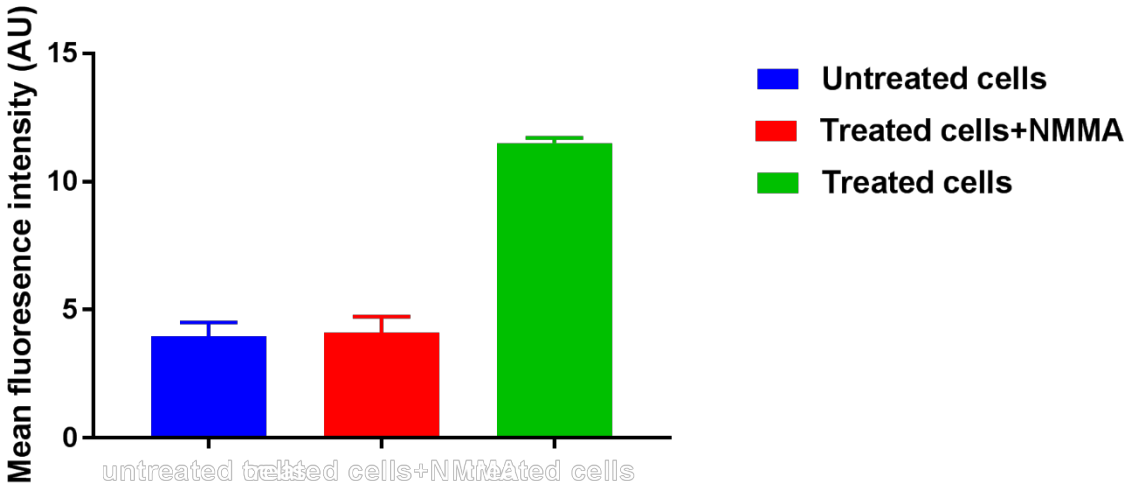

Figure S2. CB specifically detects NO produced in LPS/IFN-γ treated cells. Cells were stimulated with LPS and IFN-γ in the presence and absence of L-NMMA for 16 h, followed by 1 h incubation with CB. Images were captured on a confocal microscope after washing the cells three times with PBS. Fluorescence intensity was measured and compared to control cells where the LPS/IFN-γ were not added and is expressed as arbitrary units (AU). Mean ± standard deviation; n=3.

Chapter 6

Conclusions and Future Directions

The main focus of this thesis was to develop potent SPSB-iNOS inhibitors that are able to cross the cell membrane and inhibit the cytoplasmic SPSB-iNOS interaction. As an attempt to generate these cell permeable inhibitors, two strategies were adopted: 1) Direct structural modification of previous inhibitors to facilitate passive transport and 2) Conjugation to a carrier that allows the active transport of the peptide-conjugate.

In the first strategy, an *in silico* approach was successfully performed to design a potent cyclic pentapeptide inhibitor, INNNAbu, (**CP3**) by minimizing the size, decreasing the conformational flexibility and effective polar surface areas and increasing the lipophilicity of the previously reported heptapeptide inhibitors (**CP1** and **CP2**). To illustrate, the crystal structures of these cyclic heptapeptides in complex with the hSPSB proteins (**CP1**-hSPSB2, **CP2**-hSPSB2, **CP2**-hSPSB4) were determined and analysed. **CP3** was then designed by utilising a covalent bond in place of a main chain intramolecular hydrogen bond observed in the bound structure of **CP2**. The resulted pentapeptide binds to the iNOS binding site of hSPSB2 with strong affinity of 7 nM. It can also inhibit the interaction between hSPSB2 and endogenous iNOS in macrophage cell lysates. The crystal structure of the **CP3**-hSPSB2 complex was also determined revealing that **CP3** adapts a turn structure which may account for its enhanced potency. The pentapeptide, however, was found to be cell impermeable suggesting the need to introduce different structural modifications to **CP3** to improve its permeability.

Consequently, **CP3** analogues were designed and synthesised based on the crystal structure of **CP3**-hSPSB2. Natural and non-natural amino acids with diverse lipophilicity and hydrogen bond donor potentials replaced Ile, Abu and the middle Asn residues in **CP3**. The N-methylated Asn- modified analogue showed the strongest binding affinity among all designed analogues (K_D =10 nM). Moreover, thirteen analogues were found to bind to hSPSB2 with 20-100 fold reduction in affinity (K_D= 140-700 nM) compared to **CP3** while the rest of the analogues showed a significant loss of affinity. The designed peptides, however, failed to show any improvement in the cell permeability of **CP3**.

Alternatively, conjugation of **CP3** to CPP motifs was attempted to encourage the active transport permeability of **CP3**. A potent bicyclic peptide was designed and synthesised featuring c(FΦR4) as the CPP motif with superior internalisation and endosomal escape ability along with a **CP3** motif that can target the SPSB-iNOS interaction. Conjugation of the **CP3** to the CPP did not significantly affect the binding to SPSB2 (K_D= 65 nM). Another potent **CP3** conjugate was also generated using the well-studied CPP, linear TAT peptide. The conjugate

maintained a strong binding affinity (K_D= 10 nM) comparable to that of **CP3** (K_D= 7 nM). Furthermore, the ability of the CPP conjugates to facilitate the cellular uptake and endosomal escape was evaluated using Griess assay. However, further repeats and optimisation of the assay need to be undertaken including incubation times, number of cells and concentration of NO stimulants (LPS and IFN-γ). Other more accurate detection and quantification methods of NO need to be explored to complement the colorimetric Griess assay such as using the small molecule fluorescent probe (**CB**) described in Chapter 5. **CB** successfully detected the changes in NO levels after LPS/IFN-γ activation of RAW 264.7 macrophages using confocal microscopy. Others small molecule probe[1-3] such as 4-amino-5-methylamino-2,7-difluorofluorescein (DAF-FM)[4] can also be utilised in the future detection of NO levels following treatment of the macrophage cells with the **CP3**-CPP conjugates. Moreover, the change in iNOS protein levels can be monitored using western blots to confirm the ability of the CPP conjugates to specifically enhance NO production following SPSB-iNOS pathway inhibition.

Direct visualisation of the conjugates inside the cells can also be performed by labelling the peptides with a fluorescent dye e.g rhodamine[5] or CY-5[6] and subsequent imaging using confocal microscope. The exact subcellular localisation of the conjugates can be determined using cell organelles specific dyes[7] such as LysoTracker® green for lysosome or Rab5 transfection for early endosomes labelling. The extent of endosomal escape can also be measured using flow cytometry through calculating the ratios of signals for the pH sensitive (e.g., naphthylfluorescein) and insensitive dyes labelled peptides.[8] The cytotoxicity of the CPP conjugates should also be assessed using cell viability assay such as the standard 3-(4,5-dimethylthiazol-2-yl)-2,5-diphenyltetrazolium bromide (MTT) assay[9] or propidium iodide (PI) followed by imaging using Operetta® microscopy technique described in Chapter 5.[10]

Apart from confirming the permeability properties of the current **CP3**-CPP conjugates, other approaches can be utilised to promote the cellular uptake of SPSB-iNOS inhibitors while maintaining binding affinity. The prodrug method, for instance, has been reported to confer increased membrane permeability and better pharmacokinetics of hydrophilic compounds.[11] To illustrate, introduction of N-acyl moieties on the amide side chains of the three Asn of **CP3** may result in a biologically inactive permeable peptide that can metabolised by esterases in the cytoplasm to produce the active form of the peptide.[12] One other approach that can be explored is direct lipidation. As Ile position of **CP3** favours bulky group, it can substituted by lipoamino

acids (e.g palmitic acid) which may modulate the overall hydrophobicity of the peptide, hence enhance permeability.[13]

To summarise, a number of potent SPSB-iNOS inhibitors (cyclic pentapeptides and CPP conjugates) was generated in this thesis. The crystal structures and the SAR study presented here allow more comprehensive understanding of the nature of interaction between these inhibitors and the SPSB proteins. Future work will be aimed at extending the ideas explored in this research for the development of permeable inhibitors and addressing some of the shortcomings of the current biological assays. This study represents an important step in the progress of SPSB-iNOS inhibitors as potential anti-infective agents.

6.1 References

(1) Iverson, N.; Hofferber, E.; Stapleton, J., Nitric oxide sensors for biological applications. *Chemosensors.* **2018,** *6*, 8.

(2) Lim, M. H.; Xu, D.; Lippard, S. J., Visualization of nitric oxide in living cells by a copper-based fluorescent probe. *Nat Chem Biol.* **2006,** *2*, 375-380.

(3) Lim, M. H.; Lippard, S. J., Metal-based turn-on fluorescent probes for sensing nitric oxide. *Accounts of Chemical Research.* **2007,** *40*, 41-51.

(4) Kojima, H.; Nakatsubo, N.; Kikuchi, K.; Kawahara, S.; Kirino, Y.; Nagoshi, H.; Hirata, Y.; Nagano, T., Detection and imaging of nitric oxide with novel fluorescent indicators: Diaminofluoresceins. *Anal Chem.* **1998,** *70*, 2446-2453.

(5) Beija, M.; Afonso, C. A.; Martinho, J. M., Synthesis and applications of Rhodamine derivatives as fluorescent probes. *Chemical Society Reviews.* **2009,** *38*, 2410-2433.

(6) Nolting, D. D.; Gore, J. C.; Pham, W., Near-infrared dyes: Probe development and applications in optical molecular imaging. *Curr Org Synth.* **2011,** *8*, 521-534.

(7) Satori, C. P.; Henderson, M. M.; Krautkramer, E. A.; Kostal, V.; Distefano, M. D.; Arriaga, E. A., Bioanalysis of eukaryotic organelles. *Chem Rev.* **2013,** *113*, 2733-2811.

(8) Qian, Z.; Dougherty, P. G.; Pei, D., Monitoring the cytosolic entry of cell-penetrating peptides using a pH-sensitive fluorophore. *Chem Commun.* **2015,** *51*, 2162-2165.

(9) Stockert, J. C.; Horobin, R. W.; Colombo, L. L.; Blazquez-Castro, A., Tetrazolium salts and formazan products in Cell Biology: Viability assessment, fluorescence imaging, and labeling perspectives. *Acta Histochem.* **2018,** *120*, 159-167.

(10) Sadek, M. M.; Barzegar Amiri Olia, M.; Nowell, C. J.; Barlow, N.; Schiesser, C. H.; Nicholson, S. E.; Norton, R. S., Characterisation of a novel coumarin-based fluorescent probe

for monitoring nitric oxide production in macrophages. *Bioorg Med Chem.* **2017,** *25*, 5743-5748.

(11) Guarino, V. R.; Stella, V. J., Prodrugs of amides, imides and other NH-acidic compounds. In *Prodrugs: Challenges and Rewards Part 1*, Stella, V. J.; Borchardt, R. T.; Hageman, M. J.; Oliyai, R.; Maag, H.; Tilley, J. W., Eds. Springer New York: New York, NY, 2007; pp 833-887.

(12) Kahns, A. H.; Bundgaard, H., N-Acyl derivatives as prodrug forms for amides: Chemical stability and enzymatic hydrolysis of various N-acyl and N-alkoxycarbonyl amide derivatives. *Int J Pharm.* **1991,** *71*, 31-43.

(13) Zhang, L.; Bulaj, G., Converting peptides into drug leads by lipidation. *Curr Med Chem.* **2012,** *19*, 1602-1618.

Appendix

Other published co-authored manuscript

Biochemistry

Article

pubs.acs.org/biochemistry

The Single Disulfide-Directed β-Hairpin Fold. Dynamics, Stability, and Engineering

Balasubramanyam Chittoor,[†] Bankala Krishnarjuna,[†] Rodrigo A. V. Morales,[†] Christopher A. MacRaild,[†] Maiada Sadek,[†] Eleanor W. W. Leung,[†] Samuel D. Robinson,[†,§] Michael W. Pennington,[‡] and Raymond S. Norton*[,†]

[†]Medicinal Chemistry, Monash Institute of Pharmaceutical Sciences, Monash University, Parkville, Victoria 3052, Australia

[‡]Peptides International, Louisville, Kentucky 40299, United States

Supporting Information

ABSTRACT: Grafting bioactive peptide sequences onto small cysteine-rich scaffolds is a promising strategy for enhancing their stability and value as novel peptide-based therapeutics. However, correctly folded disulfide-rich peptides can be challenging to produce by either recombinant or synthetic means. The single disulfide-directed β-hairpin (SDH) fold, first observed in contryphan-Vc1, provides a potential alternative to complex disulfide-rich scaffolds. We have undertaken recombinant production of full-length contryphan-Vc1 (rCon-Vc1[Z1Q]) and a truncated analogue (rCon-Vc1$_{1-22}$[Z1Q]), analyzed the backbone dynamics of rCon-Vc1[Z1Q], and probed the conformational and proteolytic stability of these peptides to evaluate the potential of contryphan-Vc1 as a molecular scaffold. Backbone ^{15}N relaxation measurements for rCon-Vc1[Z1Q] indicate that the N-terminal domain of the peptide is ordered up to Thr19, whereas the remainder of the C-terminal region is highly flexible. The solution structure of truncated rCon-Vc1$_{1-22}$[Z1Q] was similar to that of the full-length peptide, indicating that the flexible C-terminus does not have any effect on the structured domain of the peptide. Contryphan-Vc1 exhibited excellent proteolytic stability against trypsin and chymotrypsin but was susceptible to pepsin digestion. We have investigated whether contryphan-Vc1 can accept a bioactive epitope while maintaining the structure of the peptide by introducing peptide sequences based on the DINNN motif of inducible nitric oxide synthase. We show that sCon-Vc1$_{1-22}$[NNN$_{12-14}$] binds to the iNOS-binding protein SPSB2 with an affinity of 1.3 μM while maintaining the SDH fold. This study serves as a starting point in utilizing the SDH fold as a peptide scaffold.

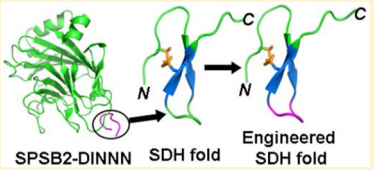

Grafting bioactive peptide sequences that target specific protein−protein interactions onto stable scaffolds is a promising approach for the development of peptide-based therapeutics.[1] Disulfide-rich peptides have proven to be valuable acceptor scaffolds, with applications as drugs, pharmacological probes, and imaging agents.[2−7] A valuable scaffold in such applications is the inhibitor cystine knot (ICK) motif,[8,9] which is found in peptides from plants, cone snails, scorpions, and spiders.[10,11] The ICK motif peptides agatoxin and Agouti-related protein (AgRP) have been engineered for *in vivo* tumor imaging[12] and targeting tumor angiogenesis,[13] respectively.

The production of correctly folded disulfide-rich peptides by chemical synthesis or recombinant expression can be challenging, especially for peptides containing three or four disulfide bridges.[14−16] Recently, contryphan-Vc1, a 31-residue peptide identified in the venom of the marine cone snail *Conus victoriae*,[17,18] has been shown to have a unique fold, designated as the single disulfide-directed β-hairpin (SDH).[19] The core structure of contryphan-Vc1 is a double-stranded antiparallel β-sheet stabilized by just a single disulfide bridge. The β-hairpin core of contryphan-Vc1 consists of two loops, the first of which comprises residues Gln4, Pro5, Gly6, and Tyr7 (QPGY), which form a type II β-turn that leads to the first β-strand. The second loop comprises residues Pro11, Val12, Leu13, and Gly14, which form a type IV β-turn. Residues from Thr19 to Tyr31 are flexible and unstructured. The β-hairpin core of contryphan-Vc1 displays an ordered structure and remarkable thermal stability and is very similar structurally to the ICK fold despite its simpler cysteine framework; these properties suggest that it may have potential as a useful scaffold for grafting.

In this study, we have investigated the stability of the SDH fold to chemical denaturation and proteolytic enzymes, as well as its resilience to truncation and the insertion of non-native peptide motifs, to evaluate its potential as a scaffold. We have undertaken recombinant production of full-length contryphan-Vc1 (rCon-Vc1[Z1Q]) by replacing the N-terminal pyroglutamic acid with a glutamine residue. We analyzed the backbone dynamics of contryphan-Vc1 to identify the ordered and flexible regions of the peptide and showed that the flexible C-terminal region could be deleted without affecting the ordered structure of the peptide. We also investigated whether contryphan-Vc1 can accept a bioactive epitope by utilizing the DINNN motif of inducible nitric oxide synthase (iNOS), which is essential for recognition of iNOS by the SPRY

Received: February 11, 2017
Revised: April 20, 2017
Published: April 24, 2017

DOI: 10.1021/acs.biochem.7b00120
Biochemistry 2017, 56, 2455−2466

Table 1. Peptide Sequences Investigated in This Study

Peptide	Sequence
sCon-Vc1$_1$	[a]ZWCQPGYAYNPVLGICTITLSRIEHPGNYDY
rCon-Vc1[Z1Q]	QWCQPGYAYNPVLGICTITLSRIEHPGNYDY
rCon-Vc1$_{1\text{-}22}$[Z1Q]	QWCQPGYAYNPVLGICTITLSR
sCon-Vc1$_{1\text{-}22}$[NNN$_{12\text{-}14}$]	ZWCQPGYAYNPNNNICTITLSR
sCon-Vc1$_{1\text{-}22}$[Z1Q,DINNN$_{4\text{-}8}$]	QWCDINNNAYNPVLGICTITLSR
sCon-Vc1$_{1\text{-}22}$[Z1Q,DINNN$_{12\text{-}16}$]	QWCQPGYAYNPDINNNICTITLSR

[a]Pyroglutamate modification is indicated as Z.

domain-containing SOCS (suppressor of cytokine signaling) box (SPSB) proteins in circulating macrophages.[20−22] The peptide analogues sCon-Vc1$_{1-22}$[Z1Q,DINNN$_{4-8}$], sCon-Vc1$_{1-22}$[Z1Q,DINNN$_{12-16}$], and sCon-Vc1$_{1-22}$[NNN$_{12-14}$] were tested for their affinity for human SPSB2 utilizing surface plasmon resonance (SPR) and analyzed conformationally by NMR.

EXPERIMENTAL PROCEDURES

Construction of Plasmids Expressing Full-Length and Truncated Contryphan-Vc1. Codon-optimized DNA corresponding to the mature peptide sequence of contryphan-Vc1 was synthesized (GenScript) with SalI and XhoI restriction sites, respectively, at the 5′ and 3′ ends. An enterokinase cleavage site was included at the 5′ end after the SalI restriction site. The gene fragment was ligated into the pET32a vector (Novagen) using the SalI and XhoI restriction sites to generate modified pET32a expressing a thioredoxin (Trx) fusion protein of full-length contryphan-Vc1. The DNA sequence of contryphan-Vc1 was then amplified with a forward primer for contryphan-Vc1 with a SalI restriction site and enterokinase cleavage site and a reverse primer with a stop codon after the Arg22 codon, and the gene fragment was ligated into the pET32a vector using the SalI and XhoI restriction sites to generate modified pET32a expressing the Trx fusion protein of truncated contryphan-Vc1 (rCon-Vc1$_{1-22}$[Z1Q]) (Table 1).

Peptide Expression and Purification. Trx fusion proteins of both full-length contryphan-Vc1 and the truncated analogue Con-Vc1$_{1-22}$ were expressed in *Escherichia coli* BL21(DE3) cells at 30 °C, induced for 4 h with 0.5 mM isopropyl β-D-1-thiogalactopyranoside. To generate ^{15}N-labeled and ^{15}N- and ^{13}C-labeled contryphan-Vc1 peptides, *E. coli* BL21(DE3) cells were grown in M9 minimal medium supplemented with 1 g/L $^{15}NH_4Cl$ and 3 g/L [^{13}C]glucose. For purification of the Trx-fused peptides, cells were resuspended in bug buster (Novagen) at a concentration of 1 g of cell paste per mL and incubated for 20 min in the presence of EDTA-free protease inhibitor cocktail (Roche) and then clarified by centrifugation at 23660*g* for 30 min at 4 °C. The supernatant was loaded onto a pre-equilibrated Ni-NTA Hitrap column (GE Healthcare, 5 mL) at a flow rate of 0.25 mL/min. Unbound material was removed by extensive washing with buffer A [20 mM Tris-HCl (pH 8), 10 mM imidazole, and 100 mM NaCl] followed by a wash with buffer A containing 0.5 M NaCl. The fusion protein was eluted with buffer A containing 250 mM imidazole and buffer-exchanged with enterokinase cleavage buffer [50 mM Tris-HCl (pH 8), 1 mM $CaCl_2$, and 50 mM NaCl]. The Trx tag was removed by incubating the fusion protein with enterokinase (NEB) at a concentration of 0.005 μg/mg of protein at 23 °C for 16 h and passing the mixture onto a Ni-NTA Hitrap column. Unbound supernatant was collected and purified by reversed-phase HPLC (RP-HPLC) on a Phenomenex Luna C18 column (100 Å, 5 μm, 100 mm × 10 mm) using a gradient from 5 to 95% B [A, 99.9% H_2O and 0.1% TFA; B, 80% acetonitrile (ACN), 19.9% H_2O, and 0.1% TFA] over 30−60 min, and then the samples were lyophilized. The peptides were further purified by peptide gel filtration using a Superdex peptide 10/300 GL column, and the purity and molecular mass of each peptide were confirmed by liquid chromatography and mass spectrometry (LC−MS) on a Shimadzu LCMS2020 instrument, incorporating a Phenomenex Luna C8 column (100 Å, 3 μm, 100 mm × 2 mm) using a linear gradient of water having 0.05% TFA for 4 min, followed by 0−60% ACN (0.05% TFA) in water over 10 min at a flow rate of 0.2 mL/min (Table 1 and Figures S1 and S2).

Peptide Synthesis. Full-length contryphan-Vc1 was synthesized using *N*-(9-fluorenyl) methoxycarbonyl (Fmoc)-Tyr (tBu)-Wang resin on a Prelude automated peptide synthesizer (Protein Technologies, Tucson, AZ). All couplings were mediated with diisopropylcarbodiimide with 6-chloro-1-hydroxybenzotriazole (6-Cl-HOBT) for 3 h. The peptide was cleaved from the resin support and simultaneously deprotected using a cocktail of trifluoroacetic acid, anisole, triisopropylsilane, thioanisole, water, and 1,2-ethanedithiol [9:1:2:1:1:1 (v/v)] for 2 h at room temperature. The crude peptide was precipitated and washed thrice with ice-cold diethyl ether, then dissolved in 50% aqueous acetic acid, and diluted in water to a concentration of 0.3 mg/mL. The pH of the peptide solution was adjusted to 7.8 with ammonium hydroxide (NH_4OH). Disulfide bond formation was accelerated by adding 1 mL of 3% hydrogen peroxide (H_2O_2), and the peptide solution was allowed to stir gently for 18 h. Other contryphan-Vc1 peptide analogues were synthesized on a PTI Instruments PS3 peptide synthesizer, using Rink amide AM resin. Peptides were deprotected with 20% piperidine in dimethylformamide (DMF), activated with 70 mL/L *N*,*N*-diisopropylethylamine (DIPEA) in DMF, and coupled with a 3-fold excess of 2-(6-chloro-1*H*-benzotriazol-1-yl)-1,1,3,3-tetramethylaminium hexafluorophosphate (HCTU) for 50 min. Cleavage from the resin was performed over 2 h with a mixture of 3,6-dioxa-1,8-octanedithiol, triisopropylsilane, 1,3-dimethoxybenzene, and trifluoroacetic acid [2.5:2.5:5:92.5 (v/v) DODT/TIPS/DMB/TFA]. The cleavage mixture was purged with nitrogen, and the crude peptide was precipitated and washed thrice with ice-cold diethyl ether, then dissolved in 0.1 M ammonium bicarbonate (pH 8.0), and allowed to fold by adjusting the concentration to 0.3 mg/mL. The crude folded peptide was purified by RP-HPLC on a Phenomenex Luna C18 column (100 Å, 5 μm, 100

DOI: 10.1021/acs.biochem.7b00120
Biochemistry 2017, 56, 2455−2466

mm × 10 mm) using a gradient of 5 to 95% B (A, 99.9% H_2O and 0.1% TFA; B, 80% ACN, 19.9% H_2O, and 0.1% TFA) over 30−60 min, and the samples were lyophilized. The purity and molecular mass of the each peptide were confirmed by LC−MS on a Shimadzu LCMS2020 instrument, incorporating a Phenomenex Luna C8 column (100 Å, 3 μm, 100 mm × 2 mm) using a linear gradient of water having 0.05% TFA for 4 min, followed by 0 to 60% ACN (0.05% TFA) in water over 10 min at a flow rate of 0.2 mL/min (Table 1 and Figures S1 and S3).

NMR Spectroscopy. All spectra were recorded on a Bruker 600 MHz spectrometer equipped with a cryogenically cooled triple-resonance probe. The lyophilized peptide was dissolved in either 93% H_2O with 7% ^2H_2O or 100% ^2H_2O (pH 4.0). One-dimensional ^1H spectra were recorded at different temperatures between 5 and 30 °C, at intervals of 5 °C, and between pH 3 and 9. Two-dimensional NMR spectra utilized for sequence-specific assignments and structure calculations were recorded at pH 4 and 20 °C. Two-dimensional homonuclear TOCSY spectra with a spin-lock time of 80 ms were recorded using the DIPSI-2 pulse sequence[23] with excitation sculpting for water suppression[24] at 15, 20, and 25 °C. Two-dimensional NOESY spectra were recorded at two different mixing times, 50 and 200 ms, to analyze the time dependence of NOE intensities. A DQF-COSY spectrum was recorded in 100% ^2H_2O for measuring J couplings. ^{13}C HSQC and ^{15}N HSQC spectra were recorded for carbon and nitrogen chemical shifts, respectively. A sine-bell squared window function was used for processing spectra. All spectra were processed using Bruker TopSpin (version 3.2) and analyzed using CcpNmr Analysis (version 2.1.5).[25] The sequence-specific resonance assignments are summarized in Table S1 and deposited in BMRB[26] (entry 30124). For the determination of potential amide backbone hydrogen bonding in rCon-$Vc1_{1-22}$[Z1Q], a series of one-dimensional ^1H spectra was recorded at 10, 15, 20, 25, and 30 °C, and the amide resonance temperature coefficients were determined from the slope of linear least-squares fits to the data.

Structure Calculation. The intensities of cross-peaks in NOESY spectra with a mixing time of 200 ms were utilized to generate distance constraints. $^3J_{HN-H\alpha}$ coupling constants were measured from one-dimensional ^1H spectra, which yielded 11 φ angle constraints. These φ angles were restrained to −120 ± 30° for $^3J_{HN-H\alpha}$ values of ≥8.0 Hz and −65 ± 25° for $^3J_{HN-H\alpha}$ values of ≤6.0 Hz. Three distance constraints were added for the disulfide bridge as follows: 2.00, 3.00, and 3.00 Å for S(i)−S(j), S(i)−Cβ(j), and S(j)−Cβ(i), respectively. The initial structures of contryphan-$Vc1_{1-22}$ were generated using CYANA (version 3.0)[27] and then refined utilizing Xplor-NIH.[28] Structure calculations were performed using 297 interproton distance constraints derived from the NOESY spectrum (88 intraresidue, 88 sequential, 66 medium-range, and 55 long-range NOE constraints), 11 dihedral angle constraints derived from $^3J_{HN-H\alpha}$ J coupling measurements from one-dimensional ^1H, two other dihedral angle constraints derived from two-dimensional DQF-COSY spectra, and three disulfide bond restraints. Conventional simulated annealing protocols were used in Xplor-NIH to generate an ensemble of 100 structures, from which the 20 lowest-energy structures were chosen to represent the solution structure of rCon-$Vc1_{1-22}$[Z1Q]. The root-mean-square deviation (RMSD) values for these structures were assessed using MolMol (version 2K.1).[29] Structural figures were prepared using PyMOL (version 1.5.0.4).

NMR Relaxation Measurements. ^{15}N relaxation experiments were performed at 20 °C on a Bruker 600 MHz spectrometer. Spin−lattice relaxation times (T_1) were obtained from a series of $^1H-^{15}N$ correlation spectra with relaxation delays of 0, 50, 100, 200, 400, 800, and 1600 ms. Spin−spin relaxation times (T_2) were obtained using spin-lock periods of 0, 20, 50, 80, 120, 150, 180, 240, and 300 ms. The T_1 and T_2 time constants were calculated using CcpNmr Analysis by plotting peak volumes versus relaxation delay times with an equation for single exponential decay. The reported errors are standard deviations derived from the fit of the data. Steady-state $^1H-^{15}N$ nuclear Overhauser enhancement (NOE) values were determined from the ratio of peak intensities for spectra recorded with and without 3 s proton presaturation. The peak intensities of residues with and without proton presaturation were calculated utilizing CARA.[30]

Reduction Assay. Tris(2-carboxyethyl)phosphine (TCEP) stock solutions (0.5 M) were prepared in Milli-Q water immediately prior to use. TCEP was added to 0.5 mM synthetic contryphan-Vc1 (sCon-Vc1) to a final concentration of 10 mM, and the sample was incubated at room temperature. Peptide samples were assayed at time intervals of 0, 1, 6, 18, 24, and 48 h using LC−MS on a Shimadzu LCMS2020 instrument incorporating a Phenomenex Luna C8 column (100 Å, 3 μm, 100 mm × 2 mm) with a linear gradient of 0.05% TFA in water for 4 min, followed by 0 to 60% ACN (0.05% TFA) in water over 10 min at a flow rate of 0.2 mL/min. One-dimensional ^1H NMR spectra were recorded on synthetic contryphan-Vc1 (sCon-Vc1) in 6 mM TCEP (pH 4 and 20 °C) after incubation for 1, 2, 16, and 24 h.

Proteolysis Assays. Proteolysis assays were performed at a 250:1 substrate (peptide):enzyme ratio with pepsin, trypsin, and α-chymotrypsin. For all assays, peptides were incubated with protease at 37 °C for up to 4 h. As a positive control to ensure that active enzyme was present, bovine serum albumin was used as a substrate. All digestion assay products were analyzed by LC−MS (0 to 60% ACN gradient, 10 min). Trypsin (EC 3.4.21.4, Sigma) and α-chymotrypsin (EC 3.4.21.1, Sigma) stocks were prepared in 50 mM Tris (pH 7.4) and 100 mM NaCl, and pepsin (EC 3.4.23.1, Sigma) stocks were prepared in 10 mM HCl (pH 2). The reactions for trypsin and α-chymotrypsin were performed in 50 mM Tris-HCl (pH 7.4), 100 mM NaCl, and 2 mM $CaCl_2$. The reaction for pepsin was performed in 1 mM HCl (pH 2). The trypsin and α-chymotrypsin reactions were quenched with 0.1% TFA, and the pepsin reaction was quenched with 50% 1 M NaOH.

Surface Plasmon Resonance. The binding affinities of the Con-Vc1 peptide analogues were analyzed by surface plasmon resonance (SPR), using a Biacore T200 instrument (GE Healthcare). All experiments were performed in degassed buffer containing 25 mM HEPES (pH 7.4), 150 mM NaCl, 3 mM EDTA, and 0.005% surfactant P-20 at 25 °C. Human SPSB2 was immobilized on a Biacore CM5 biosensor chip by amine coupling as follows. The CM-dextran matrix was activated with 0.2 M 1-ethyl-3-[3-(diethylamino)propyl]carbodiimide hydrochloride (EDC) and 0.05 M N-hydroxysuccinimide; 100 μg/mL human SPSB2 in 10 mM sodium acetate (pH 5.5) was then passed over the activated surface at a rate of 10 μL/min for 10 min. Finally, 1 M ethanolamine-HCl (pH 8.5) was injected into both target and reference flow cells to deactivate any remaining activated carboxyl groups on the surface. The binding of the contryphan-Vc1 peptide analogues to immobilized human SPSB2 was investigated in a running buffer containing 10

DOI: 10.1021/acs.biochem.7b00120
Biochemistry 2017, 56, 2455−2466

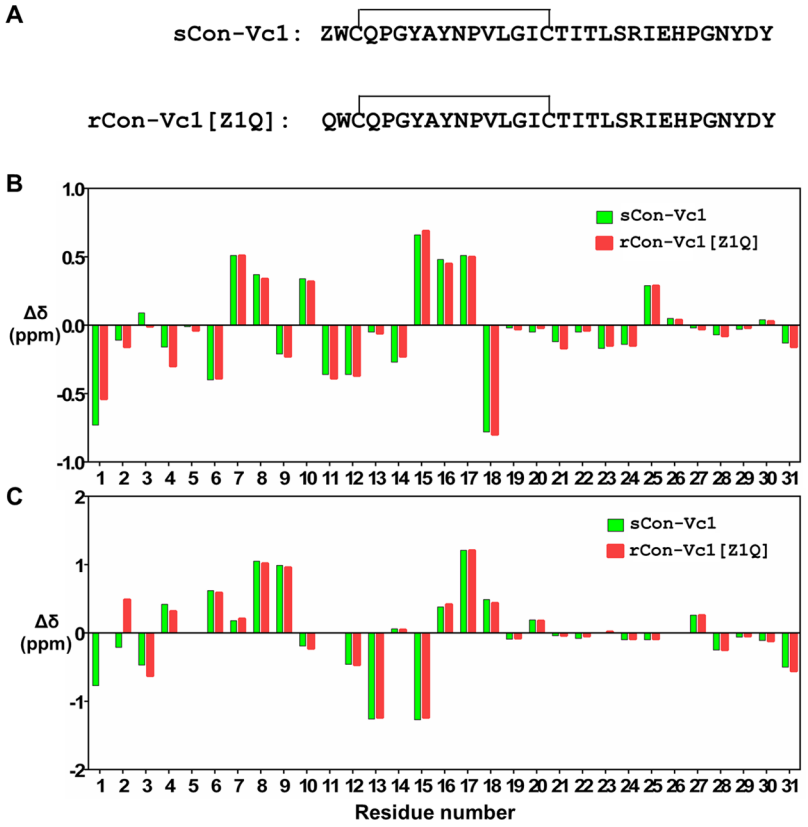

Figure 1. Secondary chemical shift difference plots for synthetic and recombinant contryphan-Vc1. (A) Sequences of sCon-Vc1 and rCon-Vc1[Z1Q] indicating disulfide connectivity. (B) H^{α} shift deviations from random coil chemical shifts. (C) H^{N} shift deviations from random coil chemical shifts.[31]

mM HEPES, 150 mM NaCl, 3 mM EDTA, and 0.005% surfactant P-20, with and without 1 mM DTT (pH 7.4). The peptides were injected onto the surface with a contact time of 100 s at a flow rate of 100 μL/min and a dissociation time for 600 s. Sensorgrams were further corrected for nonspecific binding to the surface by subtracting the signals of the reference surface from that of the human SPSB2-bound surface. The corrected signal was then fitted to a 1:1 Langmuir binding model using Biacore T200 Evaluation Software (version 2.0) to estimate the association rate, k_{on}, and dissociation rate, k_{off}. In cases in which kinetics could not be measured, SPR data were evaluated using a 1:1 steady-state binding model to determine the binding affinity (K_D).

RESULTS

Recombinant Production of Contryphan-Vc1 Peptides. Full-length contryphan-Vc1 (rCon-Vc1[Z1Q]) and a truncated analogue, rCon-Vc1$_{1-22}$[Z1Q], were expressed as Trx fusion proteins in *E. coli* BL21(DE3). The Trx fusion proteins were expressed in M9 medium to produce ^{15}N-labeled and ^{15}N- and ^{13}C-labeled peptides. The Trx fusion proteins were highly soluble, with yields of 20 mg/L from expression in both Luria-Bertani broth and M9 medium. Clarified cell lysates containing His-tagged Trx fusion proteins were loaded onto a Ni-NTA column, and then bound protein was eluted from the Ni-NTA column and cleaved with enterokinase. The cleaved fusion protein was passed through a Ni-NTA column to remove His-tagged Trx, and the desired peptide was purified by RP-HPLC. The identities and purities of the peptides were confirmed by LC−MS. RP-HPLC and LC−MS showed that purified rCon-Vc1[Z1Q] and rCon-Vc1$_{1-22}$[Z1Q] were essentially homogeneous and ∼95% pure (Figure S2).[30]

Comparison of Synthetic and Recombinant Contryphan-Vc1. Contryphan-Vc1 from the venom gland of *Conus victoriae* has an N-terminal pyroglutamate modification, which is in the proximity of the Tyr9 side chain in the structure of the peptide.[19] To assess the role of the pyroglutamate modification in the structure of the peptide, we produced recombinant full-length contryphan-Vc1 having unmodified glutamine at the N-terminus and compared its chemical shifts with those of synthetic contryphan-Vc1 with pyroglutamate at its N-terminus. Plots of the deviations of H^{α} and backbone chemical shifts from random coil values were nearly identical for the two peptides, with minor differences observed only near the N-terminus (Figure 1). This confirms that synthetic and recombinant contryphan-Vc1 have similar structures and that the pyroglutamate modification has no significant effect on the structure of contryphan-Vc1.

Backbone Dynamics of Recombinant Contryphan-Vc1. Backbone ^{1}H−^{15}N NOEs and ^{15}N R_1 and R_2 relaxation rates for rCon-Vc1[Z1Q] are shown in Figure 2. Uniform heteronuclear NOE values of ∼0.6 were observed for residues Trp2−Ile18, consistent with the dynamics of these residues being dominated by a single process on a time scale of approximately 2 ns, as would be expected for the overall tumbling of a molecule of this size. In contrast, most residues beyond Thr19 showed either negative or zero ^{1}H−^{15}N NOE values, indicating the presence of faster dynamic processes (Figure 2). Consistent with the heteronuclear NOE values, the R_1 and R_2 rates for residues Trp2−Ile18 are relatively uniform

DOI: 10.1021/acs.biochem.7b00120
Biochemistry 2017, 56, 2455−2466

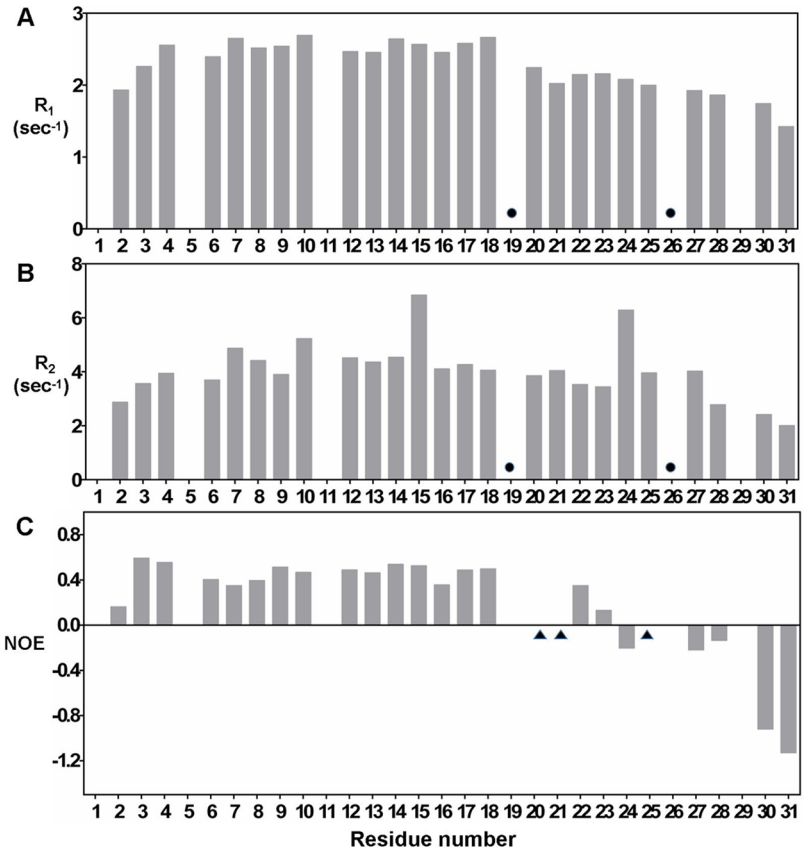

Figure 2. R_1, R_2, and $^1H-^{15}N$ NOE parameters (A–C, respectively) for recombinant full-length contryphan-Vc1. Overlapping residues are denoted with circles, and the residues with zero intensity after NOE saturation are denoted with triangles.

and larger than those of the C-terminal residues Thr19–Tyr31. Together, these relaxation data indicate a well-defined conformation and limited internal mobility for residues Trp2–Ile18 and significant flexibility across the C-terminal tail.

Sequence-Specific Resonance Assignments for rCon-Vc1$_{1-22}$[Z1Q]. Spin systems were identified through combined analysis of DQF-COSY, TOCSY (80 ms spin-lock time), and NOESY (200 ms mixing time) spectra recorded at 293 K and pH 3.9. Sequential resonance assignments were made utilizing two-dimensional NOESY and three-dimensional HNCA and HNCACB spectra. Residues containing methyl groups such as Ala8, Thr17 and -19, Leu13 and -20, and Ile15 and -18 served as good starting points for the identification of spin systems and the sequential assignment process. The spin systems for Pro5 and Pro11 were identified by the observation of strong NOE cross-peaks between Gln4$^{\alpha}$-Pro5$^{\delta}$ and Asn10$^{\alpha}$-Pro11$^{\delta}$; the presence of strong $\alpha\delta$ NOEs confirmed the *trans* conformations of both X–Pro bonds. Complete backbone and side chain proton resonance assignments were obtained for all spin systems (Table S1). Backbone resonances of recombinant full-length contryphan-Vc1 were assigned by comparing the chemical shifts with those of synthetic contryphan-Vc1.[19]

Solution Structure of Con-Vc1$_{1-22}$. To investigate the influence of the unstructured and highly flexible C-terminal tail of contryphan-Vc1, the structure of truncated contryphan-Vc1 (rCon-Vc1$_{1-22}$[Z1Q]) was determined and compared with that of full-length contryphan-Vc1.[19] Structural constraints are summarized in Table 2. rCon-Vc1$_{1-22}$[Z1Q] retained its ordered structure after deletion of the flexible C-terminal tail region and is almost identical to that of the full-length peptide,

Table 2. Structural Statistics for rCon-Vc$_{11\text{-}22}$[Z1Q]

NMR Distance and Dihedral Constraints	
no. of distance constraints	
total NOEs	297
intraresidue	88
inter-residue	
sequential ($\|i-j\|=1$)	88
medium-range ($1<\|i-j\|<5$)	66
long-range ($\|i-j\|>5$)	55
hydrogen bond	4
total no. of dihedral angle restraints	
backbone (φ angle)	12
side chain (χ_1 angle)	3
Structural Statistics	
energy[a]	
E_{NOE} (kcal mol^{-1})	0.605 ± 0.41
E_{VdW} (kcal mol^{-1})	3.02 ± 0.20
RMSD among 20 conformers (residues 2–16), average pairwise RMSD[b]	
backbone (Å) (N, Cα, C)	0.36 ± 0.12
all heavy atoms (Å)	0.91 ± 0.25
Ramachandran Analysis	
residues in most favored regions (%)	68.4
residues in additionally allowed regions (%)	31.6
residues in generously allowed regions (%)	0.0
residues in disallowed regions (%)	0.0

[a]The values for E_{NOE} were calculated from a square-well potential with force constants of 150 kcal mol^{-1} Å^2. [b]The pairwise RMSD was calculated across 20 refined structures.

DOI: 10.1021/acs.biochem.7b00120
Biochemistry 2017, 56, 2455–2466

as shown in Figure 3. Backbone superimposition of the full-length form and rCon-Vc1$_{1-22}$[Z1Q] yielded an RMSD of 0.74

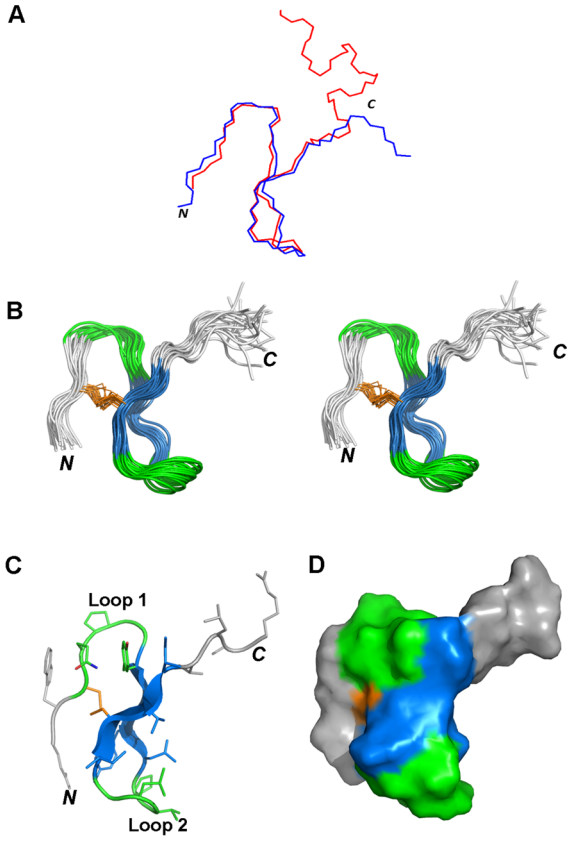

Figure 3. (A) Backbone superposition (using MolMol) of the closest-to-average structures of recombinant rCon-Vc1$_{1-22}$[Z1Q] (blue) with sCon-Vc1 (red).[19] (B) Stereoview of the ensemble of the final 20 structures of rCon-Vc1$_{1-22}$[Z1Q] from Xplor-NIH superimposed over the backbone heavy atoms (N, C$^{\alpha}$, and C) of residues 3−16. (C) PyMOL representation of the closest-to-average structure of rCon-Vc1$_{1-22}$[Z1Q]. Loop 1 and loop 2 are colored green; β-strands are colored blue, and the unstructured C-terminus is colored gray. (D) Surface representation of structure of rCon-Vc1$_{1-22}$[Z1Q], with the single disulfide bridge colored bright orange.

Å over C$^{\alpha}$ atoms of residues 3−16 (Figure 3A). The main feature of the structure of rCon-Vc1$_{1-22}$[Z1Q] is an antiparallel β-sheet with two β-strands connected by a β-turn (Figure 3B,C). The first two residues of rCon-Vc1$_{1-22}$[Z1Q], Glu1 and Trp2, were less well-defined and had R_1 and R_2 rates that were smaller than those of residues in the β-hairpin core of the peptide. Residues Gln4, Pro5, Gly6, and Tyr7 form a type II β-turn that leads to the first β-strand. Ala8, Tyr9, and Asn10 form the first β-strand, and Ile15, Cys16, and Thr17 make up the other strand. Pro11, Val12, Leu13, and Gly14 form a type IV β-turn. Residues after the second β-strand, Ile18−Arg22, are unstructured and highly flexible. The amides of Ala8, Asn10, Ile15, and Thr17 had temperature coefficients less negative than −4.75 ppb/K, indicating that these residues participate in hydrogen bonding. The hydrogen bonds inferred from the structure are between Ala8 H^{N} and Thr17 O, Asn10 H^{N} and Ile15 O, Ile15 H^{N} and Asn10 O, and Thr17 H^{N} and Ala8 O, which are all part of the antiparallel β-sheet.

Conformational Stability of Contryphan-Vc1. Contryphan-Vc1 has been shown to have remarkable thermal stability.[19] The conformational stability of the SDH fold was explored further by observing the effects of urea and pH on conformation. One-dimensional ^{1}H NMR spectra of sCon-Vc1 recorded in the presence of increasing concentrations of urea (≤7 M) showed subtle changes in the spectrum, indicating the interaction of urea with the peptide. Although subtle chemical shift changes were observed in the one-dimensional ^{1}H NMR, the chemical shift dispersion was maintained even at 7 M urea, indicating that the peptide was still folded (Figure S4). Limited unfolding of the peptide can be inferred from the appearance of a minor peak from the Trp2 indole proton around 9.6 ppm as the concentration of urea increased (Figure S4C). The degree of unfolding of the peptide was estimated from the relative intensity of this peak. The resulting urea unfolding curve (Figure S4D) shows that <30% of the peptide was unfolded at 7 M urea, confirming the exceptional conformational stability of contryphan-Vc1.

sCon-Vc1 was also examined over the pH range of 2−9. One-dimensional ^{1}H NMR spectra of sCon-Vc1 showed subtle chemical shift changes in the pH titration between pH 2 and 8, but the overall spectral dispersion was maintained. Most of the amide peaks were broadened at pH 9 because of solvent exchange (Figure S5). The titratable residues Glu24 and His25 are present in the highly flexible and unstructured C-terminal region, and their titrations have no effect on the conformation of the peptide.

Redox Stability. To test the redox stability of the SDH fold, 0.5 mM sCon-Vc1 was subjected to a high concentration of the reducing agent TCEP. Contryphan-Vc2, a seven-residue peptide that also has a single disulfide bridge, was used as control for the reduction assay.[18] Unlike sCon-Vc1, contryphan-Vc2 was completely reduced within 1 h upon incubation with 10 mM TCEP at room temperature (Figure S6A). In contrast, only <5% of sCon-Vc1 was reduced under similar conditions (Figure 4A). The reduction kinetics of sCon-Vc1 were slow at room temperature, and even after being incubated for 48 h, the peptide was not completely reduced (Figure 4A). One-dimensional ^{1}H NMR spectra and ^{13}C HSQC spectra of sCon-Vc1 (0.5 mM) showed no significant changes in the presence of a 12-fold excess of TCEP (6 mM) after incubation for 1 h at 20 °C. After incubation for 16 h with the same concentration of TCEP (Figure 4C and Figure S6C,D), a minor peak at 10.04 ppm appeared, corresponding to the Trp2 indole proton resonance of the reduced species of contryphan-Vc1. Even after incubation for 24 h with 6 mM TCEP at 20 °C, one-dimensional ^{1}H NMR spectra showed only a slight increase in the reduced species. One-dimensional ^{1}H NMR spectra recorded on contryphan-Vc1$_{1-22}$[Z1Q] incubated with 24 mM TCEP showed that the peaks disappeared completely after TCEP incubation for 7 days, showing that the disulfide bond contributes to the stability of the SDH fold (Figure S6E,F).

Proteolytic Stability of Contryphan-Vc1. *In vitro* proteolysis was performed on sCon-Vc1, rCon-Vc1[Z1Q], and rCon-Vc1$_{1-22}$[Z1Q] utilizing the enzymes trypsin, α-chymotrypsin, and pepsin to assess the proteolytic stability of contryphan-Vc1 and its analogues. In the presence of trypsin, sCon-Vc1 showed accumulation of a peak with a mass of 2464.8 Da, which corresponds to residues 1−22 (cleavage following Arg22) according to LC−MS. Tryptic digestion of rCon-Vc1[Z1Q] also showed accumulation of a peak having a mass of 2481.8 Da, also corresponding to residues 1−22 (the difference in the mass of the fragments between sCon-Vc1 and

DOI: 10.1021/acs.biochem.7b00120
Biochemistry 2017, 56, 2455−2466

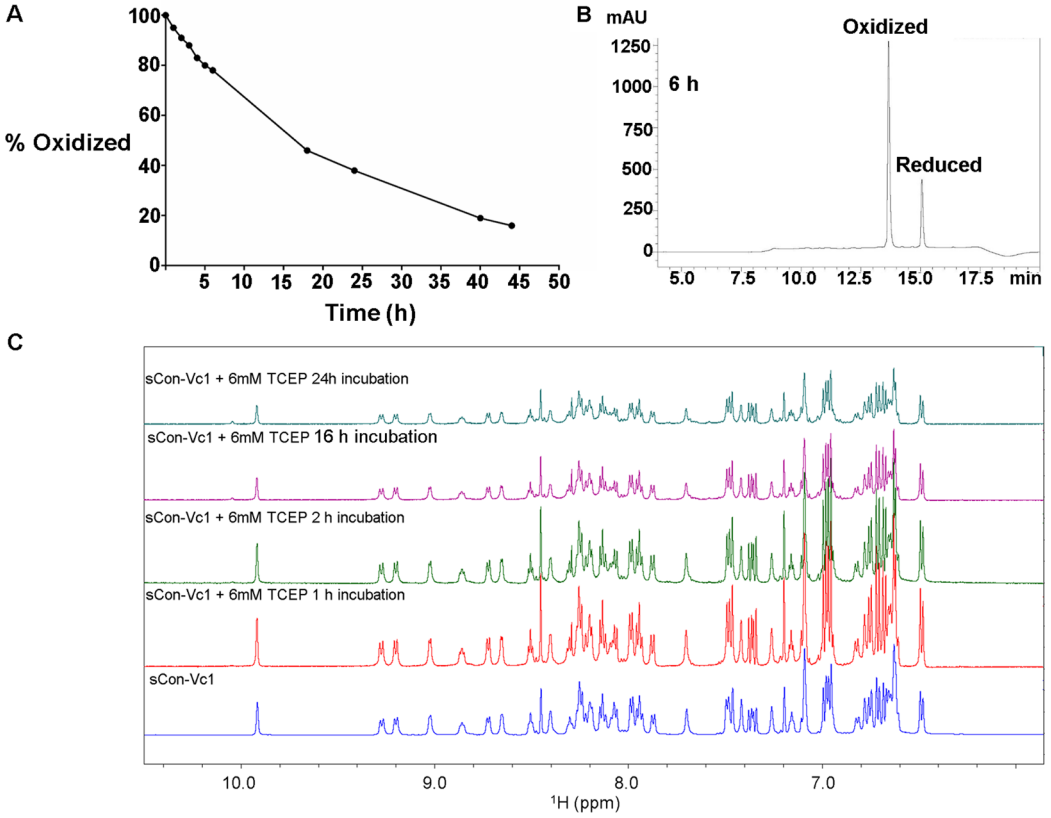

Figure 4. (A) Plot showing the percentage of oxidized species of sCon-Vc1 over the time course of 45 h in the presence of 10 mM TCEP at room temperature. (B) LC−MS chromatogram of sCon-Vc1 at the 6 h time point after incubation with 10 mM TCEP at room temperature, with observed mass differences for oxidized and reduced species of sCon-Vc1 marked. (C) Amide and aromatic regions of one-dimensional ^{1}H NMR spectra of sCon-Vc1 after incubation for 1 h, overnight, and for 24 h with 6 mM TCEP at pH 4.0 and 20 °C in water containing 7% ^2H_2O.

rCon-Vc1[Z1Q] is due to the N-terminal pyroglutamate modification). The pattern of cleavage with trypsin is expected because this protease cleaves the peptide chain mainly C-terminal to lysine and arginine (Figure 5, Figure S7, and Table S2). In contrast, trypsin did not degrade rCon-Vc1$_{1-22}$[Z1Q] over the observed time range (0.5, 1, 2, and 4 h) (Figure S7C) as the peptide has no tryptic cleavage site. In the presence of α-chymotrypsin, sCon-Vc1 showed accumulation of two major peaks in the LC−MS chromatogram with masses of 2221.5 and 1350.4 Da, which correspond to fragments 1−20 and 21−31, respectively (Figure S7A). Similarly, α-chymotrypsin digestion of rCon-Vc1[Z1Q] also showed accumulation of two major peaks with masses of 2238.6 and 1350.4 Da, also corresponding to fragments 1−20 and 21−31, respectively (Figure S7B). rCon-Vc1$_{1-22}$[Z1Q] in the presence of α-chymotrypsin shows accumulation of a single major peak with a mass of 2238.6 Da, which corresponds to fragment 1−20 in rCon-Vc1$_{1-22}$[Z1Q] (Figure 5, Figure S7C, and Table S2). Thus, the major cleavage site for α-chymotrypsin is Leu20 (Figure 5). In contrast, incubation for 1 h with pepsin resulted in significant digestion of sCon-Vc1, rCon-Vc1[Z1Q], and rCon-Vc1$_{1-22}$[Z1Q] (Figure S7).

Evaluation of a Single Disulfide-Directed β-Hairpin (SDH) Fold as an Acceptor Scaffold. To test whether the SDH fold can accommodate foreign peptide sequences, we replaced loop 1 or 2 of rCon-Vc1$_{1-22}$[Z1Q] with the DINNN motif of iNOS based on the structural similarity between this epitope bound to its target SPSB proteins and the part of the scaffold it was replacing (Figure 6A,B).[19−21] ^{1}H NMR spectra of both sCon-Vc1$_{1-22}$[Z1Q,DINNN$_{4-8}$] and sCon-Vc1$_{1-22}$[Z1Q,DINNN$_{12-16}$] showed a significant decrease in the level of peak dispersion compared to that of native rCon-Vc1$_{1-22}$[Z1Q], indicating that these peptides did not adopt the SDH fold (Figures S8 and S9). Somewhat surprisingly, however, both peptides bound to human SPSB2 with K_D values of 25 ± 8 and 5.7 ± 3 nM, respectively, comparable to the affinity of disulfide-cyclized CVDINNNC (Figure 6 and Table 3).[32] Because the majority of the direct interactions between the DINNN motif and SPSB2 are with the three Asn residues, we substituted loop 2 of sCon-Vc1$_{1-22}$ with just the NNN sequence.[21,33] ^{1}H NMR spectra of sCon-Vc1$_{1-22}$[NNN$_{12-14}$] showed good peak dispersion, and a comparison of backbone chemical shifts with those of sCon-Vc1$_{1-22}$ showed that the peptide maintained the native fold (Figures S8 and S9). The sCon-Vc1$_{1-22}$[NNN$_{12-14}$] peptide bound to the human SPSB2 protein with an affinity of 1.3 μM, which is almost 4-fold weaker than the affinity of the linear DINNN motif for the human SPSB2 protein. However, the binding affinity of sCon-Vc1$_{1-22}$[NNN$_{12-14}$] is almost 50-fold higher than that of the linear NNN epitope itself (Figure 6 and Table 3).

DISCUSSION

In this study, we have further characterized the stability of the SDH fold first described in contryphan-Vc1[19] and shown that it can be truncated without loss of ordered structure. Because the molecule is stabilized by just a single disulfide bridge, it was possible to obtain good expression in *E. coli*. We further established that the N-terminal pyroglutamate modification has

DOI: 10.1021/acs.biochem.7b00120
Biochemistry 2017, 56, 2455−2466

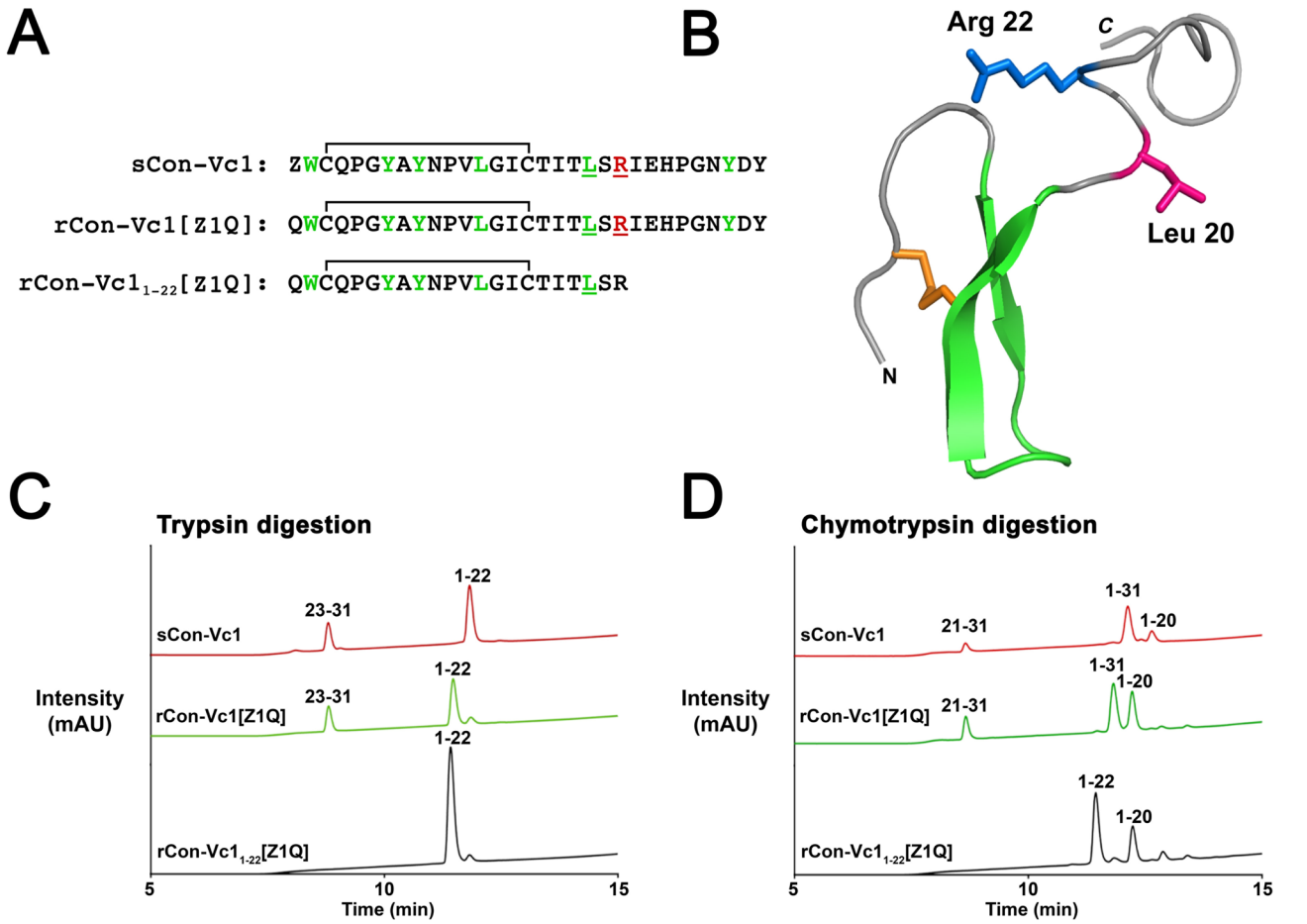

Figure 5. Reversed-phase HPLC analysis after treatment of sCon-Vc1, rCon-Vc1[Z1Q], and rCon-Vc11−22[Z1Q] with trypsin, α-chymotrypsin, and pepsin for 2 h. (A) Sequences of peptides sCon-Vc1, rCon-Vc1[Z1Q], and rCon-Vc1$_{1-22}$[Z1Q] used in the study with expected trypsin and α-chymotrypsin cleavage sites colored red and green, respectively, and the observed trypsin and α-chymotrypsin cleavage sites underlined with red and green lines, respectively. (B) Observed trypsin cleavage site Arg22 and α-chymotrypsin cleavage site Leu20 are mapped on the structure of full-length contryphan-Vc1. (C) Reversed-phase HPLC chromatogram for trypsin digestion of peptides sCon-Vc1, rCon-Vc1[Z1Q], and rCon-Vc1$_{1-22}$[Z1Q]. (D) Reversed-phase HPLC chromatogram for α-chymotrypsin digestion of peptides sCon-Vc1, rCon-Vc1[Z1Q], and rCon-Vc1$_{1-22}$[Z1Q].

a negligible effect on the core structure of the peptide, as monitored by NMR chemical shifts. Backbone ^{15}N relaxation data showed that residues Trp2−Ile18 adopt a well-defined, stable conformation. Residues beyond Thr19 showed either negative or zero ^{1}H−^{15}N NOE values and relatively lower R_1 and R_2 values, indicating that the region from residue 19 to 31 is highly disordered, with the flexibility increasing toward the C-terminus.

Contryphan-Vc1 exhibited remarkable thermal stability.[19] The secondary structure monitored by circular dichroism spectroscopy did not change even at 95 °C, and one-dimensional NMR spectra showed no change in peak dispersion up to 70 °C (the highest temperature examined).[19] To further assess the conformational stability of contryphan-Vc1, we investigated the effects of urea, pH, and reducing agents on its structure, as monitored by NMR. The peptide exhibited remarkable chemical stability in the presence of urea, showing <30% unfolding even at 7 M urea (Figure S4). Contryphan-Vc1 is also quite stable over a broad pH range, with one-dimensional NMR spectra showing no significant changes to the core structure between pH 2 and 8 (Figure S5).

One of the potential limitations of peptides having disulfide bridges as therapeutic leads is their redox stability. Most cellular compartments are reducing environments,[34] and in the circulation and extracellular space, thiol−disulfide exchange reactions[35] are performed by different members of the protein disulfide isomerase family.[36] Disulfide bridges are usually unstable in reducing environments and are susceptible to disulfide bond exchange reactions with biological thiols such as glutathione.[37,38] This can partially or completely inactivate peptides that have disulfide bridges,[39,40] rendering them more susceptible to proteolytic cleavage.[37] With less stable disulfide-cyclized peptides such as Ac-c[CVDINNNC]-NH$_2$,[41] which was shown to be reduced within 0.5 h,[41] and contryphan-Vc2[18] [used in this study (Figure S6)], 5 mM TCEP at pH 4 was sufficient to reduce these peptides within 1 h at room temperature. In contrast, to completely reduce a highly stable peptide such as sCon-Vc1, incubation with 10 mM TCEP (pH 4) for more than 2 days at room temperature was required, emphasizing the remarkable redox stability of contryphan-Vc1.

Both the calculated structures and the backbone relaxation parameters concur in showing that the N-terminal region of contryphan-Vc1 up to Thr19 adopts an ordered structure while the C-terminal region from residues Thr19−Tyr31 is flexible. To identify the minimal region sufficient to maintain the structure and to analyze the influence of the highly flexible C-terminus, a truncated variant of the peptide encompassing residues 1−22 was generated. Even though residues Thr19−

DOI: 10.1021/acs.biochem.7b00120
Biochemistry 2017, 56, 2455−2466

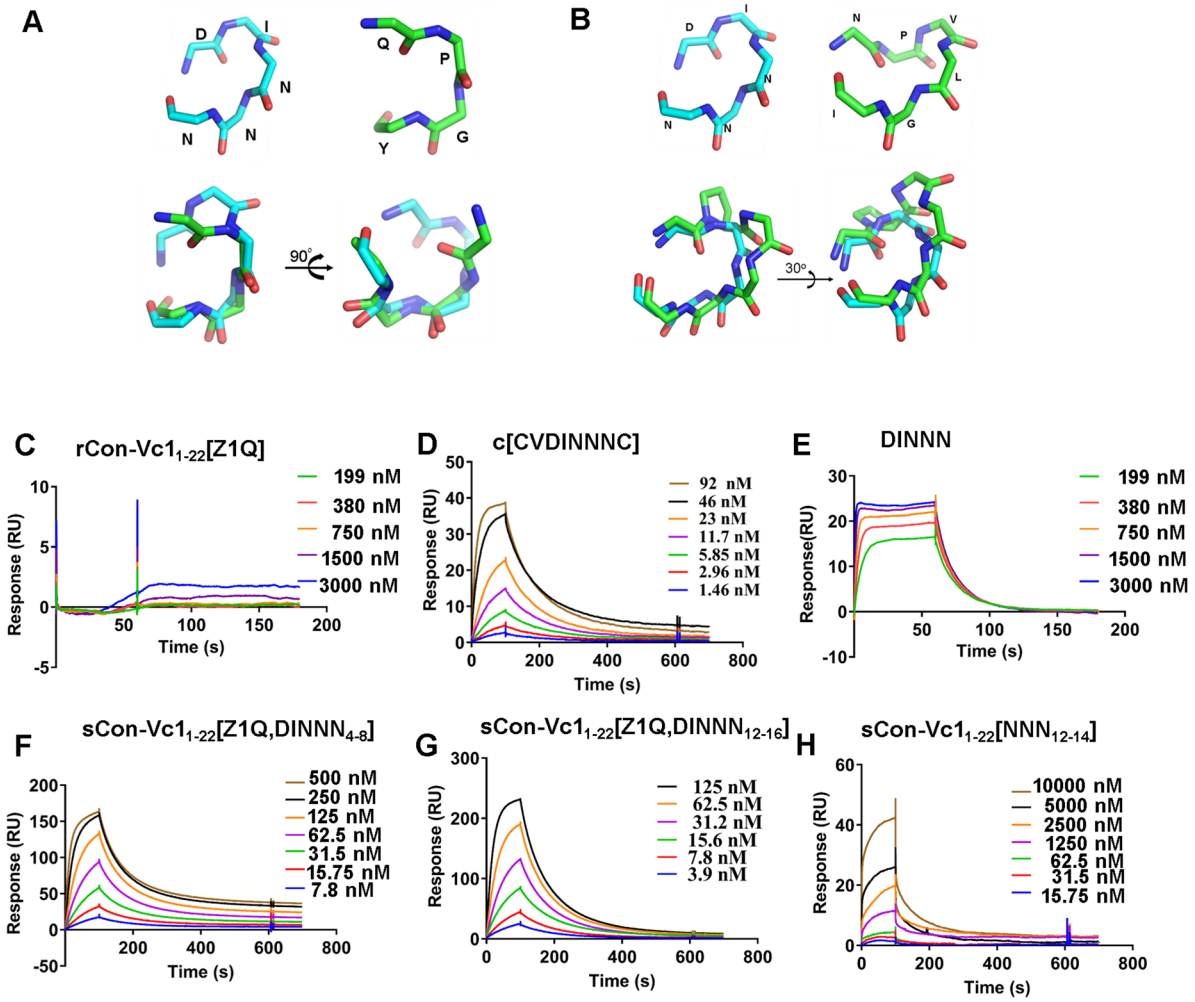

Figure 6. (A) PyMOL representation of the alignment of the DINNN motif (cyan) bound to SPSB2 (3EMW)[21] and loop 1 (QPGY) (green) of rCon-Vc11−22[Z1Q]. (B) PyMOL representation of the alignment of the DINNN motif (cyan) bound to SPSB2 (3EMW)[21] and loop 2 (PVLG) (green) of rCon-Vc1$_{1-22}$[Z1Q]. SPR sensorgrams of the interactions between immobilized human SPSB2 and the Vc1-DINNN analogues: (C) rCon-Vc1$_{1-22}$[Z1Q], (D) cystathionine-cyclized c[CVDINNNC], (E) linear DINNN, (F) sCon-Vc1$_{1-22}$[Z1Q,DINNN$_{4-8}$], (G) sCon-Vc1$_{1-22}$[Z1Q,DINNN$_{12-16}$], and (H) sCon-Vc1$_{1-22}$[NNN$_{12-14}$].

Table 3. Association Rates (k_a), Dissociation Rates (k_d), and Binding affinities (K_D) for the Vc1-DINNN Peptide Analogues and Controls

peptide	k_a (M^{-1} s^{-1})	k_d (s^{-1})	K_D (nM)
rCon-Vc1$_{1-22}$[Z1Q]	no binding	no binding	no binding
sCon-Vc1$_{1-22}$[NNN$_{12-14}$]	5.1×10^{-3}	0.007	1300
sCon-Vc1$_{1-22}$[Z1Q,DINNN$_{4-8}$]	7.9×10^{-5}	0.00064	25 ± 8
sCon-Vc1$_{1-22}$[Z1Q,DINNN$_{12-16}$]	5.7×10^{-5}	0.002695	5.7 ± 3
DINNN	1.1×10^{-6}	0.12	350
Ac-[CVDINNNC]	4.7×10^{-5}	0.0074	10
NNN[33]	*a*	*a*	74.6

[a]Association and dissociation rates were too rapid to be determined.

Arg22 are flexible, with negative or zero $^{1}H-^{15}N$ NOE values, truncation was performed at Arg22 with a view to retaining polar residues Thr19 and Ser21 and the charged Arg22, to maintain aqueous solubility. The structure of rCon-Vc1$_{1-22}$[Z1Q] revealed that the peptide retained its structure even after deletion of the C-terminal tail region (Figure 3).

A key attribute of a peptide scaffold is its resistance to proteolytic degradation.[42] Proteolysis of full-length contryphan-Vc1 with trypsin yielded a major cleavage product, corresponding to cleavage at Arg22. In contrast, the truncated peptide rCon-Vc1$_{1-22}$[Z1Q], which lacks the tryptic cleavage site, is highly resistant to trypsin cleavage. Both synthetic and recombinant contryphan-Vc1 full-length peptides showed two cleavage products upon digestion with chymotrypsin, indicating that these peptides are cleaved at a major cleavage site, identified as Leu20 (Figure 5). Cleavage of rCon-Vc1$_{1-22}$[Z1Q] with chymotrypsin yielded a single major cleavage product corresponding to fragment 1−20. Observation of a single cleavage site for contryphan-Vc1, even though there are several residues in the core β-sheet structure that can serve as cleavage sites for chymotrypsin, indicates that this structure imparts resistance to proteolysis. In contrast, both full-length and truncated peptides were found to be susceptible to pepsin cleavage, with both peptides being digested completely by this protease.

Even some peptides with the highly stable ICK fold and multiple disulfide bonds are susceptible to proteolytic degradation. Derivatives of Agouti-related protein and two squash protease inhibitors were stable to pepsin and elastase but were extensively degraded by trypsin and chymotrypsin.[43]

DOI: 10.1021/acs.biochem.7b00120
Biochemistry 2017, 56, 2455−2466

Similarly constrained peptides, including ω-conotoxin MVIIA and a hybrid of two squash trypsin inhibitors (EETI-II and MCoTI-II), were degraded by trypsin and chymotrypsin.[44,45] Multiple strategies for increasing the proteolytic stability of the peptides are emerging, including backbone cyclization,[46,47] where the N- and C-termini of the linear peptide are linked using peptide coupling agents.[48] Depending on the target of an engineered analogue of contryphan-Vc1, individual residues that are sites of proteolysis, for example, Leu20 in the case of chymotrypsin, could be replaced to enhance resistance.

To assess the capacity of the SDH fold to incorporate foreign peptide sequences and present them in a functional manner, the loops in the core structure of contryphan-Vc1 were replaced with a five-residue DINNN epitope from iNOS that interacts with SPSB proteins and mediates its proteolytic degradation.[21,49] In the sCon-Vc1$_{1-22}$[Z1Q,DINNN$_{4-8}$] analogue, the four residues comprising loop 1 of rCon-Vc1$_{1-22}$[Z1Q] (QPGY) were replaced by the DINNN motif, while the three residues in loop 2 (VLG) were substituted with the DINNN motif in the sCon-Vc1$_{1-22}$[Z1Q,DINNN$_{12-16}$] analogue. Proline is preferred at some positions of β-turns and has been shown to increase their stability;[50,51] hence, Pro11 was retained in sCon-Vc1$_{1-22}$[Z1Q,DINNN$_{12-16}$]. Even though both Vc1-DINNN analogues bound to SPSB2 with affinities of 25 ± 8 and 5.7 ± 3 nM, respectively (Figure 6), ^{1}H NMR spectra of both peptides showed poor peak dispersion, indicating that substituting loop 1 and loop 2 residues with the entire DINNN motif disrupted the native fold (Figures S8 and S9). While this indicates that there are limitations on the sequence variation that can be accommodated in either of these loops, the retention of the high binding affinity for SPSB2 implies that the incorporated DINNN sequences can adopt a conformation that is recognized by SPSB2 even as part of this larger, partially constrained peptide.[21]

In an effort to maintain the structure of the turn in the β-hairpin, we replaced the VLG residues of loop 2 with a shorter three-residue NNN epitope, noting that the majority of the direct contacts with SPSB2 are mediated by the three Asn residues.[33] The sCon-Vc1$_{1-22}$[NNN$_{12-14}$] analogue bound to human SPSB2 with an affinity of 1.3 μM, which is almost 50-fold stronger than that of the linear NNN epitope itself (Figure 6 and Table 3).[33] Moreover, ^{1}H NMR spectra of this analogue showed good peak dispersion and native-like chemical shifts, indicating that the native fold was maintained. The binding affinity for SPSB2 implies that the NNN motif is constrained appropriately for binding to SPSB2, but the absence of the Asp residue of the original DINNN motif precludes tighter binding.

In the study presented here, important structural, dynamic, and stability properties of the recently discovered contryphan-Vc1 have been evaluated. Contryphan-Vc1 offers a significant advantage in that it contains just a single disulfide bond, while exhibiting remarkable thermal, redox, and chemical stability and reasonable proteolytic stability. Contryphan-Vc1 can accept the NNN sequence without compromising the core structure of the peptide, although more substantial insertions did affect the structure. Further exploration of the capacity of rCon-Vc1$_{1-22}$[Z1Q] to accommodate other functional epitopes is clearly warranted.

■ ASSOCIATED CONTENT

Supporting Information

The Supporting Information is available free of charge on the ACS Publications website at DOI: 10.1021/acs.biochem.7b00120.

Chemical shifts for truncated contryphan-Vc1 (rCon-Vc1$_{1-22}$[Z1Q]) at pH 3.9 and 293 K (Table S1), fragments and their masses observed after proteolytic digestion of sCon-Vc1, rCon-Vc1[Z1Q], and rCon-Vc1$_{1-22}$[Z1Q] with the enzymes trypsin and α-chymotrypsin (Table S2), RP-HPLC chromatogram and ESI-MS results of the sCon-Vc1 peptide (Figure S1), LC−MS profile of recombinant full-length contryphan-Vc1 and rCon-Vc1$_{1-22}$[Z1Q] (Figure S2), LC−MS profile of contryphan-Vc1 analogues (Figure S3), one-dimensional ^{1}H NMR spectra of synthetic full-length contryphan-Vc1 titrated with increasing concentrations of urea and the urea unfolding curve for the Trp2 indole proton peak of sCon-Vc1 (Figure S4), one-dimensional ^{1}H NMR spectra of synthetic full-length contryphan-Vc1 over the pH range of 2−9 (Figure S5), LC−MS chromatograms, ^{1}H NMR spectra, and ^{13}C HSQC spectra of sCon-Vc1 incubated with TCEP (Figure S6), reversed-phase HPLC analysis after treatment of synthetic, recombinant full-length contryphan-Vc1 and rCon-Vc1$_{1-22}$[Z1Q] with trypsin, α-chymotrypsin, and pepsin (Figure S7), one-dimensional ^{1}H NMR spectra of rCon-Vc1$_{1-22}$[Z1Q], sCon-Vc1$_{1-22}$[NNN$_{12-14}$], sCon-Vc1$_{1-22}$[Z1Q,DINNN$_{4-8}$], and sCon-Vc1$_{1-22}$[Z1Q,DINNN$_{12-16}$] (Figure S8), and plots of the deviation of the chemical shifts from random coil values for Vc1$_{1-22}$[Z1Q,DINNN4$_{-8}$] and sCon-Vc1$_{1-22}$[NNN$_{12-14}$] (Figure S9) (PDF)

■ AUTHOR INFORMATION

Corresponding Author

*Medicinal Chemistry, Monash Institute of Pharmaceutical Sciences, Monash University, 381 Royal Parade, Parkville 3052, Australia. Telephone: (+61 3) 9903 9167. E-mail: ray.norton@monash.edu.

ORCID

Balasubramanyam Chittoor: 0000-0001-5460-4537
Raymond S. Norton: 0000-0001-8893-0584

Present Address

§S.D.R.: Department of Biology, University of Utah, Salt Lake City, UT 84112.

Funding

R.S.N. acknowledges fellowship support from the National Health and Medical Research Council of Australia. B.C. is supported by a Faculty of Pharmacy and Pharmaceutical Sciences Scholarship, and M.S. is supported by a Monash Graduate Scholarship.

Notes

The authors declare no competing financial interest.

■ ACKNOWLEDGMENTS

We thank Dr. Biswarajan Mohanty (Monash Institute of Pharmaceutical Sciences, Monash University) for helpful discussions regarding NMR relaxation studies.

DOI: 10.1021/acs.biochem.7b00120
Biochemistry 2017, 56, 2455−2466

ABBREVIATIONS

HSQC, heteronuclear single-quantum coherence; ICK, inhibitor cystine knot; NMR, nuclear magnetic resonance; NOE, nuclear Overhauser effect; RMSD, root-mean-square deviation; rCon-Vc1[Z1Q], recombinant contryphan-Vc1; rCon-$Vc1_{1-22}$[Z1Q], recombinant truncated contryphan-Vc1; RP-HPLC, reversed-phase high-performance liquid chromatography; RMSD, root-mean-square deviation; sCon-Vc1, synthetic contryphan-Vc1; TCEP, tris(2-carboxyethyl)phosphine.

REFERENCES

(1) Wang, C. K., Gruber, C. W., Cemazar, M., Siatskas, C., Tagore, P., Payne, N., Sun, G., Wang, S., Bernard, C. C., and Craik, D. J. (2014) Molecular grafting onto a stable framework yields novel cyclic peptides for the treatment of multiple sclerosis. *ACS Chem. Biol. 9*, 156−163.

(2) Kimura, R. H., Cheng, Z., Gambhir, S. S., and Cochran, J. R. (2009) Engineered knottin peptides: a new class of agents for imaging integrin expression in living subjects. *Cancer Res. 69*, 2435−2442.

(3) Kimura, R. H., Miao, Z., Cheng, Z., Gambhir, S. S., and Cochran, J. R. (2010) A dual-labeled knottin peptide for PET and near-infrared fluorescence imaging of integrin expression in living subjects. *Bioconjugate Chem. 21*, 436−444.

(4) Miao, Z., Ren, G., Liu, H., Kimura, R. H., Jiang, L., Cochran, J. R., Gambhir, S. S., and Cheng, Z. (2009) An engineered knottin peptide labeled with ^{18}F for PET imaging of integrin expression. *Bioconjugate Chem. 20*, 2342−2347.

(5) Terlau, H., and Olivera, B. M. (2004) Conus venoms: a rich source of novel ion channel-targeted peptides. *Physiol. Rev. 84*, 41−68.

(6) Vita, C., Vizzavona, J., Drakopoulou, E., Zinn-Justin, S., Gilquin, B., and Ménez, A. (1998) Novel miniproteins engineered by the transfer of active sites to small natural scaffolds. *Biopolymers 47*, 93−100.

(7) Wong, C. T., Rowlands, D. K., Wong, C. H., Lo, T. W., Nguyen, G. K., Li, H. Y., and Tam, J. P. (2012) Orally active peptidic bradykinin B1 receptor antagonists engineered from a cyclotide scaffold for inflammatory pain treatment. *Angew. Chem., Int. Ed. 51*, 5620−5624.

(8) Pallaghy, P. K., Nielsen, K. J., Craik, D. J., and Norton, R. S. (1994) A common structural motif incorporating a cystine knot and a triple-stranded β-sheet in toxic and inhibitory polypeptides. *Protein Sci. 3*, 1833−1839.

(9) Norton, R. S., and Pallaghy, P. K. (1998) The cystine knot structure of ion channel toxins and related polypeptides. *Toxicon 36*, 1573−1583.

(10) Craik, D. J., Daly, N. L., and Waine, C. (2001) The cystine knot motif in toxins and implications for drug design. *Toxicon 39*, 43−60.

(11) Norton, R. S., and McDonough, S. I. (2008) Peptides targeting voltage-gated calcium channels. *Curr. Pharm. Des. 14*, 2480−2491.

(12) Moore, S. J., Leung, C. L., Norton, H. K., and Cochran, J. R. (2013) Engineering agatoxin, a cystine-knot peptide from spider venom, as a molecular probe for *in vivo* tumor imaging. *PLoS One 8*, e60498.

(13) Jiang, H., Moore, S. J., Liu, S., Liu, H., Miao, Z., Cochran, F. V., Liu, Y., Tian, M., Cochran, J. R., Zhang, H., and Cheng, Z. (2013) A novel radiofluorinated agouti-related protein for tumor angiogenesis imaging. *Amino Acids 44*, 673−681.

(14) Hannig, G., and Makrides, S. C. (1998) Strategies for optimizing heterologous protein expression in *Escherichia coli*. *Trends Biotechnol. 16*, 54−60.

(15) Klint, J. K., Senff, S., Saez, N. J., Seshadri, R., Lau, H. Y., Bende, N. S., Undheim, E. A., Rash, L. D., Mobli, M., and King, G. F. (2013) Production of recombinant disulfide-rich venom peptides for structural and functional analysis via expression in the periplasm of *E. coli*. *PLoS One 8*, e63865.

(16) Salinas, G., Pellizza, L., Margenat, M., Fló, M., and Fernández, C. (2011) Tuned *Escherichia coli* as a host for the expression of disulfide-rich proteins. *Biotechnol. J. 6*, 686−699.

(17) Robinson, S. D., and Norton, R. S. (2014) Conotoxin gene superfamilies. *Mar. Drugs 12*, 6058−6101.

(18) Robinson, S. D., Safavi-Hemami, H., McIntosh, L. D., Purcell, A. W., Norton, R. S., and Papenfuss, A. T. (2014) Diversity of conotoxin gene superfamilies in the venomous snail, *Conus victoriae*. *PLoS One 9*, e87648.

(19) Robinson, S. D., Chhabra, S., Belgi, A., Chittoor, B., Safavi-Hemami, H., Robinson, A. J., Papenfuss, A. T., Purcell, A. W., and Norton, R. S. (2016) A naturally occurring peptide with an elementary single disulfide-directed β-hairpin fold. *Structure 24*, 293−299.

(20) Kuang, Z., Lewis, R. S., Curtis, J. M., Zhan, Y., Saunders, B. M., Babon, J. J., Kolesnik, T. B., Low, A., Masters, S. L., Willson, T. A., Kedzierski, L., Yao, S., Handman, E., Norton, R. S., and Nicholson, S. E. (2010) The SPRY domain-containing SOCS box protein SPSB2 targets iNOS for proteasomal degradation. *J. Cell Biol. 190*, 129−141.

(21) Filippakopoulos, P., Low, A., Sharpe, T. D., Uppenberg, J., Yao, S., Kuang, Z., Savitsky, P., Lewis, R. S., Nicholson, S. E., Norton, R. S., and Bullock, A. N. (2010) Structural basis for Par-4 recognition by the SPRY domain- and SOCS box-containing proteins SPSB1, SPSB2, and SPSB4. *J. Mol. Biol. 401*, 389−402.

(22) Lewis, R. S., Kolesnik, T. B., Kuang, Z., D'Cruz, A. A., Blewitt, M. E., Masters, S. L., Low, A., Willson, T., Norton, R. S., and Nicholson, S. E. (2011) TLR regulation of SPSB1 controls inducible nitric oxide synthase induction. *J. Immunol. 187*, 3798−3805.

(23) Shaka, A., Lee, C., and Pines, A. (1988) Iterative schemes for bilinear operators; application to spin decoupling. *J. Magn. Reson. 77*, 274−293.

(24) Hwang, T.-L., and Shaka, A. (1995) Water suppression that works. Excitation sculpting using arbitrary wave-forms and pulsed-field gradients. *J. Magn. Reson., Ser. A 112*, 275−279.

(25) Vranken, W. F., Boucher, W., Stevens, T. J., Fogh, R. H., Pajon, A., Llinas, M., Ulrich, E. L., Markley, J. L., Ionides, J., and Laue, E. D. (2005) The CCPN data model for NMR spectroscopy: development of a software pipeline. *Proteins: Struct., Funct., Genet. 59*, 687−696.

(26) Ulrich, E. L., Akutsu, H., Doreleijers, J. F., Harano, Y., Ioannidis, Y. E., Lin, J., Livny, M., Mading, S., Maziuk, D., Miller, Z., Nakatani, E., Schulte, C. F., Tolmie, D. E., Kent Wenger, R., Yao, H., and Markley, J. L. (2008) BioMagResBank. *Nucleic Acids Res. 36*, D402−D408.

(27) Güntert, P. (2004) Automated NMR structure calculation with CYANA. *Protein NMR Techniques 278*, 353−378.

(28) Schwieters, C. D., Kuszewski, J. J., Tjandra, N., and Marius Clore, G. (2003) The Xplor-NIH NMR molecular structure determination package. *J. Magn. Reson. 160*, 65−73.

(29) Koradi, R., Billeter, M., and Wuthrich, K. (1996) MOLMOL: a program for display and analysis of macromolecular structures. *J. Mol. Graphics 14*, 51−55.

(30) Keller, R. L. J. (2005) Optimizing the process of nuclear magnetic resonance spectrum analysis and computer aided resonance assignment. Ph.D. Thesis, ETH, Zurich.

(31) Wishart, D. S., Bigam, C. G., Holm, A., Hodges, R. S., and Sykes, B. D. (1995) ^{1}H, ^{13}C and ^{15}N random coil NMR chemical shifts of the common amino acids. I. Investigations of nearest-neighbor effects. *J. Biomol. NMR 5*, 67−81.

(32) Yap, B. K., Leung, E. W., Yagi, H., Galea, C. A., Chhabra, S., Chalmers, D. K., Nicholson, S. E., Thompson, P. E., and Norton, R. S. (2014) A potent cyclic peptide targeting SPSB2 protein as a potential anti-infective agent. *J. Med. Chem. 57*, 7006−7015.

(33) Leung, E. W. W., Mulcair, M. D., Yap, B. K., Nicholson, S. E., Scanlon, M. J., and Norton, R. S. (2017) Molecular insights into the interaction between the SPRY domain-containing SOCS box protein SPSB2 and peptides based on the binding motif from iNOS. *Aust. J. Chem. 70*, 191−200.

(34) Go, Y. M., and Jones, D. P. (2008) Redox compartmentalization in eukaryotic cells. *Biochim. Biophys. Acta, Gen. Subj. 1780*, 1273−1290.

(35) Kozlov, G., Määttänen, P., Thomas, D. Y., and Gehring, K. (2010) A structural overview of the PDI family of proteins. *FEBS J. 277*, 3924−3936.

DOI: 10.1021/acs.biochem.7b00120
Biochemistry 2017, 56, 2455−2466

(36) Butera, D., Cook, K. M., Chiu, J., Wong, J. W. H., and Hogg, P. J. (2014) Control of blood proteins by functional disulfide bonds. *Blood 123*, 2000−2007.
(37) Armishaw, C. J., Daly, N. L., Nevin, S. T., Adams, D. J., Craik, D. J., and Alewood, P. F. (2006) α-Selenoconotoxins, a new class of potent α7 neuronal nicotinic receptor antagonists. *J. Biol. Chem. 281*, 14136−14143.
(38) Aslund, F., and Beckwith, J. (1999) Bridge over troubled waters: sensing stress by disulfide bond formation. *Cell 96*, 751−753.
(39) Pennington, M. W., Lanigan, M. D., Kalman, K., Mahnir, V. M., Rauer, H., McVaugh, C. T., Behm, D., Donaldson, D., Chandy, K. G., Kem, W. R., and Norton, R. S. (1999) Role of disulfide bonds in the structure and potassium channel blocking activity of ShK toxin. *Biochemistry 38*, 14549−14558.
(40) Flinn, J. P., Pallaghy, P. K., Lew, M. J., Murphy, R., Angus, J. A., and Norton, R. S. (1999) Role of disulfide bridges in the folding, structure and biological activity of ω-conotoxin GVIA1. *Biochim. Biophys. Acta, Protein Struct. Mol. Enzymol. 1434*, 177−190.
(41) Yap, B. K., Harjani, J. R., Leung, E. W. W., Nicholson, S. E., Scanlon, M. J., Chalmers, D. K., Thompson, P. E., Baell, J. B., and Norton, R. S. (2016) Redox-stable cyclic peptide inhibitors of the SPSB2−iNOS interaction. *FEBS Lett. 590*, 696−704.
(42) Craik, D. J., Fairlie, D. P., Liras, S., and Price, D. (2013) The future of peptide-based drugs. *Chem. Biol. Drug Des. 81*, 136−147.
(43) Werle, M., Schmitz, T., Huang, H. L., Wentzel, A., Kolmar, H., and Bernkop-Schnurch, A. (2006) The potential of cystine-knot microproteins as novel pharmacophoric scaffolds in oral peptide drug delivery. *J. Drug Target 14*, 137−146.
(44) Zheng, K., Lubman, D. M., Rossi, D. T., Nordblom, G. D., and Barksdale, C. M. (2000) Elucidation of peptide metabolism by on-line immunoaffinity liquid chromatography mass spectrometry. *Rapid Commun. Mass Spectrom. 14*, 261−269.
(45) Werle, M., Kafedjiiski, K., Kolmar, H., and Bernkop-Schnurch, A. (2007) Evaluation and improvement of the properties of the novel cystine-knot microprotein McoEeTI for oral administration. *Int. J. Pharm. 332*, 72−79.
(46) Borchardt, R. T. (1999) Optimizing oral absorption of peptides using prodrug strategies. *J. Controlled Release 62*, 231−238.
(47) Li, P., and Roller, P. P. (2002) Cyclization strategies in peptide derived drug design. *Curr. Top. Med. Chem. 2*, 325−341.
(48) Clark, R. J., Fischer, H., Dempster, L., Daly, N. L., Rosengren, K. J., Nevin, S. T., Meunier, F. A., Adams, D. J., and Craik, D. J. (2005) Engineering stable peptide toxins by means of backbone cyclization: stabilization of the α-conotoxin MII. *Proc. Natl. Acad. Sci. U. S. A. 102*, 13767−13772.
(49) Kuang, Z., Lewis, R. S., Curtis, J. M., Zhan, Y., Saunders, B. M., Babon, J. J., Kolesnik, T. B., Low, A., Masters, S. L., Willson, T. A., Kedzierski, L., Yao, S., Handman, E., Norton, R. S., and Nicholson, S. E. (2010) The SPRY domain−containing SOCS box protein SPSB2 targets iNOS for proteasomal degradation. *J. Cell Biol. 190*, 129−141.
(50) Fu, H., Grimsley, G. R., Razvi, A., Scholtz, J. M., and Pace, C. N. (2009) Increasing protein stability by improving β-turns. *Proteins: Struct., Funct., Genet. 77*, 491−498.
(51) Watanabe, K., Masuda, T., Ohashi, H., Mihara, H., and Suzuki, Y. (1994) Multiple proline substitutions cumulatively thermostabilize *Bacillus cereus* ATCC7064 oligo-1,6-glucosidase. *Eur. J. Biochem. 226*, 277−283.

DOI: 10.1021/acs.biochem.7b00120
Biochemistry 2017, 56, 2455−2466

SUPPLEMENTARY INFORMATION

The Single Disulfide-Directed β-Hairpin Fold. Dynamics, Stability and Engineering

Balasubramanyam Chittoor[1], Bankala Krishnarjuna[1], Rodrigo A. V. Morales[1], Christopher A. MacRaild[1], Maiada Sadek[1], Eleanor W. W. Leung[1], Samuel D. Robinson[1#], Michael W. Pennington[2] and Raymond S. Norton[1*]

[1] Medicinal Chemistry, Monash Institute of Pharmaceutical Sciences, Monash University, Parkville, Victoria 3052, Australia.
[2] Peptides International, Louisville, Kentucky 40299

Current address: Department of Biology, University of Utah, Salt Lake City, UT 84112, USA.

* Corresponding Author: E-mail: ray.norton@monash.edu

Table S1. Chemical shifts for truncated contryphan-Vc1 (rCon-Vc1$_{1-22}$[Z1Q]) at pH 3.9, 293K

Residue	H^N	H^α	H^β	N	C^α	C^β	other
Gln1	NA	3.8	1.53,1.65	NA	52.6	27.1	H^γ 2.07, H^ε 6.91
Trp2	8.75	4.5	3.17	125.9	58.4	30.0	H^δ1 7.23; H^ε1 10.01; H^ε3 7.43; H^ζ2 7.43; H^ζ3 7.04,7.45; H^η2 7.20
Cys3	7.8	4.69	2.92,2.39	121.3	51.8	42.1	
Gln4	8.65	4.04	1.96,1.77	121.4	54.5	27.2	H^γ 2.17,2.05 H^ε 6.72,7.12
Pro5	-	4.37	2.37,1.91	-	64.6	31.7	H^γ 2.08, 2.20; H^δ 3.69, 3.83
Gly6	8.9	4.35,3.62	-	112.3	45.1		
Tyr7	8.31	5.05	3.35,2.39	120.1	56.4	41.6	H^δ 6.70; H^ε 6.69
Ala8	9.25	4.65	1.35	121.3	51.1	22.3	
Tyr9	9.08	4.31	2.80,3.02	124.6	59.7	39.1	H^δ 6.85; H^ε 6.57
Asn10	8.17	5.08	3.00,2.80	128.5	49.3	39.5	H^δ2 7.36, 7.76
Pro11	-	4.03	2.41	-	64.1	32.3	H^γ 2.05, 2.11; H^δ 3.90
Val12	7.57	3.75	2.11	119.5	65.4	32.1	H^γa 0.90; H^γb 1.00
Leu13	6.95	4.28	1.29	116.7	54.8	44.2	H^γ 1.52 H^δa 0.82; H^δb 0.86
Gly14	8.4	3.96,3.73	-	108.5	46.3		

Ile15	6.77	4.85	1.91	109.8	57.5	42.2	$H^{\gamma}1$ 1.172; $H^{\gamma}2$ 0.89; $H^{\delta}1$ 0.82
Cys16	8.86	5.15	3.10,2.77	120.8	56.2	42.9	
Thr17	9.35	4.85	4.28	116.6		71.6	$H^{\gamma}2$ 1.20
Ile18	8.42	3.43	1.3	124.5	62.2	38.9	$H^{\gamma}1$ 0.79, 1.06; $H^{\gamma}2$ 0.69; $H^{\delta}1$ 0.67
Thr19	8.19	4.29	3.96	121.3	61.7	69.6	$H^{\gamma}2$ 1.07
Leu20	8.31	4.38	-	126.2	54.9	42.6	H^{γ} 1.59; $H^{\delta}a$ 0.83; $H^{\delta}b$ 0.90
Ser21	8.33	4.42	3.83	117.8	58.3	63.8	
Arg22	8.06	4.21	1.72,1.86	127.6	57.4	31.5	H^{γ} 1.58; H^{δ} 3.18; H^{ε} 7.18

30124 - BMRB accession number for the chemical shifts of rCon-Vc1$_{1-22}$[Z1Q]

Table S2. Fragments and their masses observed after proteolytic digestion of sCon-Vc1, rCon-Vc1[Z1Q] and rCon-Vc1$_{1-22}$[Z1Q] with the enzymes trypsin and α-chymotrypsin.

Peptide	Fragment sequence	[1]MH+1 (calculated)	[1]MH+1 (observed)
sCon-Vc1 1-31	ZWCQPGYAYNPVLGICTITLSRIEHPGNYDY	3554.7	3554.6
sCon-Vc1 1-22	ZWCQPGYAYNPVLGICTITLSR	2466.2	2464.8
sCon-Vc1 23-31	IEHPGNYDY	1107.5	1107.1
sCon-Vc1 1-20	ZWCQPGYAYNPVLGICTITL	2221.1	2224
sCon-Vc1 21-31	SRIEHPGNYDY	1350.4	1350.4
rCon-Vc1[Z1Q]1-31	QWCQPGYAYNPVLGICTITLSRIEHPGNYDY	3573	3573
rCon-Vc1[Z1Q]1-22	QWCQPGYAYNPVLGICTITLSR	2481.9	2482.2
rCon-Vc1[Z1Q] 23-31	IEHPGNYDY	1107.1	1107.1
rCon-Vc1[Z1Q]1-20	QWCQPGYAYNPVLGICTITL	2238.6	2240
rCon-Vc1[Z1Q] 21-31	SRIEHPGNYDY	1350.4	1350.4
rCon-Vc1$_{1-22}$[Z1Q]	QWCQPGYAYNPVLGICTITLSR	2481.9	2482.2
rCon-Vc1$_{1-22}$[Z1Q]	QWCQPGYAYNPVLGICTITL	2238.6	2240

[1] Mono Isotopic mass

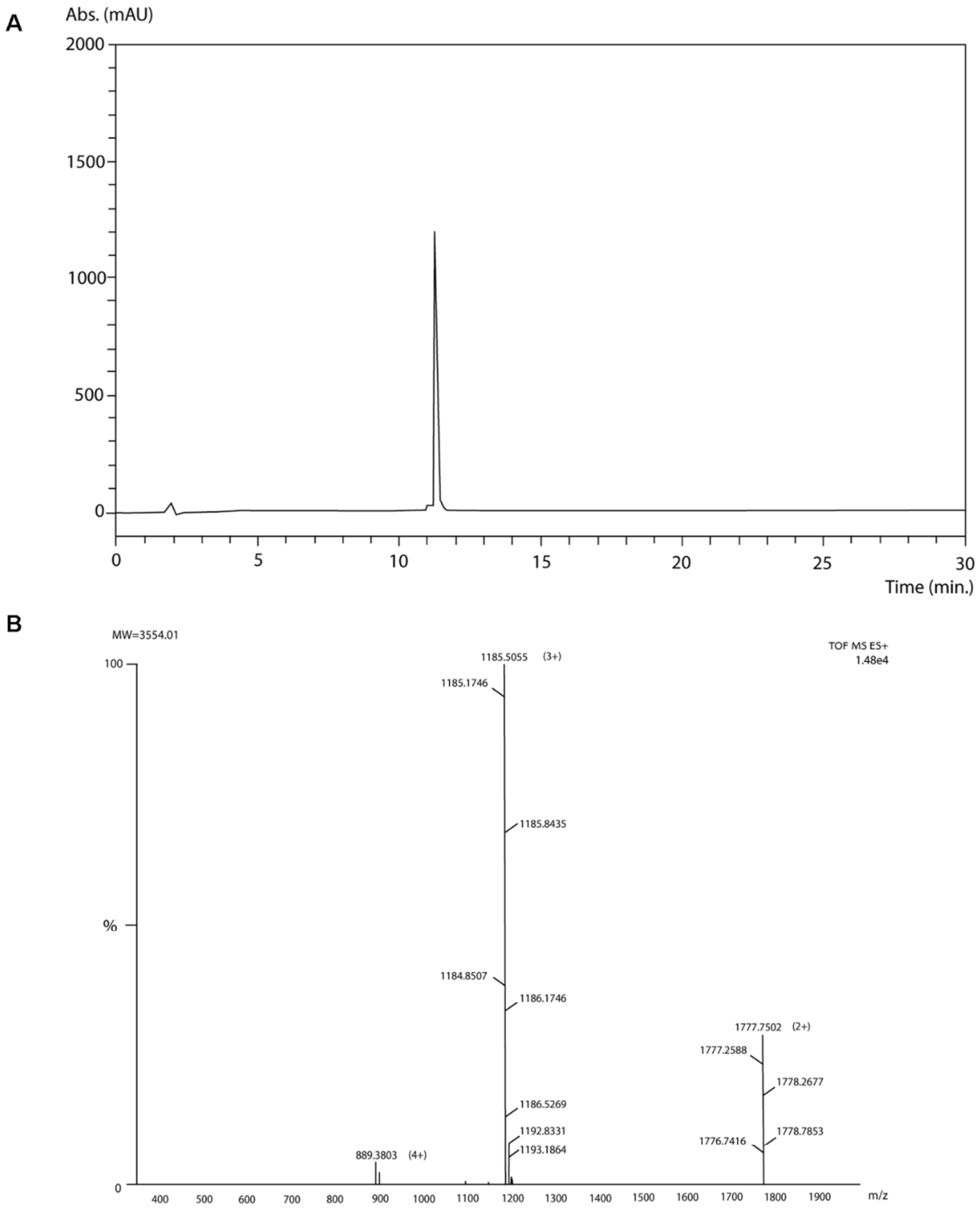

Figure S1. A. RP-HPLC chromatogram of sCon-Vc1 using an ODS-silica column gradient from 10-70% B in 30 min at 1 mL/min. Absorbance at 220 nm. **B.** ESI-MS results for purified sCon-Vc1 peptide. Molecular ion peaks of MH^{+2}, MH^{+3} and MH^{+4}, indicating a molecular mass of 3554.01.

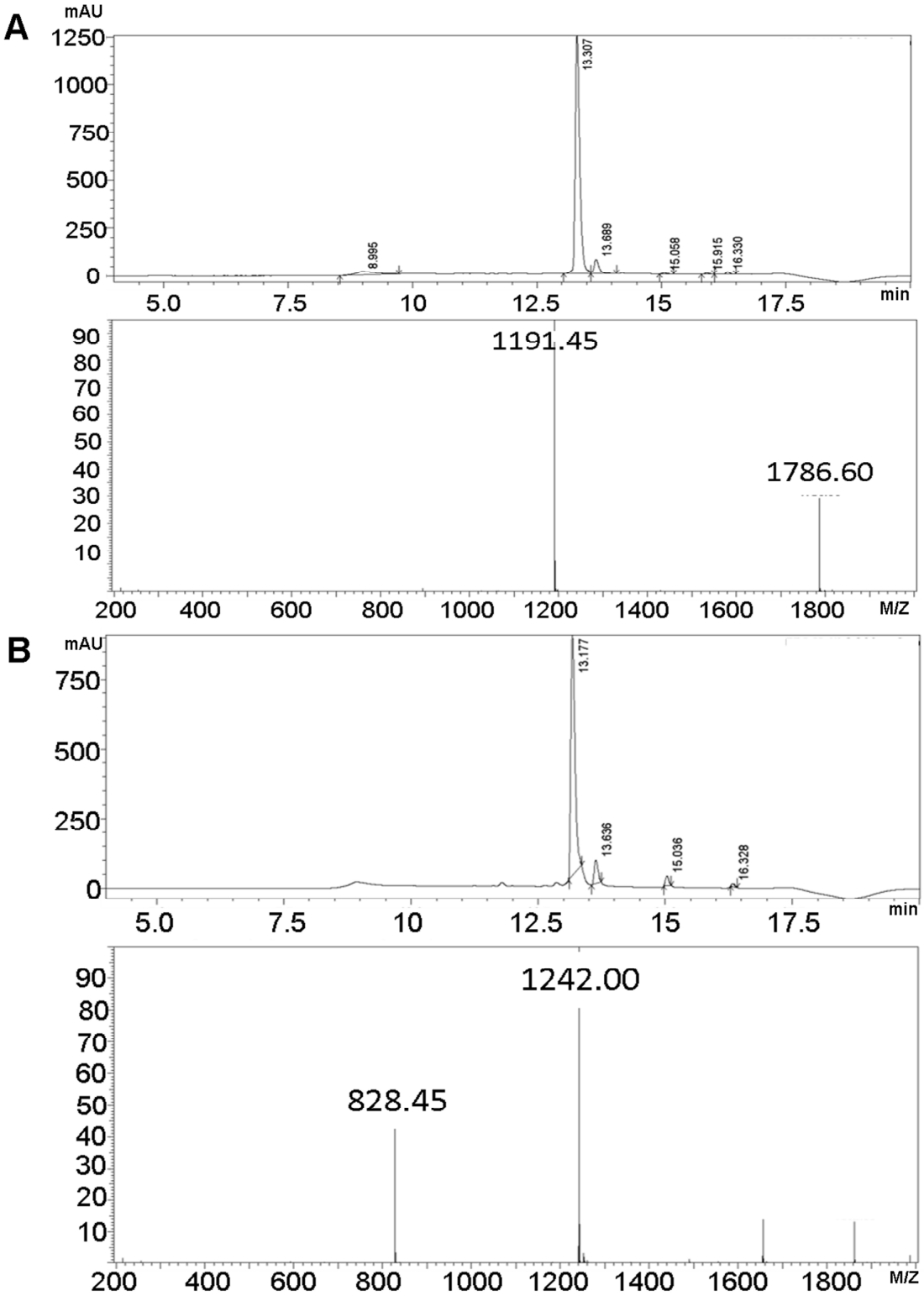

Figure S2. A. LC-MS profile of recombinant full-length contryphan-Vc1. **B.** LC-MS profile of recombinant rCon-Vc1$_{1\text{-}22}$[Z1Q].

A

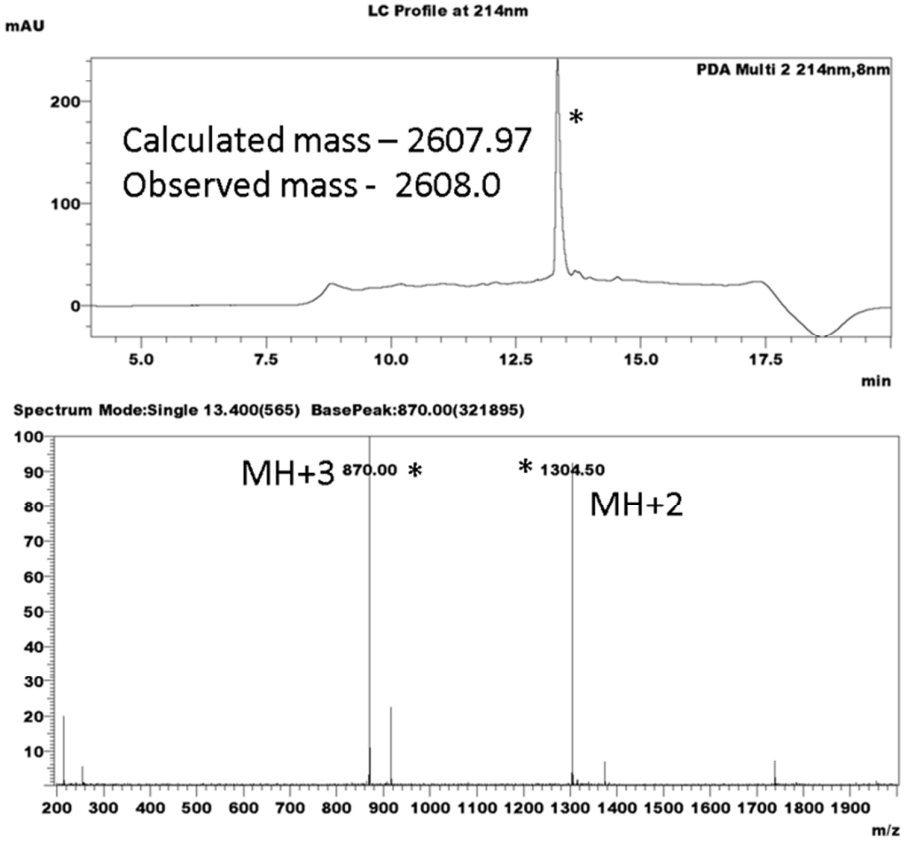
LC Profile at 214nm
mAU
PDA Multi 2 214nm,8nm
Calculated mass – 2607.97
Observed mass - 2608.0
*
200
100
0
5.0
7.5
10.0
12.5
15.0
17.5
min
Spectrum Mode:Single 13.400(565) BasePeak:870.00(321895)
MH+3 870.00 *
* 1304.50
MH+2
100
90
80
70
60
50
40
30
20
10
200 300 400 500 600 700 800 900 1000 1100 1200 1300 1400 1500 1600 1700 1800 1900
m/z

B

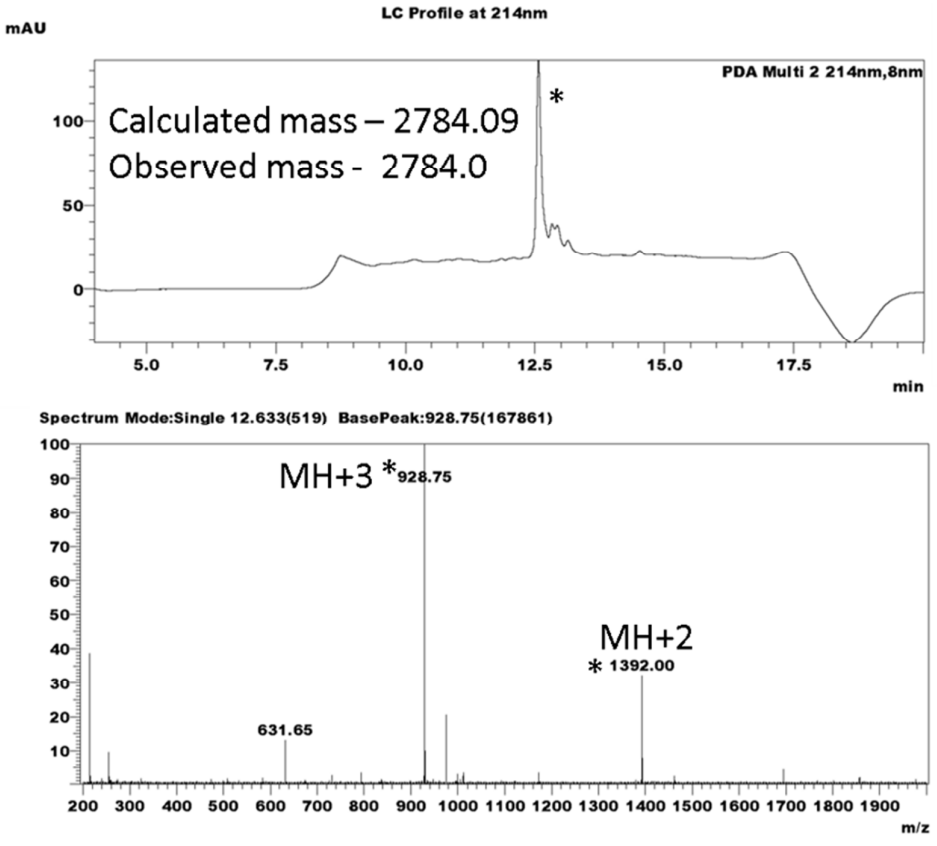
LC Profile at 214nm
mAU
PDA Multi 2 214nm,8nm
Calculated mass – 2784.09
Observed mass - 2784.0
*
100
50
0
5.0
7.5
10.0
12.5
15.0
17.5
min
Spectrum Mode:Single 12.633(519) BasePeak:928.75(167861)
MH+3 *928.75
MH+2
* 1392.00
631.65
100
90
80
70
60
50
40
30
20
10
200 300 400 500 600 700 800 900 1000 1100 1200 1300 1400 1500 1600 1700 1800 1900
m/z

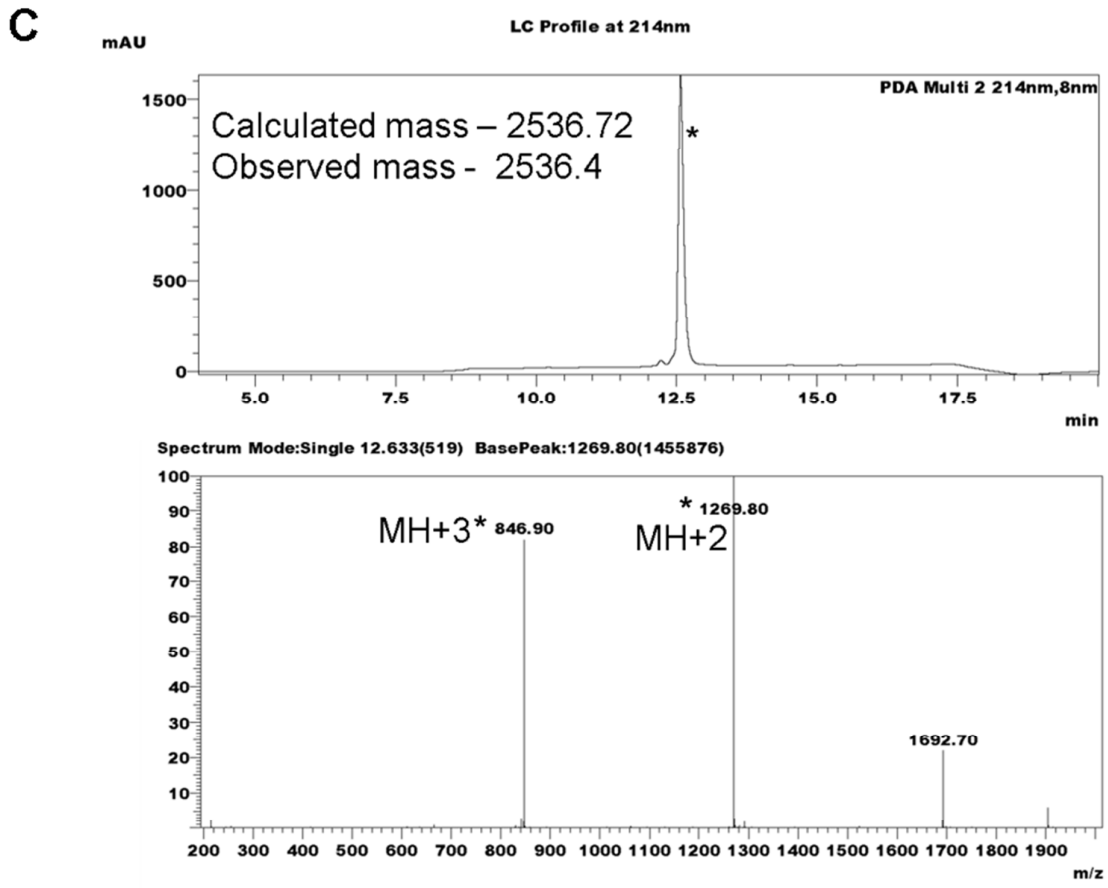

Figure S3. A. LC-MS profile of sCon-Vc1$_{1\text{-}22}$[Z1Q,DINNN$_{4\text{-}8}$]. **B.** LC-MS profile of sCon-Vc1$_{1\text{-}22}$[Z1Q,DINNN$_{12\text{-}16}$] and **C.** sCon-Vc1$_{1\text{-}22}$[NNN$_{12\text{-}14}$].

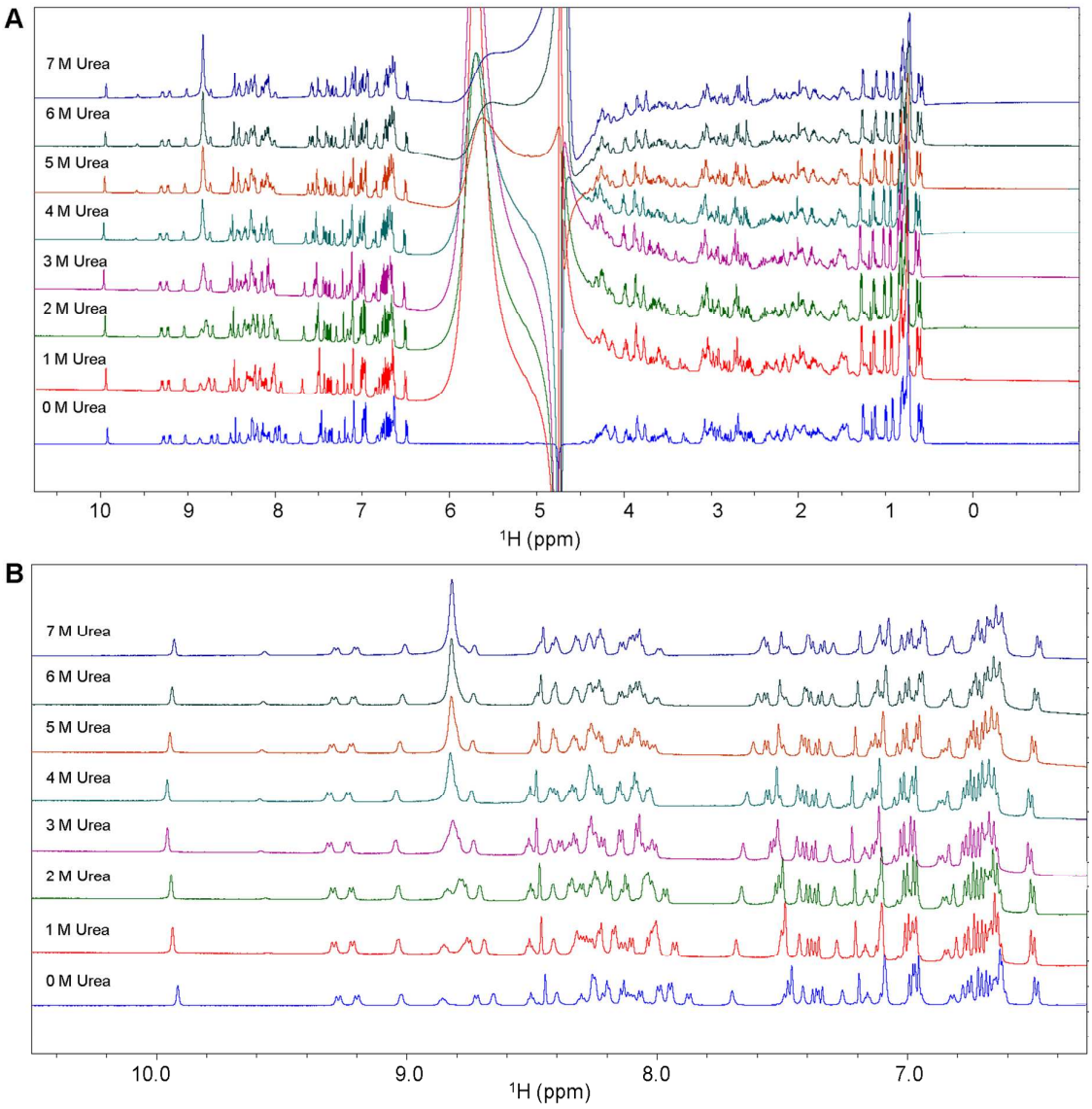
A
7 M Urea
6 M Urea
5 M Urea
4 M Urea
3 M Urea
2 M Urea
1 M Urea
0 M Urea
10
9
8
7
6
5
4
3
2
1
0
¹H (ppm)
B
7 M Urea
6 M Urea
5 M Urea
4 M Urea
3 M Urea
2 M Urea
1 M Urea
0 M Urea
10.0
9.0
8.0
7.0
¹H (ppm)

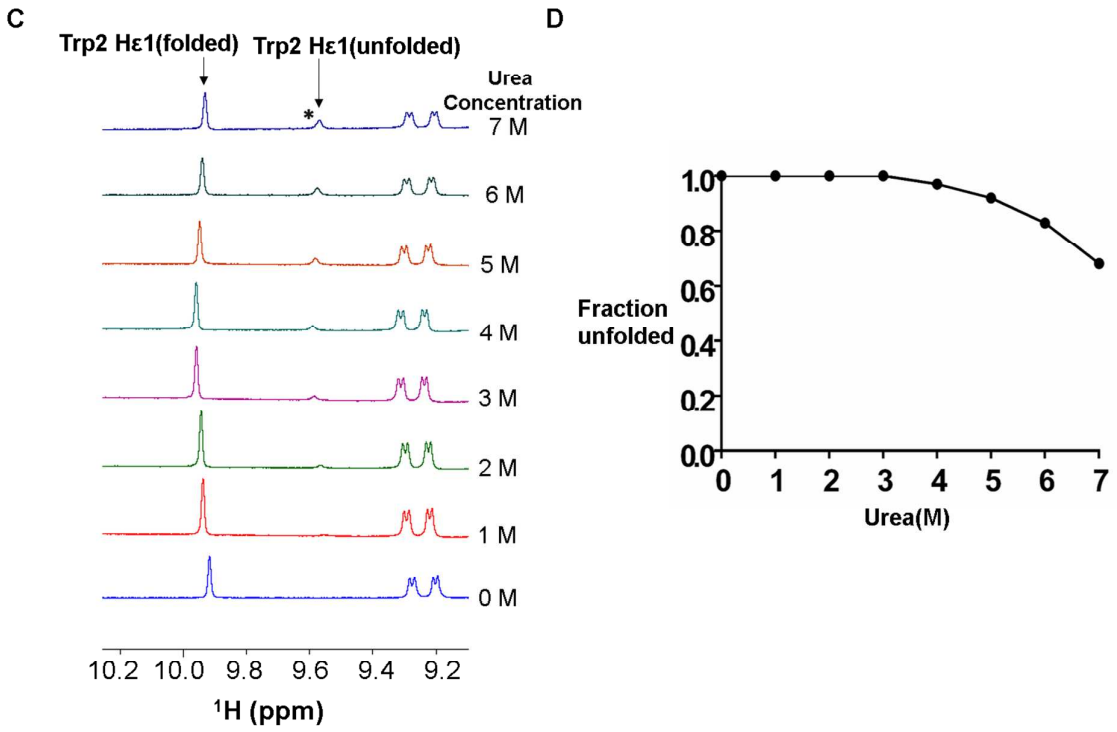

Figure S4. A. 1D ^{1}H NMR spectra of synthetic full-length contryphan-Vc1 with increasing concentrations of urea to 7 M at pH 4.0 and 20°C in water containing 7% $^{2}H_2O$. Broad signal at 5.5 ppm is due to urea. **B.** Amide and aromatic regions of spectra in A. **C.** Region of 1D ^{1}H NMR spectra showing Trp2 indole peak of both folded and unfolded conformations of sCon-Vc1. **D**. Urea unfolding curve for Trp2 indole proton peak of sCon-Vc1. Fraction of unfolded peptide was obtained from the relative intensities of the unfolded and folded resonances of Trp2 indole NH.

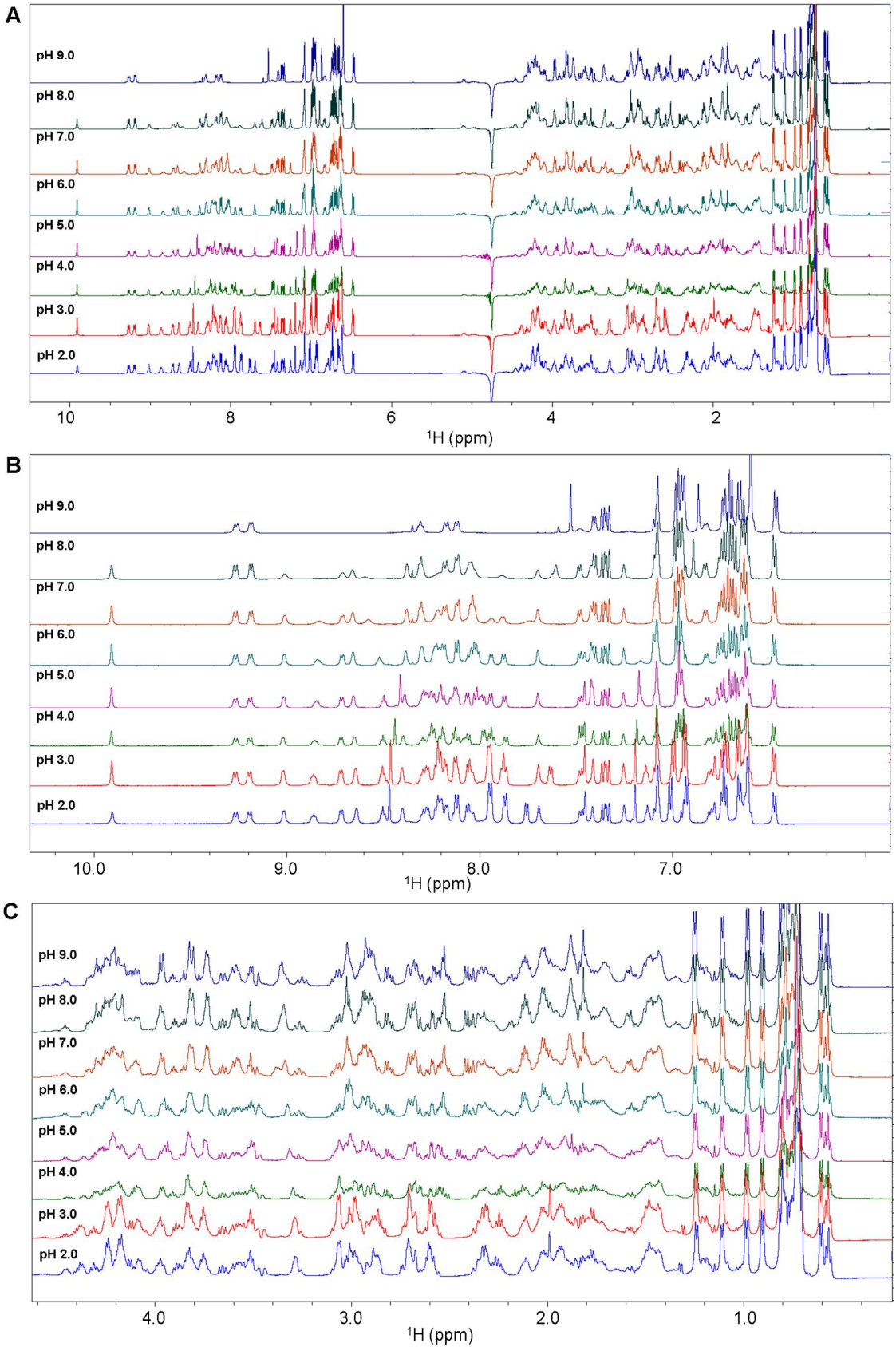
A
pH 9.0
pH 8.0
pH 7.0
pH 6.0
pH 5.0
pH 4.0
pH 3.0
pH 2.0
10
8
6
4
2
¹H (ppm)
B
pH 9.0
pH 8.0
pH 7.0
pH 6.0
pH 5.0
pH 4.0
pH 3.0
pH 2.0
10.0
9.0
8.0
7.0
¹H (ppm)
C
pH 9.0
pH 8.0
pH 7.0
pH 6.0
pH 5.0
pH 4.0
pH 3.0
pH 2.0
4.0
3.0
2.0
1.0
¹H (ppm)

Figure S5. A. One-dimensional ^{1}H NMR spectra of synthetic full-length contryphan-Vc1 over the pH range 2-9 at 20°C in water containing 7% $^{2}H_2O$. **B.** Amide and aromatic region of spectra in A. **C.** Aliphatic region of spectra in A.

A

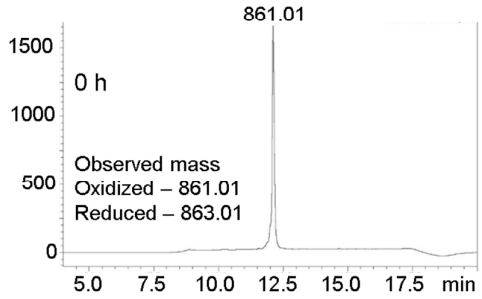
861.01
1500
1000
500
0
0 h
Observed mass
Oxidized – 861.01
Reduced – 863.01
5.0 7.5 10.0 12.5 15.0 17.5 min

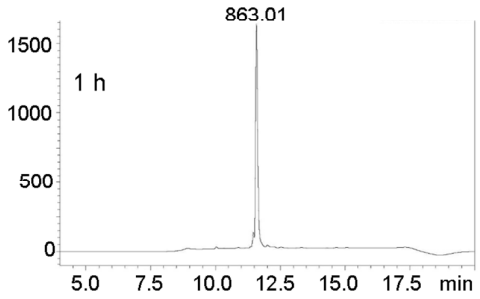
863.01
1500
1000
500
0
1 h
5.0 7.5 10.0 12.5 15.0 17.5 min

B

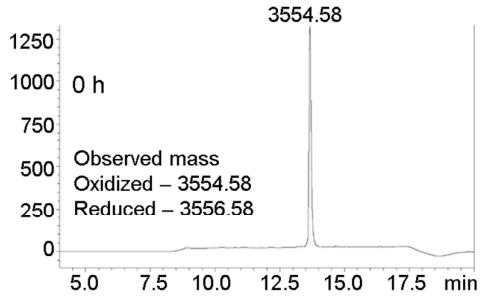
3554.58
1250
1000
750
500
250
0
0 h
Observed mass
Oxidized – 3554.58
Reduced – 3556.58
5.0 7.5 10.0 12.5 15.0 17.5 min

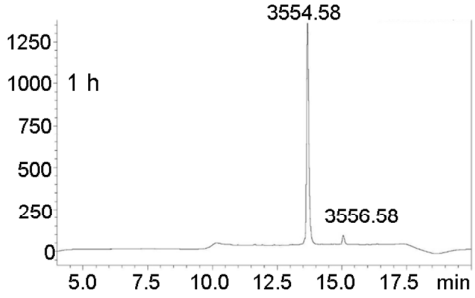
3554.58
1250
1000
750
500
250
0
1 h
3556.58
5.0 7.5 10.0 12.5 15.0 17.5 min

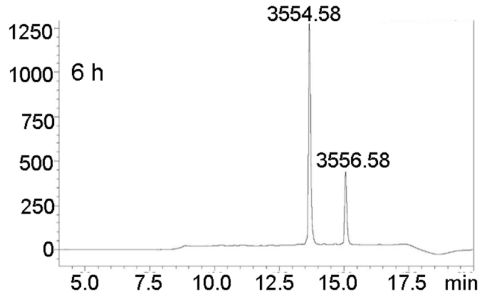
3554.58
1250
1000
750
500
250
0
6 h
3556.58
5.0 7.5 10.0 12.5 15.0 17.5 min

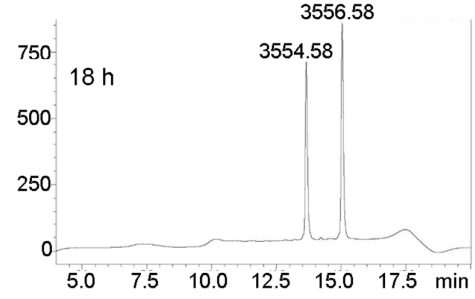
3556.58
3554.58
750
500
250
0
18 h
5.0 7.5 10.0 12.5 15.0 17.5 min

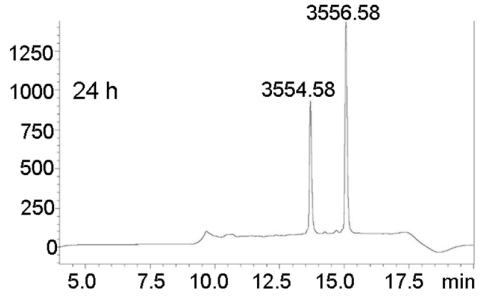
3556.58
1250
1000
750
500
250
0
24 h
3554.58
5.0 7.5 10.0 12.5 15.0 17.5 min

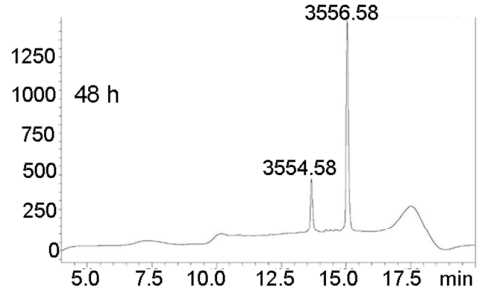
3556.58
1250
1000
750
500
250
0
48 h
3554.58
5.0 7.5 10.0 12.5 15.0 17.5 min

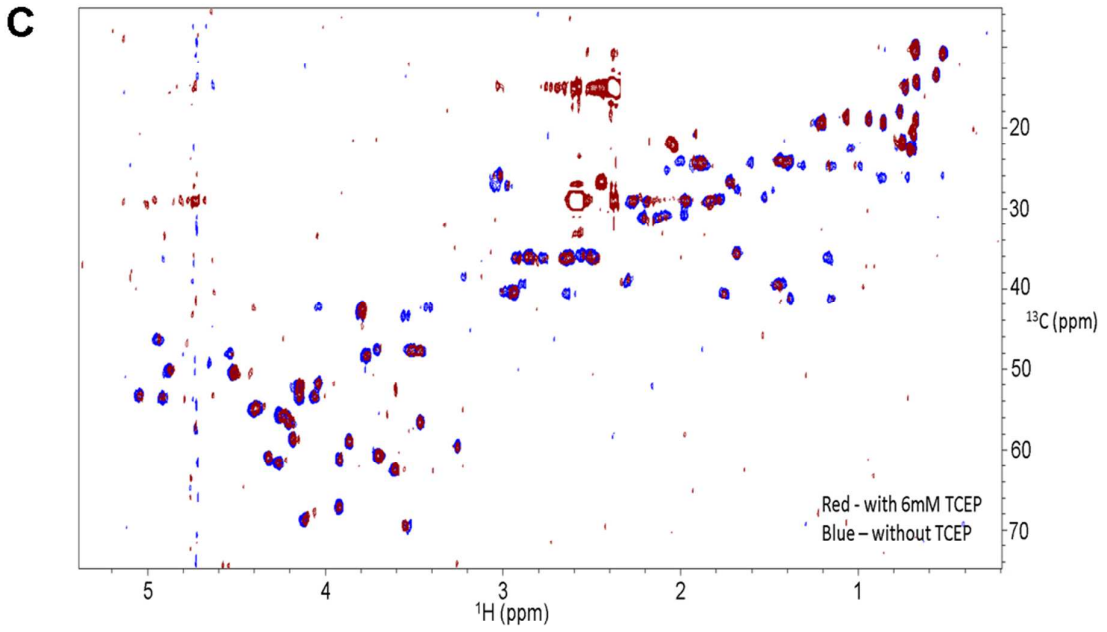
C
Red - with 6mM TCEP
Blue – without TCEP
^{13}C (ppm)
^{1}H (ppm)

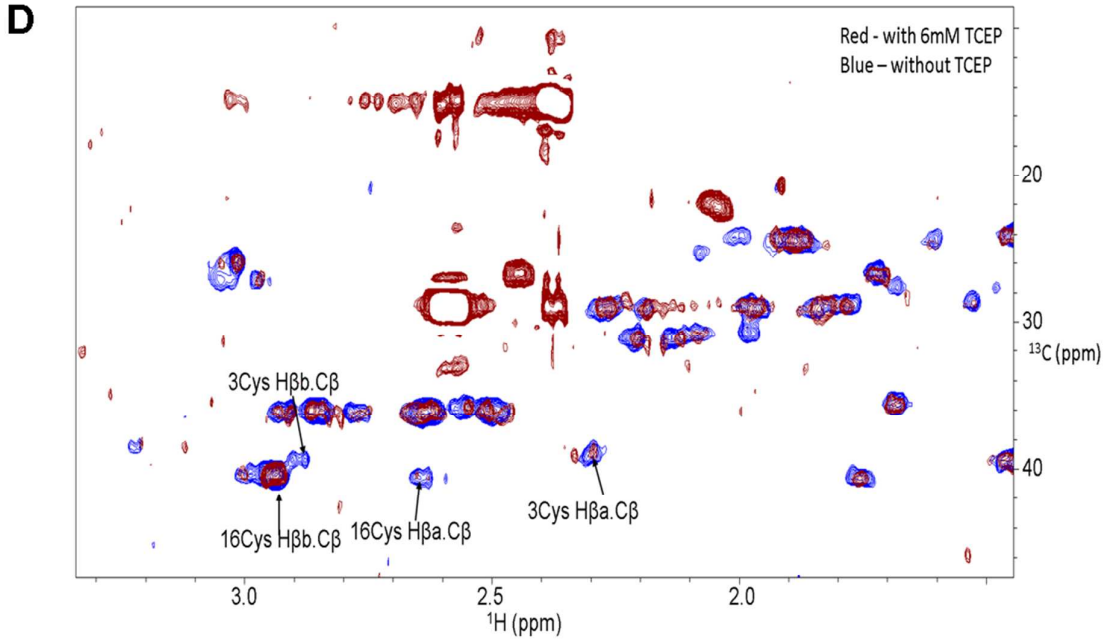
D
Red - with 6mM TCEP
Blue – without TCEP
3Cys Hβb.Cβ
16Cys Hβb.Cβ
16Cys Hβa.Cβ
3Cys Hβa.Cβ
^{13}C (ppm)
^{1}H (ppm)

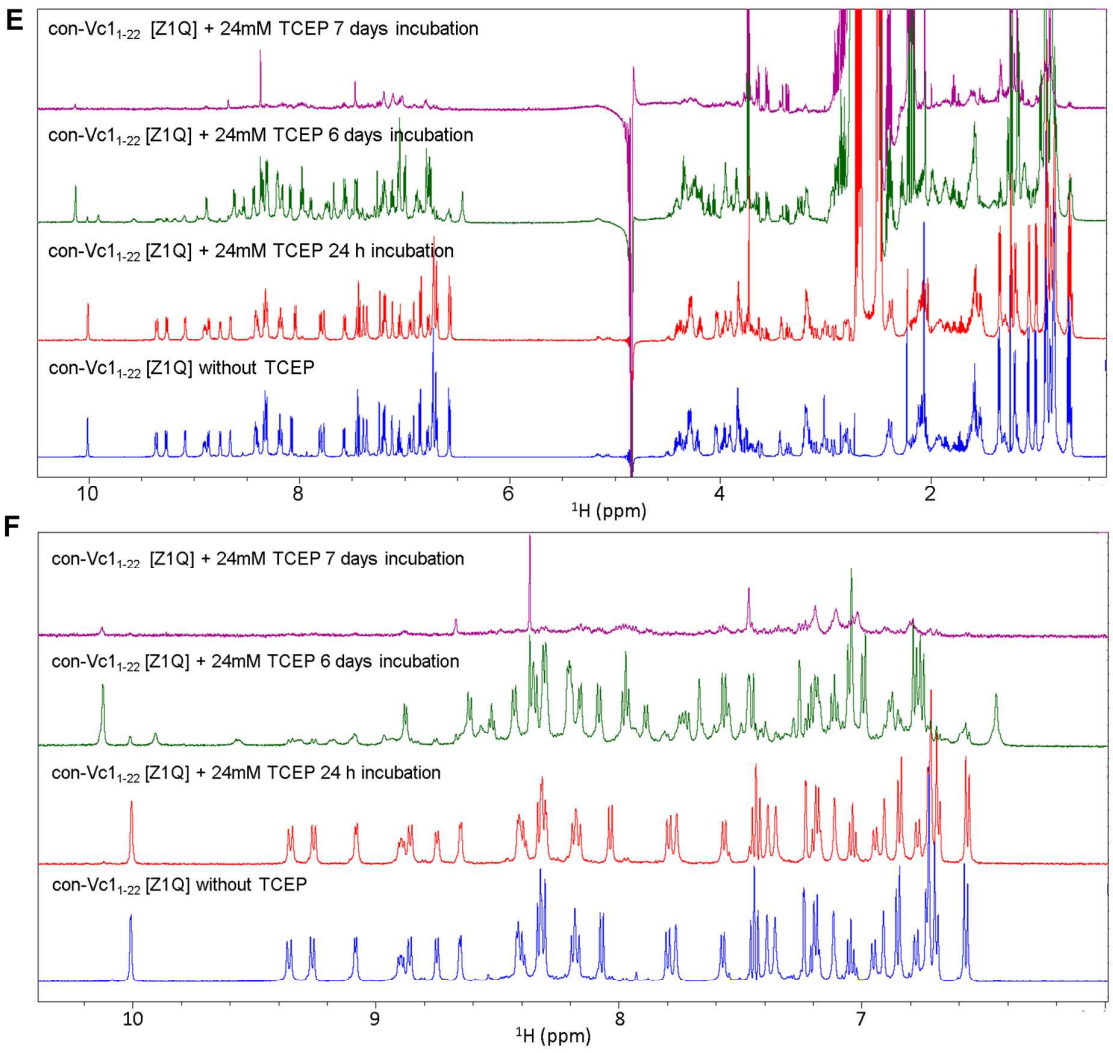

Figure S6. A. LC-MS chromatogram of contryphan-Vc2 before and after 1 h incubation with 10 mM TCEP at room temperature. **B.** LC-MS chromatogram of sCon-Vc1 at different time points after incubation with 10 mM TCEP at room temperature, with observed mass difference for oxidized and reduced species of sCon-Vc1marked. **C.** Overlay of ^{13}C HSQC spectra of sCon-Vc1 in presence and absence of 6 mM TCEP. **D.** Region of ^{13}C HSQC spectra of sCon-Vc1 showing $^{\beta}$H peaks for Cys 3 and Cys16. **E.** One-dimensional ^{1}H NMR spectra of contryphan-Vc1$_{1-22}$[Z1Q] in the presence of 24 mM TCEP at 24 h , 6 days and 7 days at 20°C, pH 4.0 in water containing 7% ^2H_2O.**E.** Amide and aromatic region of spectra in A.

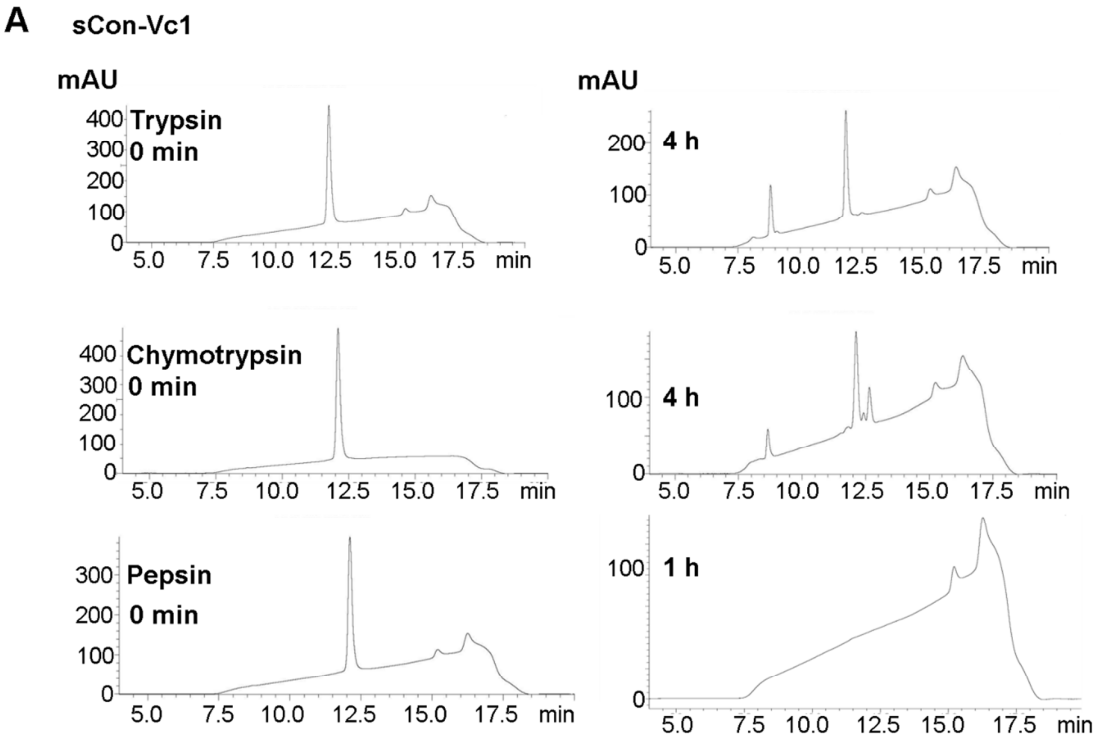
A
sCon-Vc1
mAU
Trypsin
0 min
4 h
Chymotrypsin
0 min
4 h
Pepsin
0 min
1 h
min

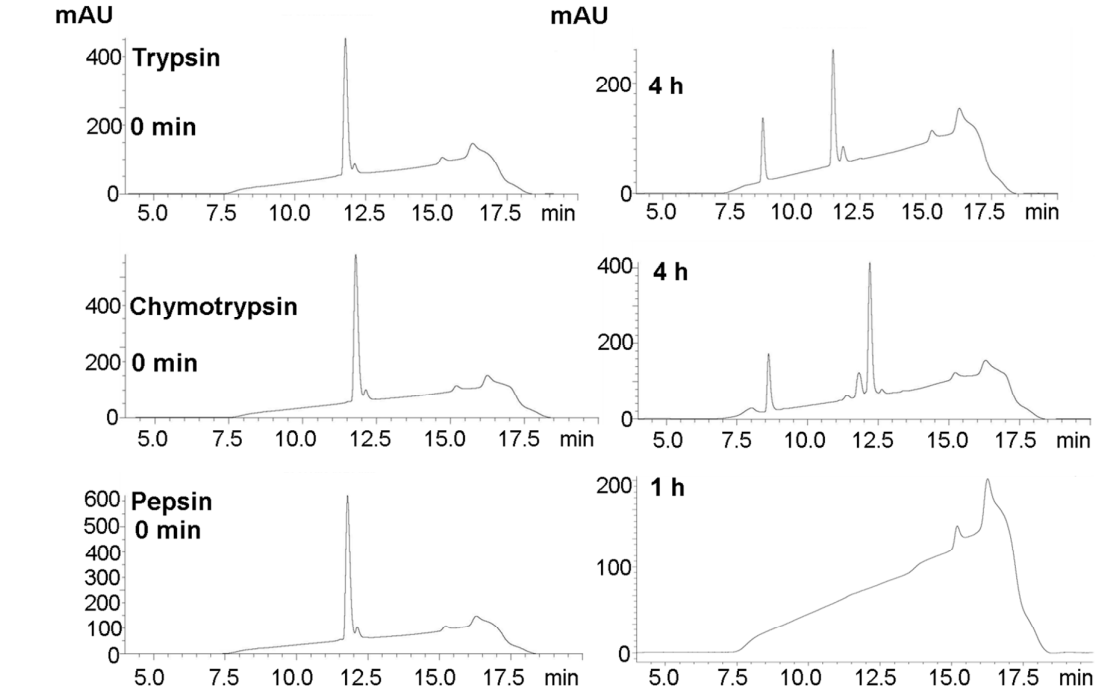
B
rCon-Vc1[Z1Q]
mAU
Trypsin
0 min
4 h
Chymotrypsin
0 min
4 h
Pepsin
0 min
1 h
min

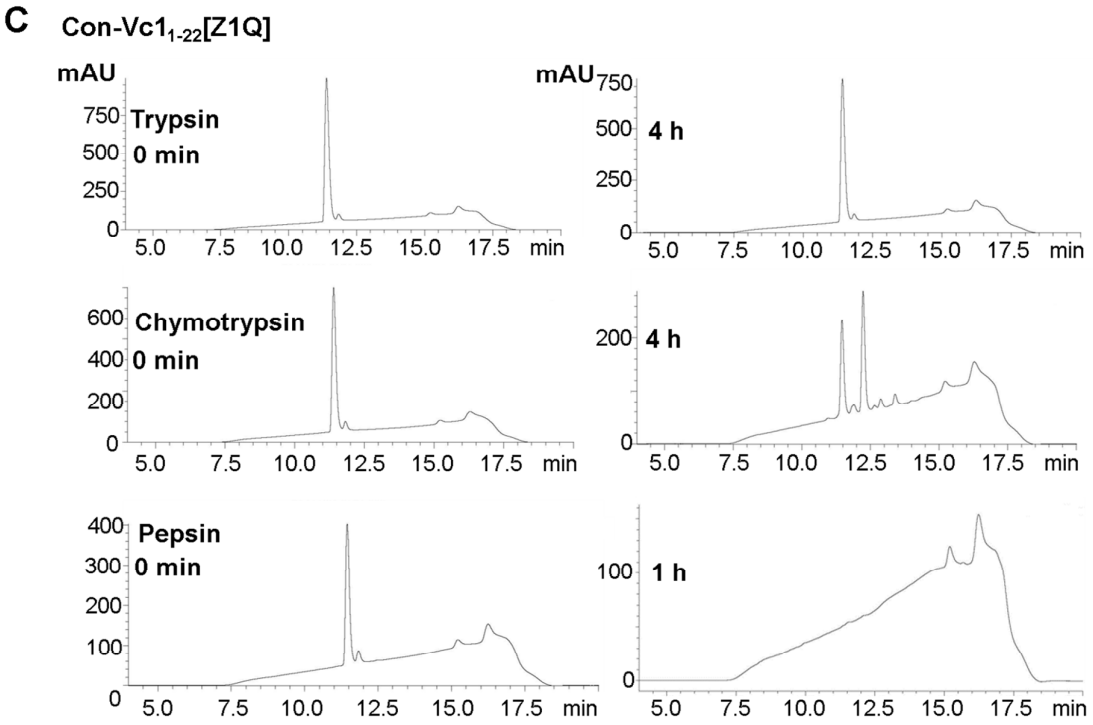
C
Con-Vc1$_{1-22}$[Z1Q]
mAU
Trypsin
0 min
4 h
Chymotrypsin
0 min
4 h
Pepsin
0 min
1 h
min

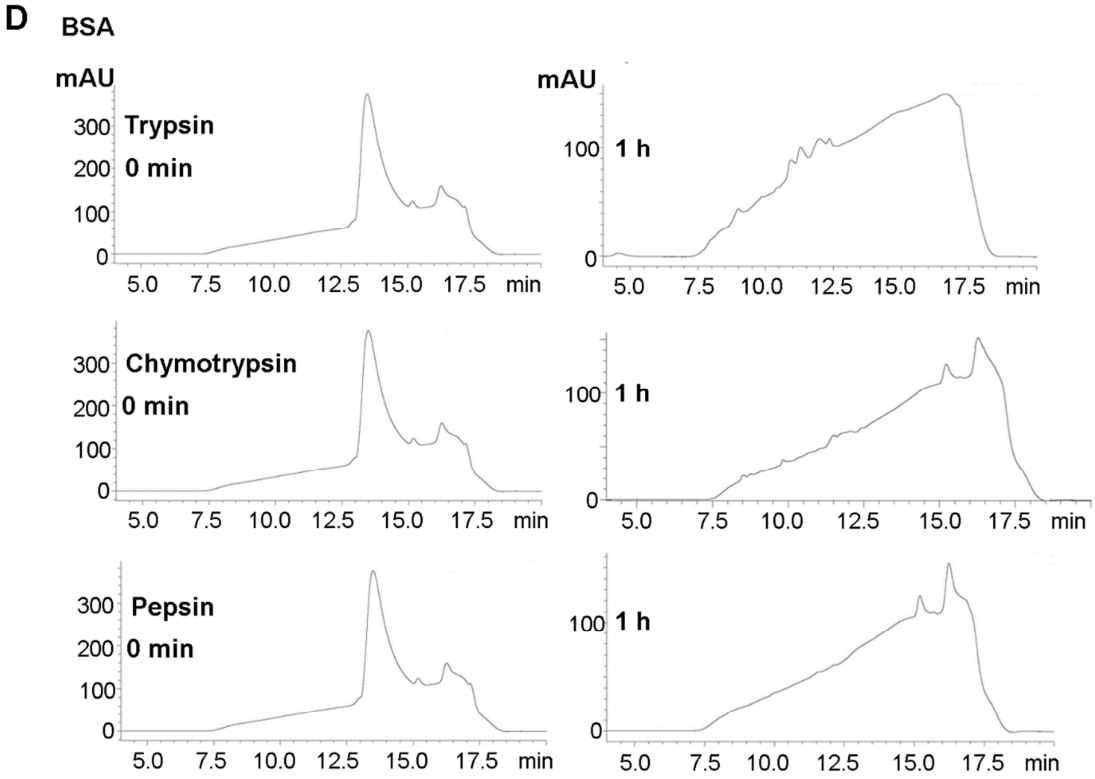
D
BSA
mAU
Trypsin
0 min
1 h
Chymotrypsin
0 min
1 h
Pepsin
0 min
1 h
min

Figure S7. Reversed-phase HPLC analysis of synthetic, recombinant full-length contryphan-Vc1 and rCon-Vc1$_{1-22}$[Z1Q] treated with trypsin, α-chymotrypsin and pepsin. **A.** Chromatograms for synthetic full-length contryphan-Vc1 digested with trypsin, α-chymotrypsin and pepsin. **B.** Chromatograms for recombinant full-length contryphan-Vc1 digested with trypsin, α-chymotrypsin and pepsin. **C.** Chromatograms for rCon-Vc1$_{1-22}$ [Z1Q] digested with trypsin, α-chymotrypsin and pepsin. **D.** Chromatograms for bovine serum albumin control digested with trypsin, α-chymotrypsin and pepsin.

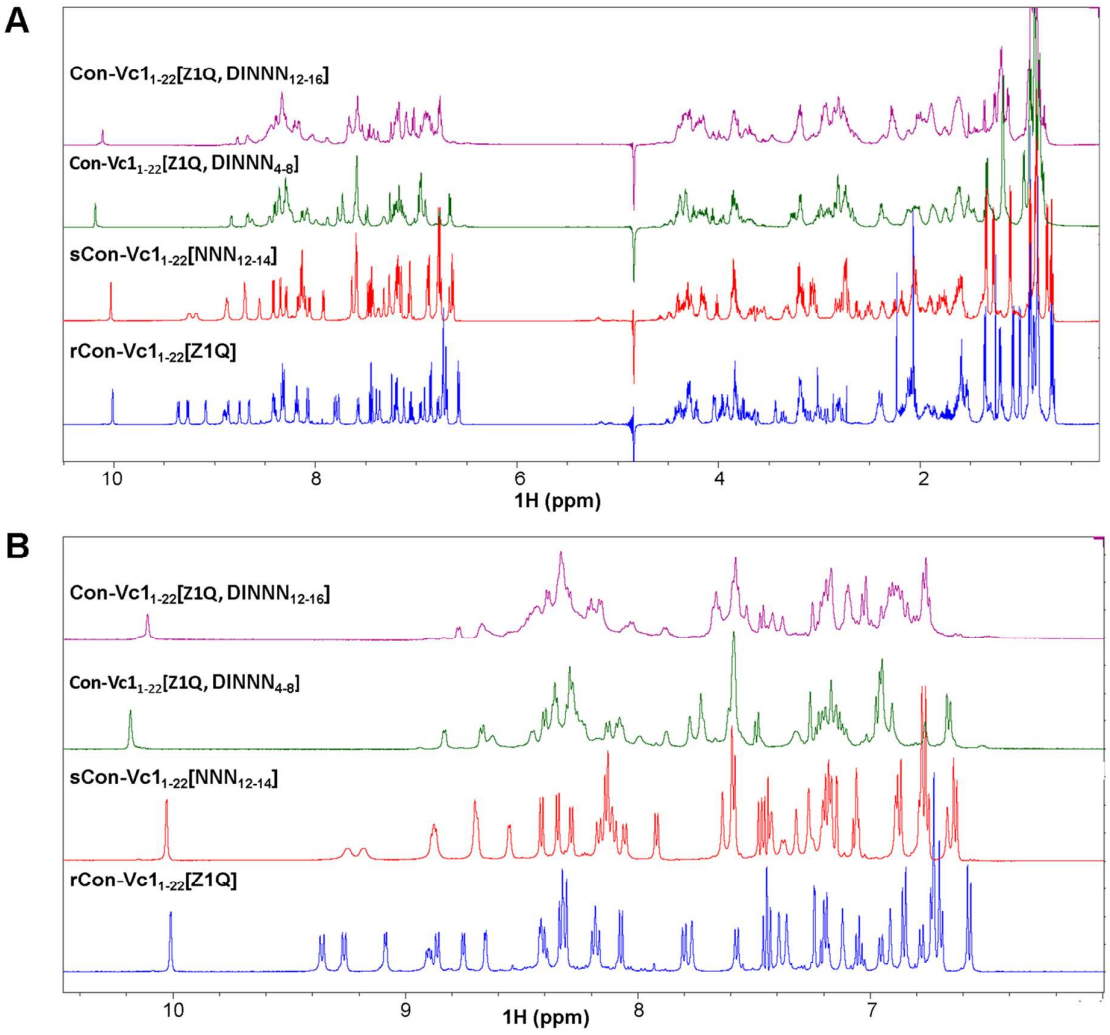

Figure S8. A. One-dimensional ^{1}H NMR spectra of rCon-Vc1$_{1-22}$[Z1Q], sCon-Vc1$_{1-22}$[NNN$_{12-14}$], sCon-Vc1$_{1-22}$[Z1Q,DINNN$_{4-8}$] and sCon-Vc1$_{1-22}$[Z1Q,DINNN$_{12-16}$] at pH 4 at 20°C in water containing 7% $^{2}H_2O$. **B.** Amide and aromatic regions of spectra in A.

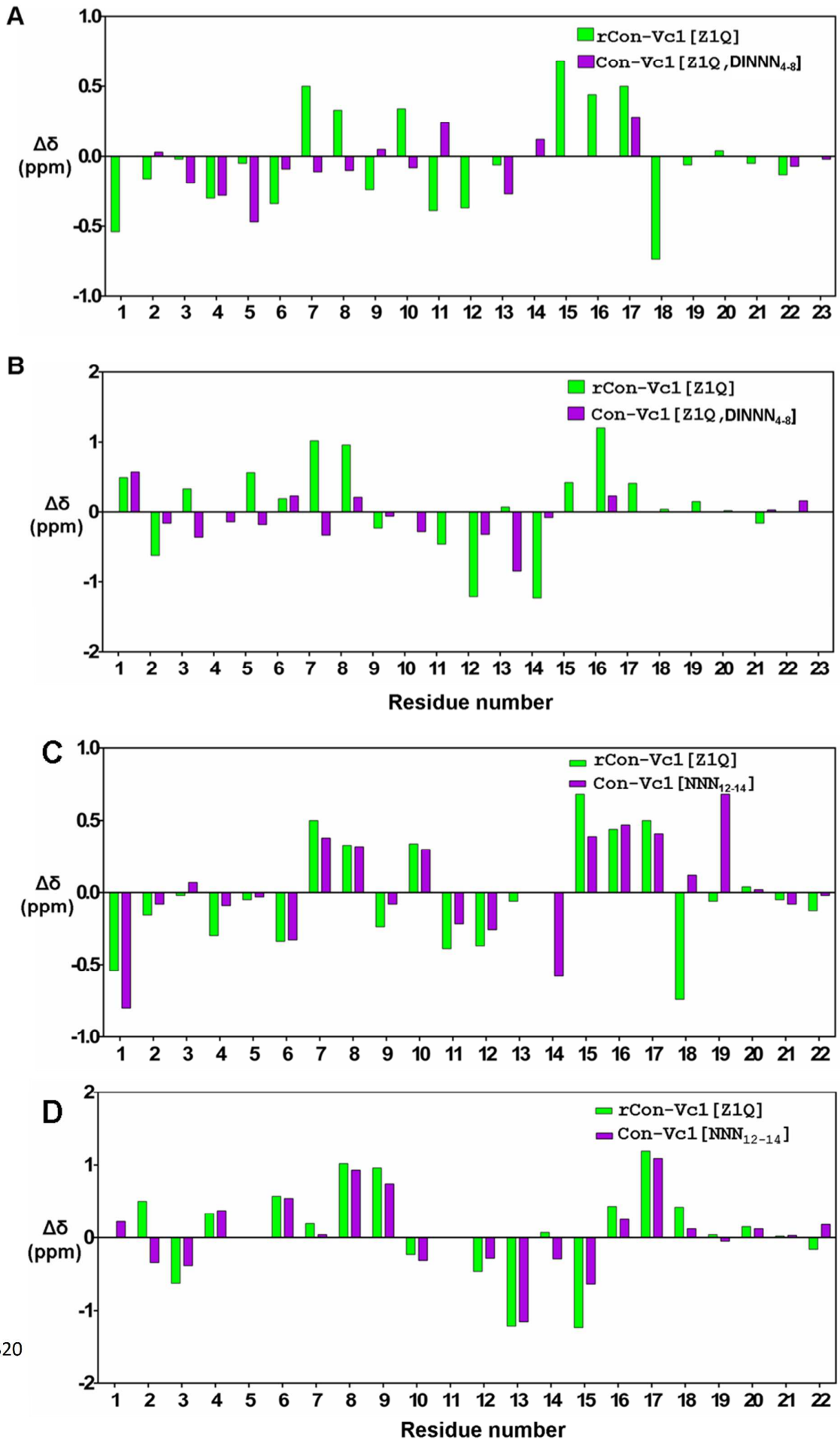
A
rCon-Vc1 [Z1Q]
Con-Vc1 [Z1Q,DINNN4-8]
Δδ (ppm)
B
rCon-Vc1 [Z1Q]
Con-Vc1 [Z1Q,DINNN4-8]
Δδ (ppm)
Residue number
C
rCon-Vc1 [Z1Q]
Con-Vc1 [NNN12-14]
Δδ (ppm)
D
rCon-Vc1 [Z1Q]
Con-Vc1 [NNN12-14]
Δδ (ppm)
Residue number

Figure S9. Deviations from random coil chemical shifts for rCon-Vc1$_{1-22}$[Z1Q], sCon-Vc1$_{1-22}$[NNN$_{12-14}$] and sCon-Vc1$_{1-22}$[Z1Q,DINNN$_{4-8}$] **A.** H^{α} chemical shift comparison between rCon-Vc1$_{1-22}$[Z1Q] and sCon-Vc1$_{1-22}$[Z1Q,DINNN$_{4-8}$] . **B.** H^{N} chemical shift comparison between rCon-Vc1$_{1-22}$[Z1Q] and sCon-Vc1$_{1-22}$[Z1Q,DINNN$_{4-8}$].**C.** H^{α} chemical shift comparison between rCon-Vc1$_{1-22}$[Z1Q] and sCon-Vc1$_{1-22}$[NNN$_{12-14}$]. **D.** H^{N} chemical shift comparison between rCon-Vc1$_{1-22}$[Z1Q] and sCon-Vc1$_{1-22}$[NNN$_{12-14}$].[1]

References

1. Wishart, D. S., Bigam, C. G., Holm, A., Hodges, R. S., and Sykes, B. D. (1995) ^{1}H, ^{13}C and ^{15}N random coil NMR chemical shifts of the common amino acids. I. Investigations of nearest-neighbor effects. *J Biomol NMR 5*, 67-81.